EFFECT OF TREHALOSE AND LITHIUM IN MOLECULAR MECHANISM OF NEUROPROTECTION IN ALZHEIMER'S DISEASE

by

Yue Xu

A thesis
presented to the University of Waterloo
in fulfillment of the
thesis requirement for the degree of
Doctor of Philosophy
in
Physics (Nanotechnology)

Waterloo, Ontario, Canada, 2024

© Yue Xu 2024

Examining Committee Membership

The following served on the Examining Committee for this thesis. The decision of the Examining Committee is by majority vote.

External Examiner:	François Lagugné-Labarthet Professor, Dept. of Chemistry, Western University
Supervisor(s):	Zoya Leonenko Professor, Dept. of Physics and Astronomy, University of Waterloo
Internal Member:	Michel Gingras Professor, Dept. of Physics and Astronomy, University of Waterloo
Internal-External Member:	Michael A. Beazely Associate Professor, School of Pharmacy, University of Waterloo
Other Member(s):	Joseph H. Sanderson Associate Professor, Dept. of Physics and Astronomy, University of Waterloo

Author's Declaration

This thesis consists of material all of which I authored or co-authored: see Statement of Contributions included in the thesis. This is a true copy of the thesis, including any required final revisions, as accepted by my examiners.

I understand that my thesis may be made electronically available to the public.

Statement of Contributions

This work has been performed by myself under the guidance and supervision of Dr. Zoya Leonenko. I contributed to the development of the hypothesis, experimental design and methodology, and performed all experiments, except for several parts listed below which were done with the help of other students. I performed all data analysis, wrote all manuscript drafts, and wrote all parts of the thesis.

Chapter 6 has been published in a peer-reviewed journal (*Biophysical Journal*, 2024), where I am the first author. All other chapters were written in the format of manuscripts and are (or will be) submitted to peer-reviewed journals. The following parts listed below included the work of other students who collaborated with me to help with my thesis work:

- Chapter 4 was completed in collaboration with PhD student Irina Bukhteeva and undergraduate student Yurii Potsiluienko. Irina conducted the experiments and data collection related to the gramicidin protein and drafted a part of the introduction about gramicidin. Yurii optimized the protocol for the BLM experiment and performed test experiments with lipids only. I did all the work involving amyloid protein and completed the writing of the manuscript, which combined data for both gramicidin and amyloid proteins and I wrote chapter 4.

- In Chapter 5, a part of the lipid monolayer samples was imaged by postdoctoral fellow Dr. Danielle M. McRae. Most of the experiments and all of the data analysis and writing were done by me.

- In Chapter 6, PhD student Carina Teresa Filice helped me with optimizing experimental protocols and provided training with BLM. All the experiments and data analysis were completed by me. I wrote a first draft of the manuscript. Dr. Zoya Leonenko and Carina Filice contributed to the manuscript writing for publication.

  Citation: Yue Xu, Carina T. Filice and Zoya Leonenko. Protective effect of trehalose sugar on amyloid-membrane interactions using BLM electrophysiology. *Biophysical Journal*, 123(12):1690–1704, 2024. doi:10.1016/j.bpj.2024.05.012. [Journal Cover].

- Chapter 8 was done in collaboration with PhD student Kartar Singh, under the supervision of Dr. Zoya Leonenko and Dr. Michael Beazely using equipment in Dr.Beazely's Lab at the School of Pharmacy. Kartar and I designed experimental protocols for MTT cell viability experiments together. Kartar conducted cell culture and MTT assays. I performed the data analysis and wrote the manuscript draft and the chapter except for the Materials and Methods section, which was written by Kartar.

- In Chapter 10, a part of the lipid monolayer samples was imaged by postdoctoral fellow Dr. Danielle M. McRae. Most of the experiments and all of the data analysis and writing were done by myself.

- I completed Chapter 11 with the help of undergraduate student Lunlun Guan, who was co-supervised by me in the Lab. Lunlun helped me collect part of the data. I performed most of the BLM experiments and data analysis. I did all the writing entirely.

Publications

1. Yue Xu, Carina T. Filice and Zoya Leonenko. Protective effect of trehalose sugar on amyloid-membrane interactions using BLM electrophysiology. *Biophysical Journal*, 123(12):1690-1704, 2024. [Journal Cover].

2. Robert D. E. Henderson, Nanqin Mei, Yue Xu, Ravi Gaikwad, Shawn Wettig, Zoya Leonenko. Nanoscale Structure of Lipid-Gemini Surfactant Mixed Monolayers Resolved with AFM and KPFM Microscopy. *Nanomaterials*, 14(7):572, 2024

3. Yue Xu, Danielle M. McRae, Zoya Leonenko. Effect of trehalose and NaCl on the structure and electrostatic properties of Langmuir lipid monolayers by atomic force microscopy and Kevin probe force microscopy. *Langmuir*, under review.

4. Yue Xu, Danielle M. McRae, Zoya Leonenko. Quantitative Analysis of Influence of Trehalose on Aβ Binding to Membranes by Localized Surface Plasmon Resonance Spectroscopy. *ACS Omega*, under review.

Oral presentations

1. Chemical Biophysics Symposium, Toronto, Trehalose Sugar Protects Lipid Membrane Against Amyloid-beta Toxicity in Alzheimer's Disease, Apr 26-28, 2024.

2. NANO In BIO, Guadeloupe, Trehalose Sugar Protects Lipid Membrane Against Amyloid-beta Toxicity in Alzheimer's Disease, Apr 14-20, 2024.

Poster presentations

1. Biomedical Engineering and Technology Research Day, University of Waterloo, Canada, Trehalose Sugar Protects Lipid Membrane Against Amyloid-beta Toxicity in Alzheimer's Disease, July 24, 2024.

2. Biophysical Society (BPS) Meeting - Molecular Biophysics of Membranes, Tahoe Lake, USA, Trehalose Sugar Protects Lipid Membrane Against Amyloid-beta Toxicity in Alzheimer's Disease, Jun 2-7, 2024.

3. Canadian Association of Physicists Meeting, Hamilton, Canada, Protective Effect of Trehalose Sugar Against Amyloid-β Toxicity in Model Lipid Membranes, Jun 5-10, 2022.

4. Biophysical Society of Canada Meeting, Ottawa, Canada, Comparison of Protein Channels Formed by Amyloid-β and Gramicidin in Model Lipid Membranes, May 25-27, 2022.

5. Biophysical Society of Canada Meeting, online, Effect of Trehalose on Model Neuronal Membrane and Amyloid-β Toxicity, May 25-28, 2021.

Abstract

Alzheimer's Disease (AD) is still a challenging issue for humans since its first case was identified by Alois Alzheimer over one hundred years ago. Approximately thirty years ago, the "Amyloid cascade hypothesis" was proposed, which is a milestone that began to reveal the mystery of AD. The aggregation and deposition of endogenous amyloid-beta (Aβ) proteins in brains are known to be one of the main pathogenic factors of AD. One of the pathways to neurodegeneration driven by Aβ proteins involves Aβ damage to neuronal membranes, which may result in neuron impairment and death. On the other hand, Aβ proteins have antimicrobial properties, suggesting they may serve functionally in the brain. This could be one of the reasons to explain the severe side effects seen in clinical anti-Aβ treatment for AD.

Instead of focusing on anti-Aβ, I aim to explore a therapeutic strategy that focuses on membrane protection. The goal of my work is to investigate the potential of membrane-targeted agents, trehalose and lithium, to protect lipid membranes against Aβ toxicity.

Trehalose, a natural-derived sugar, is explored as a potential treatment for neurodegenerative Parkinson's Disease. Lithium, as a mood stabilizer, is commonly used for treating bipolar disorder. Both of the agents are investigated for neurological disorders and can interact with cellular membranes with distinct mechanisms. In this thesis, I ask whether their interaction with lipid membranes can protect membranes from Aβ-induced damage, thereby lowering Aβ neurotoxicity.

Hence, the entire thesis addresses two main questions.

- How does trehalose/lithium affect membrane properties?
- Can trehalose/lithium protect membranes from Aβ toxicity?

To explore the two questions for trehalose and lithium, respectively, the thesis is divided into two parts: Part I - trehalose (Chapters 3 to 8) and Part II - lithium (Chapters 9 to 11).

In Part I, I used Langmuir-Blodgett (LB) Trough, atomic force microscopy (AFM), and Kelvin probe force Microscopy (KPFM) to explore the influence of trehalose on the

mechanical and electrostatic properties of model lipid monolayers composed of DPPC, POPC lipids and cholesterol. The study found that trehalose can enhance the fluidity and alter the electrostatic properties of lipid monolayers, with modulation by NaCl.

To assess whether trehalose can protect lipid membranes from Aβ damage, I utilized black lipid membrane (BLM) electrophysiological techniques to evaluate the quality and permeability of membranes exposed to trehalose and Aβ. Results from BLM experiments demonstrated trehalose alleviates Aβ-induced membrane disruption. Furthermore, I explored the binding of Aβ to lipid membranes in the presence of trehalose solutions by localized surface plasmon resonance (LSPR) spectroscopy and found that trehalose can reduce Aβ binding to lipid membranes. Finally, I confirmed the unique neuroprotection of trehalose in cell studies, where trehalose decreased the cell mortality rate caused by toxic Aβ proteins.

Part II explored the potential of lithium in mitigating Aβ toxicity on lipid membranes. Similarly, I used LB trough, AFM and KFPM to compare the influence of LiCl and KCl on lipid membranes. The results demonstrated the distinct contribution of Li^+ and K^+ on the mechanical and electrostatic properties of DPPC-POPC-Chol lipid monolayers. Li^+ has a pronounced effect on reducing the lipid molecular area, increasing monolayer fluidity, and strongly competing with K^+ in interacting with lipid monolayers. Lastly, BLM was employed to evaluate the membrane permeability in exposure to Aβ and LiCl. The membrane conductance results obtained by BLM suggested that the modulation of LiCl at the therapeutic level enhances membrane resilience to Aβ-induced damage.

This research exposes the modulation of membrane-active trehalose and lithium on lipid membrane properties and their protective role in AD. It contributes to exploring a new therapeutic approach against Aβ toxicity that focuses on membrane protection, which may aid in developing prevention and treatment strategies for AD.

Acknowledgments

First and foremost, I would like to express my deepest gratitude to my supervisor, Zoya Leonenko, for her invaluable guidance and support throughout this research. I vividly remember a call from Dr. Leonenko on a weekend in the summer during the COVID-19 quarantine time four years ago. She asked, "Do you want to transfer to a PhD?" That call marked the formal beginning of my research career.

I would also like to thank the members of my committee, Michel Gingras, Joseph Sanderson, and Michael Beazely, for their constructive feedback and practical suggestions provided every year, which significantly enhanced the quality of this thesis and my presentation skills.

I am grateful to the entire Leonenko lab, Danielle McRae, Carina Filice, Irina Bukhteeva, Kartar Singh, Brenda Lee, Nanqin Mei, James Livingstone, Morgan Robinson and the undergraduates who worked with me, Nikolas Zelem, Lunlun Guan and Yurii Potsiluienko, creating a supportive and stimulating environment. I sincerely appreciated their collaboration, training, discussion, and brainstorming to tackle problems. In particular, special thanks to Danielle, Carina and Nicolas who proofread my thesis. This work could not have been done without their dedicated help.

I am deeply appreciative to my parents, Shaochun Xu and Zhangping Yin, and my sister and brother, Xing Xu and Hui Xu for their endless love, support and encouragement throughout my life.

I thank my friends, Yifan Ding and Wei Zhou, for their encouragement and support in my academic journey. I also would like to thank my partner, Yuming Zhao, for his patience, companionship and love. It was really motivating to me when we worked on our theses together.

I acknowledge the financial support from NSERC, making this research possible.

Dedication

To my mom and dad.

Table of Contents

Examining Committee ii

Author's Declaration iii

Statement of Contributions iv

Abstract vii

Acknowledgments ix

Dedication x

List of Figures xviii

List of Tables xxii

1 Introduction 1

1.1 Role of Amyloid-β Proteins in Alzheimer's Disease 2

1.2 Membrane Toxicity Induced by Aβ Oligomers 3

1.3 Aβ as a Potential Antimicrobial Peptide 5

1.4 Current Pharmaceutical Strategies Targeting Aβ Peptides 7
1.4.1 Drugs Targeting Depletion of Aβ Production 7
1.4.2 Drugs Inhibiting Aβ Aggregation 8
1.4.3 Drugs Enhancing Aβ Clearance 9
1.4.4 Small Molecules Modulate Membrane Stability Against Aβ Toxicity 11
1.5 Conclusion 13
1.6 Overview of the Thesis 13
1.6.1 Research Goal 13
1.6.2 Research Questions 14

2 Methodology **15**
2.1 Black Lipid Membrane Electrophysiology 15
2.2 Localized Surface Plasmon Resonance 17
2.3 Langmuir-Blodgett Trough 20
2.3.1 Surface Pressure-Area Isotherm 22
2.3.2 Lipid Monolayer Deposition 23
2.4 Atomic Force Microscopy 25
2.4.1 Kelvin Probe Force Microscopy 28
2.5 MTT Cell Viability Assay 29

Results **31**

I Trehalose **32**

3 Introduction of Part I **33**
3.1 Impact of Trehalose on Aβ Proteins 34

3.2 Interaction of Trehalose with Lipid Membranes 35
3.3 Metabolism and Existence of Trehalose in Vertebrates 36
3.4 Conclusion 37

4 Small Amyloid-β Oligomers can Form Ion Channels as Small as Gramicidin in Model Lipid Membranes 38

4.1 Introduction 39
4.2 Materials and Methods 41
4.2.1 Reagents 41
4.2.2 Sample Preparation 41
4.2.3 Black Lipid Membrane 43
4.2.4 Atomic Force Microscopy (AFM) 43
4.3 Results and Discussion 44
4.3.1 AFM Images of Aβ1-42 Oligomers and Fibrils 44
4.3.2 BLM Electrophysiology for Aβ1-42 & Gramicidin-membrane Interaction 46
4.3.3 Interactions of Aβ1-42 Oligomers with Suspended Lipid Membranes 47
4.3.4 Comparison of Aβ1-42-induced Step-like Current with Gramicidin . 50
4.4 Conclusion 53

5 Effect of Trehalose and NaCl on the Structure and Electrostatic Properties of Langmuir Lipid Monolayers by Atomic Force Microscopy and Kevin Probe Force Microscopy 54

5.1 Introduction 55
5.2 Materials and Methods 58

5.2.1 Pressure-Area Isotherm . . . 58
5.2.2 Monolayer Deposition . . . 58
5.2.3 AFM, KPFM and Image Analysis . . . 59
5.3 Results and Discussion . . . 59
5.3.1 Pressure - Area Isotherm . . . 59
5.3.2 Elastic Compressibility Modulus . . . 62
5.3.3 AFM and KPFM . . . 64
5.4 Conclusion . . . 72

6 Protective Effect of Trehalose Sugar on Amyloid-membrane Interactions using BLM Electrophysiology 73

6.1 Introduction . . . 74
6.1.1 Amyloid-β and Alzheimer's Disease . . . 74
6.1.2 Protecting Membranes against Aβ using Small Molecules . . . 75
6.1.3 Trehalose, Aβ, and Membranes . . . 76
6.2 Materials and Methods . . . 79
6.2.1 Black Lipid Membrane Electrophysiology . . . 79
6.2.2 Atomic Force Microscopy (AFM) . . . 81
6.3 Results and Discussion . . . 83
6.3.1 Black Lipid Membrane Study of the Effect of Trehalose on Aβ-Membrane Interactions . . . 83
6.3.2 Single-event Recordings of Induced Membrane Damage (Current Versus Time) . . . 91
6.3.3 Atomic Force Microscopy . . . 96
6.4 Conclusion . . . 101

7 Quantitative Analysis of the Influence of Trehalose on Amyloid-β Binding to Membranes by Localized Surface Plasmon Resonance Spectroscopy 102

7.1 Introduction . . . 103

7.1.1 Theoretical Background of LSPR . . . 105

7.2 Materials and Methods . . . 106

7.2.1 Reagents . . . 106

7.2.2 Vesicle Preparation . . . 107

7.2.3 Aβ Solution Preparation . . . 107

7.2.4 LSPR Experiments . . . 107

7.2.5 AFM Imaging . . . 110

7.3 Results and Discussion . . . 111

7.3.1 Determination of Membrane Thickness . . . 111

7.3.2 Visualization of Membranes on LSPR Sensors . . . 113

7.3.3 Quantitive Estimation on Aβ Adsorbate Layer . . . 115

7.4 Conclusion . . . 118

8 Trehalose, but not Other Sugars, Protects HT22 Cells against Amyloid-β Toxicity 119

8.1 Introduction . . . 120

8.2 Materials and Methods . . . 121

8.3 Results . . . 123

8.4 Discussion . . . 125

8.5 Conclusion . . . 126

II Lithium **127**

9 Introduction of Part II **128**

9.1 Lithium as a Medical Treatment in Bipolar Disorder . . . 129

9.2 Impact of Li^+ on Lipid Membranes . . . 130

9.3 Connection between BD and AD . . . 130

9.4 Lithium as a Potential Neuroprotective Agent for AD . . . 131

9.5 Conclusion . . . 131

10 Influence of Lithium and Potassium on the Electrostatic Properties of Lipid Membranes **132**

10.1 Introduction . . . 133

10.2 Materials and Methods . . . 136

10.2.1 Materials . . . 136

10.2.2 Pressure-Area Isotherm . . . 136

10.2.3 Monolayer Deposition . . . 137

10.2.4 AFM, KPFM Imaging and Image analysis . . . 137

10.3 Results and Discussion . . . 138

10.3.1 Compression Isotherms . . . 138

10.3.2 Elastic Compressibility Modulus . . . 141

10.3.3 AFM and KPFM Images . . . 145

10.4 Conclusion . . . 148

11 Lithium Reduces Amyloid-β induced Damage in DPPC-POPC-Cholesterol Membranes **150**

11.1 Introduction . . . 151

11.2 Materials and Methods . . . 153
11.2.1 Materials . . . 153
11.2.2 Lipid Preparation and Lipid Membrane Formation . . . 153
11.2.3 Aβ Preparation . . . 154
11.2.4 Black Lipid Membrane Electrophysiology . . . 154
11.3 Results and Discussion . . . 155
11.3.1 Membrane Suspended in KCl and LiCl solutions . . . 155
11.3.2 Influence of LiCl on Aβ Ion Channels . . . 158
11.3.3 Influence of LiCl on Aβ-induced Transient Pores . . . 160
11.4 Conclusion . . . 163

12 Conclusion and Future Work **164**
12.0.1 Conclusion . . . 164
12.0.2 Future Work . . . 166

References **168**

APPENDICES **211**

A Supplementary Materials **212**
A.1 Membranes Embedded with Amyloid-β . . . 212
A.2 Determination of Sensor Sensitivity m . . . 213
A.3 Comparison between Vertical BLM and Horizontal BLM . . . 214
A.3.1 Amyloid-beta Behaviours in Horizontally-suspended Membranes vs Vertically-suspended Membrane . . . 215

List of Figures

1.1 Multiple mechanism of Aβ perturbance on lipid membrane 4

1.2 Anti-Aβ antibodies 10

2.1 Schematics of Black Lipid Membrane 16

2.2 Schematics of Surface Plasmon Resonance. 18

2.3 Working principle for a typical LSPR instrument. 19

2.4 Front (left) and side (right) schematics of a Wilhelmy plate immersed in the aqueous subphase 21

2.5 Pressure-area isotherm and lipid phase transition 22

2.6 Deposition of the lipid monolayer on the mica substrate 24

2.7 Atomic force microscopy 25

2.8 Lennard-Jones force model. 27

2.9 Reduction of MTT to formazan by mitochondrial reductase 30

3.1 Chemical structure of trehalose 34

4.1 Aβ/gramicidin-membrane interaction 39

4.2 Chemical structures of DPPC, POPC and cholesterol. 42

4.3 Aβ1-42 aggregates deposited on mica imaged by AFM and corresponding histogram . . . 45
4.4 Ion current increases induced by Aβ and gramicidin measured at 100 mV. . 47
4.5 Dwell time and conductance of ion current events caused by Aβ1-42 oligomers-membrane interaction . . . 48
4.6 The comparison of Aβ ion channels and gramicidin channels . . . 51

5.1 Pressure-area isotherm and monolayers produced by LB Trough in water subphase. . . . 60
5.2 Averaged isotherms of ternary lipids (DPPC-POPC-Chol 4:4:2) in different subphases . . . 61
5.3 Compressibility modulus of monolayers in different subphase . . . 63
5.4 Height (AFM) and contact potential difference (CPD) images (KPFM) of monolayers formed from water and trehalose subphase . . . 65
5.5 Height (AFM) and contact potential difference (CPD) images (KPFM) of monolayers formed from NaCl and Treh-NaCl subphase . . . 68
5.6 Sodium ion (Na^+) coordinates with three water molecules and three oxygen from phosphate and carbonyl group of DMPC lipids . . . 71

6.1 Hypothesis of trehalose protection mechanism against Aβ damage to lipid membranes . . . 78
6.2 Schematic of electrophysiological planar bilayer recording system . . . 79
6.3 *I-V* dependence curves to estimate integral membrane permeability in buffers with and without trehalose . . . 85
6.4 *I-V* curves to estimate membrane conductance in the presence of Aβ1-42 . 88
6.5 Aβ-membrane interactions and current fluctuation induced by Aβ damage 92
6.6 Membrane conductance of single current fluctuation events . . . 93

6.7 Aβ oligomers on mica imaged by AFM 96
6.8 Representative AFM images of lipid membranes and corresponding cross-section profiles 98

7.1 Schematic of LSPR experiments 109
7.2 LSPR response to membrane formation and membrane thickness 112
7.3 AFM images of the LPSR sensor and membranes on the sensors 114
7.4 AFM images of dehydrated membranes and crossections on gold sensors . . 115
7.5 Model for LSPR binding layers 116
7.6 LSPR response to Aβ binding to lipid membranes $\Delta\lambda_2$ and corresponding thickness 117

8.1 Viability of HT22 cells incubated with trehalose and Aβ1-42 oligomers. . . 123
8.2 Viability of HT22 cells incubated with sugars and Aβ1-42 oligomers 124

9.1 Lithium and lithium ion. A lithium atom loses one electron and becomes a lithium ion (Li^+). 128

10.1 Pressure-area isotherms of the DPPC-POPC-Chol lipid mixture in the Li/K subphases 138
10.2 The average change in molecular area in Li/K subphases 139
10.3 compressibility modulus in Li/K subphase 142
10.4 Average number of monovalent cations bound to the sites on POPC lipid molecules with possible combinations 144
10.5 AFM and KFPM images of lipid monolayers deposited in Li/K subphases . 146

11.1 *I-V* profiles of lipid membranes in 150 mM LiCl and 150 KCl 156

11.2 I-V profiles of lipid membranes in 0.8 mM and 4 mM LiCl 157
11.3 Results of voltage-dependence tests of lipid membrane with and without Aβ1-42 159
11.4 Ion currents caused by Aβ1-42 oligomers measured at 90 mV 160
11.5 Membrane conductance due to Aβ-induced transient pore. 161

A.1 Supported lipid bilayer (SLB) embedding with Aβ oligomers 213
A.2 LSPR peaks corresponding to glucose solutions with different RI 214
A.3 Characteristic current signals due to Aβ-membrane interaction at 100 mV in vBLM. 215
A.4 Comparison of Aβ-induced signals between hBLM and vBLM. 217

List of Tables

2.1 Lipid phases and corresponding elastic compressibility modulus values . . . 23

4.1 Conductance and dwell time of Aβ-induced current signals 48

5.1 Molecular area ($\AA^2$) of DPPC-POPC-Chol monolayer at the air/liquid interface at different pressures and subphases 61

5.2 Elastic compressibility modulus (mN/m) of DPPC-POPC-Chol lipid mixture at different surface pressures and subphases 63

5.3 The height (Δh) and electric surface potential differences (ΔESP) between ordered (L_o) and disordered (L_d) domains within monolayers made in water and trehalose subphase 66

5.4 The height (Δh) and electric surface potential differences (ΔESP) between ordered (L_o) and disordered (L_d) domains within monolayers deposited on mica from NaCl and trehalose-NaCl subphase 69

6.1 Peak and mean conductance values corresponding to each condition. 94

7.1 Lipids-induced LSPR response and membrane thickness 112

7.2 Aβ-induced LSPR response and 2nd layer thickness 117

10.1 Average molecular area of lipid molecules (A_m) in $\AA^2$ as a function of subphase and surface pressure 140

10.2 Elastic compressibility modulus values (mN/m) of monolayers on different subphases in response to pressure increase. 142

10.3 Height (Δh) and potential difference (ΔESP) between L_o and L_d domains of monolayers deposited in Li/K subphase 146

A.1 Result comparison between hBLM and vBLM 217

Chapter 1

Introduction

Longer lifespans resulted in the discovery of age-related diseases that were previously unseen such as neurodegeneration. Alzheimer's Disease (AD), one of the most common neurodegenerative diseases, frequently appears in the elderly. It causes severe symptoms over time, including but not limited to memory loss, cognition deficits, and language impairment [1], that profoundly affect patients and their families. To overcome the problem, many pharmaceutical studies over the decades have focused on seeking an ideal drug candidate. Amyloid, a well-known hallmark of AD, has become a target of interest in a large portion of pharmaceutical research studies. These studies aim to decrease the amyloid level in the brain, either by disrupting the amylogenic pathway or by removing existing amyloid. While most drug candidates failed their clinical trials, the recent anti-amyloid drugs Aducanumab and Lecanemab, were approved by the Food and Drug Administration (FDA). Despite these breakthroughs, controversy regarding these drugs still exists. Additional studies are still ongoing. Instead of targeting amyloid peptides directly, some researchers have begun exploring drugs that can protect neuronal cellular membranes against amyloid-induced toxicity.

This chapter will begin by providing a brief introduction to the pathogenic amyloid protein in Alzheimer's disease (AD) and its impact on lipid membranes. It will also review current pharmaceutical strategies and potential candidates targeting membrane protection

that are being investigated. The main subjects studied in this thesis, trehalose and lithium, will be discussed separately in Part I and Part II, and their modulation on lipid membranes and efficacy on membrane protection will be elucidated in the following chapters.

1.1 Role of Amyloid-β Proteins in Alzheimer's Disease

The amyloid-beta (Aβ) cascade hypothesis, proposed in the last century, suggests that the abnormal accumulation of misfolded amyloid proteins is one of the main pathogenic causes of Alzheimer's Disease (AD) [2]. Excessive accumulations of amyloid plaques and fibrillated tangles within the brains of patients are considered to be key molecular biomarkers of Alzheimer's disease (AD). Aβ peptides, the primary constituents of amyloid plaques, are identified as the key pathogenic factors in the progression of AD. The source of Aβ peptides can be traced back to the transmembrane amyloid-β precursor protein (APP) found in neuron cell membranes. The successive cleavage of APP by β-secretase and then γ-secretase in membranes produces amyloid fragments, which can fold into β-sheet [3]. The cleaved fragments can consist of anywhere from 39-43 amino acids, bringing the variety to the family of Aβ peptides [4]. The differences in sequence can correspond to functional differences as evidence indicates that Aβ1-42 has stronger neurotoxicity than the more abundant Aβ1-40 form in extracellular plaques [5, 6, 7]. Single Aβ peptides, defined as Aβ monomers, are extremely unstable and aggregate quickly. The aggregation of Aβ monomers produces diverse protein aggregates from oligomers to protofibrils and fibrils. Eventually, these aggregates accumulate in the brain and form amyloid plaques. The Aβ oligomers specifically are believed to be the major pathogenic component that can cause synaptic dysfunction, cell death and consequent impairment of brain function [8, 9, 10]. Aβ oligomers can disturb neuronal activities via multiple routes. For instance, the binding of Aβ oligomers with multi-valent ions like Zn^{2+}, Cu^{2+} can trigger oxidative stress by increasing reactive oxygen species (ROS) levels and induce oxidative damage to the brain [11]. Aβ oligomers can also bind a variety of transmembrane receptors [12], such N-methyl-D-aspartate (NMDA) receptors [13, 14] , insulin receptors [15], etc. This Aβ-receptor binding can disturb receptor-mediated Ca^{2+} influx, perturb cellular trafficking and

signaling, cause synaptic dysfunction and eventually lead to cell death [16, 17, 14, 18]. In addition to these receptor-mediated mechanisms, Aβ oligomers also have a strong affinity for lipid membranes and damage them [19], which is discussed in the following section.

1.2 Membrane Toxicity Induced by Aβ Oligomers

The affinity of Aβ for the lipid membrane comes from the hydrophobic residues in the peptide. However, not all forms of Aβ aggregates can bind to the lipid membrane, as this affinity is determined by the protein structure. The Aβ monomers have minor interaction with membranes [20] and fibrils are likely to adhere to the membrane surface [21]. The oligomers, especially Aβ1-42 oligomers, are the most preferable species to bind the membrane and change the permeability and electric properties of membranes [20].

Aβ oligomers binding to the cellular membrane can alter membrane permeability and electric properties through pore formation and the thinning of the membranes [22]. These pores increase membrane permeability by creating ion leakages, leading to homeostasis imbalance and cell apoptosis. Multiple mechanisms can explain the formation of these peptide-induced pores on lipid membranes, as shown in Fig. 1.1. In 1993, Arispe *et al.* revealed that Aβ protein could form ion channels that enable the transport of Ca^{2+} [23]. A study by Bode *et al.* specified that Aβ1-42 oligomers, instead of Aβ1-40, could form non-selective ion channels in the cellular membranes [20], transporting cationic ions like Ca^{2+} and Cs^{+} across the membrane [23]. AFM images showed that Aβ oligomers have a globular structure with diameters ranging from 1-10 nm [24]. When added to supported lipid bilayers (SLB), the Aβ oligomers formed ion channels comprised of 6 to 8 subunits oriented in a β-barrel structure [24]. The embedding of Aβ1-42 ion channels into cellular membranes can trigger Ca^{2+} uptake and disrupt homeostasis [25]. An atomic force microscopy (AFM) membrane study also showed that Aβ oligomers have a detergent-like effect on lipid membranes, causing lipid molecules dissociating from membranes, thus inducing membrane degradation [21]. A Langmuir monolayer study by Vander Zanden *et al.* also confirmed that globular Aβ1-40 oligomers remove lipid molecules, destabilizing

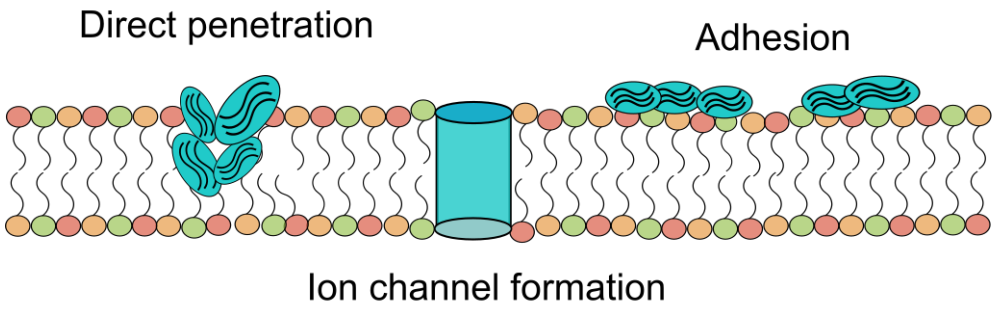


Figure 1.1: Multiple mechanisms of Aβ perturbance on lipid membrane. These Aβ aggregates may penetrate the membrane directly, form ion channels or stick to the membrane surface.

the lipid monolayer at the air/liquid interface [26]. Numerous studies on electrophysiological recordings across brain lipid extracts and artificial lipid bilayers demonstrate that the Aβ-induced membrane defects trigger ion flow and increase membrane permeability [27, 28, 20, 29]. This membrane disruption eventually accelerates neuronal dysfunction and cell degradation, regardless of the method of interaction by Aβ. Moreover, this effect is not restricted to plasma membranes as Aβ can damage mitochondrial membranes, leading to mitochondria dysfunction [30].

The extent to which Aβ binds and interferes with cellular membranes depends on the properties and composition of the membranes themselves. Previous studies show that Aβ prefers to interact with anionic membranes [31, 32, 33]. Anionic lipids were understood to induce conformational change of Aβ peptides when inserting the membranes and promote forming β-barrel ion channel structure [33, 31]. However, a recent neutron scattering study claims that membrane charges have little modulation effect on Aβ conformation when comparing Aβ insertion in anionic lipids versus zwitterionic lipids [34]. Regardless, multiple investigations indicate that plasma membrane composition itself influences the Aβ-membrane interaction. For instance, Aβ has a greater affinity in the regions of cellular membranes rich in cholesterol [35], a lipid capable of catalyzing and accelerating Aβ aggregation thereby promoting membrane insertion and pore formation [36].

Numerous previous studies *in vitro* and *in vivo* insinuate the significant connection between lipid alteration and AD pathogenesis [37, 38, 39, 40]. Lipids and AD have a mutual influence on each other. For instance, ganglioside (monosialotetrahexosylganglioside, GM1) presents as lipid rafts in neuronal membranes and regulates vital neuronal functions and growth. Whereas, it can bind with Aβ peptides tightly and promote aggregation, negatively impacting neurons in AD [41]. ω-3 fatty acids such as Docosahexaenoic acid (DHA) are unsaturated fatty acids with antioxidant functions beneficial to brains. The depletion of unsaturated fatty acid levels was found in the brains of AD patients, impacting their cognition function [42, 43, 44]. Similarly, sphingomyelin (SM) is an essential sphingolipid that can form lipid rafts with cholesterol within membranes. Its levels change depending on disease stages during AD progression; it was found to increase at the prodromal stage while decreasing at the lateral stage of AD [45, 46]. The decrease was revealed through cellular studies partially caused by Aβ oligomers. Aβ activates the expression of sphingomyelinase, which is an enzyme that can degrade SM and thus lower the SM level and lead to the apoptosis of neurons [45]. In addition, the oxidative stress induced by Aβ causes elevated cholesterol levels in AD brains [47]. These aberrant lipid metabolisms in AD brains not only change the lipid composition but also the properties of neuronal membranes.

Drolle *et al.* created complex membrane models to better mimic healthy neuronal membranes and diseased membranes at the early and late stages of AD and found that diseased membranes are more sensitive to Aβ binding [28]. Lipids undergo a composition change naturally during aging, which is difficult to reverse even when not associated with AD progression [47]. Given the strong correlation between lipid membrane, Aβ and AD, investigations into membrane protection against Aβ toxicity may help reduce Aβ-induced dysfunction and death and improve AD symptoms.

1.3 Aβ as a Potential Antimicrobial Peptide

It appears that the existence of amyloid is a tragedy to humans. Abundant evidence confirmed that abnormal expression and accumulation of Aβ contribute to AD pathogenesis.

However, amyloid peptides are ubiquitous proteins found in nature, from bacteria to humans, and are responsible for essential physiological functions [48]. They are present in the normal human brain for the entire life and regulate synaptic function, plasticity, neuronal protection, and brain development [49, 50]. For instance, functional amyloid Pmel17 found in human eye tissue was confirmed to promote the synthesis of melanin that protects the human body against UV radiation [51]. In addition, amyloids also involve the storage of peptide hormones in humans; the peptide hormones are adapted to an Aβ-like conformation to be stored in secretory granules [48, 52]. An animal study found that mice without the amyloid precursor protein (APP) gene suffered from synaptic impairment and cognitive decline during aging; it revealed that amyloid peptides play a crucial role in maintaining normal functions in mammal brains [53]. The functions of Aβs are determined by their concentration and conformation. Amyloid monomers and oligomers at the picomolar level are beneficial to the enhancement of long-term potentiation, synaptic plasticity as well as memory, while the abnormal excess production of Aβ oligomers has the opposite effect, which contributes to the pathogenesis of the AD [54].

Researchers have proposed that Aβ is a type of antimicrobial peptide (AMP), which is supported by various evidence. Soscia *et al.* compared the Aβ peptide with LL-37, a common AMP in humans and found the efficacy of Aβ peptides against eight microorganisms could be equivalent to or even superior to that of LL-37 [55]. They also revealed that the antimicrobial activity in the homogenates of AD brains was significantly higher than that in non-AD brains, positively correlating to the Aβ level in the brain tissues. The reduction of Aβ level caused by Aβ-targeted antibodies attenuated the antimicrobial activity in the brain homogenates. Some researchers proposed that the aberrant Aβ production and deposition could be triggered by an infection from viruses or bacteria that may stimulate the inherent immune system [56, 50].

AMPs share many common features with Aβ peptides. Similar to Aβ, many amyloid-like AMPs are enriched in β-sheet structures, which increase their membrane affinity, promoting their insertion into the lipid membrane [56]. Both amyloid AMPs and Aβ can form cation ion channels in the membrane and induce the disruption of homeostasis [56]. The diverse conductance of Aβ ion channels observed in electrophysiological studies implies a

variety of Aβ channels in size. These channels are distinct from innate ion channels with homogenous conductance present in neuronal and muscular membranes but resemble the channels formed by protegrin-1 (PG-1) [56], an AMP that promotes cell defence against bacteria and viruses and is clinically used for human wounds [57]. In addition, both Aβ and AMP have detergent-like effects on lipid bilayers, which extract lipid molecules from the membrane, leading to pore formation and membrane destabilization [58, 21].

1.4 Current Pharmaceutical Strategies Targeting Aβ Peptides

Given the complexity of AD pathogenesis, the pharmaceutical strategies to treat AD focus on inhibiting the pathogenetic factors of the disease, including Aβ and tau proteins, oxidative stress, inflammation and so on[59]. Some drugs intend to relieve the symptoms induced by AD and target cognitive enhancement. The development of anti-Aβ drugs can be mainly classified into three approaches: depleting Aβ production, inhibiting Aβ aggregation and enhancing the clearance of Aβ [60].

1.4.1 Drugs Targeting Depletion of Aβ Production

As mentioned before, the amyloidogenic pathway to produce Aβ peptide requires the cleavage of transmembrane amyloid precursor protein (APP) by β- and γ- secretases. The inhibition of β- and γ- secretases may effectively decrease Aβ levels. Chang *et al.* discovered that a β-secretase inhibitor, GRL-8234, relieves cognition decline by reducing soluble Aβ in the brains of transgenic mice [61]. However, during phase 3 clinical trials for AD, several β-secretase inhibitors, like Verubecestat, Lanabecestat, and CNP520 have failed due to a lack of efficacy in patients with different levels of AD progression [59]. Most of these drugs were also found to aggravate cognitive decline in trials [59]. Unlike β-secretase inhibitors, γ-secretase inhibitors may increase Aβ production and promote Aβ deposition despite the decrease in activity, thereby accelerating the cognitive decline [62]. This

inhibitor-mediated disturbance to γ-secretase may mimic a pathogenic subunit mutation in γ-secretase, leading to Aβ overexpression and neurodegeneration [62]. In addition to amyloid peptide, γ-secretase also modulates the cleavage of various proteins, like Notch receptors, neurotrophin receptors and a sodium channel subunit [60]. Hence, overcoming other non-specific effects is another challenge in developing γ-secretase inhibitors. Several γ-secretase inhibitors entered phase 3 clinical testing but all failed. Semagacestat had severe adverse effects on patients although it effectively decreased Aβ levels in the plasma and central nervous system [60]. Tarenflurbil not only failed to improve the decline of cognition but also worsened the anemia, infection, and dizziness in patients with mild AD [63].

1.4.2 Drugs Inhibiting Aβ Aggregation

Pharmaceutical strategies also include inhibiting Aβ aggregation, given that large Aβ oligomers have the predominant neurotoxicity. Tramiprosate, an ionic molecule that can bind soluble Aβ, was found to decrease amyloid plaques in mice brains in a dose-dependent manner by constraining Aβ aggregation [64]. However, MRI results in a phase 3 clinical study showed no significant improvement in individuals with mild-to-moderate AD when treated with Tramiprosate [65]. According to the animal studies conducted by Faux *et al.*, the chelating agent PBT2 was discovered to be effective in reducing the Aβ1-42 oligomers in the cerebrospinal fluid (CSF) and restoring the cognition of mice (Faux *et al.* 2010). PBT2 can bind and remove Cu^{2+} and Zn^{2+} ions from the surrounding environment as these ions can accelerate Aβ aggregation and stabilize amyloid plaques [66]. However, the studies also found no clear correlation between the level of Aβ in the CSF and the change in cognition [66]. Valiltramiprosate (ALZ-801), an oral inhibitor targeting Aβ oligomers, is currently undergoing phase 3 clinical trials [67]. Despite the lack of phase 3 data, the phase 2 studies show that ALZ-801 significantly lowered the plasma level of Aβ1-40 and Aβ1-42 which reduced the amyloid-induced elevation of phosphorylated tau protein in plasma [68]. Other agents, such as grapeseed extract, Valacyclovir, Contraloid acetate etc., have shown inhibition or prevention effects on Aβ aggregation, but further investigation and clinical

studies are needed [67].

1.4.3 Drugs Enhancing Aβ Clearance

Currently, most anti-Aβ therapy focuses on the clearance of Aβ aggregates and deposits. Particularly, immunotherapy targeting Aβ is the most popular and promising approach for AD drug development. Monoclonal anti-Aβ antibodies are designed to regulate the production, aggregation, and deposition of Aβ peptides. In general, the underlying mechanism for these antibodies is to encourage their specific binding to Aβ peptides and interfere with or delay the amyloid-induced pathogenic pathways in AD. Various anti-Aβ antibodies in trials target different Aβ aggregation states, such as monomers or oligomers, that appear in AD progression, as shown in Fig. 1.2 [69]. For example, the binding of anti-Aβ antibody to monomers may stop the formation of toxic Aβ oligomers. The neurotoxicity induced by oligomers can also be attenuated by the direct binding of antibodies. In addition, some antibodies may perturb the fibril formation while others can stimulate phagocytosis by microglia to enhance the clearance of plaques [69].

Aducanumab, the first monoclonal anti-Aβ antibody approved by the FDA in 2021, has been used as a medication for AD patients despite the controversy over its clinical efficacy [70]. It has been confirmed to effectively decrease Aβ plaques in a dose- and time-dependent manner [71]. Although high-dose aducanumab has a significant relief in cognitive decline, scientists also found its adverse effect on patients at the early stage of AD in the long-term treatment [71]. Specifically, amyloid-related imaging abnormalities (ARIA) appeared among AD patients treated with Aducanumab [72]. ARIA is a type of brain abnormality observed in MRI imaging, correlating to the treatment of monoclonal anti-Aβ antibodies [72]. While ARIA may not cause obvious symptoms, it may lead to serious impairment or even death [73]. Hence, the clinical medication must have a black-out period of 2-4 weeks to reduce the risk of ARIA [73]. FDA approved another anti-Aβ antibody, Lecanemab, in 2023. It binds Aβ protofibrils, thereby enhancing the clearance of amyloid deposits. Clinical studies indicated that Lecanemab slightly reduced cognitive and functional decline in patients compared to placebos, but caused some adverse effects in pa-

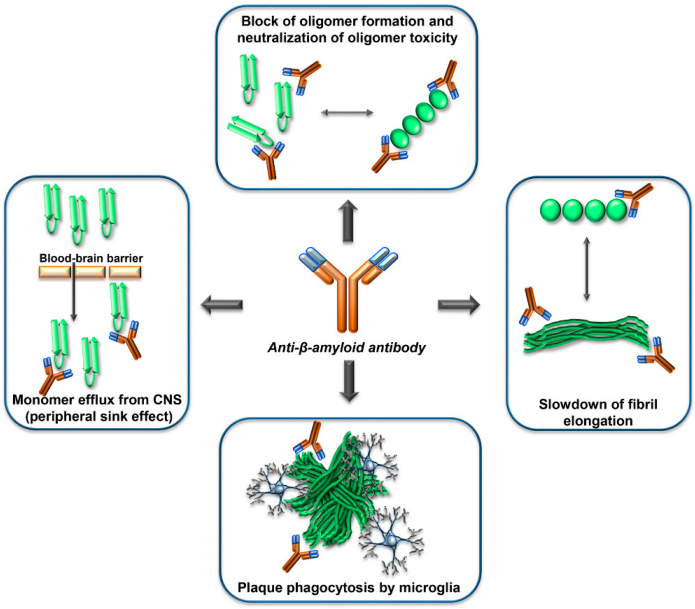


Figure 1.2: Anti-Aβ antibodies are designed to target various forms of Aβ, ranging from monomers to fibrils, and they function through different mechanisms [69]. Note: The 'peripheral sink effect' has been confuted. Reprinted from *Biology (Basel)*, Vaccination against β-amyloid as a strategy for the prevention of Alzheimer's disease. F. Mantile and A. Prisco. 9(12), 2020.

tients [74]. Similar to Aducanumab, Lecanemab may also cause ARIA although it appears to be less frequent [70]. Other monoclonal antibodies targeting Aβ like Gantenerumab and Solanezumab, are still under investigation in clinical trials. Although anti-Aβ antibodies bring hope to AD patients, the severe side effects cannot be ignored. Moreover, Aβ proteins, with antimicrobial peptide properties, may serve functionally in biological systems. Hence, removing Aβ proteins in brains might not be an optimal therapeutic strategy for AD. Considering the tight relationship between lipid membranes and Aβ in AD, seeking protection on lipid membranes can be another orientation as a preventive or therapeutic strategy for the disease.

1.4.4 Small Molecules Modulate Membrane Stability Against Aβ Toxicity

Currently, some scientists are exploring the potential of small molecules to protect the membrane against amyloid neurotoxicity. These membrane-interactive molecules, such as melatonin, curcumin and aminosteriols, may modulate the properties of lipid membranes to interfere with Aβ binding, thereby attenuating the Aβ-induced cytotoxicity.

Melatonin. Melatonin is a neural hormone produced by the pineal gland to regulate the circadian rhythm. It has been found to reduce neurodegeneration in AD. Early studies in 1998 revealed that melatonin can bind to Aβ peptides, disrupt fibrilization, and prevent protein plaques in the brain [75]. Recently, many biophysical studies have focused on the ability of melatonin to modulate lipid membrane properties. Melatonin was found to increase the membrane fluidity and reduce membrane thickness by incorporating into the lipid headgroup region [76, 77, 78, 79]. The fluidization of membranes by melatonin counteracts the increased rigidity caused by lipid peroxidation, which pathogenically contributes to AD [80]. The melatonin-mediated membrane change may serve as a protective mechanism against Aβ binding and induced damage [79, 76].

Curcumin. Curcumin, a natural extract from the spice turmeric, was found to reduce Aβ-associated neurotoxicity and improve cognitive function in rat brains in a study conducted by Thapa *et al.* [81]. Their results demonstrated that curcumin can protect lipid membranes by shielding the membrane from Aβ binding and reducing leakages induced by Aβ insertion [81]. Experimental and simulation studies by Khondker *et al.* showed that curcumin softens and thins the membrane, making it unfavorable for the β-sheet structure and inhibiting Aβ aggregation in the vicinity of the lipid membrane [82]. Membrane-mediated drugs, like curcumin and melatonin, affect not only the membrane properties but also the Aβ behaviours.

Aminosterols. Aminosterols, including trodusquemine, squalamine and their derivatives, are a group of compounds that were first discovered in dog sharks in 1993 [83]. Trodusquemine is able to adsorb to the neuronal membrane surface, bind to lipid polar head groups, and partially penetrate the lipid bilayers, causing membrane expansion and reduction in membrane thickness [84]. Modulation by trodusquemine enhances membrane resistance to the binding of abnormal misfolded proteins such as Aβ aggregates in AD and α-synuclein, the pathogenic protein in Parkinson's disease [84, 85]. In addition, trodusquemine may dissociate the Aβ oligomers from the neuronal membrane surface, reducing the Aβ binding and associated neurotoxicity, despite its ability to accelerate Aβ aggregation and fibrilization [86]. Squalamine, like trodusquemine, can displace Aβ and promote the dissociation of Aβ oligomers from membranes [87]. Recent studies have shown that the binding of aminosterols, both natural and synthetic, to membranes can neutralize negative charges at the membrane surface, reorganize lipid distribution, and improve the mechanical resistance of the lipid membrane to different extents [88]. As a result, aminosterols can protect the plasma membrane from Aβ-related toxicity with varying degrees of efficacy.

Other Molecules. Additional candidates that may protect the membrane from Aβ toxicity are currently being investigated. Model membrane studies by Torres *et al.* supported that 2-hydroxydocosahexaenoic acid (OHDHA) can integrate into lipid-raft-rich membranes and reduce the membrane binding of oligomeric and fibrillar Aβ [89]. Similarly, K162, a fluorene-based molecule, can preserve the physiologically functional amyloid monomers beneficial to neurons and reduce the production of membrane-toxic oligomers, mitigating the membrane permeation induced by the binding of Aβ oligomers [90]. Apart from the above molecules targeting plasma membrane protection, some researchers also explore the potential agents to protect mitochondria membrane from Aβ toxicity [30, 91]. For example, tauroursodeoxycholate (TUDC) was found to suppress Aβ-induced mitochondrial membrane disruption and potentially reduce mitochondria dysfunction caused by Aβ toxicity [30].

1.5 Conclusion

As mentioned before, many anti-Aβ drugs have been developed over the past few decades; unfortunately, none of these drugs can provide a full cure for AD patients. Although many drugs showed excellent performance in reducing Aβ levels in phase 1 and phase 2 trials, they eventually failed to show clinical improvement in patients. While FDA-approved Aducanumab and Lecanemab have shown some positive effects on mild-to-moderate AD patients, the severe side effects are still a significant concern. Considering that Aβ is a potential antimicrobial peptide which may serve essential functions in the brain, it raises the question whether the anti-Aβ strategy is the appropriate approach for AD treatment. Therefore, a shift in research strategies has prompted investigations into membrane-modulating small molecules to explore their potential for membrane protection against Aβ toxicity. In my research, I examined the effects of trehalose and lithium on lipid membranes and their potential protection on membranes from Aβ damage, which will be introduced in the lateral chapters (Chapters 4 to 8, 10 and 11).

1.6 Overview of the Thesis

1.6.1 Research Goal

The overall research goal is to investigate the potential of trehalose and lithium to protect lipid membranes against the membrane disruption caused by the binding of amyloid-β proteins. Both of these substances can interact with the hydrophilic regions of the lipid membrane, thereby modulating membrane properties. Naturally, one may wonder if the modulation of trehalose/lithium can change membrane properties to make it more resistant to Aβ damage or reduce the damage extent caused by Aβ peptides. In this thesis, Chapter 1 introduces the research background in terms of amyloid-beta proteins in Alzheimer's Disease, as well as current pharmaceutical progress for AD treatment. Chapter 2 illustrates the biophysical techniques and their principles applied in this study.

The specific research questions for each project are listed below, corresponding to the main Chapters 4 to 8, 10 and 11.

1.6.2 Research Questions

The main chapters were divided into two parts. Part I (Chapters 3 to 8) focuses on studies regarding trehalose and Part II (Chapters 9 to 11) focuses on lithium.

Part I - Trehalose

- Chapter 3: Introduction to trehalose
- Chapter 4: How does Aβ affect lipid membrane permeability?
- Chapter 5: What is the influence of trehalose on membrane properties?
- Chapter 6: Can trehalose protect the membrane from Aβ toxicity?
- Chapter 7: Does trehalose reduce the Aβ binding to membranes?
- Chapter 8: Can trehalose protect neuronal cells from Aβ toxicity?

Part II - Lithium

- Chapter 9: Introduction to lithium
- Chapter 10: What is the effect of Li^+ on lipid monolayers?
- Chapter 11: Can Li^+ protect membranes against Aβ toxicity?

Chapter 2

Methodology

2.1 Black Lipid Membrane Electrophysiology

Black lipid membrane (BLM) is an electrophysiological recording technique that measures ion currents across suspended artificial lipid bilayers. Interactions between a lipid bilayer and membrane-active substances can then be detected by measuring electrical properties, such as current, conductance, and resistance [92]. Planar lipid bilayers are created by painting or folding and then suspended over a small hole with a diameter of tens to hundreds μm in a wall separating two compartments, as shown in Fig. 2.1. The compartments are filled with electrolyte solutions such as KCl or NaCl to create a conductive environment. The thickness of the artificial lipid membrane is as small as a few nanometers. As a result, the light reflected from the water-lipid interface interferes destructively with the light reflected from the lipid-water interface on the other side [92]. This makes the membrane appear black, hence the name of the technique. [92] Traditional BLM instruments feature two silver electrodes placed on opposite sides of the membrane that control voltages across and record currents through the membrane. As the hydrophobic cores of lipid bilayers provide insulation for their inner regions, the bilayer acts as a non-conductive capacitor, impermeable to the transport of ions or charges. The application of alternating voltages with triangle waves allows for the measurement of membrane capacitance, which is used

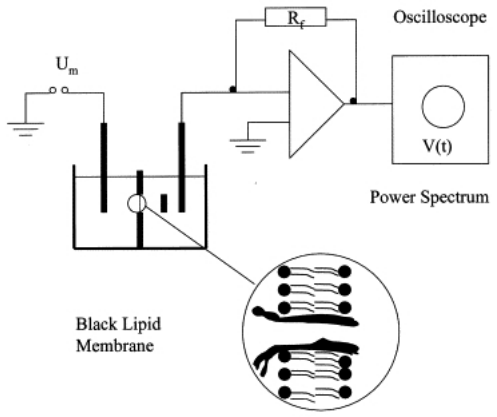


Figure 2.1: Schematics of Black Lipid Membrane. The artificial lipid membrane is suspended on the hole between two chambers filled with electrolyte solution. Two electrodes are separately placed in the two chambers. They can apply voltages and record the ion current across the membrane via an electric circuit. Reprinted from *Current Opinion in Colloid & Interface Science*, Black lipid membranes, M. Winterhalter. Vol 5, Issues 3-4, P250-255. 2000. Copyright (2000), with permission from Elsevier.

to evaluate membrane quality. The recorded current in this scenario is negligible because of the impermeability of the lipid bilayers to ions.

When membrane-interactive proteins are added to the electrolytes, they may bind to the suspended membrane via diffusion, generating pores or disrupting membrane integrity. The ion leakage induced by the proteins inserting into the membrane appears as a current shift. The binding of proteins to the membrane can occur through different mechanisms: insertion of protein ion channels, membrane disruption, generation of lipid-protein micelles, and others [93]. While the current change represents the occurrence of membrane-protein interaction, it cannot reveal the membrane properties directly. Sometimes, when the protein detaches from the membrane, the membrane can recover its original integrity, causing the current to return to zero after a current shift. When the protein inserts the membranes and forms an ion channel, the membrane may not recover instantly, and the current will not return to zero for a long time.

The measured transmembrane current (I) at its corresponding applied voltage (V) in-

dicates membrane permeability, which can be quantified as conductance, g, and calculated as Eq. (2.1) [94],

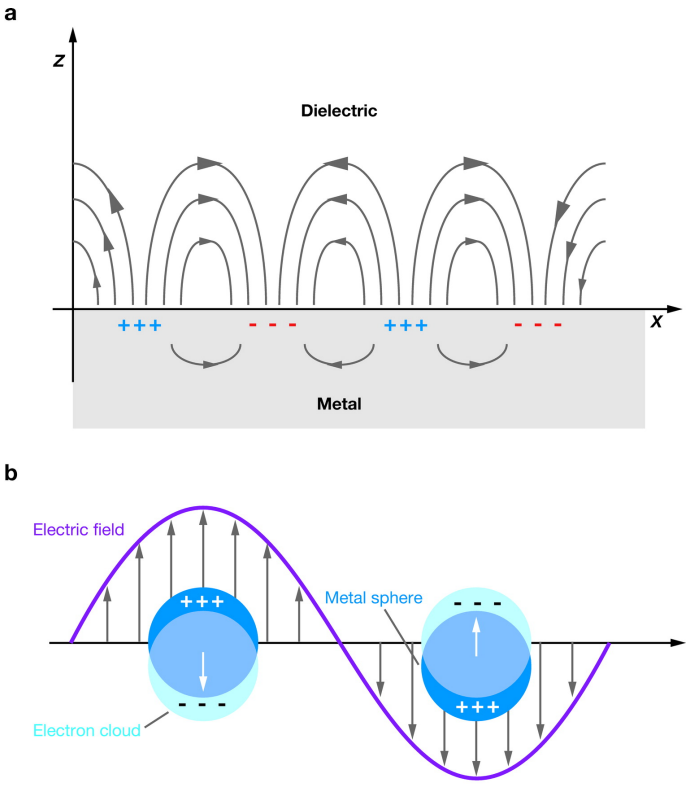
$$g = \frac{I}{V}. \tag{2.1}$$

A membrane with high stability has a very small conductance, showing its lack of permeability to ions. Pore formation and disruption of membranes result in an increase in membrane conductance, which indicates an increase in membrane permeability.

BLM recordings can be analyzed to study protein ion channels or the interactions between charged substances and lipid membranes. In my research, I used BLM to study the level of destruction sustained by lipid membranes due to interactions with amyloid beta proteins by evaluating membrane permeability in the presence of lithium ions and trehalose.

2.2 Localized Surface Plasmon Resonance

Localized surface plasmon resonance (LSPR) spectroscopy is a powerful tool that leverages physical principles to detect the binding of molecules. As it can provide an aqueous environment during experiments, it is widely used to detect biomolecule interactions like DNA hybridization, receptor-ligand binding, protein-membrane binding, etc. [95]. A wavelength shift can be observed in LSPR spectroscopy once molecules bind to a sensor surface.



Willets KA, Van Duyne RP. 2007.
Annu. Rev. Phys. Chem. 58:267–97

Figure 2.2: Schematics of surface plasmon. (a) A surface plasmon polariton propagating in the $x-$ and $y-$direction and decaying evanescently in the $z-$direction. (b) A localized surface plasmon that oscillates locally [96]. Reprinted with permission from *Annual Review of Physical Chemistry*, Localized surface plasmon resonance spectroscopy and sensing. Katherine A. Willets and Richard P. Van Duyne. Vol 58, P267-297. 2007; permission conveyed through Copyright Clearance Center, Inc.

LSPR is developed from surface plasmon resonance (SPR), a physical phenomenon where the oscillation of electrons in a noble metal is excited by light incident with a specific angle at the metal-dielectric interface. The oscillation generates an evanescent electromagnetic (EM) wave that propagates along the dielectric-metal interface ($x-$ and $y-$ direction) and decays exponentially in the z-direction, perpendicular to the sensor

surface, as shown in Fig. 2.2 (a). The EM wave is characterized by the decay length l_d of approximately ~ 200 nm, determining the detection range of SPR [96, 97]. When the size of a metal nanoparticle is smaller than the incident light wavelength, the electrons of a metal atom are confined to the vicinity of nuclei, and the plasmon oscillates locally (Fig. 2.2 (b)). The oscillation of localized plasmons generates a stronger EM field compared to traditional SPR, leading to a decay length smaller than 40 nm [97]. Accordingly, the detection range of LSPR sensors is reduced, eliminating the bulk response seen in SPR [98], increasing the detection accuracy and allowing for binding detection at small concentrations. In order to obtain an enhanced EM field for LSPR, the dielectric constant (ε) of metal particles should meet $\varepsilon = -2\varepsilon_m$, where ε_m is the dielectric constant of the medium [99]. Both gold and silver meet the criteria. Given its chemical stability, gold is the ideal metal to produce an LSPR sensor.

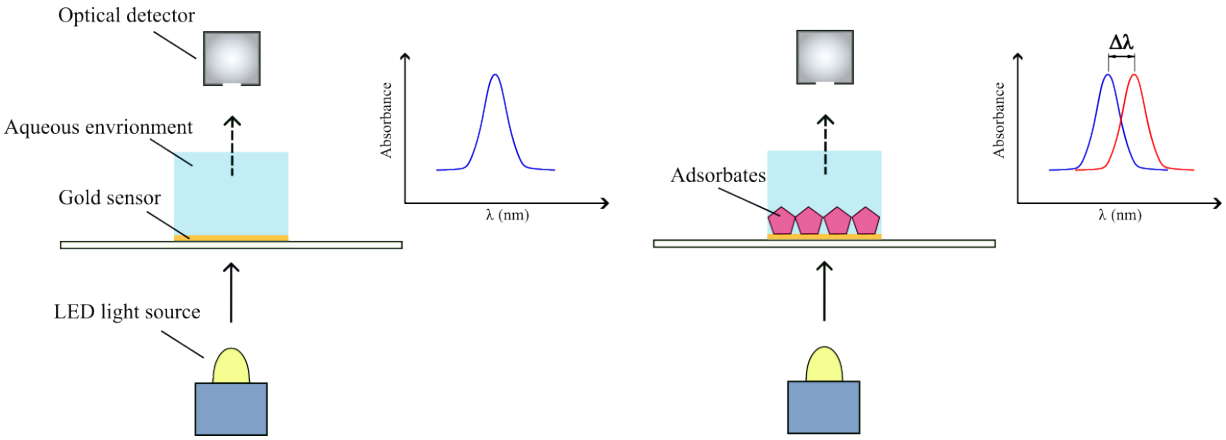


Figure 2.3: Working principle for a typical LSPR instrument. It detects the wavelength shift ($\Delta\lambda$) caused by the binding of molecules to the sensor surface. The binding of molecules change the refractive index (RI) at the vicinity of the LSPR sensor surface thereby inducing the wavelength change of adsorbed light.

An LSPR sensor is typically composed of gold nanoparticles, where UV-visible light is sufficient to excite the generation of surface plasmons. In a typical LSPR instrument, UV-visible light from an LED source is shone on the back of the sensor, with some light being absorbed and the rest transmitted (Fig. 2.3). Absorbance occurs when the resonance

condition is achieved, that is, when the frequency of incident light matches the plasmon resonant frequency, gold nanoparticles will absorb the light at that frequency, causing LSPR. Transmitted light is collected by a photodetector to identify the maximum absorbance peak [100].

As shown in Fig. 2.3, the maximum extinction wavelength to generate LSPR is extremely sensitive to the refractive index (RI) in the vicinity of the sensor [99]. The binding of molecules to the sensor can cause a change in RI (Δn), thereby inducing the wavelength shift ($\Delta\lambda$) given by

$$\Delta\lambda = m\Delta n \left[1 - \exp\left(-\frac{2d_a}{l_d}\right)\right], \tag{2.2}$$

where m is the local sensitivity of the sensor, d_a is the thickness of the adsorbate layer, and l_d is the decay length of the electric field associated with the metal nanosphere [101]. This equation shows that the wavelength shift due to binding depends not only on the change in RI, but also on the thickness of the adsorbate layer, assuming that only one adsorbate layer exists in this scenario [101]. Accordingly, d_a can be quantitively estimated if other parameters or constants in this equation can be obtained by measurement or from literature. For the case of multiple adsorbate layers, it will be discussed in detail in Chapter 7.

In my trehalose-related studies, I used LSPR technique to study the effect of trehalose on the binding of Aβ1-42 to lipid membranes. The LSPR instrument was used to detect the binding of lipid vesicles to the gold sensor and the binding of Aβ proteins to the lipid membrane in the absence and presence of trehalose.

2.3 Langmuir-Blodgett Trough

Langmuir-Blodgett (LB) trough is a technique for making monolayers and measuring surface tension at air-liquid interfaces. Lipid molecules, which are typically insoluble in aqueous solution, are spread onto the surface of an aqueous subphase and compressed by two barriers in an LB trough to create Langmuir films or measure surface tension changes with

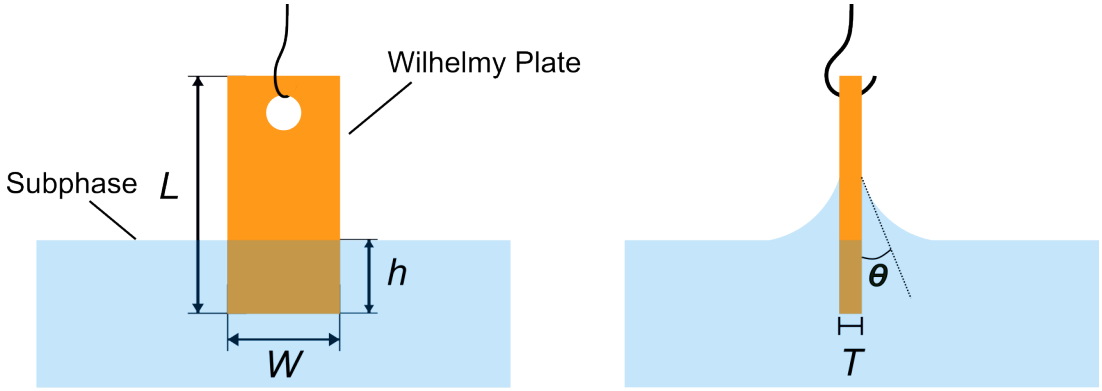


Figure 2.4: Front (left) and side (right) schematics of a Wilhelmy plate immersed in the aqueous subphase

a Wilhelmy plate. The Wilhelmy plate is a paper or platinum plate that connects to a microbalance via a hook (Fig. 2.4). It is partially submerged in the liquid subphase so that the microbalance can detect the forces exerted on the plate, thereby measuring the surface tension on the subphase.

The net force that works on the Wilhelmy plate is composed of the force of gravity acting on the plate, the surface tension, and the buoyant force [102]. So, the equation below could be used to compute the force on the plate:

$$F = \underbrace{\rho_p g L W T}_{\text{Force of Gravity}} + \underbrace{2\gamma\,(WT)\,(\cos\theta)}_{\text{Surface Tension Force}} - \underbrace{\rho_l g W T h}_{\text{Buoyant Force}}\,, \tag{2.3}$$

where L, W, and T correspond to the dimensions (length, width, thickness) of the plate, ρ_p and ρ_ℓ are the densities of the plate and liquid subphase, respectively, h is the height at which the plate immerses into the subphase, γ is the surface tension, θ is the angle at which the liquid contacts the plate and represents liquid surface tension. When the plate is completely wet, the surface pressure (Π) is given by:

$$\Pi = \gamma_0 - \gamma = -\Delta\gamma = -\left[\frac{\Delta F}{2(T+W)}\right] = -\frac{\Delta F}{2W},\ \text{if } W \gg T. \tag{2.4}$$

Here, γ_0 and γ is the surface tension of pure subphase and the surface tension of subphase with monolayer deposited, respectively.

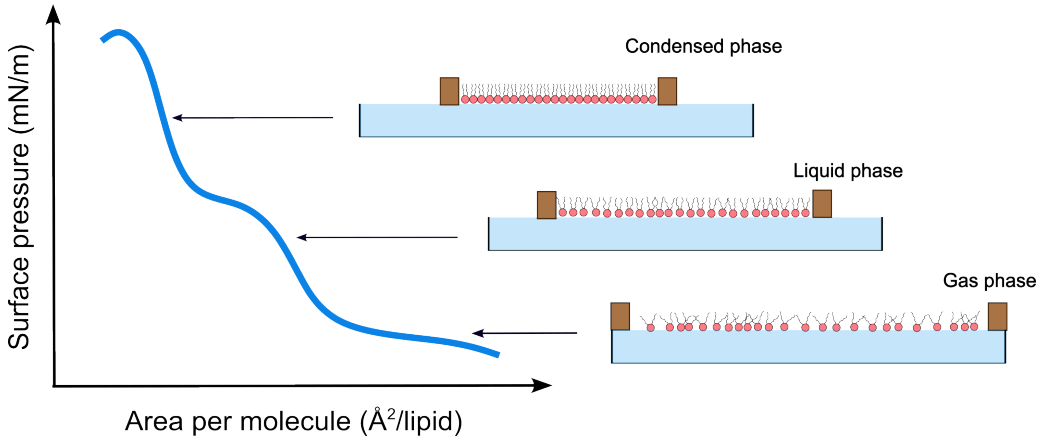


Figure 2.5: Pressure-area isotherm and lipid phase transition. Lipid molecules spread on the aqueous subphase are compressed by barriers. Surface pressure change in response to area change is monitored via the Wilhelmy plate connected to a microbalance. Lipids experience the phase transition from gas phase to liquid phase and condensed phase until the lipid monolayer collapses.

2.3.1 Surface Pressure-Area Isotherm

The pressure-area isotherm of lipid molecules can be obtained using the LB trough. It demonstrates changes in surface pressure as the area between two barriers reduces. Lipid molecules that are first dissolved in organic solvents are spread onto a liquid subphase between two barriers. After evaporation of the organic solvents, the lipid molecules align themselves with the hydrophilic head group facing water and the hydrophobic tail facing air. The barriers start closing and reduce the molecular area of the lipids through compression, causing an increase in surface pressure. A Wilhelmy plate connected to a microbalance monitors the surface pressure change with respect to the area between the two barriers until the lipid monolayer collapses, indicated as a steep drop of pressure in the pressure-area isotherm (Fig. 2.5).

A typical compression isotherm indicates the nature of lipid molecules in response to surface pressure change. As shown in Fig. 2.5, when the barriers are fully open, the surface pressure is close to zero, and the lipid molecules are sparsely distributed on the surface, indicating that they are in the gas phase (G). As the distance between the two barriers

decreases and the intermolecular distance decreases, the lipid monolayer becomes more rigid and transitions to the liquid phase and eventually the condensed (C) phase. The liquid phase can be further divided into the liquid-expanded (LE) phase and the liquid-condensed (LC) phase [103]. Sometimes, the lipids may also experience the coexistence of LE and LC phases (LE-LC phase), which is shown as a plateau in the isotherm curve [104]. In complex lipid systems with multiple compositions, the phase transition is not so obvious that it can be deduced directly from the isotherm curve like for a single lipid; it is possible that the lipid phase transits from G to LC phase without plateauing [105].

The elastic compressibility modulus ${C_s}^{-1}$ of a lipid monolayer can be determined from the compression isotherm curve by taking the derivative of surface pressure (Π) with respect to the molecular area (A) [106],

$$ {C_s}^{-1} = -A \left(\frac{\partial \Pi}{\partial A} \right). \tag{2.5} $$

Compressibility describes the ease of the monolayer to be compressed and so implies the stiffness of monolayers. A large ${C_s}^{-1}$ value indicates that monolayers tend to be rigid and hard to compress. Moreover, the phases of a monolayer can be roughly determined by the elastic compressibility modulus, as shown in Table 2.1.

Phase	Elastic compressibility modulus (${C_s}^{-1}$, mN/m)
Liquid-expanded (LE)	12.5 – 50 [106]
Liquid	50 – 100 [105]
Liquid-condensed (LC)	100 – 250 [106]
Condensed	$>$ 250 [106, 105]

Table 2.1: Lipid phases and corresponding elastic compressibility modulus values

2.3.2 Lipid Monolayer Deposition

Another application of the LB trough is producing Langmuir films by deposition. Amphiphilic molecules like phospholipids and conjugated polymers can be spread onto the

surface of an aqueous subphase and transferred to a solid substrate by compression and lifting [107].

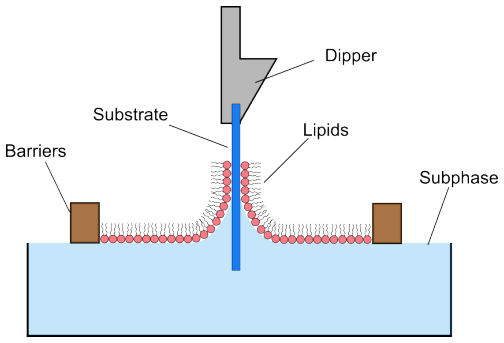


Figure 2.6: Deposition of the lipid monolayer on the mica substrate. Lipids are deposited before lifting the mica from the aqueous subphase.

The deposition method varies slightly depending on whether the substrate is hydrophilic or hydrophobic. Figure 2.6 display a general way to deposit lipid monolayers on a hydrophilic mica substrate. A dipper with an adjustable height has a mica edge attached, with the mica faces parallel to the barriers. Lowering the dipper allows the mica to be immersed into the aqueous subphase. After most of the mica is beneath the subphase surface, the lipids in the volatile organic solvent are deposited onto the subphase, like the deposition procedure for the compression isotherm. After the evaporation of the organic solvent, the lipids are compressed to a desired pressure to encourage monolayer formation on the subphase. Because of the hydrophilicity of both the lipid head group and the mica surface, lifting the mica allows the monolayer to transfer to the substrate. The characteristics of monolayer samples can be studied by X-ray diffraction [108, 109], atomic force microscopy [110, 111], Brewster angle microscopy [112], etc. In addition, multilayers can be created by repeating the deposition.

2.4 Atomic Force Microscopy

Atomic force microscopy (AFM) is a type of scanning probe microscopy (SPM) that produces a topographical image of a sample surface by scanning the surface with a nano-scale tip. During the scanning, the tip and the cantilever to which it is attached move up and down due to uneven surface heights. Meanwhile, the interaction force between the tip and sample bends the cantilever towards or away from the surface. As illustrated in Fig. 2.7, the movement of the tip and deformation of the cantilever is tracked by a laser with a feedback loop system. The incident laser is deflected by the backside of the tip onto a mirror, and then reflected to a piezoelectric photodiode module, which collects and converts the optical signal to an electrical signal [113]. When the tip encounters height changes on the surface, the feedback loop generates a correction command to adjust the deflection of laser such that it is always aimed at the center of the photodiodes. The topography information can be obtained from the error signals associated with the correction in the feedback loop.

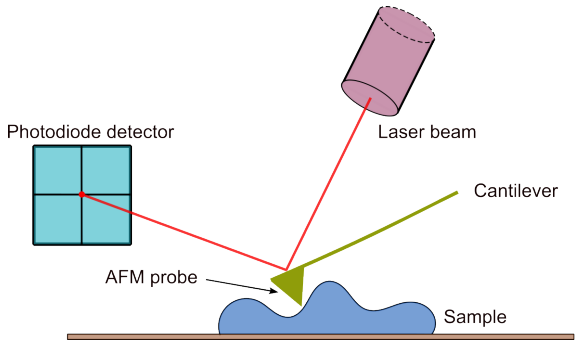


Figure 2.7: Atomic force microscopy

The AFM cantilevers are made of an elastic material — analogous to a spring. The force exerted on the cantilever can be described by Hooke's Law,

$$F = -kx, \tag{2.6}$$

where k is the spring constant of cantilever, and x is the deformation of the cantilever due to tip-sample interaction [114].

The working modes of AFM can be divided into contact mode, intermittent mode, and non-contact mode [113], each relying on different interaction forces between the tip and the sample. The interaction between tips and samples can be approximated by the Lennard-Jones potential, $U(r)$ [114, 115],

$$U\left(r\right) = -\frac{A}{r^6} + \frac{B}{r^{12}}, \tag{2.7}$$

where r represents the gap between the tip and the sample, and A and B are constants approximately equal to $10^{-77}\mathrm{J}\cdot\mathrm{m}^6$ and $10^{-134}\mathrm{J}\cdot\mathrm{m}^{12}$ respectively [114].

Then the interaction force between the tip and sample $F(r)$ is found by differentiating the potential with respect to r [114],

$$F\left(r\right) = -\frac{\partial U}{\partial r}, \tag{2.8}$$

demonstrating that the tip-sample force is determined by the tip-sample distance, as illustrated in Fig. 2.8. When the tip is far from the sample surface, the net force is almost zero. As it comes closer, the tip tends to attract the surface and the cantilever will bend slightly towards the sample. The attractive force between the sample and tip is what contributes to the image in non-contact mode; it reaches its maximum at a critical distance indicated by the bottom of the valley in Fig. 2.8. As the tip keeps approaching the surface, the repulsive force increases even though the net force is still predominantly attractive. At sufficiently small distances, the repulsive force completely counteracts the attractive force and becomes the dominant force between the tip and sample – this domain is considered contact mode. The force in intermittent mode hovers in the middle region of the force model.

The central characteristic of contact mode is that the tip directly touches the sample surface. In contact mode, the AFM can be set to 'constant height' or 'constant force'. In constant height imaging, the height of cantilever is maintained, and the system alters the force applied to the sample according to cantilever deflection [113]. The other imaging mode, which is used more commonly, is constant force imaging. The force applied on the surface is held constant while the cantilever height changes due to the change of surface

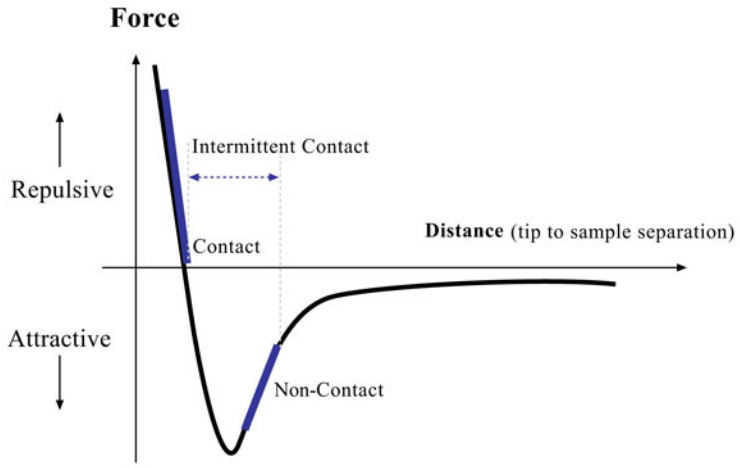


Figure 2.8: Lennard-Jones force model [116]. Reprinted from *The Open Neuroimaging Journal*, Review of progress in atomic force microscopy. S Maghsoudy-Louyeh, M Kropf, and BR Tittmann. 12(1), 2018.

height during scanning. Topographic information follows directly from the cantilever deflection. Since the tip is in close contact with the sample, the imaging resolution is very high. This method is good for visualization of solid dry samples. However, the close contact may cause physical damage to sample surfaces, especially for soft biological samples.

In intermittent mode, the cantilever oscillates on the sample surface at its resonance frequency so that the contact of the tip to the sample is discontinuous, which is different from contact mode. The oscillation amplitude is preset as a setpoint value prior to imaging. When the tip encounters higher parts of the sample surface, the amplitude is damped; the feedback loop will try to adjust the cantilever height to hold it at the setpoint amplitude [113]. The adjustment produces an error signal that indicates the difference between the measured amplitude and the setpoint amplitude. Additionally, differences in mechanical properties, such as softness and adhesion, can cause a phase shift in the cantilever oscillation, which can be used to create phase images in intermittent mode [113]. These phase images make it possible to distinguish texture or components in the sample. The intermittent mode of tip-sample contact in AFM reduces the risk of damaging sample surfaces.

Additionally, it can be performed in either air or liquid, making it suitable for biological samples that require hydration.

The non-contact mode in atomic force microscopy involves oscillation of the cantilever where the tip does not touch the surface at all. This method reduces the damage caused by tips to samples to a great extent. However, this mode is rarely used because the tip is easily interfered with by interaction forces between the tip and the sample or between the tip and the water or solution in which the sample is submerged, leading to imaging artifacts [113].

2.4.1 Kelvin Probe Force Microscopy

Kelvin probe force microscopy (KPFM) is a derivative of AFM, which is used for mapping the electric potential distribution of a sample's surface with a conductive tip. It is usually used to estimate the electric properties of conductive or semi-conductive nanostructures [117]. The KPFM measures contact potential difference (V_{CPD}), determined by the difference in work functions of the tip (ϕ_{tip}) and of the sample (ϕ_{sample}) [117],

$$V_{\mathrm{CPD}} = \frac{\phi_{\mathrm{tip}} - \phi_{\mathrm{sample}}}{-e}. \tag{2.9}$$

The work function, defined as the difference between the Fermi energy level and vacuum level, represents the minimal energy required for an electron to be removed from the metal surface [118]. The separation of the tip and sample makes them analogous to a capacitor. The Fermi level of the tip and the sample are different. When the tip gets close to the sample surface, electrons will start transferring until they reach an equilibrium state [117]. The previously mentioned contact potential difference (V_{CPD}) is a result of the electrons having been transferred. To find V_{CPD}, an alternating current (AC) voltage (V_{AC}) is applied to the tip to drive its oscillation. An external direct current (DC) bias (V_{DC}) is applied to counteract V_{CPD}. Therefore, the net voltage exerted on the tip is given by

$$V_{\mathrm{tip}} = V_{\mathrm{DC}} + V_{\mathrm{AC}} \sin(\omega t), \tag{2.10}$$

where ω is the oscillation frequency of the tip [117]. The potential difference between V_{CPD} and the voltage imposed on the tip can be expressed as

$$\Delta V = V_{\mathrm{tip}} \pm V_{\mathrm{CPD}} = V_{\mathrm{DC}} \pm V_{\mathrm{CPD}} + V_{\mathrm{AC}} \sin(\omega t). \tag{2.11}$$

If V_{DC} is applied on the tip, the sign is negative $(-)$; if V_{DC} is applied on the sample, the sign is positive $(+)$ [117]. Consequently, the force between the tip and sample in KPFM can be determined using ΔV as well as the capacitance gradient in the tip-sample capacitor,

$$F(z) = -\frac{1}{2}\Delta V^2 \frac{dC(z)}{dz}, \tag{2.12}$$

where z represents the direction orthogonal to the sample surface [117]. The electrostatic force can be rewritten by combining the two equations above,

$$F(z,t) = -\frac{1}{2}\left[V_{\mathrm{DC}} \pm V_{\mathrm{CPD}} + V_{\mathrm{AC}} \sin(\omega t)\right]^2 \frac{dC(z)}{dz}. \tag{2.13}$$

The surface potential difference of a lipid monolayer can be measured using KPFM. Although a biological sample is not as conductive as a metallic surface, the dipole moments of lipid molecules contribute to the dipole potential of the sample surface, making the measurement feasible [119].

2.5 MTT Cell Viability Assay

MTT assay is a biological technique to evaluate cell viability, metabolic activity, drug efficiency, etc. [120]. The mechanism was developed based on the chromogenic biochemical reaction occurring between MTT reagents and mitochondria in live cells. MTT (3-(4,5-dimethylthiazol-2-yl)-2,5-diphenyl-2H-tetrazolium bromide) is an organic and lipophilic molecule that can enter the mitochondria [121]. As shown in Figure 2.9, the enzyme in mitochondria reduces yellow MTT to aqueous-insoluble formazan with a dark blue colour during metabolic activity [121, 122]. In dead cells, the functional enzyme is absent, and formazan cannot form. Based on the redox reaction, the cell viability can be measured according to the concentration of formazan, which indicates the density of live cells.

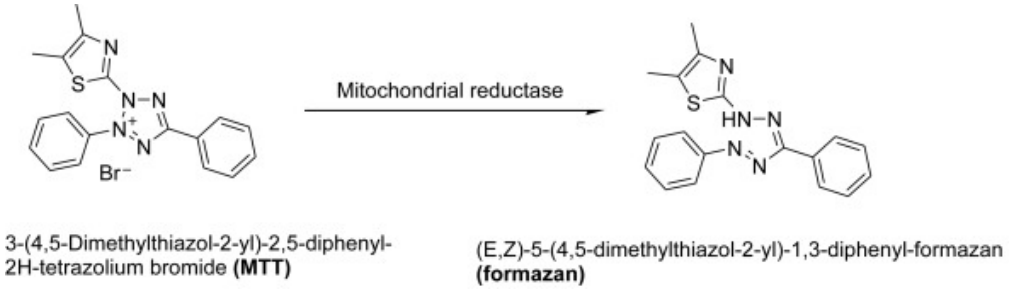


Figure 2.9: Reduction of MTT to formazan by mitochondrial reductase [123]. Reprinted from *Medicinal Spices and Vegetables from Africa*, Chapter 10 - Anticancer Activities of African Medicinal Spices and Vegetables. V. Kuete, O. Karaosmanoğlu, and H. Sivas. P271-297, 2017. Copyright (2017), with permission from Elsevier.

Results

- Part I Trehalose
- Part II Lithium

The next part of the thesis presents my results, which are written in the way of several publications that are either published or submitted. They are presented in the following chapters (Chapters 3 to 11) and are split into two parts: Part I - trehalose (Chapters 3 to 8) and Part II - lithium (Chapters 9 to 11).

Part I (Chapters 3 to 8) includes the results and discussion of studies that focus on trehalose. First, the properties, functions and previous relevant studies of trehalose are introduced in Chapter 3. Then, Chapters 4 to 8 report the major works on exploring the influence of trehalose on lipid monolayers and its potential in membrane and cellular protection from Aβ toxicity.

Part II (Chapters 9 to 11) presents the results and discussion of studies on lithium. Chapter 9 presents an introduction to the research background of lithium — its role in the neuronal system and bipolar disorder and its relevance to AD. Chapters 10 and 11 show my results of investigating the impact of lithium on lipid monolayer properties and Aβ-membrane interaction.

Part I Trehalose

Chapter 3

Introduction of Part I

Trehalose (Fig. 3.1) is a non-reducing sugar composed of two glucose molecules and can be found in plants and fungi [124]. It is relatively non-toxic to humans and daily intake may benefit overall health [125]. In addition, it is often used in biological laboratories to preserve cells or proteins against freezing, dehydration, oxidation or mechanical stress [124]. In recent decades, researchers have started to explore the potential of trehalose as a drug candidate for various diseases, including diabetes, osteoporosis, metabolic disorders and neurodegenerative diseases [125]. Animal studies have revealed that the neuroprotective role of trehalose in neurodegenerative diseases affects the accumulation of aberrant proteins, such as Alzheimer's disease (AD), Parkinson's disease (PD), and Huntington's disease (HD) [125]. While the therapeutic mechanism is still under investigation, previous studies have determined that trehalose can act as a molecular chaperone capable of modifying the conformation of misfolded proteins [126, 127]. It can also induce autophagy, a cellular activity that promotes the clearance of abnormal proteins and organelles [128, 129]. Of note, trehalose prefers to interact with and modulate membranes by establishing hydrogen bonds with the polar headgroup regions of lipid bilayers [130, 131, 132]. This opens the possibility of exploring trehalose as a protective small molecule against AD pathology.

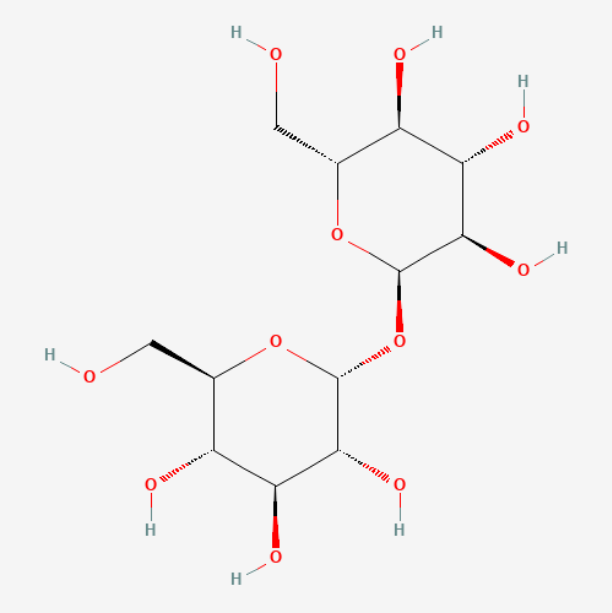


Figure 3.1: Chemical structure of trehalose

3.1 Impact of Trehalose on Aβ Proteins

Trehalose can alter protein structure and inhibit the aggregation of several misfolded peptides associated with neurodegenerative diseases. For example, trehalose prevents the aggregation of α-synuclein, the hallmark protein in Parkinson's disease, and causes protofibrils and fibrils to disassemble into smaller pieces at low concentrations [126]. At high concentrations trehalose impedes α-synuclein folding into a β-sheet structure and completely blocks fibril production [126]. Additional studies show a similar inhibitory and refolding effect of trehalose on Aβ aggregates, with varying efficacy based on peptide species [133]. For example, Aβ1-40 peptide refolds into an α-helix structure with the assistance of trehalose, thereby reducing the β-sheet structure and suppressing protein aggregation promoted by misfolding [127]. Incubating Aβ peptides with trehalose prior to application to the cells can inhibit the formation of both fibrillar and oligomeric Aβ1-40, improving the cell survival rate in a dose-dependent manner [133]. However, in the case of Aβ1-42, trehalose only decreases its production and fails to prevent the formation of oligomers,

which are regarded as the most toxic species to neurons. Consequently, incubating Aβ1-42 with trehalose does not attenuate the cytotoxicity effects of Aβ1-42 oligomers on neuronal cells [133]. A recent study highlighted that the ionic strength of an aqueous solution determines the efficacy of trehalose's inhibitory effects on Aβ fibrilization [134]. For example, in the absence of NaCl, the fibrilization of lysozyme and insulin is successfully suppressed by trehalose. However, the addition of this salt allows fibrilization to proceed. This indicates a competitive relationship between ions and trehalose when interacting with proteins.

3.2 Interaction of Trehalose with Lipid Membranes

Trehalose serves as a cryopreservative for biological samples, maintaining the integrity of lipid membranes during dehydration and rehydration by diminishing the phase transition of lipids to the gel phase. The underlying mechanisms for trehalose-lipid interactions are under debate. One hypothesis, known as the 'water replacement hypothesis', proposes that the trehalose replaces the water molecules at the lipid hydrophilic region by creating hydrogen bonds with lipid head groups [135, 136, 130]. This binding of trehalose to the lipid headgroups reduces their phase transition during dehydration thereby stabilizing the lipid membranes. Another hypothesis suggests trehalose establishes a hydration layer at the solvent/lipid interface that then undergoes vitrification [137, 138]. The accumulation of trehalose into a layer at the lipid bilayer surface builds up a concentrated sugar analog to glass. The vitrification of the trehalose layer increases the membrane tolerance and maintains membrane stability against external environment changes. A recent simulation study by Maiti and Daschakraborty has shown the modulation of trehalose on the properties of *Escherichia coli* (*E.coli*) bacterial membrane [139]. The viscous trehalose layer helps to attenuate the movement of lipid molecules and maintain membrane fluidity under dehydration. The water replacement and vitrification hypotheses can be combined to explain the interaction between trehalose and the membrane [139]. Despite differences in proposed mechanisms, these hypotheses agree that the maintenance of membrane stability under dehydration is achieved by the reduction of the fluid-to-gel phase transition of lipids by trehalose. This effect is not limited to dehydration as in hydrated environments, trehalose

was also found to bind to lipid molecules and replace adjacent water molecules thus altering the membrane dipole potential [131]. Currently, most trehalose-related membrane studies are based on simulation results focusing on single-component membranes and dehydration conditions. Further experimental studies with single-component membranes or complex membrane systems and external conditions are required to consolidate previous simulation studies and verify these hypotheses.

3.3 Metabolism and Existence of Trehalose in Vertebrates

Although vertebrates lack the ability to synthesize and store trehalose, they can degrade trehalose via the enzyme trehalase, located in the small intestine [140]. As trehalose is present in common components of the human diet, such as mushrooms and plants, trehalase in the gut can rapidly hydrolyze trehalose into two glucose during digestion processes [141]. Similar to lactose intolerance, a small percentage of people have difficulty digesting trehalose, which may cause some adverse effects, including diarrhea, discomfort, etc. [124]. The trehalose intolerance is due to the deficiency of the trehalase enzyme but can be improved by supplementation with exogenous trehalase [124].

Some reports have confirmed the existence of trehalose in blood, liver, and kidney, but the origin and function in these locations are still unclear [141]. Martano *et al.*. discovered endogenous trehalose present in the hippocampus of rodents along with the corresponding enzyme trehalase located at the soma of neurons in both hippocampus and cortex [142]. This trehalose, synthesized by primary astrocytes, promotes the arborization of neuron cells and modifies neuron morphology, suggesting an essential role of trehalose during neuron maturation [142].

3.4 Conclusion

Currently, the neuroprotective effect of trehalose is mainly attributed to its direct or indirect activation on autophagy; an important cellular process responsible for degrading damaged components and misfolded proteins. However, there is controversy surrounding the mechanisms of trehalose-induced autophagy as the process is still unclear [141]. Trehalose has another pathway to attenuate the neurotoxicity of protein aggregates. It can inhibit protein aggregation with varying rates of efficacy on a wide range of proteins, including tau, α-synuclein, Aβ etc. [141], but it cannot effectively inhibit the generation of Aβ1-42 oligomers [134], which can disrupt cellular membranes and have prevalent neurotoxicity in AD. It is noticeable that trehalose can protect lipid membranes from extreme conditions. Hence, it is reasonable to hypothesize that trehalose's neuroprotection may not be due to its inhibition of Aβ proteins but can be determined by its protection on cellular membranes. The verification of the hypothesis was demonstrated in Chapters 4 to 8.

Chapter 4

Small Amyloid-β Oligomers can Form Ion Channels as Small as Gramicidin in Model Lipid Membranes

Aim of Work and Summary. In membrane electrophysiology studies, the membrane disruption caused by Aβ peptides is indicated as increased ion current flow across the membrane. Given that the activities of Aβ interacting with membranes are heterogenous and different from a traditional protein ion channel, we are interested in analyzing the features of ion current flow caused by Aβ's binding, thus deducing the Aβ's activities when bound to the membranes from the electrophysiological experiment results. In this work, we compared the features of ion current caused by small Aβ oligomers interacting with lipid membranes composed of DPPC, POPC and cholesterol with current flux created by the well-studied gramicidin protein. Our results found that Aβ-induced current features are more diverse than gramicidin's, implying the heterogeneity of Aβ-membrane interactions. In addition, our findings also showed that small Aβ oligomers can form protein ion channels with a size similar to the gramicidin ion channels. This study confirmed the Aβ's disruption and damage to lipid membrane via multiple routes.

This chapter is drafted into a manuscript and prepared for submission to a peer-reviewed

journal.

4.1 Introduction

Soluble Aβ1-42 oligomers have strong cytotoxicity that may lead to neuron dysfunction and neurodegeneration in Alzheimer's Disease [143]. They have profound membrane affinity and can disturb lipid membranes [144] via several mechanisms [145], as indicated in Fig. 4.1(a), such as detergent-like effects extracting lipid molecules from the membrane [21], forming non-selective ion channels that transport Ca^{2+} [23] and monovalent ions, and adhesion and embedment into lipid membranes thus thinning membranes [145, 146]. These membrane changes caused by Aβ1-42 oligomers eventually lead to unexpected ionic transport, thereby disturbing Ca^{2+}-associated homeostasis [19].

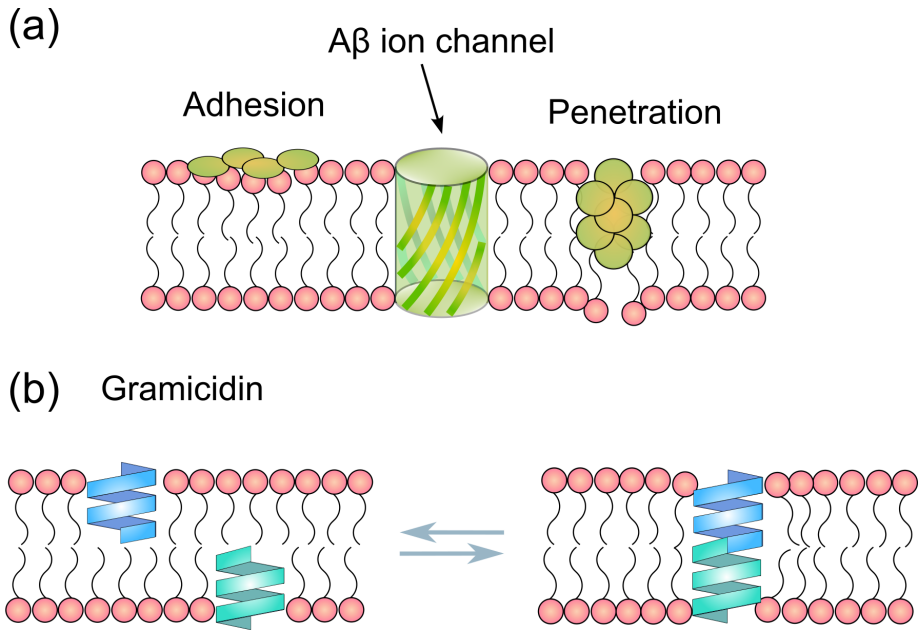


Figure 4.1: Aβ/gramicidin-membrane interaction. (a) Aβ oligomers can interfere with lipid membranes via multiple mechanisms. (b) Gramicidin ion channel formation.

The detergent-like effect of Aβ oligomers can accelerate the degradation of supported

lipid bilayers, as evidenced by AFM images [21], suggesting that Aβ peptides have antimicrobial properties [50], as discussed in Chapter 1. Esbjörner *et al.* observed that larger amyloid aggregates can penetrate cellular membranes and enter and aggregate within the cells [147]. Modelling studies suggested that Aβ1-42 can form β-barrel ion channels with a diameter of 1 to 2 nm [148, 149]. Bode *et al.* experimentally confirmed the formation of Aβ1-42 ion channels on the cellular membrane [20]. Their TEM and patch clamp results showed that the ion channels composed of Aβ1-42 oligomers with sizes of 5 to 20 nm can form ionic pores with a size from 1.7 to 2.4 nm [20]. These experimental [20, 147] and simulation [148, 149] studies demonstrated the variety of Aβ-membrane interactions. However, these diverse Aβ-membrane interactions can happen simultaneously, making it difficult to specify the behaviors of Aβ and identify their individual contributions to membrane destabilization. In addition, another reason making it challenging is the heterogeneity of Aβ aggregates, of which size varies with aggregated subunits [150]. For this reason, we produced small Aβ oligomers with limited sizes and used gramicidin D as a well-identified channel model for a comparison to identify and categorize the oligomeric Aβ-membrane interactions.

Gramicidin D (a natural mixture of gramicidin A, B, and C — the majority is gramicidin A) is a naturally occurring antimicrobial peptide produced by the bacterium Bacillus brevis [151, 152]. In its natural form, two subunits of β-helical gramicidin form a dimer that can insert into lipid bilayers and form a transmembrane pore, which retains the β helicity [153], as shown in Fig. 4.1(b). This pore, with a diameter of 0.4 nm (4 Å), acts as a highly selective ion channel for monovalent cations, such as sodium and potassium ions [154]. The study of gramicidin ion channels has provided valuable insights into the mechanism of ion transport across biological membranes and has contributed to the understanding of ion channel function [155]. Therefore, gramicidin, as one of the most studied and well-defined channels, is an ideal model protein to study the ion channels formed by Aβ1-42.

In this study, we aimed to identify and classify the actions of small Aβ oligomers on the lipid membranes by using atomic force microscopy (AFM) and black lipid membrane (BLM) electrophysiology. The AFM was employed to confirm the formation of small Aβ1-42 oligomers, and BLM was applied to record the instantaneous ion current events

created by Aβ1-42 oligomers and gramicidin interacting with suspended lipid membranes. The Aβ-membrane interactions were classified according to the shape of ionic currents and compared with gramicidin channels. Our results found that small Aβ1-42 oligomers preferred to form ion channels with a similar size as gramicidin channels.

4.2 Materials and Methods

4.2.1 Reagents

Lipids, 1,2-dipalmitoyl-sn-glycero-3-phosphocholine (DPPC), 1-palmitoyl-2-oleoyl-sn-glycero-3-phosphocholine (POPC) and cholesterol were purchased from Sigma Aldrich (ON, Canada). All the chemicals, including potassium chloride (KCl), 1,1,1,3,3,3-hexafluoroisopropanol (HFIP), 4-(2-Hydroxyethyl) piperazine-1-ethanesulfonic acid (HEPES), decane and butyl alcohol, were also purchased from Sigma Aldrich (ON, Canada). Synthetic Aβ1-42 (HFIP) powder was obtained from rPeptide (USA). Gramicidin D powder was purchased from Sigma Aldrich (ON, Canada).

4.2.2 Sample Preparation

Lipid Preparation for Artificial Planar Bilayers

DPPC, POPC, and cholesterol (Fig. 4.2) were pre-dissolved in a mass ratio of 4:4:2 with 9:1 (v/v) chloroform and methanol to make 10 mg/mL lipid stock, stored at $-$ 20 °C. To prepare lipid solution for BLM experiments, The lipid mixture was dried with nitrogen gas to evaporate chloroform and methanol completely. Then, dried lipids were resuspended in 50:1 (v/v) decane and butyl alcohol at 10 mg/mL for use [156].

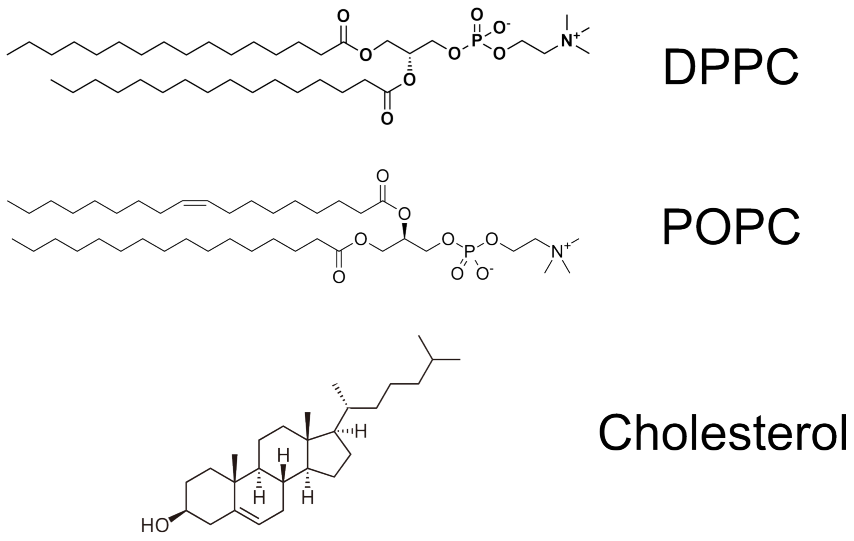


Figure 4.2: Chemical structures of DPPC, POPC and cholesterol.

Aβ Oligomers Preparation

1 mg synthetic Aβ1-42 powder was dissolved with 1 mL HFIP and distributed into aliquots. After the evaporation of HFIP in the fume hood overnight for 24 h, dried Aβ1-42 samples were stored in the freezer at -20 °C. To generate Aβ1-42 oligomers, Aβ1-42 was resuspended in a salt buffer (150 mM KCl and 20 mM HEPES) at a concentration of 122 μM. Aβ1-42 solution was incubated at 4 °C overnight (18 to 24 h) to obtain small Aβ1-42 oligomers and then used for extracellular electrophysiological measurement, according to the protocol by Stine *et al.* [157].

Gramicidin Preparation

10 μg of Gramicidin D powder was dissolved in 5.32 mL of ethanol to produce a 10 μM solution. The solution was then stored in a freezer at -20 °C and used for electrophysiological recordings without any further modifications.

4.2.3 Black Lipid Membrane

The black lipid membrane (BLM) technique is an electrophysiological technique in which membrane permeability can be estimated by measuring the ion currents in a suspended lipid membrane [92]. It was used to study the Aβ- and the gramicidin-membrane interaction in this work. The functions and working principle of BLM electrophysiology have been introduced in Chapter 2.

Suspended Membrane Preparation

Membrane electrophysiological recording was conducted with an Orbit mini instrument from Nanion Technologies (Germany) in the 150 mM KCl and 20 mM HEPES buffer. Artificial lipid membranes were suspended over 150 μm holes in MECA chips (Nanion, Germany) with 4 recording channels by painting via a Teflon sheet or bubbling via a 2 μL pipette. Aβ1-42 solution and gramicidin D were added directly into the chip, respectively. The final concentration of Aβ1-42 solution in the chip is 32 μM, and the final concentration of gramicidin D is 668 pM. The current increase induced by protein-membrane interaction was recorded at 100 mV with 5 kHz sampling rate and SR/20 final bandwidth. The time duration, mean and maximum current (I) of one event from the beginning of the current increase to the current drop were collected for statistical analysis.

4.2.4 Atomic Force Microscopy (AFM)

The existence of Aβ oligomers and fibrils was verified by AFM imaging. AFMs, configured in tapping mode (JPK NanoWizard, Bruker), were used to image the Aβ1-42 oligomers and estimate their sizes. Dried protein samples were imaged in intermittent mode (air) with PPP-NCH probes (Systems for Research (SFR), Canada) with frequencies ranging from 297 kHz to 300 kHz and a spring constant of 42 N/m.

Aβ Oligomers and Fibrils for AFM Imaging

The Aβ oligomers were prepared by suspending Aβ1-42 (HFIP) powder in a salt buffer (150 mM KCl and 20 mM HEPES) at 122 μM and incubated at 4 °C overnight. The Aβ fibrils were prepared with the same solution and incubated at room temperature overnight. Incubated Aβ1-42 was diluted with DI water and the 10 μL protein solution was deposited on mica. After a 5-minute waiting time, the Aβ-deposited mica was washed with 20 μL DI water four times and gently dried with nitrogen gas. Finally, samples were stored in a desiccator overnight before AFM imaging.

Data Collection and Statistical Analysis

For BLM data, the membrane conductance (C) was calculated as the ratio of current (I) to corresponding voltages (V) measured by BLM ($C = I/V$). Statistical analysis (ANOVA, Tukey's test) was conducted with OriginPro 2020. The preliminary AFM images were processed by Gwydion 2.56. Statistics and histograms for the z-height distribution of the Aβ1-42 were produced by Matlab.

4.3 Results and Discussion

4.3.1 AFM Images of Aβ1-42 Oligomers and Fibrils

Aβ oligomers incubated at 4 °C and fibrils incubated at room temperature ($\sim$ 22 °C), which were deposited on mica substrate, were imaged by AFM, as shown in Fig. 4.3.

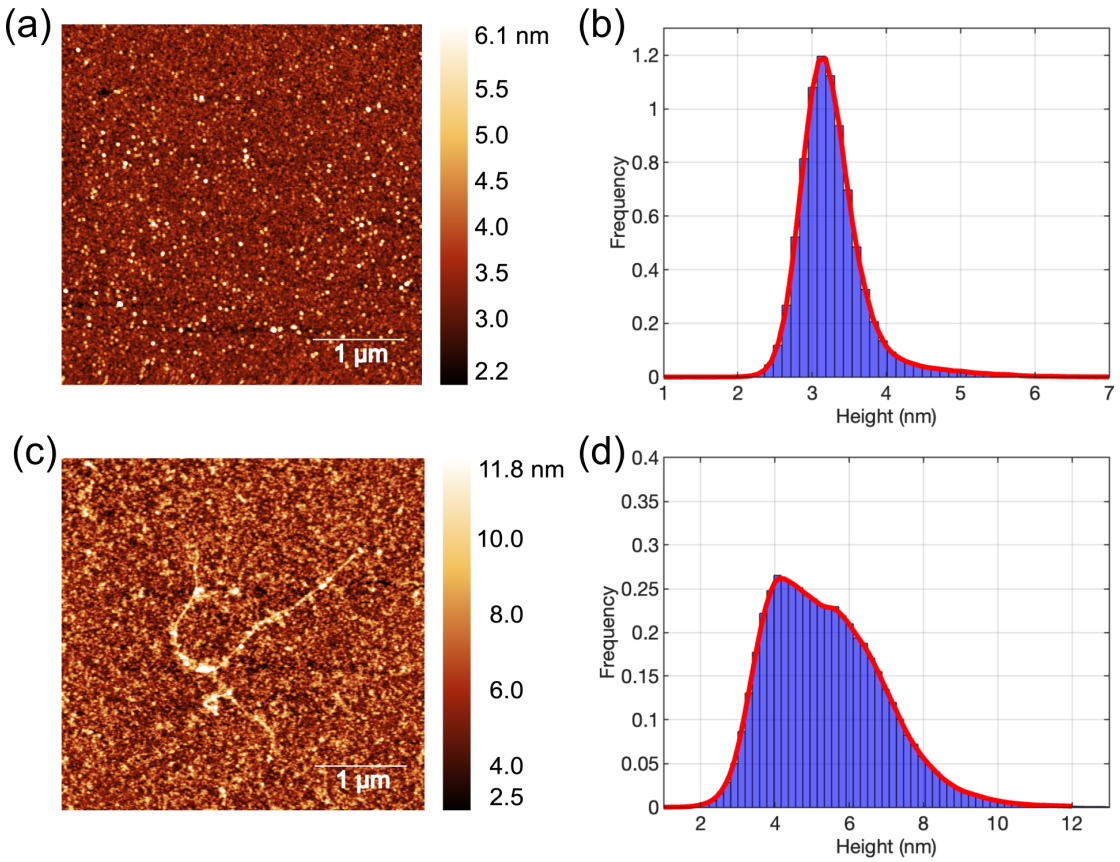


Figure 4.3: Aβ1-42 aggregates deposited on mica imaged by AFM and corresponding histogram. a) Aβ1-42 oligomer particles (white dots in the images) incubated at 4 °C overnight and (b) the corresponding histogram that shows the z-height distribution. c) Aβ1-42 fibrils incubated at room temperature overnight and (d) corresponding histogram of z-height distribution. Size: 4 μm by 4 μm.

The AFM image (Fig. 4.3(a)) confirmed that the Aβ prepared via overnight incubation at 4 °C is present in the form of small oligomers. These Aβ1-42 oligomeric particles appear spherical in shape and mostly lie between 2.6 - 4 nm, according to the histogram of z-height distribution in Fig. 4.3(b). The average height of Aβ1-42 oligomers is 3.28 $\pm$ 0.49 nm (mean $\pm$ SD). AFM results identified that the majority of Aβ particles prepared according to our method and used for BLM are small oligomers. The oligomeric form of Aβ1-

42 is known to have strong membrane affinity and toxicity, which can induce membrane permeation by forming ion channels or pores [150, 158]. In comparison, Aβ1-42 peptides were also incubated at ambient temperature overnight and then imaged by AFM, as shown in Fig. 4.3(c). The AFM image showed the Aβ1-42 fibrils formed on the mica surface. Other than fibrils, large Aβ1-42 oligomers are also seen. The histogram in Fig. 4.3(d) displays the z-height distribution of Aβ1-42 aggregates, ranging from 3 to 10 nm and with an average z-height of 5.39 $\pm$ 1.54 nm. The Aβ1-42 aggregates incubated at room temperature are larger than those incubated at 4°C, suggesting that the aggregation of Aβ proteins is a temperature-dependent process — higher temperatures promote Aβ aggregation and fibrilization.

4.3.2 BLM Electrophysiology for Aβ1-42 & Gramicidin-membrane Interaction

The Aβ1-42 oligomers produced by incubation at 4 °C, as shown in Fig. 4.3(a), were applied to study Aβ-membrane interactions with BLM electrophysiology. BLM was used to measure the current change across a membrane incubated with small Aβ1-42 oligomers at 100 mV. Figure 4.4 displayed increased current flux as the protein interacted with the suspended artificial membranes. The increased currents induced by Aβ1-42 could be categorized into three types: spike, bump, and step (Fig. 4.4(a)-(c)), implying three types of Aβ activities in lipid membranes. To refine our understanding of the Aβ-induced pores, we used the well-studied and understood gramicidin channel as a comparison. Combining the two gramicidin hemichannels in the lipid membrane generates a single transmembrane ion channel, as shown in Fig. 4.1(b). The ion current, due to the formation of a single gramicidin ion channel in the BLM, is featured in step shape in Fig. 4.4(d). The statistical analysis of ion current events caused by protein-membrane interactions in planar lipid bilayers is displayed in Fig. 4.5 and Fig. 4.6.

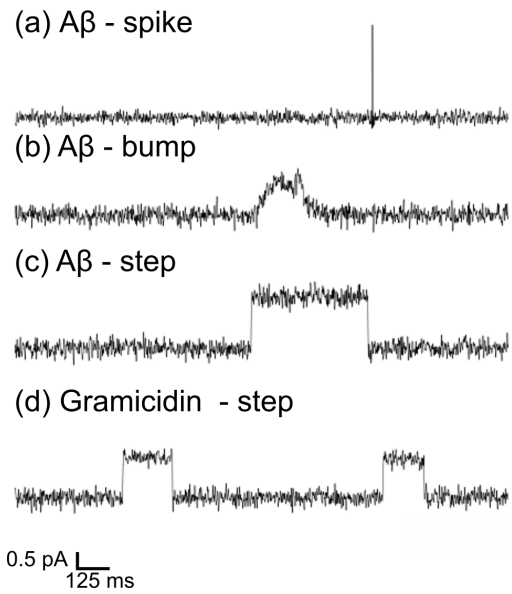


Figure 4.4: Ion current increases induced by Aβ-membrane interactions and gramicidin ion channel formation measured at 100 mV. (a)-(c) Aβ1-42 oligomers-induced ion current flow with the shape of spike, bump and step. (d) Step-like currents due to gramicidin ion channel formation. Horizontal scale bar: 125 ms; vertical scale bar: 0.5 pA.

4.3.3 Interactions of Aβ1-42 Oligomers with Suspended Lipid Membranes

The lifetime and conductance were measured to understand the characteristics of each type of event, as shown in Fig. 4.5. The mean and maximum conductance of ion current events reflected the average and maximum membrane permeability due to the pore or ion channel formation.

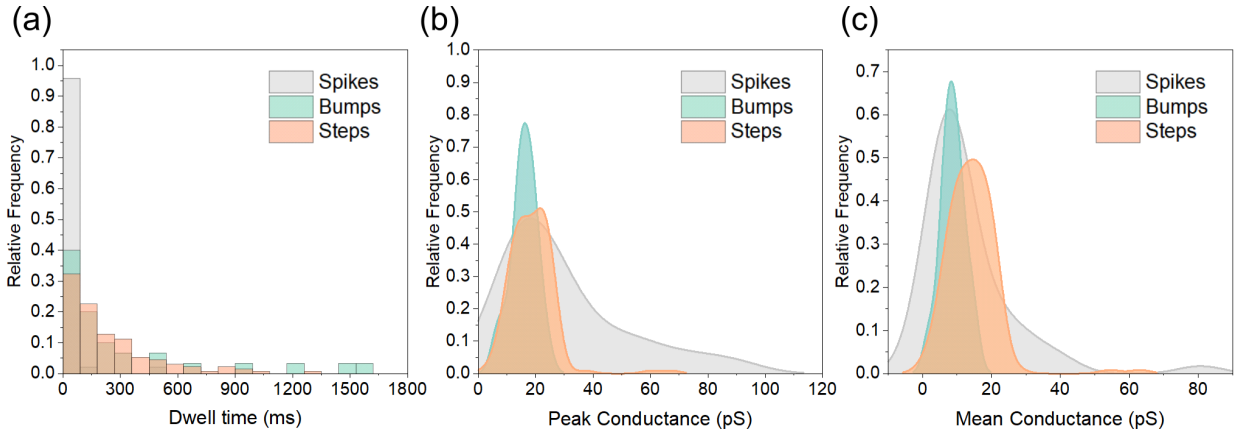


Figure 4.5: Dwell time and conductance of ion current events caused by Aβ1-42 oligomers-membrane interaction. (a) Dwell time of three events (spike, bump, step). (b) peak and (c) mean conductance of three ion current events. Table 4.1 shows the value of conductance.

Signal Type	**Number of events**	**Peak conductance (pS)**	**Mean conductance (pS)**
Spike	49	29.88 ± 21.42	13.20 ± 13.36
Bump	31	15.92 ± 4.34	8.79 ± 3.34
Step	137	18.85 ± 7.98	14.40 ± 7.64

Table 4.1: Conductance and dwell time of Aβ-induced current signals. The data was shown as mean $\pm$ SD.

The spike signal is characterized by an acute increase in current (Fig. 4.4(a)) and an extremely short dwell time at tens of milliseconds (Fig. 4.5(a)). The peak conductance of spike-like currents is significantly larger than step-like and bump-like currents (ANOVA, $p < 0.05$), implying the momentary ion current leakage in the membrane during the spike event is more severe than in step and bump events. The short lifetime of these pores suggests that the membrane recovers and pores are closed instantaneously; therefore, the ion current flow disappears very quickly. Those spike signals could be attributed to the instantaneous ion leakage due to the quick penetration of Aβ peptides in the lipid membrane

[93]. Despite the Aβ1-42 applied to BLM being predominantly oligomeric, there were still minor monomeric Aβ1-42 present in the samples, which inserted membranes and caused spike-like currents in BLM output.

In contrast to spikes, bumps exhibited a gradual increase and decrease in current with a longer lifetime (Fig. 4.4(b))., which was rarely observed in past studies. It could be a random disruption or slow penetration by the Aβ1-42 oligomer. The step-like current (Fig. 4.4(c)) shows a sudden increase in current, which is stable as a plateau for tens to hundreds of milliseconds before returning to the baseline (Fig. 4.5(a)). The step signals appear most frequently among the three types of signals (Table 4.1). Similar ion currents were observed in previous electrophysiological recordings involving different types of proteins, such as alpha-hemolysin, alamethicin, and gramicidin, suggesting the presence of protein ion channels [159, 160, 161]. This suggests that the step-like shape induced by Aβ1-42 corresponds to the 'open' state of protein ion channels [93].

Another noticeable thing is the peak and mean conductance distribution of the three events, as shown in Fig. 4.5(b & c). Spike events have a broader distribution in conductance (both mean and peak), implying the randomness and uncertainty of the events. The conductance of bump and step events is more clustered, with the majority of the conductance (mean and peak) below 30 pS, except in a few cases that exceed 50 pS. This could correlate with the size of Aβ1-42 oligomers, which also shows a relatively constrained range in this work (Fig. 4.3(b)). This suggests that some activities of Aβ on the membrane are influenced by Aβ sizes.

Overall, three characteristic current shapes (step, spike, bump) induced by Aβ oligomers confirm that Aβ can interact with membranes in multiple ways [145]. Particularly, small Aβ1-42 oligomers prefer to form ion channels with short lifespans compared to the other two types of interactions.

4.3.4 Comparison of Aβ1-42-induced Step-like Current with Gramicidin

The step-like currents appeared in Aβ- and gramicidin-membrane interaction, implying the formation of Aβ and gramicidin ion channels. The lifetime and the mean conductance of the two ion channels are compared in Fig. 4.6. 75% of gramicidin ion channels have a lifetime smaller than 165 ms, while close to 50% of Aβ1-42 ion channels remain in the lipid membrane longer than 200 ms (Fig. 4.6(a)), indicating Aβ could be more destructive than gramicidin. The lifetime of gramicidin channels relies on the combination time of two subunits, which is affected by the composition of lipid membranes and the membrane-aqueous interface [161]. The dissociation of two subunits shortend the lifetime of the gramicidin channel, while the Aβ ion channels composed of a single unit are unaffected by this (Fig. 4.1). For this reason, Aβ can retain longer in the lipid membrane. Nevertheless, most of the Aβ ion channels ($> 75\%$) in our study still had a shorter dwell time (< 400 ms) than the claim in previous studies, which summarized that the typical dwell time for Aβ ion channel was above 500 ms [146]. The short lifetime of the Aβ ion channel in lipid membranes suggests that small Aβ1-42 oligomers may stay in the membranes for a short time and then enter the cells.

The mean conductance of gramicidin channels was 11.73 ± 3.13 pS ($n = 151$). The mean conductance of Aβ channels was 14.40 ± 7.64 pS ($n = 137$). Statistically, the Aβ channels were significantly larger than the gramicidin channels (t-test, $p < 0.05$). The distribution of conductance values for the Aβ channels is more dispersed than that of the gramicidin channels, completely overlapping the range of gramicidin conductance values, as shown by the conductance distribution plot (Fig. 4.6b). This means some small Aβ oligomers could form ion channels with conductance equivalent to gramicidin-formed ion channels; some could be larger. Assuming that both gramicidin and Aβ channels are cylindrical, the relation between conductance and pore size can be expressed as [162],

$$G = \frac{\sigma \pi d^2}{4l}, \tag{4.1}$$

where σ is the conductivity of the solution, d is the inner diameter of the nanopore, and l

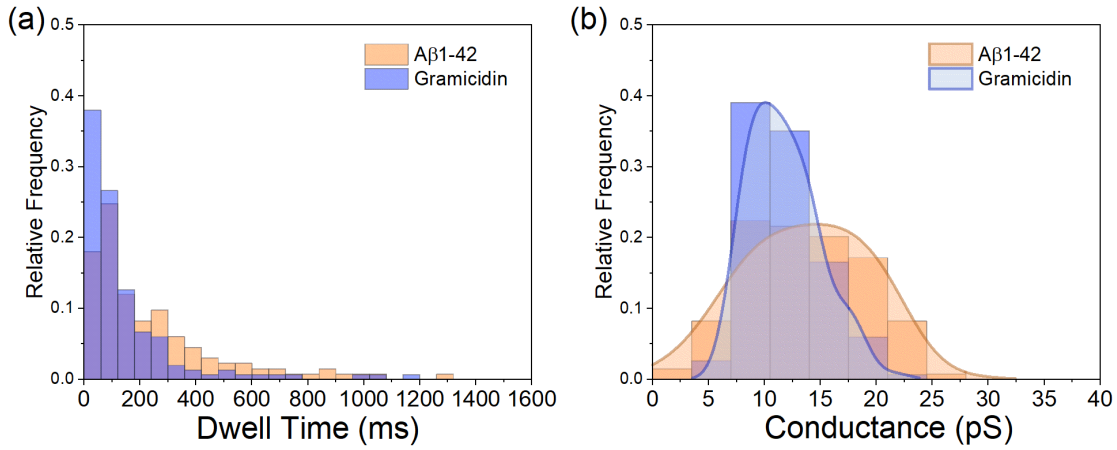


Figure 4.6: The comparison of Aβ ion channels and gramicidin channels. Histograms of (a) Lifetimes of each channel and (b) Ion channel conductance corresponding to step-like currents due to Aβ1-42 and gramicidin ion channels.

is the height of the channel, which correlates to the length of the hydrophobic tails in lipid membranes [163]. Since we used the same lipid model and ionic solutions, it is reasonable to assume that the l value and the σ were the same in the measurement of gramicidin and Aβ channel conductance. The diameter of the gramicidin A ion channels, which is the main component of gramicidin D, is approximately 4 Å in phospholipid membranes [164]. Based on the ratio of gramicidin averaged conductance (11.73 pS) to Aβ1-42 conductance (14.40 pS), the average diameter of the Aβ ion channels calculated by Eq. (4.1) is 4.43 Å, which is slightly larger than gramicidin A channel but at the same magnitude level. Taking the distribution into account (Fig. 4.5(b)), the diameters of Aβ channels have a broader range than that of gramicidin A channel, because of the diversity of Aβ sizes.

In previous studies, the Aβ oligomers were shown to form ion channels with β-barrel structure in the cellular membranes [20, 163]; the typical conductance of these Aβ channels is larger than 250 pS [146]. Some studies also found Aβ-induced conductance larger than 200 pS in artificial lipid membranes and neurons via electrophysiological recordings [29, 163]. However, our results for the Aβ ion channel (14.40 $\pm$ 7.64 pS) are more than 10

times smaller than the previous observation [146, 29, 163]. While we could not reconcile the differences in the conductivity of electrolytes and lipid composition between different experimental setups, the huge difference in the conductance suggested Aβ ion channels are variable and depend on the size of Aβ aggregates. The inner diameter of Aβ ion channels is reported to be 1 to 2 nm as the size of Aβ oligomers lies in 6 to 10 nm [165, 166, 167, 168]. In our experiments, the small Aβ1-42 oligomers with a mean size of 3.28 ± 0.49 nm formed ion channels with inner size below 5 Å, which have never been reported before.

Other than small Aβ1-42 ion channels generating small ion currents reported in this study, the huge current flow above 20 pA with irregular shape represents the destructive effect of Aβ oligomers on membranes, which was frequently seen in previous Aβ studies [27, 156]. It shows the direct Aβ destruction to membrane integrity, leading to dramatic ion leakage. The current flux with erratic shapes and uncertain lasting time can be caused by the random destruction due to Aβ oligomers with diverse sizes and anomalous shapes [146] and difference in lipid membrane compositions [28].

The electrophysiological measurements from BLM exhibit the various damage routes of Aβ1-42 to membranes, despite that the thorough classification of the current features and corresponding activity is still ambiguous. The actual Aβ-membrane interaction associated with bump-shape current (Fig. 4.4(b)) remains unclear. The previous studies of Aβ-membrane interactions using electrophysiological recordings classified the current features as step-like, spiky, and burst events [169, 170]. In addition, evidence shows that Aβ is regarded as an antimicrobial peptide (AMP) as it shares similarities with many other AMPs with amyloid structures and can aggregate at cell surfaces to induce cell dysfunction or death. The Aβ-membrane interaction is analogous to the behaviours of antimicrobial peptides (AMP), which can also insert into membranes and cause pore formation [56, 50]. Saigo *et al.* categorized the current features in electrophysiological recordings and built up protein-membrane models to explain the interaction mechanisms for AMPs, including Clavanin A, Cecropin A and magainin [93]. The classification includes steps, multilevel, erratic, and spike signals according to the shapes of currents [93], which are also observed in our Aβ-membrane measurements. The diversity of current features caused by Aβ-membrane interaction suggests the diverse routes for Aβ oligomers to interact with lipid

membranes acting like AMPs.

Our study revealed that small Aβ1-42 oligomers at the early aggregation stage can form ion channels with a size comparable to gramicidin channels in the lipid membrane. Despite large Aβ aggregates being thought to bring more destruction to membrane stability by inducing huge conductance fluctuation according to planar lipid bilayers studies, cell viability studies showed the opposite size-dependency on Aβ toxicity — smaller Aβ oligomers (1 to 2 nm) have been found to shown more cytotoxicity than larger ones [150]. Our findings demonstrate that small Aβ oligomers can form smaller ion channels with shorter lifetimes in lipid membranes. This suggests these oligomers may disrupt the ionic balance and rapidly enter cells, leading to cytotoxicity.

4.4 Conclusion

In this work, we produced small Aβ1-42 oligomers with an average size of $\sim$ 3 nm and tested these proteins on horizontally and vertically suspended planar bilayers. AFM images confirmed the uniformity of the Aβ1-42 oligomers and their spherical conformation when incubated in a salt buffer at physiological pH. The results of electrophysiological measurements across the artificial lipid membranes incubated with Aβ oligomers showed distinct current shapes, including step-like currents with short lifespans. The step-like current can be identified as the ionic transport due to an ion channel formed by small Aβ1-42 oligomers in the membrane. The size of Aβ1-42 ion channels smaller than those found in previous studies [146] strongly resembles that of gramicidin D channels.

Chapter 5

Effect of Trehalose and NaCl on the Structure and Electrostatic Properties of Langmuir Lipid Monolayers by Atomic Force Microscopy and Kevin Probe Force Microscopy

Aim of the Work and Summary. This work explores the impact of trehalose on the biophysical properties of lipids. We used the Langmuir-Blodgett trough to obtain the compression isotherm of lipid models and to produce lipid monolayers in the different subphases (water, trehalose, NaCl, trehalose + NaCl) for AFM and KPFM imaging. The membrane fluidity and electric potential difference between ordered and disorder domains were evaluated based on isotherms and KPFM data. The results found that trehalose at the coordination of NaCl can enhance lipid fluidity and alter the electrostatic properties within monolayers, confirming the modulation of trehalose on membrane biophysical properties.

This chapter has been drafted into a manuscript with the same title and will be submitted to a peer-reviewed journal.

5.1 Introduction

Trehalose, a unique sugar among the disaccharide family, has been found to have a cryoprotective function and is commonly used as a preservative for biological samples, ranging from proteins and lipids to cells and tissues [171]. Additionally, trehalose can serve as a molecular chaperone, modifying the structures of misfolded proteins. Based on this feature, it attracts attention from scientists and is being explored as a therapeutic candidate for treating neurodegenerative diseases associated with intrinsically disordered proteins, such as Alzheimer's disease (AD) [172, 125]. The prevailing view is that trehalose's neuroprotection is attributed to its regulation during metabolism, particularly its enhancement in autophagy, which promotes the clearance of disordered proteins [173, 128, 141, 174]. However, the molecular mechanisms of why trehalose can regulate autophagy are still under investigation. Other than the role of trehalose in metabolic regulation pathways in biological systems, another pronounced effect of trehalose is its stabilization of lipid membranes under mechanical stress [175], dehydration [176, 177] and undergoing freeze/thaw processes [178, 179]. The distance between lipid molecules is sharply reduced, and the lipid membrane undergoes a reinforced phase transition from liquid-crystalline to gel phase due to the absence of structural water [171]. Trehalose can retain the spacing between lipid molecules, restricting the phase transition and maintaining membrane fluidity during dehydration and freezing [171]. Multiple hypotheses have been proposed to explain the cryopreservation mechanism of trehalose by implicating the trehalose-lipid interaction. Generally, these hypotheses can be divided into two categories: one supports the intimate interaction between trehalose and lipids by replacing adjacent water molecules (water replacement theory) [135, 130] or generating a glass-like trehalose layer (vitrification theory) [171, 137, 138]. In contrast, others think that the exclusion of trehalose molecules maintains the water-lipid interaction, thereby retaining the hydration of the membrane (exclusion theory) [171]. Some believe the two categories of theories are complementary, not contradictory [139], depending on the concentration of trehalose [180]. A Raman spectroscopy study by Leonov *et al.* discovered that trehalose at low concentrations (< 0.2 M) can closely interact with POPC membranes, while concentrated trehalose (> 0.4 M)

is more likely to be repelled from the membrane surface [180]. Even though the actual trehalose-lipid interaction is still under debate, there is no doubt that trehalose can change the membrane properties. Despite this, the impact of trehalose on lipid membranes is rarely considered an essential factor in neuronal and metabolic studies, which are greatly affected by membrane properties. Firstly, misfolded amyloid-β (Aβ) protein is a key factor involved in AD and can disrupt the integrity of cellular membranes, leading to cell impairment and death [21, 26]. The composition of lipid membranes, which determine membrane properties and structural change during AD progression, affects Aβ-membrane interactions [28]. Membrane properties are also important for removing disordered proteins driven by membrane lipid trafficking [181]. Thus, the role of trehalose on membrane properties is important to explore in this regard.

The role of trehalose in cryoprotection and against dehydration is well documented: for example, using differential scanning calorimetry, Crowe *et al.* found that trehalose can mitigate deleterious phase transitions during dehydration by lowering the melting temperature of DPPC from gel to liquid-crystalline phase [182]. This effect of trehalose is attributed to decreased mobility of headgroups and increased disorder of the acyl chain of DPPC due to trehalose binding, as observed in nuclear magnetic resonance spectroscopy studies by Lee *et al.* [183]. Molecular simulation by Kumar *et al.* found that increased trehalose content during dehydration can change the orientation of POPC molecules, regulate the homogeneity of membrane thickness, and enhance the charge density of the POPC membranes, thereby influencing the structural and electrostatic properties of lipid membranes [184]. These changes can be attributed to the direct binding of trehalose to lipid headgroups. A Fourier-transform infrared spectroscopy study by Luzardo *et al.* showed that trehalose changed the polarity of the lipid headgroup through the establishment of hydrogen bonds between the hydroxyl group of trehalose and the carbonyl group of the phospholipid [185], thereby altering the electrostatic properties of the membrane. For instance, trehalose decreased the dipole potentials of DPPC and DPMC by 30 mV [131] and 70 mV [185], respectively, indicating the distinct influence of trehalose on the properties of different lipids. Nevertheless, studies on sugar-lipid interaction mainly focus on single- or binary-component membrane systems, deviating from the real cellular membranes that

involve complex compositions. Recently, Maiti and Daschakraborty explored the influence of trehalose on *Escherichia coli* membranes in hydrated and dehydrated environments by molecular simulation [139] and found that trehalose leads to the expansion of the lipid area and the reduction of membrane thickness because of trehalose-induced lipid disordering [139]. This disordering of lipid molecules stabilizes the fluid phase of the membrane against the lipid ordering and gelling under dehydration [139].

Although plenty of research has been done on trehalose-lipid interactions and various interaction mechanisms have been proposed, experimental studies in terms of multiple-component membrane systems have rarely been conducted. Additionally, although trehalose can alter the surface potentials of single-component lipid membranes [131, 185], it is still unclear how trehalose influences the electrostatic properties in a complex membrane system that shows nanoscale lipid phase separation. These electrostatic properties, in turn, influence the binding of membrane-associated peptides [186], the displacement of transmembrane proteins with charged residue and the accumulation of counterions, among other processes [187, 188].

To address this problem, we explored the changes in nanoscale morphology and electric surface potential distribution in the three-component lipid models (DPPC-POPC-Cholesterol 4:4:2) exposed to trehalose and NaCl. We used a Langmuir-Blodgett (LB) trough to study the elastic compressibility modulus of lipid monolayers at the air/water interface [189, 190, 28] and to prepare supported lipid monolayers on mica for atomic force microscopy (AFM) and Kelvin probe force microscopy (KPFM) to study nanoscale structure and electric surface potential (ESP) distribution in supported monolayers formed with and without trehalose. Furthermore, to account for the physiological environment, we compared the impact of trehalose on lipid monolayers in the absence and presence of NaCl. Our results provide important insights into the role of trehalose on the properties of lipid membranes and the additional effect of physiological salts on the trehalose-lipid interaction, contributing to understanding the physical mechanisms of the metabolic activities induced by trehalose in biological systems.

5.2 Materials and Methods

All lipids (1-palmitoyl-2-oleoyl-glycero-3-phosphocholine (POPC), 1,2-dipalmitoyl-sn-glycero-3-phosphocholine (DPPC), cholesterol (Chol)), trehalose and sodium chloride were purchased from Sigma-Aldrich (Oakville, Canada). DPPC, POPC and Chol were dissolved in chloroform with the mass ratio (4:4:2) to produce a 1 mg/mL lipid mixture for compression isotherms and monolayer deposition by Langmuir-Blodgett (LB) trough (Biolin Scientific, Sweden).

5.2.1 Pressure-Area Isotherm

The compression isotherm (or pressure-area isotherm) is used to study the phase transitions and elastic properties of lipid monolayers under mechanical compression [191]. To obtain the compression isotherm curves for the lipid model, 10 μL of 1 mg/mL lipid mixture in chloroform was deposited onto the surface of the LB trough filled with the appropriate aqueous solution (deionized water, 100 mM trehalose, 150 mM NaCl and 150 mM NaCl-100mM trehalose) as subphase for monolayers. After the evaporation of the chloroform, two symmetric barriers were fully opened to reach a surface pressure close to 0 mN/m. Then, the dispersed lipids on the air-water interface were compressed by barriers at the speed of 5 mm/min. The compression adjusted the alignment of lipid molecules and induced the continuous increase of surface pressure. The compression isotherm (as a change of surface pressure respective to the area) was recorded by the KSV NIMA LB software. At least 7 independent repeats were performed for each subphase to guarantee the reproducibility of isotherms. The room temperature for pressure-area isotherm experiments and monolayer deposition was 22.5 $\pm$ 0.3 °C.

5.2.2 Monolayer Deposition

For microscopy work, the lipid monolayers were deposited on mica slides from the air/water interface of the LB trough. Freshly cleaved mica was submerged beneath the aqueous

subphase, and lipids deposited on the air/water interface were compressed to a target pressure between 20 to 35 mN/m and held for 12 - 14 minutes for stabilization. Then, the submerged mica was lifted at a constant speed of 2 mm/min, and the monolayer was deposited on the hydrophilic mica surface. After deposition, the monolayer sample was dried in a desiccator filled with N_2 for 24 h and then used for AFM and KPFM imaging. At least three independent samples were produced for each subphase.

5.2.3 AFM, KPFM and Image Analysis

The monolayer samples were imaged by AFM (JPK NanoWizard II, Bruker) for topographical information and by KPFM (Aist-NT SmartSPM^{TM}) for electric surface potential distribution. The AFM imaging was conducted in tapping mode in air, using PPP-NCH probes (Nanosensors, Switzerland) with a resonance frequency of approximately 300 kHz and a spring constant of 42 N/m. In KPFM imaging, the monolayer sample was wrapped in aluminum foil and fixed with conductive tape. KPFM was performed in Amplitude Modulation (AM)-KPFM mode with HQ: NSC14/Cr-Au probes (MikroMasch, USA), with a nominal resonance frequency of 160 kHz and a spring constant of 5.0 N/m. The bias voltage amplitude was 4.0 V. All images and cross-section analysis from AFM and KPFM were processed using Gwyddion software.

5.3 Results and Discussion

5.3.1 Pressure - Area Isotherm

Pressure-area isotherms were collected with LB trough and display the surface pressure vs surface area (or molecular area of lipid molecules), as shown in Fig. 5.1(a). The isotherm is a smooth curve showing no pronounced phase transitions at lower compressions and shows the only plateau at higher compression (40 mN/m), which represents the beginning of the collapse and is indicative of multilayer formation during slow collapse process, in agreement with previous reports [192, 193].

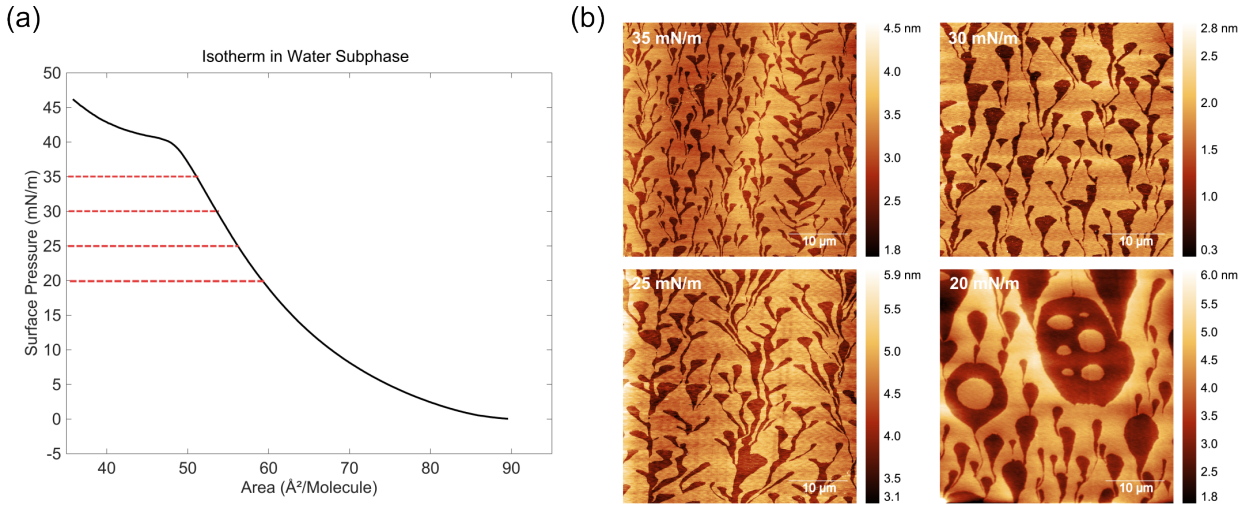


Figure 5.1: Pressure-area isotherm and monolayers produced by LB Trough in water subphase. (a) Isotherm curve of monolayers compressed on water subphase. It was averaged from 9 independent curves. (b) AFM images of DPPC-POPC-Chol (4:4:2) monolayer on the water subphase and AFM images (40 × 40 μm) of lipid monolayers deposited at 20, 25, 30, and 35 mN/m, corresponding to the pressures labelled in red dash lines on the isotherm curve in Fig. 5.1(a).

The AFM images of supported monolayers are shown in Fig. 5.1(b) and demonstrate the co-existence of ordered and disordered domains. The higher domains (bright regions) are in liquid-ordered (L_o) phase, enriched with cholesterol and DPPC [194]. The lower domains (dark regions) are enriched with POPC, with less cholesterol [194], and are in the liquid-disordered (L_d) phase. The surface area of L_o and L_d domains gradually changes when compression increases from 20 mN/m to 35 mN/m, indicating the growing proportion of L_o domains when the compression increases.

Following measurement of the pressure-area isotherm with water subphase, the subphase was changed for 100 mM trehalose (Treh), 150 mM NaCl and 150 mM NaCl + 100 mM Treh. In all the isotherms, the lipid area shows a declining trend in response to the increase in surface pressure (Fig. 5.2 & Table 5.1).

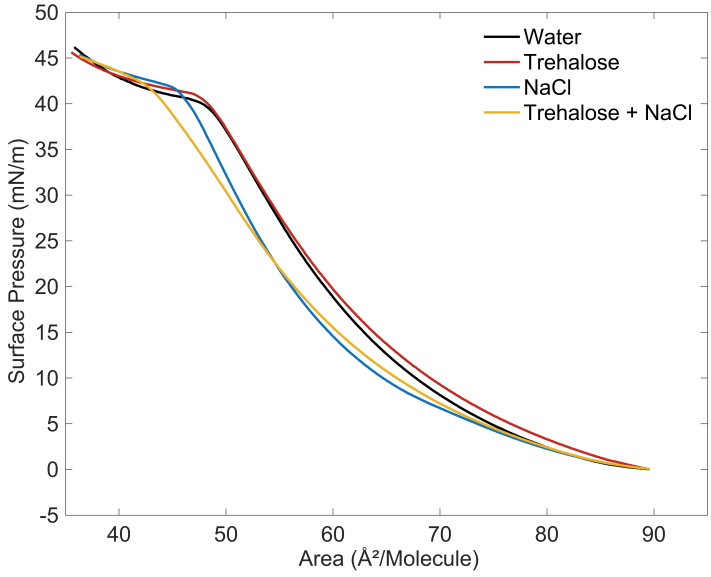


Figure 5.2: Averaged isotherms of ternary lipids (DPPC-POPC-Chol 4:4:2) in different subphases. Black: water. Red: 100 mM Trehalose (Treh). Blue: 150 mM NaCl. Yellow: 150 mM NaCl + 100 mM Treh. The isotherm was averaged from independent repeats (sample size: $n \geq 7$). The average molecular areas (mean ± SE) at each compression pressure are indicated in Table 5.1.

Subphase	**Deposition pressure**				
	5 mN/m	**15 mN/m**	**25 mN/m**	**30 mN/m**	**35 mN/m**
Water	74.7 ± 0.2	62.9 ± 0.4	56.2 ± 0.6	53.6 ± 0.7	51.1 ± 0.7
Treh	76.6 ± 0.1	63.8 ± 0.4	56.6 ± 0.6	53.7 ± 0.7	51.2 ± 0.8
NaCl	73.4 ± 0.2	59.7 ± 0.5	53.3 ± 0.7	51.0 ± 0.8	48.8 ± 0.9
Treh + NaCl	74.0 ± 0.3	60.4 ± 0.9	53.1 ± 1.5	50.2 ± 1.7	47.4 ± 1.5

Table 5.1: Molecular area ($\mathring{A}^2$) of DPPC-POPC-Chol monolayer at the air/liquid interface at different pressures and subphases

As shown in Fig. 5.2, trehalose alone has little effect on the isotherm curve (red) and lipid area compared to the curve obtained in the water subphase (black), which correlates

with previously reported simulation studies for DPPC [130, 131, 195], DPPE [195] and a DPPC:DPPE mixture, with a subtle change in lipid area induced by trehalose [195], implying a superficial interaction of trehalose with these lipid headgroups. However, the presence of 150 mM NaCl shifts the isotherms to the left (blue, Fig. 5.2), representing the condensation of lipid molecules and the reduction of the molecular area per lipid induced by the binding of NaCl to lipid head groups. For instance, the lipid area at 25 mN/m is 56.2 ± 0.6 $\AA^2$ in water and 56.6 ± 0.6 $\AA^2$ in 100 mM Treh subphase, is reduced to 53.3 ± 0.7 $\AA^2$ in 150 mM NaCl and 53.1 ± 1.5 $\AA^2$ in 150 mM NaCl-100 mM Treh subphases. Hence, NaCl solutions remarkably affect the trehalose-lipid interactions, which is aligned with the observation in a relevant sugar-DPPC study by Clark *et al.* in 2015 [196]. They found that NaCl significantly influenced the sugar-membrane interaction, inducing a shift of the isotherm curves, which was attributed to the remarkable affinity of Na^+ ions to lipid headgroups [196]. The binding of cations to lipids can induce a conformation change at the lipid headgroups [197, 198], which may promote the access of carbohydrates like glucose and trehalose to head groups [196].

5.3.2 Elastic Compressibility Modulus

The elastic compressibility modulus of the lipid monolayer can be determined from the pressure-area isotherm. The elastic compressibility modulus C_s^{-1} describes the ease of compressing a lipid monolayer laterally and is given by Eq. (5.1) when the surface area is reduced [199]:

$$C_s^{-1} = -A\frac{\mathrm{d}\pi}{\mathrm{d}A}, \tag{5.1}$$

where A is the molecular area, and π is the surface pressure. A large compressibility modulus value indicates that the monolayer is rigid and difficult to compress.

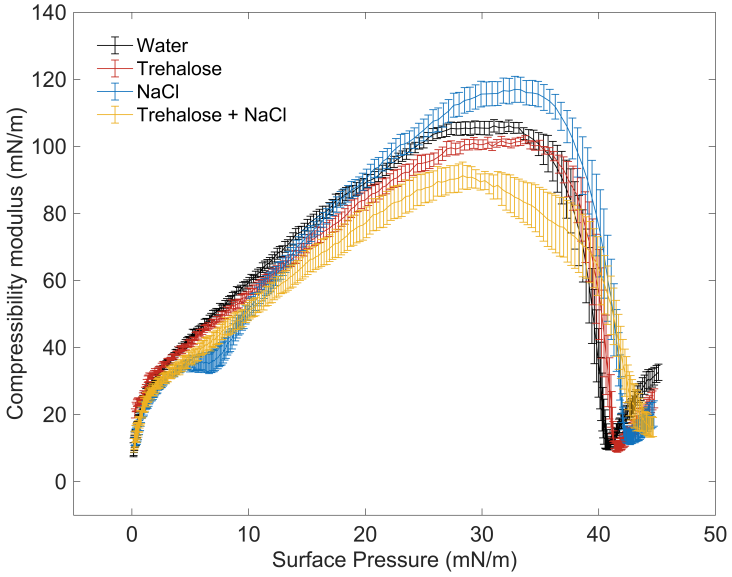


Figure 5.3: Changes in compressibility modulus of ternary lipid monolayers in response to the increasing surface pressure of the monolayer at the air/liquid interface in different subphases. Black: water. Red: 100 mM Treh. Blue: 150 mM NaCl. Yellow: 150 mM NaCl + 100 mM Treh. Data: mean ± SE ($n \geq 7$).

Subphase	**Deposition pressure**				
	5 mN/m	**15 mN/m**	**25 mN/m**	**30 mN/m**	**35 mN/m**
Water	42.3 ± 0.9	76.5 ± 1.8	101.2 ± 1.7	105.5 ± 2.0	100.7 ± 3.5
Treh	41.6 ± 0.9	70.5 ± 2.2	95.2 ± 2.4	100.6 ± 1.4	100.3 ± 1.5
NaCl	35.2 ± 1.9	73.4 ± 2.4	104.9 ± 3.3	115.6 ± 3.8	115.6 ± 3.8
Treh + NaCl	36.7 ± 1.9	65.5 ± 3.7	87.6 ± 4.4	89.4 ± 2.4	80.5 ± 7.3

Table 5.2: Elastic compressibility modulus (mN/m) of DPPC-POPC-Chol lipid mixture at different surface pressures and subphases. Results were shown as mean ± SE.

As shown in Fig. 5.3, the elastic compressibility modulus of the monolayers calculated by Eq. (5.1) tends to reach a maximum in the region of 25 mN/m to 35 mN/m. When

compared to monolayer compressibility modulus in water subphase (105.5 ± 2.0 mN/m) at 30 mN/m, it was found that trehalose reduced the compressibility modulus to 100.6 ± 1.4 mN/m, whereas NaCl increased it to 115.6 ± 3.8 mN/m (Table 5.2). This indicates that trehalose and NaCl have opposing effects on the mechanical properties of lipid monolayers. Trehalose improves the fluidity of lipid monolayers, while NaCl enhances their rigidity. Previous experimental studies also reported that trehalose improved the fluidity of goat sperm membranes before freezing [200]. The increased membrane rigidity induced by the strong binding of NaCl to the headgroups of zwitterionic lipids has been reported in previous simulations and experimental studies [201, 202, 203, 204]. Interestingly, the co-existence of trehalose and NaCl had a more pronounced effect on improving lipid fluidity than trehalose alone, suggesting that NaCl amplified the fluidization effect of trehalose on lipid monolayers. It implies that the interaction of trehalose with the lipid headgroups is regulated by the presence of NaCl, which is aligned with our observation in pressure isotherms and the studies of Clark *et al.* [196]. NaCl may promote the interaction of trehalose with lipid headgroups [196], thereby leading to a higher lipid membrane fluidity.

5.3.3 AFM and KPFM

Monolayers Deposited on Mica Substrates from the Water and Trehalose Subphase

Monolayers were deposited on mica at 25 mN/m using Langmuir-Blodgett deposition from the water and 100 mM trehalose subphase, dried and imaged with AFM in air (Fig. 5.4).

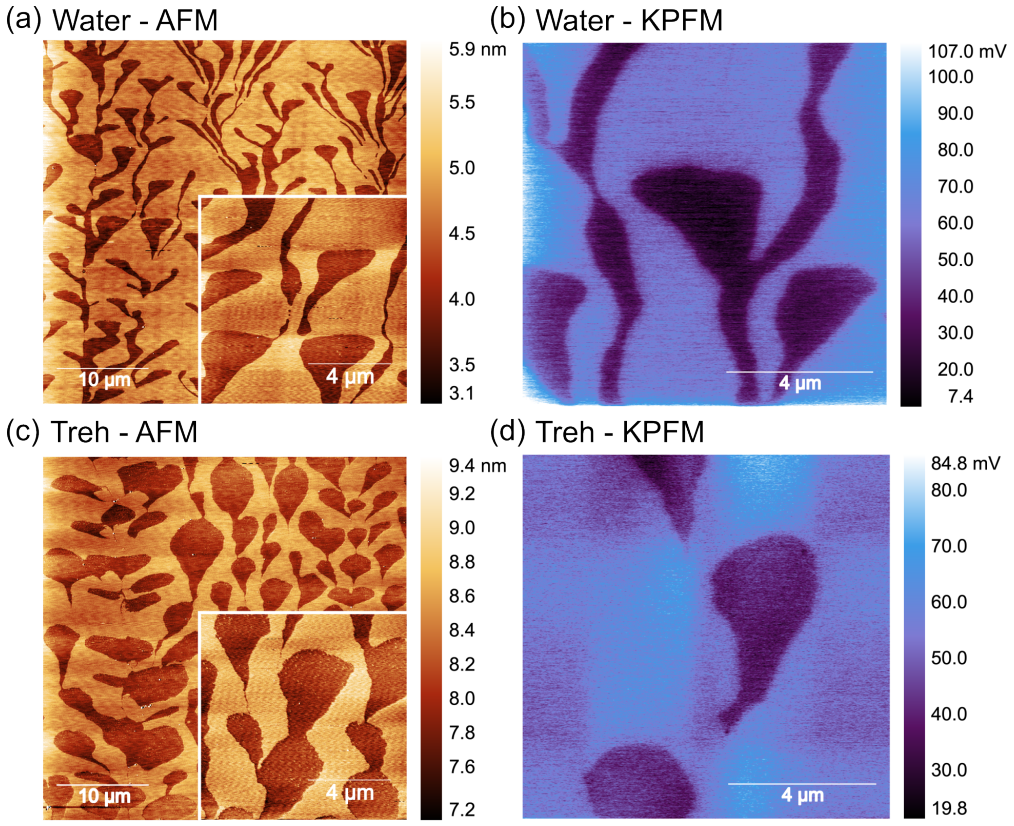


Figure 5.4: Height images (AFM) and contact potential difference (CPD) images (KPFM) of monolayers formed from water and trehalose subphase. (a) AFM and (b) KPFM images of monolayers formed from the water subphase. (c) AFM and (d) KPFM images of monolayers formed from 100 mM-Treh subphase. These monolayers were deposited on mica slides at a surface pressure of 25 mN/m. Size of AFM images: 40 × 40 μm, inset: 10 × 10 μm. CPD images: 10 × 10 μm. Treh: Trehalose.

Monolayer subphase	**Height difference (Δh)**	**Electric Surface Potential difference (ΔESP)**
Control (DI water)	0.63 ± 0.06 nm	31.38 ± 0.79 mV
100 mM Trehalose	0.57 ± 0.02 nm	21.75 ± 1.54 mV

Table 5.3: The height (Δh) and electric surface potential differences (ΔESP) between ordered (L_o) and disordered (L_d) domains within monolayers made in water and trehalose subphase determined from AFM and KPFM images cross-sections. Results were shown as mean $\pm$ SE.

As shown in Fig. 5.4, both monolayers deposited from water and trehalose subphase at 25 mN/m have the characteristics of droplet-like patterns of L_d domains (dark) embedded within L_o domains (bright). The morphological similarity between monolayers in water (Fig. 5.4(a)) and the trehalose subphase (Fig. 5.4(c)) suggested that trehalose has subtle impact on phase separation and membrane morphology, in agreement with previous studies [205, 177, 139].

KPFM images (Fig. 5.4(b) & (d)) display the electric surface potential distribution measured in monolayers supported on mica slides from water and Treh subphase. As previously reported, ESP at the air/water interface relates to the dipole potentials of the lipid molecules, defined by their chemical structure and packing density (or phase) [206]. In Fig. 5.4 (b), the L_o region (bright) enriched with DPPC and cholesterol has higher ESP than the POPC-rich L_d region (dark). The difference in electric surface potential is determined by the dipole potentials that correlate to the dipole moment and the tilt of the lipid molecules, given by Eq. (5.2) [207],

$$\Delta V = \frac{12\pi\mu_{\perp}}{A} = \frac{12\pi\left(\mu_1 + \mu_2 + \mu_3\right)}{A}, \tag{5.2}$$

where A is the area per lipid molecule and $\mu_{\perp}$ is the part of the dipole moment of the phospholipid perpendicular to the subphase surface. This is defined as the sum of the partial dipole moment of the water molecules surrounding the lipid headgroups (μ_1), the head groups (μ_2) and the hydrocarbon chain (μ_3). The electric surface potential difference

(ΔESP) between L_o (ΔV_o) and L_d domains (ΔV_d) can be defined as

$$\Delta\text{ESP} = \Delta V_o - \Delta V_d. \tag{5.3}$$

However, KPFM does not measure the ΔV directly. Instead, it maps the contact potential difference (CPD) between the scanning probe and the sample surface. From the CPD images (Fig. 5.4(b) & (d)), the relative potential difference between two regions with distinct potentials can be measured. Hence, ΔESP can be derived by the difference of CPD between L_o (CPD_o) and L_d domain (CPD_d),

$$\Delta\text{ESP} = \Delta\text{CPD}_o - \Delta\text{CPD}_d. \tag{5.4}$$

The height difference ($\Delta h = h_o - h_d$) and the potential differences between the L_o and L_d domains (ΔESP) determined by Eq. (5.4) are shown in Table 5.3. The change of Δh in the two subphases is subtle, which is 0.63 ± 0.06 nm in water and 0.57 ± 0.02 nm in 100 mM trehalose. Remarkably, ΔESP in supported monolayers was reduced from 31.38 ± 0.79 mV in water to 21.75 ± 1.54 mV in trehalose subphase (Table 5.3). The reduction of ΔESP is mainly caused by trehalose's interaction with the lipid headgroup [208], which influences the tilt angle of lipid molecules and headgroup polarity [184], thereby altering $\mu_\perp$ of lipid molecules and the electrostatic properties of lipid membranes.

Monolayers Deposited in NaCl and Trehalose-NaCl Subphase

After comparing supported monolayers deposited on mica from water and trehalose subphases, we next studied the monolayers deposited from the subphases of 150 mM NaCl and 150 mM NaCl - 100 mM trehalose (Treh) for comparison.

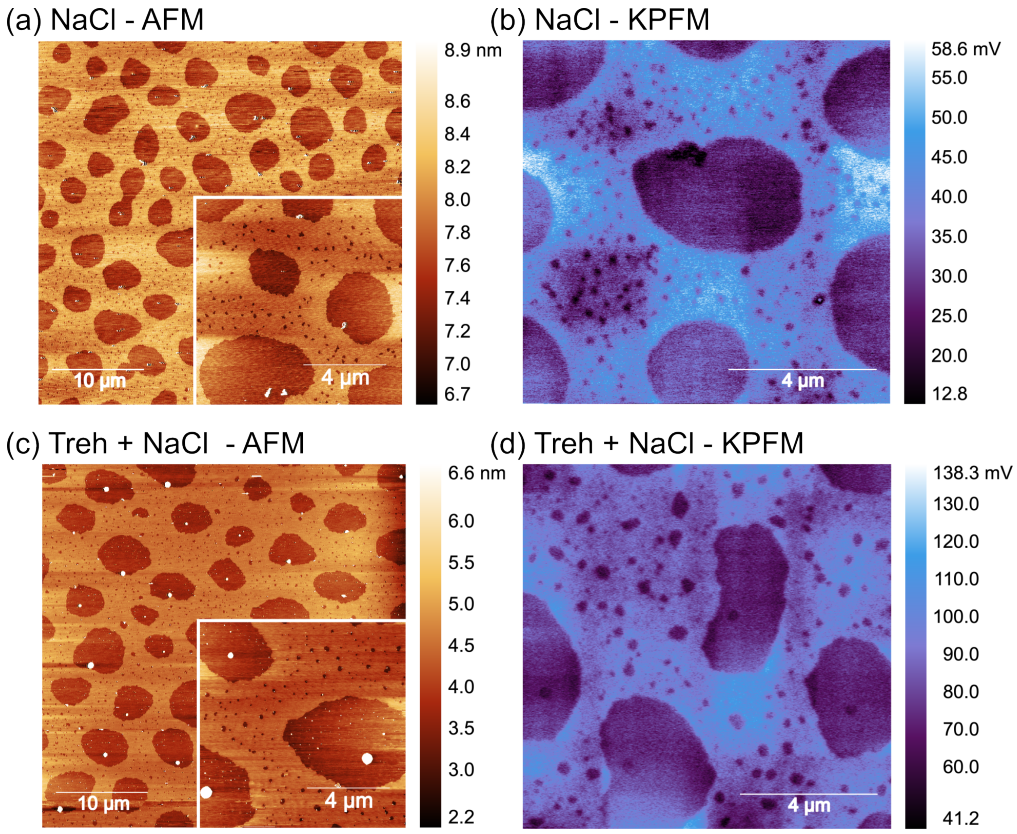


Figure 5.5: Height images (AFM) and CPD images (KPFM) of monolayers formed on the NaCl and NaCl-Treh subphases deposited on mica at 25 mN/m. (a) AFM and (b) KPFM images of monolayers formed from 150 mM NaCl subphase. (c) AFM and (d) KPFM images of monolayers formed from 150 mM NaCl – 100 mM Treh subphase. Size of AFM images: 40 $\times$ 40 μm, inset: 10 $\times$ 10 μm. CPD images: 10 $\times$ 10 μm. Treh: trehalose.

Monolayer subphase	**Height difference (Δh)**	**Electric Surface Potential difference (ΔESP)**
150 mM NaCl	0.50 ± 0.04 nm	21.28 ± 0.98 mV
150 NaCl-100 mM Treh	0.59 ± 0.03 nm	40.32 ± 2.33 mV

Table 5.4: The height (Δh) and electric surface potential differences (ΔESP) between ordered (L_o) and disordered (L_d) domains within monolayers deposited on mica from NaCl and Treh-NaCl subphase determined from AFM and KPFM images cross-sections. Results were shown as mean $\pm$ SE.

Unlike the monolayers in water and trehalose without the presence of NaCl in the aqueous subphase (Fig. 5.4), the monolayers in NaCl both with and without trehalose are characterized by large patch-like L_d regions (dark), surrounded by interconnected L_o regions (bright) featuring smaller L_d regions (Fig. 5.5). The change in domain morphology (from droplet-like to spherical shape) of NaCl monolayers implies that NaCl mitigates lipid mobility and enhances the adsorption of the lipid headgroup on the mica substrate. The reduction of lipid mobility can be attributed to the stabilizing effects of Na^+ ions interacting with lipid molecules [202], which may also contribute to forming small L_d domains.

Monolayers deposited from the NaCl-Treh subphase are similar to those deposited on the NaCl subphase, suggesting the profound influence of NaCl on lipid monolayers even in the presence of trehalose. Additionally, we observed small spherical clusters (white spots) with a z-height of tens nm in the L_d regions in the NaCl-Treh monolayer in Fig. 5.5(c). This observation could be explained by the co-binding of trehalose and NaCl to lipid headgroups, which promotes the formation of lipid clusters under lateral compression.

In 150 mM NaCl, Δh was reduced to 0.50 $\pm$ 0.04 nm and ΔESP was reduced to 21.28 $\pm$ 0.98 mV (Table 5.4), which is similar in trehalose where ΔESP is 21.75 $\pm$ 1.54 mV (Table 5.3). This suggests that individual binding of trehalose and NaCl to the lipid headgroup has a screening effect on the original lipid molecule dipoles, diminishing the ESP difference between lipid domains. The screening of lipid dipoles by highly concentrated salts has been demonstrated by previous studies [209]. However, when the NaCl and

Treh are incorporated into the lipid monolayer, they have the opposite effects on the lipids. Compared to the monolayer on water with $\Delta h = 0.63 \pm 0.06$ nm, Δh was almost maintained on the NaCl-Treh subphase (0.59 ± 0.03 nm). Noticeably, the ΔESP in the NaCl-Treh subphase has increased to 40.32 ± 2.33 mV, around ~ 10 mV higher than that on water and ~ 20 mV higher than on NaCl and Treh subphases, although its morphological structure is still similar to that on NaCl. Therefore, the electrostatic difference between the two phases was enhanced due to the co-existence of NaCl and trehalose.

The positively charged choline group and the negatively charged phosphate group contribute to the dipole moment in the polar lipid headgroup of phosphatidylcholine (PC) groups, particularly those of DPPC and POPC, in our studies. The simultaneous interactions of NaCl, trehalose and water with the lipid headgroup contribute to the change of the dipole moment defined by the choline and phosphate groups, thereby altering the dipole potentials. According to a study by Vácha *et al.* (2009), Na^+ preferably binds to the negatively charged phosphate group while Cl^- binds to the positive choline group [210]. However, the binding of Na^+ to headgroups of zwitterionic lipids is dominant, and most Cl^- ions prefer to stay in solution [211]. As well as binding with a phosphate group, Na^+ may simultaneously coordinate with carbonyl groups (C=O) of three POPC molecules [202]. In addition, water molecules can also be attracted to lipid headgroup due to the presence of Na^+, as shown in Fig. 5.6 [212]. The incorporation of Na^+ has been shown to induce a reduction in the area per lipid molecule and a change in headgroup orientation and dipole potential, leading to the increase of the ESP of the DOPC membrane [210]. The Na^+ binding to the lipid headgroup generated a dipole opposed to the direction of the phosphate-choline dipole; however, the presence of water (Fig. 5.6) compensates for the opposite dipole and attenuates the effect of Na^+ on the lipid headgroup, while Na^+ still significantly changes the membrane surface potential [210].

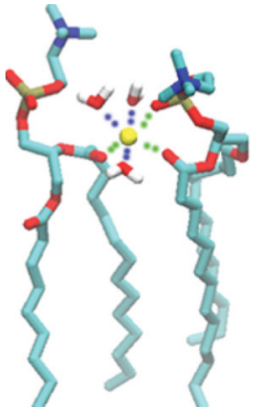


Figure 5.6: Sodium ion (Na^+) coordinates with three water molecules and three oxygen from phosphate and carbonyl group of DMPC lipids. Yellow: Na^+. Red: oxygen. Light blue: carbon. White: hydrogen. Adapted with permission from *Journal of Chemical Theory and Computation*, Specific ion binding at phospholipid membrane surfaces. J. Yang, C. Calero, M. Bonomi, and J. Martí. 11(9):4495–4499, 2015. Copyright (2015) American Chemical Society.

In our case, substantial water is absent in the monolayer samples, and the contribution of Na^+ to the surface electrostatic potential is greater than in an aqueous environment. Therefore, Na^+ enormously changes the surface potential and screens the original dipole potential of the lipid molecules, reducing the potential difference between L_o and L_d regions (ΔESP) in our ternary lipid system. As trehalose supplants the role of water, the polarity of the lipid increases. Trehalose at 100mM has previously been shown to decrease the surface potential of DMPC lipid monolayers in hydration, according to previous simulation results [185]. However, Langmuir monolayer studies by Lambruschini *et al.* revealed that trehalose increases the ESP via binding to DPPC headgroups [213]. Therefore, we speculate that trehalose compensates for the absence of water molecules and neutralizes the screening of Na^+ to the ESP. Since both trehalose and Na^+ions can interact with the C=O groups of phospholipids [185, 202], they may have competitive or cooperative binding with lipid headgroups. The influence of trehalose on lipid molecules is diverse, specific to lipid composition and regulated by the presence of salts, thereby leading to a distinct potential difference between domains with different lipid compositions. Therefore, the influence of

trehalose and Na^+ in current lipid models can be expanded to include other diverse monovalent ions abundant in physiological conditions and to more complex multi-component lipid systems in future studies.

5.4 Conclusion

This study explored the influence of trehalose sugar and NaCl on morphological and electrostatic properties of supported lipid monolayers with the composition of DPPC-POPC-Chol (4:4:2) using atomic force microscopy and Kelvin probe force microscopy and the elastic compressibility modulus of free-floating monolayers at the air/water interface using Langmuir-Blodgett monolayer techniques. The data demonstrate that the membrane fluidity can be improved by trehalose and further enhanced by the presence of NaCl. Trehalose alone helps preserve the original membrane morphology and phase separation while adding NaCl changes these properties. Both height difference (Δh) and electric potential differences (ΔESP) between lipid domains were compared. ESP differences between domains are reduced by trehalose alone but enhanced with NaCl-trehalose. These results have shown that the trehalose-lipid interaction is mediated by NaCl, present in physiological environments, which provides important insight and may explain its protective membrane-active role in biological systems.

Chapter 6

Protective Effect of Trehalose Sugar on Amyloid-membrane Interactions using BLM Electrophysiology

Aim of the Work and Summary

Since trehalose can affect membrane biophysical properties, as confirmed in Chapter 5, one may wonder whether trehalose's modulation can make the membrane more durable for Aβ's damage. In order to investigate the potential protection of trehalose on lipid membranes against Aβ's destruction effect, we used AFM to visualize the lipid membrane surface incubated with Aβ and trehalose in liquid and use BLM to evaluate the membrane permeability by measuring the ion current across the membranes. AFM images showed the penetration of Aβ into the lipid membrane, causing pore formation. BLM results indicated that the increase of membrane permeability due to Aβ damage is suppressed by the presence of trehalose. Our findings implied the modulation of trehalose makes lipid membranes more resistant and stable to Aβ-induced damage.

This chapter was reproduced with minor modifications with permission from Yue Xu, Carina T. Filice, and Zoya Leonenko. Protective effect of trehalose sugar on amyloid-

membrane interactions using blm electrophysiology. *Biophysical Journal*, 123(12):1690–1704, 2024. [Journal Cover].

6.1 Introduction

6.1.1 Amyloid-β and Alzheimer's Disease

Amyloid-β plaques are considered one of the main pathological features of Alzheimer's Disease (AD) [214, 215, 216]. These plaques are attributed to the overproduction and aggregation of amyloid-β (Aβ) peptides [217], and are found on the surface of neuronal cells [218, 2, 219]. As the neuronal cell membrane is of critical importance in neural physiology [219] and is recognized as a target for Aβ attack [220, 221, 222], it provides an opportunity to explore new strategies to protect the neuronal cell from Aβ-induced damage [40].

It has been shown that small Aβ oligomers rather than large fibrils are most toxic to neuronal cells [223, 224, 163, 225], with Aβ1-42 as the most toxic species [5, 6]. The proposed mechanism of Aβ1-42 oligomer-mediated neurotoxicity suggests that Aβ1-42 binds to neuronal cellular membranes and causes membrane disruption by creating various defects, including ion channel-like pores, which lead to membrane damage, ion leakage and ionic imbalance [163, 166, 145, 29], thus contributing to the dysfunction, degeneration, and death of neurons [143, 166].

Due to the importance of cellular membranes [226, 227], they have attracted a lot of attention in connection to AD pathology. Previous studies suggest a strong correlation between the progression of AD and the alteration of lipid compositions in plasma membranes [37, 38, 39, 40, 228, 229, 47]. In addition, the reduction of sphingomyelin levels and elevation of cholesterol due to abnormal lipid metabolism was found in AD brains, presumably as a result of disease progression [45, 47]. Such alteration in lipid composition significantly influences the interactions of membranes with Aβ [230, 35, 36, 231, 232, 233]. It has been shown by Drolle *et al.* that model lipid membranes which mimic healthy

neuronal membranes are less susceptible to Aβ damage than membranes mimicking AD neurons [28]. This evidence indicates a pertinent relationship between Aβ induced neurotoxicity and lipid membrane properties and suggests Aβs can recognize the changes in lipid membranes. As there is currently no cure available for AD and multiple drug candidates targeting Aβ aggregation are failing in clinical trials [1, 50, 234, 235], it becomes important to explore potential preventive approaches, specifically targeting lipid membrane properties, as this may reduce Aβ neurotoxicity.

6.1.2 Protecting Membranes against Aβ using Small Molecules

Consequently, inspired by this novel idea to focus on membrane protection strategies, current AD research has highlighted various small membrane-active molecules capable of blocking or reducing the insertion of Aβ oligomers in neuronal membranes, such as melatonin [236, 79, 82], curcumin [81], various aminosterols [88] etc. Specifically we have demonstrated in vitro that melatonin reduces the binding of Aβ to model membranes, thus protecting the membranes from Aβ-induced damage [237]. In studies completed by Limbocker *et al.*, aminosterols such as trudosquemine and squalamine bind to cellular membranes and displace toxic Aβ1-42 oligomeric species from neuronal cells in addition to modifying Aβ1-42 aggregation mechanisms in solution [86, 85, 87]. Errico *et al.* expounded upon these findings by discovering that this aminosterol-mediated oligomer displacement from cell membranes occurs through the alteration of membrane properties such as lipid organization, lipid packing, and surface charge [88, 238]. Other research groups have also reported neuroprotective effects of curcumin [81], tauroursodeoxycholate [30], and 2-hydroxydocosahexaenoic acid [89] against Aβ toxicity by reducing binding and increasing membrane stability. Inspired by the membrane protection strategies, our studies aimed at exploring the influence of trehalose on Aβ-membrane interactions in AD.

6.1.3 Trehalose, Aβ, and Membranes

Trehalose is a non-reducing disaccharide of glucose often found in biological laboratories as an essential component of solutions used to preserve tissues, organs, and other biological samples [239]. Trehalose can protect biomolecules (i.e. lipids, proteins) from extreme conditions such as high temperature and mechanical stress [239], with effective cryoprotection concentrations ranging from 2.6 μM [240] to 1M [241] depending on sample composition. Additionally, trehalose, as a dietary sugar, shows little toxicity to humans, even with an average daily intake of 42.37 g from both natural sources and processed food [242]. Most individuals can metabolize trehalose using the intrinsic enzyme trehalase; however, a small subset of the population may lack this enzyme, leading to side effects like diarrhea, discomfort, borborygmus, etc. which can be alleviated by oral ingestion of trehalase [124]. In clinical ophthalmology, trehalose is an important component in novel topical dry-eye treatments that have shown improvements in animal models and clinical patients suffering from dry eye [243, 244, 245]. Currently, trehalose is regarded as a bioactive agent and is also being explored for its therapeutical potency in diabetes, osteoporosis and neurodegenerative diseases [242, 125]. Animal studies have revealed the neuroprotection role of trehalose in neurodegenerative diseases correlating to the accumulation of aberrant proteins, such as Alzheimer's disease (AD), Parkinson's disease (PD), and Huntington's disease (HD) [125].

Previous studies suggest that trehalose can directly interact with membranes by replacing water molecules adjacent to membrane phospholipids and forming hydrogen bonds with the lipid headgroups [130, 132, 131, 246]. As cellular membranes play an important role in Aβ toxicity in AD, this provides an important avenue to explore the possibility of protecting the membrane and to prevent or reduce Aβ toxicity by modifying the membrane properties itself.

Trehalose is being investigated as a potential therapy for AD [247]. In principle, we may consider two pathways where trehalose can protect against Aβ1-42 oligomers toxicity. The first pathway focuses on trehalose altering Aβ aggregation in solution. Previous studies by other research groups indicate that, over large periods of time, trehalose triggers the conformational change of Aβ and inhibits the formation of Aβ deposits in vivo [133, 127,

248, 247]. In a study conducted by Liu *et al.*, trehalose showed different suppression effects on the aggregation of Aβ1-40 and Aβ1-42 respectively [133]. The authors reported that the cytotoxicity of Aβ1-40 was reduced by inhibiting the formation of Aβ oligomers [133]. Trehalose was also found to alter the conformation of Aβ1-40 oligomers from toxic β-sheets into the less toxic α-helix structure, thereby reducing Aβ insertion to membranes [246, 127]. Conversely, the inhibition effect of trehalose on Aβ1-42 aggregation in solution was limited; while aggregation was reduced and fibril formation inhibited, the conformation of Aβ1-42 oligomers was not altered and therefore the toxicity was not fully eliminated [133]. This proposed pathway of trehalose protection can be suppressed by the presence of salt (NaCl) at concentrations larger than 25 mM as indicated in studies observing trehalose interactions with similar β-sheet peptides lysozyme and insulin [134]. Therefore, while trehalose shows a suppressive effect on fibril formation in solution, the toxic Aβ1-42 oligomers persist and thus continue to cause damage to membranes.

The second, less-studied pathway of trehalose protection focuses on protecting the membrane from Aβ damage. In addition to the reported effects of trehalose on plant [249] biomembranes and Aβ proteins respectively [134, 248, 133], trehalose also reduced liposome permeability caused by Aβ1-40 oligomers [250]. However, to our knowledge, most studies regarding incorporative behaviours of Aβ proteins and trehalose on lipid membranes concentrate on these aspects at the theoretical level alone (i.e., molecular dynamics simulations). Previous experimental studies investigated only Aβ1-40 rather than its more toxic counterpart, Aβ1-42. Therefore, the protective effect of trehalose against Aβ1-42 at the membrane level is not known and is the subject of this study.

We hypothesize that similarly to protecting the plant membranes against harsh conditions, the trehalose can bind to the surface of neuronal cellular membranes and protect them from toxic Aβ-induced damage (Fig. 6.1). In this work, we aim to study the effect of trehalose on Aβ1-42 toxicity against model neuronal membranes composed of DPPC, POPC and cholesterol in a weight ratio of 4:4:2. Zwitterionic lipids with PC groups were chosen as the main constituent of our proposed simple neuronal lipid model as neutral-charged lipids constitute the main component of the cellular lipid membrane in neurons [190, 28], despite anionic lipid membranes being the focus of many Aβ-membrane studies

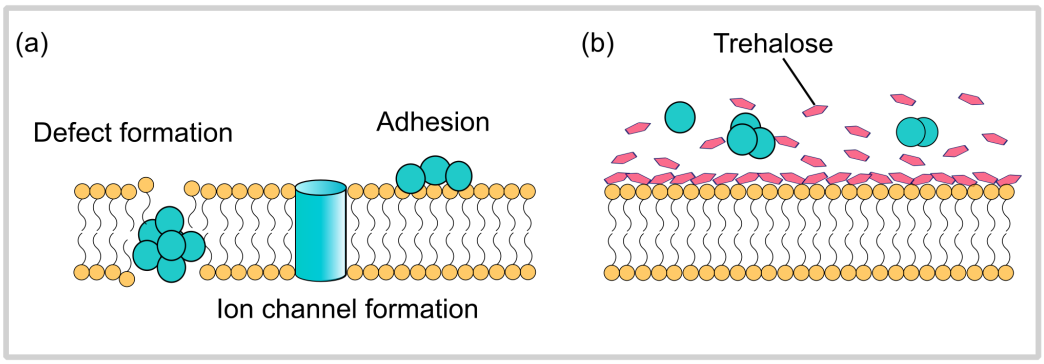


Figure 6.1: Hypothesis of trehalose protection mechanism against Aβ damage to lipid membranes. (a) Multiple mechanisms of Aβ1-42 damaging lipid membranes. (b) A potential mechanism that trehalose protects membranes against Aβ1-42 toxicity.

[79, 251, 246]. As shown in Fig. 6.1, Aβ1-42 oligomers can bind to the cellular membranes and produce various defects (Fig. 6.1(a)), increasing membrane damage. We propose that trehalose can protect the membranes against Aβ1-42 toxicity by binding to the membrane surface and by creating a protection barrier to resist Aβ-induced damage (Fig. 6.1(b)).

The research focuses on studying membrane integrity during treatment with trehalose and damage from Aβ1-42 oligomers. We used the black lipid membrane (BLM) electrophysiology technique to investigate the protective effect of trehalose in model lipid membrane against damaging effects of Aβ1-42 by measuring membrane permeability, complemented by atomic force microscopy (AFM) used to visualize the Aβ aggregates and the damage induced by Aβ1-42 oligomers in the membranes. Our results demonstrate that high concentrations of trehalose improve membrane stability after the destruction of Aβ to the membrane and reduce the damage induced by toxic Aβ oligomers.

6.2 Materials and Methods

6.2.1 Black Lipid Membrane Electrophysiology

BLM is a popular electrophysiology method used to measure the permeability of model lipid membranes, where membranes are suspended over a micrometer-sized pore, and ion current is measured as an indication of the membrane permeability, directly related to membrane damage (Fig. 6.2).

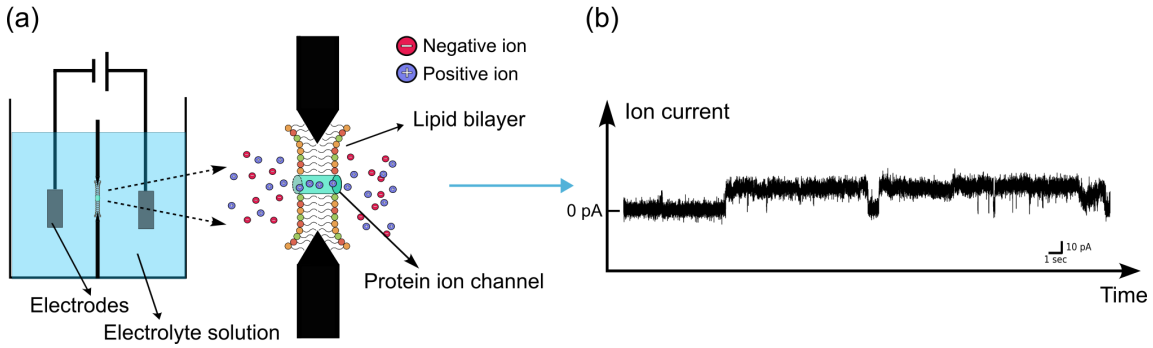


Figure 6.2: Schematic of electrophysiological planar bilayer recording system used in (a) BLM technique to detect protein ion channels in lipid bilayers and (b) a representative current trace of Aβ1-42 ion channel forming in suspended lipid bilayers in KCl-HEPES buffer at 120 mV, obtained from single-event recording experiments.

Lipid and Model Membrane Preparation for BLM

Model membranes were composed of 1,2-dipalmitoyl-sn-glycero-3-phosphocholine (DPPC), 1-palmitoyl-2-oleoyl-sn-glycero-3-phosphocholine (POPC) and cholesterol (Sigma-Aldrich, Oakville, ON, Canada) in mass ratio 4:4:2. Powdered lipids were dissolved in 9:1 chloroform and methanol (v/v) to prepare a stock solution at a concentration of 10 mg/mL, which was stored at -20 °C. To create a working lipid solution for BLM experiments, an appropriate amount of 10 mg/mL lipid stock in chloroform and methanol (9:1 v/v) was evaporated by

N_2 gas until completely dried into a film. Then, n-decane and butyl alcohol (50:1 v/v) were added to resuspend the lipid solution to a final concentration of 10 mg/mL.

Aβ Preparation for BLM

Aβ solution was added to the liquid chamber with suspended membrane at concentration of 110 μM. Aβ1-42 (Ultra-Pure, NaOH, rPeptide, Watkinsville, GA) was dissolved at 0.5 mg/mL in 150 mM KCl and 20 mM HEPES buffer (final concentration 110 μM). Aβ1-42 solution was distributed into aliquots and stored at -20 °C. At these conditions, we obtained small soluble oligomers. Prior to addition in BLM, these pre-dissolved aliquots were sonicated for 30 second to 1 minute.

BLM Recordings

We used BLM instrument from Elements (Cesena, Italy). Prior to lipid membrane formation, a 1.3 mL Delrin cuvette and chamber were filled with electrolyte solutions. Potassium chloride (KCl) was used as the electrolytes, given its supreme conductivity. The electrolyte solutions in our experiments were (a) 150 mM KCl and 20 mM HEPES buffer, (b) with 50 mM trehalose, and (c) with 100 mM trehalose respectively. Ag/AgCl electrodes were placed in reservoirs on either side of the cuvette aperture to record the current change across the suspended membrane over time. To create a suspended lipid membrane, the working lipid solution was painted over the 150 μm aperture in the Delrin cuvette using a shaved pipette tip. Once a stable membrane was formed, Aβ1-42 solution was added into the chamber to a final concentration of 5 μM. Measurements were conducted with BLM instrument with eONE amplifier (Elements), and real-time recording was monitored by Element Data Reader (EDR) software. The sampling rate (SR) was set as 5 kHz and a filter was applied to the real-time trace to generate a final bandwidth of SR/20. The applied current across the membrane was recorded at a range of constant voltages selected based on findings from voltage dependence tests described below.

1. Voltage Dependence Test. The voltage dependence method measures the integral membrane conductance before and after the formation of stable ion channels, which were able to stay in the membrane at least 2 min and evaluate the destruction level of membranes [252, 253]. Currents were recorded in a series of stepwise voltages from −120 mV to + 120 mV in increments of 10 mV. Then, membrane conductance was obtained by I-V plot in terms of Ohm's Law $C = \frac{I}{V}$, where I is recorded current and V is applied voltage [254]. At least 6 effective I-V curves were collected for each experiment condition.

2. Single-event Ion Current Recording. Single-event ion currents were recorded over time to study the acute and instantaneous membrane current fluctuation due to peptide-membrane interactions. Large current changes induced by protein-membrane interaction were observed and recorded in the voltage range of 60 to 175 mV. This method evaluates the magnitude of single ion current events caused by interaction of Aβ1-42 with membranes [254]. Single events for each treatment were collected from at least 10 effective traces with observable current increase due to Aβ insertion.

Data Acquisition and Statistics for BLM

Data that included currents and corresponding voltages were obtained by EDR software and were processed using Clampfit 11.2 software. Figure generations, data analysis, and hypothesis testing (one-way ANOVA, Tukey's test) was performed in OriginPro 2020.

6.2.2 Atomic Force Microscopy (AFM)

Atomic force microscopy is a high-resolution imaging technique capable of generating nanometer-scale resolution images of biological samples in physiologically relevant conditions [255]. We used tapping mode (intermittent contact mode) AFM [256] imaging in air to evaluate the size of Aβ1-42 oligomers and in liquid to visualize the membrane and Aβ-membrane interactions.

Aβ1-42 Oligomers Preparation for AFM

The method of Aβ solution preparation for AFM is similar to that for BLM measurement. Aβ1-42 (Ultra-Pure, NaOH, rPeptide, USA) was dissolved in 150 mM NaCl and 20mM HEPES buffer to a final concentration of 110 μM. The Aβ-buffer solution was distributed into aliquots and stored in -20 °C. Prior to addition in liquid cell, aliquot was sonicated for 1 minute to reach room temperature and to ensure the protein uniformly distributed in solution. Aβ1-42 oligomers dry sample is prepared for AFM imaging in air. 10 μL Aβ-buffer solution was deposited onto the freshly cleaved mica cleaned by UV-ozone for 3 minutes. After 5 min of incubation, excess unbound Aβ was washed with 20 μL DI water 3-4 times. The sample was then dried under gentle N_2 gas until water evaporated and stored in a desiccator at room temperature prior to AFM imaging.

Supported Lipid Bilayers for AFM

Individual chloroform stocks of 1,2-dipalmitoyl-sn-glycero-3-phosphocholine (DPPC), 1-palmitoyl-2-oleoyl-sn-glycero-3-phospho-choline (POPC) and cholesterol (Sigma-Aldrich, Canada) were created (10mg/mL each). Lipids were mixed by volume in a mass ratio of 4:4:2 and were then dried with N_2 gas to form a thin film. The lipid film was resuspended in NaCl solution and 100 mM Treh – NaCl solution respectively to reach a final concentration of 1mg/mL. The final lipid vesicle solution was prepared by alternating sonication and stirring for 15 minutes, respectively, until the solution became clear. To form an SLB, 150 - 250 μL of the vesicle solution was deposited on freshly cleaved mica that was previously treated with UV-ozone for 3 minutes and incubated for 30 - 40 minutes. After incubation, the SLB was washed with 8 - 15 mL DI water to remove excess solutions and imaged in DI water.

SLBs Incubated with Aβ1-42 for AFM

Once SLBs were formed as described, appropriate amounts of the 110 μM Aβ1-42 aliquot solution were added to SLB gently to a final concentration of 5 μM in the liquid cell. The

SLB was incubated for 1 hour with Aβ1-42 prior to imaging.

AFM Imaging

NanoWizard II (JPK/Bruker, Berlin, Germany) AFM instrument was used in intermittent contact mode to image Aβ1-42 oligomers in air and SLBs in liquid. PPP-NCH probes (Systems for Research (SFR), Canada) with spring constant 42 N/m were used to image dry Aβ-1-42 samples in air at resonance frequency of 293 kHz. QP-Bio-AC probes (SFR) with spring constant 0.3 N/m were used to image SLBs with and without Aβ1-42 in water at the resonance frequency of 25 - 35 kHz. Imaging for SLBs with Aβ1-42 began only after a pre-incubation period of 1 hour with Aβ1-42. Images were processed by JPK Data Processing software 5.1.4.

6.3 Results and Discussion

6.3.1 Black Lipid Membrane Study of the Effect of Trehalose on Aβ-Membrane Interactions

In this study, we used BLM recordings to elucidate how membrane permeability is altered by the presence of Aβ and trehalose. The BLM electrophysiological technique records ion current fluctuations as the result of protein interactions with the lipid membrane suspended over the micrometer pore separating two compartments of a liquid chamber connected with two electrodes. The suspended membrane acts as a capacitor with an extremely low conductance (Fig. 6.2(a)). A stable suspended membrane blocks the ion current efficiently with the initial current readout very close to 0 pA. When pore-forming proteins are added, they bind to the suspended membrane, interfere with membrane integrity and induce ion leakage as indicated by Fig. 6.2(b) [20].

Using the BLM technique, we performed two types of measurements: first, we performed voltage dependence tests, which measure membrane conductance (current) versus voltage

to evaluate the stability of membranes at various voltages applied with and without Aβ or trehalose. Currents were recorded in a series of stepwise voltages from -120 mV to 120 mV in increments of 10 mV. The slope of the curves plotted by current (I) vs voltage (V) in Fig. 6.3 and Fig. 6.4 indicated the membrane conductance. Secondly, we recorded ion currents at constant voltage over time to study the effect of Aβ binding and trehalose protection and evaluate the type of membrane damage observed. Single-event currents were recorded and analyzed at a constant voltage, ranging from 60 to 175 mV. This method was previously used to evaluate the single events and associating conductance caused by the interaction of Aβ1-42 with membranes [254].

BLM I-V Dependence Tests

I-V dependence tests are commonly used to evaluate membrane permeability and electric properties by measuring membrane conductance via stepwise voltages [257]. Here, we used voltage-dependence measurements to evaluate the integral quality of membranes in buffers with and without trehalose, as well as to measure the membrane permeability before and after Aβ1-42 damage. This I-V relationship can also show the dependency of membrane conductance with respect to alterations in applied voltage. Effect of trehalose on lipid membrane conductance Considering the intrinsic ion leakage of lipid bilayers and ion currents through protein ion channels, the total currents across the membrane can be given by

$$I = (g_L + g_p P_{\text{open}})\,(V - E_0)\,, \tag{6.1}$$

where g_L is membrane leakage conductance, g_p is pore conductance, P_{open} is probability that ion channels open,V is applied voltage, E_0 is Nernst potential, which is equal to zero since the ion concentrations on both sides of membranes are identical [94]. Since there were no protein-induced events in the Aβ-free membranes and no ion concentration gradient, both $g_p P_{\text{open}}$ and E_0 were expected to be zero in Eq. (6.1). Thus, the total current was attributed to the intrinsic leakage current and could be given by the following equation [94]

$$I = g_L V\ . \tag{6.2}$$

Figure 6.3 shows that the averaged I-V profile of untreated membranes fitted to this equation, demonstrating that the membrane conductance, g_L, was voltage-independent and constant.

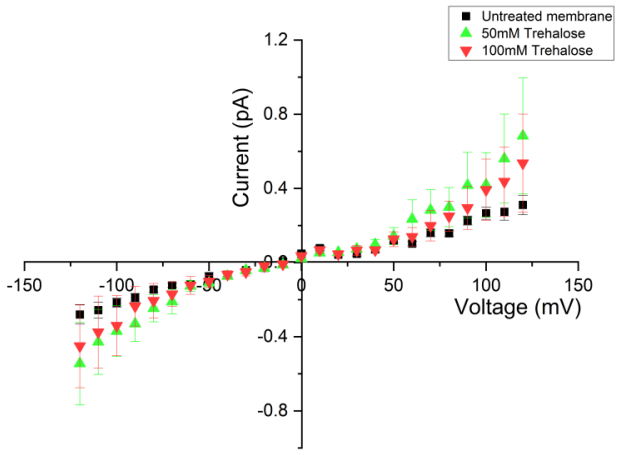


Figure 6.3: I-V dependence curves to estimate integral membrane permeability in buffers with and without trehalose by voltage dependence measurements. Currents across each membrane were measured at -120 mV to 120 mV in increments of 10 mV. Black square, model lipid membranes tested in the 150 mM KCl - 20 mM HEPES salt buffer without trehalose; green triangle, membranes tested in 50 mM trehalose salt buffer; red triangle, membranes tested in 100 mM trehalose salt (150 mM KCl and 20 mM HEPES) buffer. Error bar: standard error (SE) of the mean currents.

The I-V curves of membranes formed in pure salt buffer without trehalose (Fig. 6.3, black square) followed the linear relationship of Ohm's Law with an average membrane conductance of 2.02 ± 0.08 pS (mean $\pm$ SE, $n = 10$), which confirmed the inherent membrane stability and low ion permeability of our chosen lipid model. The symmetric and linear I-V relationship not only established that an even distribution of mixed lipid molecules was present on both sides of the cuvette aperture (membrane formation) but also demonstrated the constant and voltage-independent nature of the resulting membrane conduc-

tance. Despite the theoretical notion that pure lipid membranes are impermeable to ions, the experimentally generated black lipid membranes showed a slight current due to the thermodynamic fluctuation of lipids—a process thought to trigger lipid pores [94]. However, the low conductance of the untreated lipid bilayers (2.02 ± 0.08 pS) established that such fluctuations had minimal effects on overall membrane stability.

The I-V profiles of membranes formed in 50 mM and 100 mM trehalose, however, revealed the sugar's ability to alter the electric properties of Aβ-free membranes (Fig. 6.3). These alterations were observed as small changes in conductance at lower applied voltages until the applied voltage reached $|V| > 60$mV, wherein the current exponentially increased with each measured increase of applied voltage. The resulting I-V profile of trehalose membranes showed a deviation from the expected linear relationship of pure membranes when $|V| > 60$mV were applied and instead resulted in an exponential relationship. Therefore, trehalose seemed to slightly reduce the robustness of treated membranes against higher voltages. In this case, the linear-fitted membrane conductance in both 50 mM trehalose (Fig. 6.3, green triangle) and 100 mM trehalose (red triangle) was slightly higher than the trehalose-free membrane (black square). Specifically, the membranes incubated in 50 mM trehalose showed a larger magnitude of current increases and higher conductance (2.48 ± 0.14 pS, n =12) as $|V| > 60$mV compared to both untreated membranes (2.02 ± 0.08 pS, n =10) and 100 mM trehalose treated membranes (2.04 ± 0.16 pS, n = 10). This indicated that membranes in 50 mM trehalose buffer were the least robust to voltage changes, and therefore had the least stability, when compared to trehalose-free or 100 mM trehalose buffers. The instability at low concentrations of trehalose can be explained by trehalose-lipid interactions.

Trehalose forms hydrogen bonds with the head groups of phospholipids and replaces water molecules at the lipid-solvent interface, thereby decreasing membrane dipole potential [185, 131, 132]. As mentioned in a thermodynamic study by Villarreal *et al.*, both the trehalose-membrane electrostatic interaction and the substitution of water binding to lipid head groups by trehalose molecules are essential factors for the establishment of effective trehalose-lipid binding [131]. As more trehalose binds to the membrane, water molecules near the lipids are replaced and some trehalose buries into the hydrophilic region of lipids

[131]. Given that trehalose is a polar molecule, the accumulation of the sugar enhances the charge distribution not only at the lipid-solvent hydrophilic interface but also within the hydrophobic cores [131]. Consequently, the displacement and dehydration process alter the thermodynamic environments and change electrostatic properties of lipid membranes.

Therefore, to ensure effective protection of these membranes, an adequate number of trehalose molecules and trehalose-lipid hydrogen bonding must occur to trigger the vital environmental and biophysical changes to these lipid membranes. In 50 mM trehalose, although membrane electric properties were altered, confirming the trehalose-lipid interaction, the number of trehalose molecules was insufficient to establish an effective barrier near the bilayer surface and instead reduced membrane stability. In 100 mM trehalose, the higher number of trehalose molecules was more effective at binding to lipid headgroups and forming a protective barrier, as indicated by the lower and more stable membrane conductance at high voltages. It is also possible that the massive accumulation of trehalose surrounding the lipids reduced the thickness of membranes. Molecular simulation studies show that trehalose can expand the lipid molecular area and decrease the thickness of phospholipid bilayers in DPPC and POPC membranes [184, 130, 176]. Moreover, the homogeneity of bilayer thickness is influenced by the trehalose/water ratio. Low concentrations of trehalose can trigger a heterogeneous distribution of bilayer thickness that might lead to the instability of bilayers, while higher concentrations can make the bilayer thickness distribution more uniform [184]. This phenomenon may explain why moderate membrane instability appeared in 50 mM trehalose treated membranes instead of those treated with 100 mM trehalose. Overall, the moderate changes to membrane electrostatic properties had little effect on the stability of membranes suspended in trehalose buffer, according to the membrane conductance values obtained from the I-V profiles (Fig. 6.3).

Effect of Aβ on Lipid Membrane Conductance

Next, we added Aβ1-42 to suspended membranes and performed BLM recordings. The I-V curves generated by voltage-dependence measurements showed that the membranes incorporated with Aβ 1-42 had different electric characteristics when in the presence of

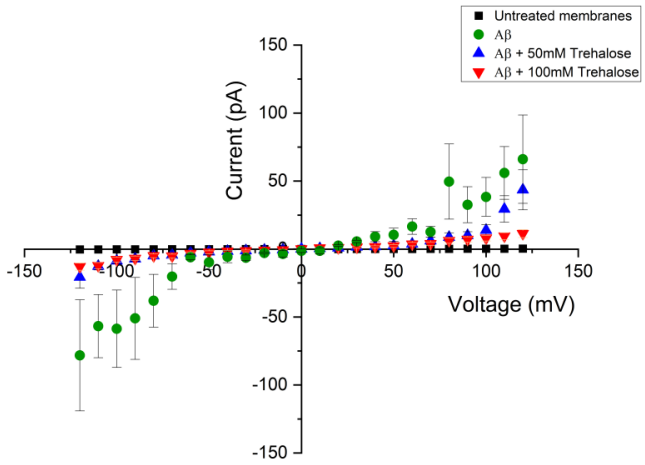


Figure 6.4: I-V curves to estimate membrane conductance in the presence of Aβ1-42. Membranes were suspended in three buffers (pure salt buffer, 50 mM trehalose salt buffer and 100 mM trehalose salt buffer) and incubated with 5μM Aβ1-42 prior to recording at -120 mV to 120 mV in increments of 10 mV. Black square, membranes in the salt buffer; Green dot, membrane in salt buffer incubated with Aβ1-42. Blue triangle, Aβ1-42 and 50 mM trehalose salt buffer. Red triangle, Aβ1-42 and 100 mM trehalose salt buffer. Error bar: SE of the mean currents.

trehalose compared to salt buffer alone (Fig. 6.4). Currents across membranes exposed to Aβ1-42 without trehalose (green dot) increase linearly from $-$ 60 mV to + 60 mV, the membrane conductance was 154.45 $\pm$ 14.11 pS; as $|V| > 70$ mV, current flow increased abruptly and lead to a larger membrane conductance 431.36 $\pm$ 35.92 pS. The integral membrane conductance for these membranes (from -120 mV to 120 mV) is 168.84 $\pm$ 17.02 pS ($n = 6$). In agreement with previous literature [20], our results demonstrated that Aβ aggregates in trehalose-free membranes induced a high degree of current fluctuation and dramatically altered membrane conductance specifically when voltage amplitudes exceeded 70 mV ($|V| > 70$ mV). This increase of current magnitude quickly became disproportional to the controlled increase of the applied voltage (Fig. 6.4, green dot). Towards the limits of the voltage ranges ($|V|$ >70 mV) we observed membrane damage induced by Aβ1-42

oligomers as indicated by this stronger response to voltage changes and greater current flux. Compared to the untreated membrane, the membrane conductance was dramatically increased from 2.02 ± 0.08 pS (n = 10, black square) to 168.84 ± 17.02 pS (n =6, green dot), as a consequence of Aβ1-42 damage.

I-V profiles of Aβ1-42-exposed membranes confirmed that Aβ1-42 oligomers interacted with lipid membranes, causing increases in membrane permeability to ions and ultimately leading to the disruption of membrane integrity (Fig. 6.4). Notably, when 80 mV was applied to membranes with Aβ present, there was an abrupt current increase (green dot); this increase in applied voltage may promote ion channel formation or larger pore sizes. Since Aβ is negatively charged at physiological pH (pH 7.4) [258], the application of higher voltages could increase the mobility of ions as well as charged Aβ, which in turn promotes Aβ insertions in the membrane. A similar scenario was observed in the cellular membranes of SH-SY5Y and cortical neuron cells, where a large current fluctuation caused by Aβ occurred at – 80 mV, which is close to the cells' resting potential [29]. This study could not exclude the possibility that Aβ causes robust membrane instability during insertion events when higher voltages are applied. Both Aβ damage and membrane deformation by electrostriction under high voltages can lead to dramatic conductance increases and promote membrane disruption.

Effect of Trehalose on Aβ-induced Membrane Conductance

In order to evaluate the protective effect of trehalose we added trehalose solution in combination with Aβ to suspended membranes. I-V profiles of Aβ1-42-exposed membranes with trehalose are shown in Fig. 6.4 (red and blue triangles). Although Aβ-induced damage was still observed, it was greatly reduced by trehalose. Specifically, the Aβ1-42-induced currents were reduced in the presence of 50 mM trehalose at $|V| < 70$mV, where membrane conductance was 43.09 ± 2.23 pS. However, it still displayed exponential growth at $|V| >$ 70mV (blue triangle, $n = 7$) with a membrane conductance of 99.89 ± 11.67 pS, generating the integral membrane conductance of 46.71 ± 3.40 pS. Conversely, the membranes in 100 mM trehalose buffer demonstrated very little fluctuation in the Aβ-induced currents at $|V|$

$>$ 70mV (red triangle, $n = 6$). In 100 mM trehalose, membrane conductance was 51.55 $\pm$ 0.00 pS at $|V| <$ 70mV and was 84.10 $\pm$ 6.00 pS at $|V| >$ 70mV; the integral membrane conductance from -120 mV to 120 mV was 66.36 $\pm$ 3.44 pS. Despite the persistence of Aβ-membrane interactions in the presence of trehalose, both concentrations (50mM, 100 mM) of trehalose decreased the overall membrane conductance and the amplitude of Aβ(1-42)-induced current flow as compared to the trehalose-free buffer. The shape and trends of the I-V profiles observed in all treatments demonstrated exponential growth at higher voltage (Figs. 6.3 and 6.4). However, those membranes treated with trehalose in the presence of Aβ showed a lower membrane conductance, suggesting that trehalose suppressed current flow across Aβ-damaged membranes, and thus acted as a protective agent against Aβ toxicity.

While Aβ1-42 ion channels/insertion events were still seen in the presence of trehalose, the recorded current flux and membrane conductance in 50 mM and 100 mM decreased remarkably from 168.84 pS to 46.71 pS and 66.36 pS respectively (Fig. 6.4). The lowered membrane conductance can be explained by two potential mechanisms: 1) Trehalose suppressed the conformational change of Aβ1-42 as it inserts into suspended membranes by limiting pore diameters therefore limiting ion flux created by Aβ oligomers. Previous studies show that Aβ undergoes conformational changes during insertion into lipid bilayers [24]. The binding of trehalose to lipid membrane headgroups could potentially restrict this membrane-induced conformation change during insertion and consequently reduce the original ion-channel pore sizes formed by Aβ. 2) The lipid dehydration by trehalose and the generation of this protective barrier maintained membrane stability when exposed to Aβ1-42 by avoiding membrane collapse during peptide insertion events. In addition to generating ionic pores, Aβ1-42 can also damage membranes by lowering bilayer dielectric barriers, consequently increasing membrane conductance [259]. Once bound, trehalose molecules worked as a protective barrier and prevented Aβ access to the membrane, hindering the considerable drop of dielectric barriers and stabilizing membrane structure. Consequently, trehalose-containing lipid bilayers became less permeable to ions compared to sugar-free membranes when in the presence of Aβ. Although trehalose failed to block Aβ1-42-membrane interactions completely, membrane conductance during these

interactions was significantly reduced at higher trehalose concentrations. Specifically, the reduction of membrane conductance in the 100 mM trehalose buffer showed the alleviation of Aβ oligomer-induced damage to lipid membranes as a result of the sugar's presence.

6.3.2 Single-event Recordings of Induced Membrane Damage (Current Versus Time)

The single-event recordings were conducted to estimate the instantaneous damage level to membranes after Aβ exposure. A constant voltage in the range of 60 to 175 mV was applied, and the current fluctuation was recorded over time while the suspended membranes were exposed to an Aβ solution, with and without trehalose present. Current vs time plots are shown in Fig. 6.5 and display several types of current fluctuations: single spike currents and broader collective current bursts. Figure 6.5(a) shows representative current flux caused by Aβ1-42 insertion into a suspended membrane at 120 mV.

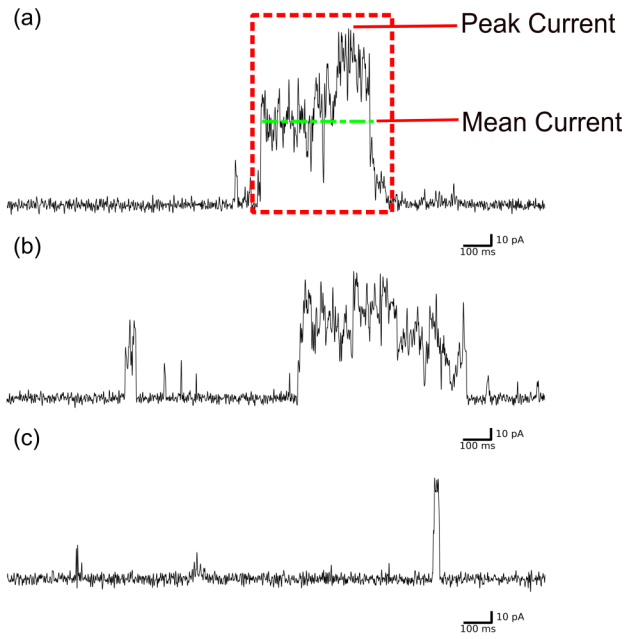


Figure 6.5: Aβ-membrane interactions and current fluctuation induced by Aβ damage to membranes respect to the time. Representative current flux insertion events caused by Aβ1-42 in (a) 0 mM trehalose, (b) 50 mM trehalose, (c) 100 mM trehalose buffers at 120 mV. The baseline was 0 pA. The peak current (pointed by a red line) was taken at the maximum value of current in a single event as the current increased. The mean current (green dash) was obtained by averaging the current values within a single event, from where the current dramatically increased to where it dropped to the baseline. Horizontal scale bar: 100 ms; vertical scale bar: 10 pA.

Figure 6.5(b) shows the currents observed due to Aβ1-42 insertion into the suspended membrane in the presence of trehalose at 50 mM and Fig. 6.5(c) at 100 mM trehalose. The maximum (peak) and mean conductance correlating to peak and mean currents of single events in Fig. 6.5 were analyzed; the results of the analysis are shown in Fig. 6.6 and Table 6.1. A combination of the single-spike event and broad distribution of ion currents in Fig. 6.5 is in agreement with the Aβ-membrane hypothesis which states that Aβ is capable of forming various types of defects in the membrane, such as single well-defined ion channels, as well as larger pores of various sizes and lipid dissociation due to detergent-like

effects [145, 21], which in turn may be attributed to the variety of sizes and conformations of Aβ aggregates, interacting with membranes [145]. As shown in Fig. 6.1(a), in addition to forming ion channels, Aβ aggregates may penetrate the membrane directly or adhere to the membrane surface [145].

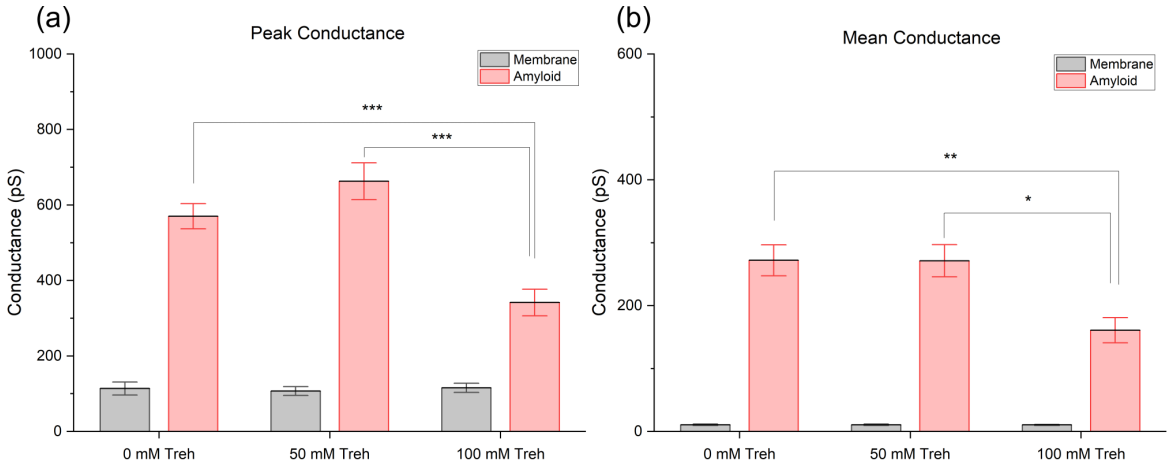


Figure 6.6: Membrane conductance of single current fluctuation events. (a) Peak and (b) Mean conductance of single events allows evaluation of instantaneous Aβ destruction to membranes. Currents of single Aβ insertion events in membranes exposed to 5 μM Aβ1-42 were recorded and compared to those suspended in Aβ-free salt buffers. The peak conductance was calculated from dividing the maximum value of a single insertion event (AB insertion induced current increase) by the corresponding applied voltage. The mean conductance was calculated by the average value of a single current increase caused by Aβ-membrane interaction divided by corresponding voltages. Black, Aβ-free membranes; Pink, Aβ1-42-interacted membranes. Left column, salt buffer without trehalose; middle, 50 mM trehalose salt buffer; right, 100 mM trehalose salt buffer. Results represent the mean $\pm$ SE of conductance. $^{*}p < 0.05$; $^{**}p < 0.01$; $^{***}p < 0.001$. The values of conductance (peak and mean) for each condition are in Table 6.1. Treh: trehalose

Table 6.1: Peak and mean conductance values corresponding to each condition. Mem, membrane; n, sample size.

Condition	n	**Peak Conductance (pS)**	**Mean Conductance (pS)**
Mem	48	113.73 ± 17.12	10.55 ± 1.15
Mem + Aβ1-42	213	570.11 ± 33.39	272.06 ± 24.58
Mem + 50 mM Treh	53	107.07 ± 11.80	10.55 ± 1.14
Mem + 50 mM Treh + Aβ1-42	118	662.85 ± 48.78	271.35 ± 25.56
Mem + 100 mM Treh	56	115.56 ± 12.06	10.35 ± 0.88
Mem + 100 mM Treh + Aβ1-42	114	365.67 ± 33.98	160.21 ± 20.18

During the electrophysiological recordings, single events of current escalation observed in the real-time readout represented current leakage and decreased membrane stability due to short-term interactions between Aβ1-42 oligomers and the suspended membranes. The duration of current fluctuation has various lifetimes (Fig. 6.2 & Fig. 6.5)—from a few milliseconds to thousands of milliseconds—indicative of both varying methods of Aβ1-42 interaction with membranes, as well as the diverse size of Aβ1-42 aggregates. The level of instantaneous conductance increase caused by the proteins correlates to the size of pores in the membrane [20]. Due to this, peak conductance and mean conductance could be derived from a single signal, and therefore, both parameters were considered for the estimation of membrane damage caused by Aβ1-42. Peak conductance uses the single highest measurement of current recording to evaluate maximum membrane damage after Aβ1-42 insertion while mean conductance was used to evaluate the average destruction level as the protein-induced damage occurred. The peak and mean conductance of membranes in Aβ-free buffers with and without trehalose demonstrated a low level of current flow indicating membrane stability under these conditions (Fig. 6.6). However, the addition of Aβ1-42 to the membrane and subsequent interaction triggered current leakage, indicated by the observed increase in instantaneous currents and conductance in all three buffer types (Fig. 6.5). The 50 mM trehalose demonstrated the levels of current leakage across the membrane similar to pure salt buffers without trehalose (Fig. 6.6), comparing the peak and mean conductance (one-way ANOVA; $p > 0.05$); suggesting that the 50 mM

concentration has failed to protect the membrane.

Conversely, the higher concentration of trehalose (100 mM) significantly enhanced the resistance of membranes to Aβ toxicity and maintained stability, indicating membrane protection from peptide damage. The peak conductance of membranes incubated with Aβ (570.11 $\pm$ 33.39 pS, $n = 213$) decreased significantly in the 100 mM trehalose buffer (365.67 $\pm$ 33.98 pS, $n = 114$), according to the results of a one-way ANOVA ($p < 0.01$, DF = 444) and Tukey's test ($p < 0.001$), as shown in Fig. 6.6(a). Moreover, the mean conductance of current fluctuation in single events was also lowered in 100 mM trehalose (Fig. 6.6(b), one-way ANOVA: $p < 0.01$, DF = 444; Tukey's test, $p < 0.01$). This indicates that 100 mM trehalose is capable of suppressing Aβ1-42-induced current flux across the membrane. It is also worth mentioning that the Aβ-membrane insertion events were observed with a lower event occurrence in both trehalose solutions according to the number of effective events (sample size in table 1). While 50 mM trehalose failed to effectively inhibit Aβ damage, high concentrations of trehalose (100 mM) not only reduced the insertion of Aβ proteins into membranes but also reduced damage, thereby preserving membrane stability. The difference in results between sugar concentrations (50 mM vs 100 mM) indicated that the protective nature of trehalose may be concentration-dependent.

Previously published molecular dynamics simulations by Izmitli *et al.* showed that trehalose shortened the retaining time of Aβ peptide in lipids and encouraged the rapid insertion [260, 246]. Trehalose can reduce the contact period for lipid membranes and Aβ thereby reducing the lateral damages from Aβ proteins. The fast movement of Aβ across the membrane may also decrease the loss of lipid molecules due to protein retention and provide the membrane more time to recover the integrity from Aβ in the presence of trehalose. In addition, the simulation studies elucidated that the trehalose subphase quantitively decreased the insertion of Aβ to lipids, compared to the water subphase [246], which is consistent with our observation in experiments – the occurrence of single insertion events was lowered in trehalose solutions (Table 6.1). While we could not exclude the impact of trehalose on protein mobility, we deduced that trehalose at high concentrations maintained the stability of membranes after Aβ destruction and reduced the probability of membrane–protein interaction by preventing Aβ1-42 access to the membrane. Thus,

high concentrations of trehalose (100 mM) can create a sufficiently protective barrier and reduce ion flux for suspended membranes against the interference and damage induced by Aβ1-42, thus supporting our hypothesis illustrated in Fig. 6.1.

6.3.3 Atomic Force Microscopy

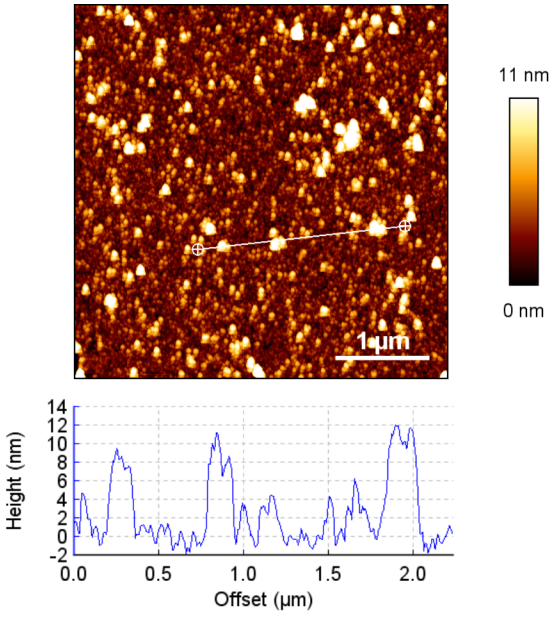


Figure 6.7: Aβ oligomers on mica imaged by AFM. Scale bar: 1 μm

Next, we used AFM imaging to visualize and confirm formation of Aβ1-42 oligomers (Fig. 6.7) at the same conditions as they interacted with suspended membranes in BLM experiments, and to visualize the membrane damage in lipid membranes as a result of Aβ binding to the membranes (Fig. 6.8). To confirm the aggregation state of the peptide used in BLM experiments, the aliquot of Aβ1-42 was allowed to incubate on mica for 5 minutes, rinsed gently, dried with nitrogen and imaged with AFM in air. As can be seen in Fig. 6.7, the Aβ peptide formed small spheric oligomers, with most ranging between 2-10 nm in height according to AFM cross-sections, with a few larger particles exceeding

10 nm present. The sizes of Aβ1-42 oligomers were aligned with the range of Aβ oligomers reported by previous studies [261].

Figure 6.8(a) shows an AFM topographical image of the model membrane surface with its associated cross-section (4:4:2, DPPC: POPC: Cholesterol by weight). The image and cross-section indicate that the membrane surface was relatively flat with smaller, dispersed lower (dark) domains with a height difference of $\sim$ 0.6 nm. Similar scenarios appeared in the cholesterol-enriched membrane in previous studies [262, 263]. The abundance of cholesterol in the membrane could be the reason behind the absence of explicit phase separation and the formation of nanodomains. The cholesterol tends to condense with phospholipids, which can make the fluidic POPC more rigid, while it reversely fluidizes the gel-phase DPPC at room temperature [264]. This can attenuate the phase separation due to the difference of lipid components in the SLB. After imaging the membrane, Aβ1-42 was added to the sample at a final concentration of approximately 5 μM. After incubation with 5 μM Aβ1-42 oligomers for 1 hour, Aβ-induced pores of varying lateral sizes were observed on the membrane surface (Fig. 6.8(b)). The higher features with ambiguous edges next to each pore indicate Aβ1-42 embedding into the bilayer. This phenomenon is consistent with observations in previous AFM studies that show pore formation in model membranes as a result of small-size Aβ oligomers [265]. In Fig. 6.8(b), the height of the Aβ aggregates embedded in the membrane was approximately 4.5 nm. These aggregates induced nearby pore formation in the lipid membrane, indicated in the cross-section as a depression with a height of 3 nm. Aside from these pore-forming Aβ aggregates, some small Aβ penetrated the lipid bilayers without causing pores (Fig. A.1 in the Appendix A). The AFM images confirmed the variety of Aβ-membrane interaction, aligned with BLM recordings (Fig. 6.5). AFM images of the Trehalose-SLB also showed a flat membrane with small nanodomains, elucidating a subtle change in membrane morphology (Fig. 6.8(c)) compared to SLB without trehalose (Fig. 6.8(a)). This observation is consistent with previous neutron diffraction studies by Kent *et al.*, which confirmed that trehalose does not change the structure of lipid membranes in the hydration environment [177]. Additionally, recent simulation studies also reported that trehalose was more likely to maintain the original phase separation and fluidity of lipid membranes instead of changing them [139]. Therefore, it is rational that the

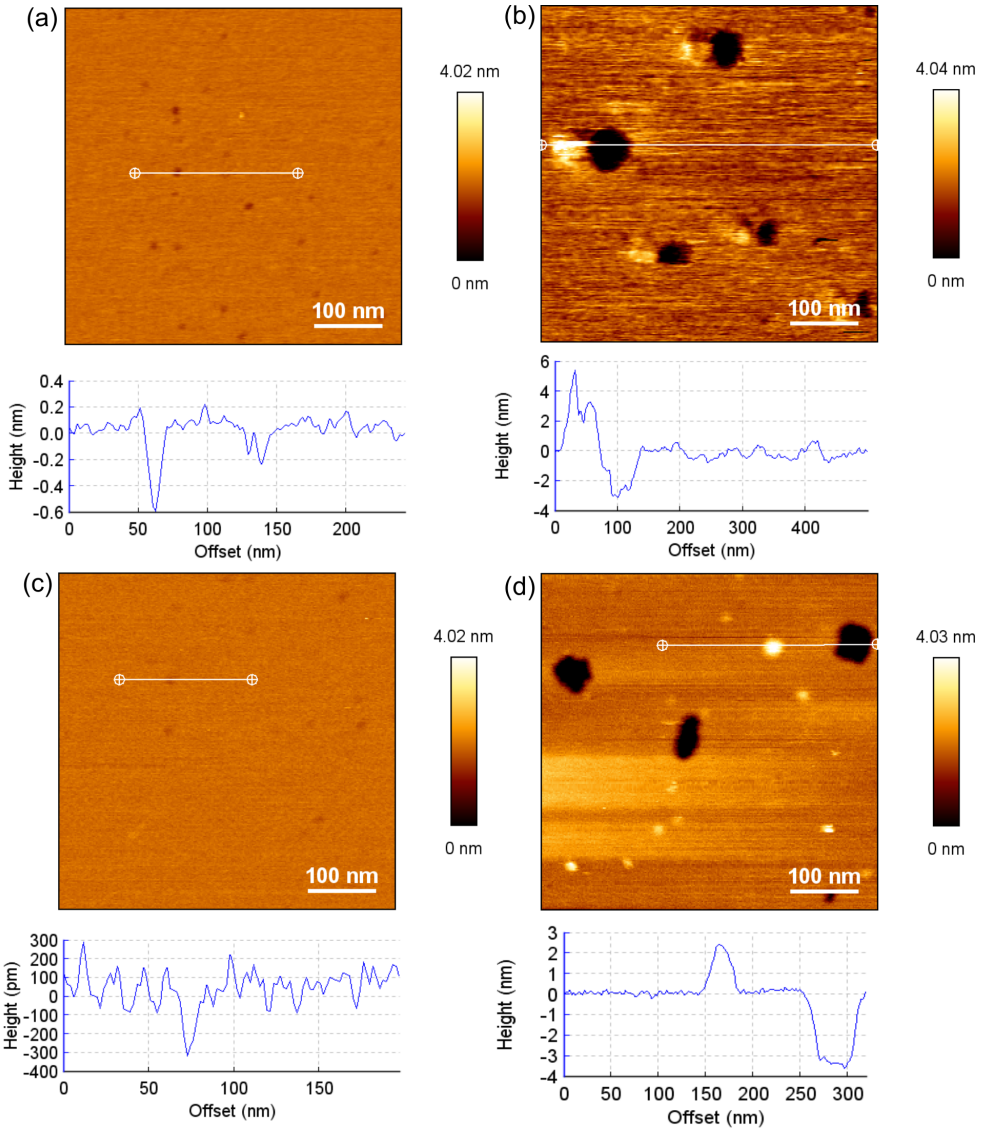


Figure 6.8: Representative AFM images of lipid membranes and corresponding cross-section profiles. (a) supported lipid bilayers (SLB) composed of DPPC, POPC and cholesterol in 4:4:2 weight ratio. (b) SLBs incubated with Aβ1-42 at 5 μM for 1h, displaying the Aβ-induced pore in SLBs. (c) Intact SLB made in 100 mM trehalose (Treh-SLB), imaged in water. (d) Trehalose-SLB incubated with Aβ1-42 oligomers. Scale bar: 100 nm.

original morphology of the lipid membrane was preserved in trehalose. Trehalose-SLB were incubated with Aβ1-42 oligomers for 1h and the corresponding topographic images were obtained, as shown in Figure (8(d)). Like SLB with Aβ1-42 in Fig. 6.8(b), the Aβ-treated Trehalose-SLB also featured pore formation with Aβ1-42 proteins embedded in the surface. In conclusion, AFM results indicated that the Aβ1-42 oligomers can induce pore formation in SLBs without trehalose as well as in Trehalose-SLBs, consistent with the BLM results where the Aβ-induced ion leakage could be detected in both suspended membranes with and without trehalose.

Membrane Protection Mechanism of Trehalose

In our study, we hypothesized that trehalose protection mechanism works on a membrane level and helps maintain integrity of lipid membranes during interaction with Aβ1-42. AFM images of SLBs showed that the Aβ1-42 damage to membranes existed and membrane disruption occurred in all conditions (with and without trehalose), in alignment with the observation from the single event recordings by BLM. Whereas, according to the voltage dependence measurements, the lowered membrane conductance in 100 mM trehalose indicated that trehalose maintained membrane integrity even after damage by Aβ1-42. Additionally, the reduction of instantaneous conductance in trehalose solutions showed that trehalose stabilized the membrane as the insertion events occurred. Hence, our AFM and BLM studies reveal that trehalose can significantly protect membranes. It works on a membrane level instead of blocking Aβ1-42 in solution. Currently, there is a lack of experimental evidence regarding the interaction between trehalose, Aβ oligomers, and membranes. Previous molecular dynamics simulation studies only report the interactions of monomeric Aβ with membranes [260], and while these studies demonstrate the ability of trehalose to mitigate the conformational change of Aβ during membrane insertion [246], they focus on a single Aβ peptide rather than toxic Aβ oligomers. Another possible explanation suggests that trehalose changes the packing of lipid molecules [139] and strengthens the bilayer resistance to Aβ oligomer damaging effects, thereby attenuating Aβ-induced membrane damage and maintaining membrane stability. Further research is necessary to

fully understand the impact of trehalose on Aβ oligomer insertion into lipid membranes, both theoretically and experimentally. The current therapeutic protection of trehalose in neurodegenerative disorders, including AD, is mainly attributed to the activation of autophagy, evidenced in animal models [125, 266, 174, 267]. Nevertheless, while autophagy induced by trehalose can occur in various regions in biological systems [125], the role of trehalose in nervous systems is still unclear. Although trehalose is already found in blood plasma, kidney and liver, it is still unknown whether trehalose can be transported across the blood-brain barrier (BBB) into human brains. Martano *et al.* found endogenous trehalose, and correlated trehalase in the hippocampus and cortex of rodent brains [142]. The trehalose can be produced by primary astrocytes and contributes to neuronal arborization and morphology development [142], implying a nervous function of trehalose in vertebrates' brains. Our studies demonstrate a potential mechanism of neuroprotection conducted by trehalose in AD — trehalose can attenuate the Aβ-mediated membrane disruption, thereby protecting neuronal membranes. Given the complexity and diversity of lipid composition within brains, it is worth further investigation on the ability of trehalose to protect more complex membrane systems.

Currently the clinical trials of trehalose in AD patients are undergoing and mainly administrated by oral intake and infusion [125]. The improvement of the therapeutic usage of trehalose is being realized by chemical modification of trehalose, which can reduce the dosage, enhance the trehalose penetration into neurons, elevate therapeutic effect and mitigate trehalose-induced adverse effects, etc.[125]. In addition, the incorporation of trehalose in drug delivery systems (e.g. liposome, nanoparticles) may assist transportation of trehalose across BBB and increase its specificity [268]. While these relevant studies shed light on trehalose as a drug candidate for neuroprotection in AD, understanding the molecular mechanisms of trehalose protection in the model membranes can benefit the exploration of interdisciplinary pharmaceutical strategies for neurodegenerative diseases.

6.4 Conclusion

In summary, our BLM and AFM data demonstrate that trehalose can protect model lipid membranes from the damaging effects of Aβ oligomers. The results of voltage dependence tests and single-event measurements performed in the BLM system indicate that trehalose changed the electric and biophysical properties of pure membranes and Aβ-exposed membranes. The lowered membrane conductance in the trehalose-Aβ environment verified the ability of trehalose to protect model neuronal membranes against Aβ1-42 toxicity. This study provides new insights into understanding the molecular mechanism of protective agents against Aβ neurotoxicity with a focus on the properties of the membrane itself and thus may promote the development of novel directions for preventive strategies in Alzheimer's disease. Thus, trehalose membrane protection against Aβ toxicity is worthy of more exploration in cellular studies and animal models in future.

Chapter 7

Quantitative Analysis of the Influence of Trehalose on Amyloid-β Binding to Membranes by Localized Surface Plasmon Resonance Spectroscopy

Aim of the work and summary. This chapter aims to study whether trehalose can reduce Aβ peptides' binding to the lipid membranes. The LSPR biosensing technique was applied to detect and evaluate the binding of the protein to the membranes. AFM was used to image the LSPR sensor surface and confirm the formation of lipid membranes before Aβ's binding. The results demonstrated that trehalose at 100 mM could reduce the binding of Aβ to lipid membranes, thereby reducing the damage from Aβ's binding; it also decreased the membrane thickness significantly, implying that trehalose enhances the fluidity of lipid membranes.

This chapter has been drafted into a manuscript with the same title and will be submitted to a peer-reviewed journal.

7.1 Introduction

Trehalose, a natural disaccharide that can be found in plants and microbes [124], is being investigated for the treatment of neurodegenerative diseases involving misfolded proteins in pathogenesis, such as amyotrophic lateral sclerosis (ALS), Huntington's disease, Alzheimer's disease (AD) etc. [172, 125]. Animal studies have shown that trehalose exerts its neuroprotective effects through various biological routes during metabolism; this includes modifying and regulating disordered proteins, enhancing anti-oxidation and anti-inflammation, and modulating gut microbiota [172], but the molecular mechanisms of trehalose-modulated neuroprotection in biological systems have not been fully understood.

One of the noticeable influences of trehalose in neurodegenerative diseases is its regulation on misfolded protein [126, 127]. It can work as a molecular chaperone to promote the refolding of misfolded proteins, thereby lowering the level of aberrant protein aggregates [126, 133]. Specifically, trehalose can suppress the aggregation of amyloid-β (Aβ) proteins [133], notably accumulated and deposited in AD patients' brains and regarded as the feature of AD. Aβ aggregation results in diverse aggregate products, from monomers and oligomers to fibrils, which eventually become Aβ plaques in AD brains [145]. Among these aggregates, the monomeric and oligomeric Aβ proteins can bind to the lipid membrane [144, 143, 6, 5] and cause neuronal membrane impairment, leading to homeostasis imbalance and even cell death [143, 224]. Previous studies have shown that trehalose slows down Aβ fibril formation in both Aβ1-40 and Aβ1-42 fibrils [133]. However, the conformational modification of trehalose on Aβ peptides is limited and is more effective on Aβ-40 fragments [133, 127, 260, 133] over Aβ1-42. Incubating Aβ peptides with trehalose can inhibit the formation of Aβ1-40 oligomers by refolding but fails to suppress Aβ1-42 oligomerization [133]. As the Aβ1-42 exhibits more toxicity on damaging the lipid membrane [143, 6, 5].], studies on the effectiveness of trehalose in regulating the cytotoxicity of Aβ1-42 oligomers are highly desirable. Since trehalose has the unique ability to modify the membrane properties itself, the trehalose protection against Aβ1-42 oligomers should be investigated by exploring the Aβ1-42-membrane interactions.

Trehalose is known to be a well-established cryopreservative agent for biomolecules and can stabilize cell membranes under extreme conditions [124]. This membrane action of trehalose may be important to explore membrane-targeted protection as a prevention strategy for AD. As reported in the previous studies, trehalose can maintain membrane stability by eliminating deleterious phase transitions, thereby maintaining membrane fluidity during dehydration [124]. Trehalose can form hydrogen bonds with water and hydrophilic headgroups of lipids at the water/membrane interface [130, 131, 132]. Different hypotheses have been proposed to explain the interaction between trehalose and lipid membranes, such as the water replacement hypothesis [136, 130], water entrapment hypothesis[269, 137, 138], and hydration force hypothesis [179], among others. Even though the protection mechanisms of trehalose on biomembranes are still under debate, evidence has shown that some of these hypotheses could be complementary, conjointly explaining trehalose-mediated membrane protection [139, 270]. A simulation study by Archita and Senehasis found that trehalose can simultaneously replace water and form a viscous layer on the *Escherichia coli* bacterial membranes [139], supporting both the water replacement hypothesis and the vitrification hypothesis. Trehalose can compensate for water loss and reduce the dehydration level of the membranes [139]. In addition, the viscous layer formed by trehalose slow down the motion of lipid molecules, thereby maintaining membrane fluidity [139].

As trehalose influences both Aβ proteins and lipid membranes, it is important to study the influence of trehalose on their interaction, which is a crucial pathological mechanism in AD. Simulation studies by Reddy *et al.* in 2009 demonstrated that trehalose could increase the insertion of Aβ(29-40) in DPPC membranes [260]. This could be due to trehalose promoting the conformational transition of Aβ(29-40) monomer from the random coil to α-helix structure [260], facilitating its insertion into lipid membranes. However, another simulation study by Izmitli *et al.* elucidated that the insertion of Aβ(1-40) in DPPG membranes was decreased by the presence of trehalose in aqueous environment [246]. Trehalose reduces the insertion depth of Aβ(1-40) peptides but speeds up the peptide insertion by mitigating the conformational change upon insertion into the membranes. These studies focused on Aβ-40 fragments rather than Aβ1-42 [260, 246]. Moreover, experimental investigation about the effect of trehalose on the binding of Aβ to lipid membranes is still

missing.

Given the protection role of trehalose on biomembranes, we proposed that trehalose may protect neuronal membranes against the deleterious effects and disruption induced by the misfolded protein like Aβ. Recent electrophysiological studies in our group found that the amount of membrane disruption induced by Aβ1-42 oligomers is attenuated by the presence of trehalose in a dose-dependent manner [156]. Based on the protection mechanism of trehalose on membrane stability and integrity, we hypothesized that the binding of trehalose at the hydrophilic region of lipid membranes may establish a barrier to reduce or prevent the binding of Aβ1-42 to the lipid membrane, thereby attenuating Aβ-induced membrane disruption. In this work, we used localized surface plasmon resonance (LSPR) spectroscopy to study the binding of Aβ protein to DPPC-POPC-Chol model lipid membranes exposed to trehalose.

7.1.1 Theoretical Background of LSPR

Localized surface plasmon resonance is produced by incident light, exciting the oscillation of electrons of the metal nanoparticle and generating a locally enhanced electromagnetic field. This results in a strong optical absorption at wavelength (λ_m), which is influenced by the dielectric environment in the vicinity of the nanoparticle surface [96].Any changes in the dielectric environment, such as those involving the change in local refractive index (RI) n or adsorbate thickness d due to adsorption of biomolecule layer, can cause the wavelength shift ($\Delta\lambda$) [271, 272],

$$\Delta\lambda = m\Delta n \left[1 - \exp\left(-\frac{d}{\delta}\right)\right]. \tag{7.1}$$

Here m is the bulk sensitivity of the sensor, δ is the decay length of the intensity of the electromagnetic (EM) field [271, 272], also known as the probe length of the sensor [101, 100]. It is worth denoting that δ can be substituted by $\frac{l_d}{2}$ in Eq. (7.1) shown in some papers [101, 96]. Distinct from δ, l_d is the characteristic decay length of EM field, which is twice the value of δ. The binding or adsorption of biomolecules to the LSPR sensors induces the alteration of the dielectric environment thereby generating the LSPR wavelength shift

($\Delta\lambda$), which depends on the RI (n) and thickness of adsorbates (d) according to Eq. (7.1). Therefore, the binding of molecules can be quantified to the thickness of the adsorbate layer [101]. To evaluate the thickness of the membrane and Aβ proteins bond to the LSPR sensor, the m, δ, and refractive index change Δn require estimation and measurements.

According to the quantitative analysis of LPSR signals, trehalose was found to reduce the binding of Aβ1-42 peptides to the membranes. In addition, we confirmed the formation of lipid membranes on the LSPR gold sensor by AFM imaging and visualized the alteration of lipid membranes in the presence of trehalose in hydrated and dehydrated states. LSPR results showed that trehalose decreases the thickness of lipid membrane, implying trehalose enhancement to membrane fluidity. The AFM images clearly displayed that the degradation of the lipid membrane is delayed by the presence of trehalose during dehydration. This study demonstrates a suitability of LSPR to study Aβ–membrane interactions and provides new experimental evidence that membrane–active properties of trehalose may help to protect biomembranes against Aβ toxicity and thus may contribute to developing membrane-targeted therapies for Alzheimer's disease.

7.2 Materials and Methods

7.2.1 Reagents

POPC (1-palmitoyl-2-oleoyl-glycero-3-phosphocholine), DPPC (1,2-dipalmitoyl-sn-glycero-3-phosphocholine), cholesterol, trehalose, NaCl, HFIP (1,1,1,3,3,3-Hexafluoro-2-propanol), HEPES (4-(2-hydroxyethyl)-1-piperazineethanesulfonic acid), were obtained from Sigma Aldrich (ON, Canada). Aβ1-42 (HFIP) was purchased from rPeptides (USA). The unfunctionalized gold sensors (SEN-AU-100-10) were purchased from Nicoya Lifesciences (ON, Canada).

7.2.2 Vesicle Preparation

Lipids were suspended in chloroform and combined to reach the target weight ratio of 4:4:2 POPC:DPPC:Cholesterol. Then, the lipid chloroform solution was dried under N_2 flow until all the solvent was evaporated, leaving semi-transparent lipid residues at the bottom of the vial. The dried lipids were re-suspended in the same aqueous buffer as the corresponding working buffer in LSPR experiments. In order to create vesicle solutions, the aqueous lipid solution underwent sonication for 15 minutes followed by 15 minutes of stirring at ambient temperature. This cycle of sonication and stirring was repeated until the solution became transparent, indicating the formation of lipid vesicles. Final vesicle concentrations were 0.5 and 1 mg/mL POPC and 0.5 mg/mL lipid mixture.

7.2.3 Aβ Solution Preparation

Aβ1-42 powder was resuspended in HFIP and distributed into aliquots. The centrifuge tubes containing the Aβ solution were placed in a desiccator in the fume hood for 24 hours to remove HFIP as much as possible. After 24 h, HFIP was evaporated, and Aβ powder was left in the tubes. The distributed Aβ powder was stored in the freezer at -20 °C. Before starting the LSPR experiments, the Aβ powder was resuspended in the working buffer at 50 μM and sonicated for 10 min for monomerization.

7.2.4 LSPR Experiments

OpenSPR 3.0 instrument from Nicoya Lifescience (ON, Canada) was used for the detection of lipids and protein binding with and without the presence of trehalose. The real-time recording and data collection were performed in Nicoya Lifescience software 3.11.

Detection on Lipid Membranes and Protein Bindings with LSPR

To investigate the effect of trehalose on the membrane and Aβ binding, three working solutions involved below,

1. 150 mM NaCl 20mM HEPES, pH 7.4
2. 50 mM trehalose 150 mM NaCl 20mM HEPES, pH 7.4
3. 100 mM trehalose 150 mM NaCl 20 mM HEPES, pH 7.4

As shown in the Figure 7.1, the working solutions (RI = n_s) acted as a background for the membrane and protein binding signals and were maintained the same for each experiment. The flowing speed in the entire experiment was kept at 20 μL/min. Each test consisted of two types of injections in sequence: vesicle injection, followed by Aβ1-42 injection. First, 200 μL 0.5 mg/mL lipid vesicles composed of POPC, DPPC and cholesterol were injected into the system and transferred to the sensor at 20 μL/min. The vesicle injection was repeated 3 - 4 times to ensure the full coverage of membranes on the sensor surface. The injection of lipid vesicles and membrane formation on the sensor produced a wavelength shift ($\Delta\lambda_1$) as the first LSPR signal. After a 20 - 30 min wait time for vesicle rupture and membrane stabilization, 200 μL 50 μM Aβ1-42 was injected and transferred to the membrane-covered sensor at 20 μL/min. The binding of Aβ to the membrane generated the second LSPR wavelength shift ($\Delta\lambda_2$). As the Aβ injection finished, the experiment was stopped after 20 min.

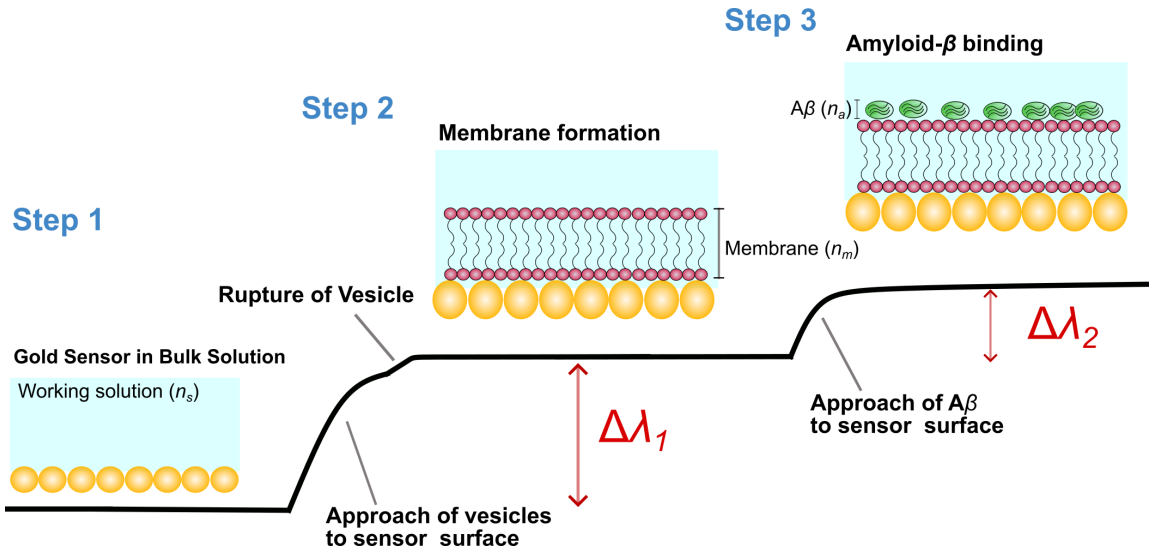


Figure 7.1: Schematic of LSPR experiments. From left to right: Step 1. The working solution keeps continuously flushed over the sensor surface, circulating the LSPR system. Step 2: Injection and rupture of lipid vesicles produce lipid membranes, resulting in the first wavelength shift $\Delta\lambda_1$. Step 3: The injection and binding of $A\beta$ to the membrane-covered sensor surface produces the second wavelength shift $\Delta\lambda_2$. n_s: RI of working solution. n_m: RI of lipid membrane. n_a: RI of Aβ1-42 protein.

Evaluation of Local Sensitivity by Glucose Gradient Concentration

The local sensitivity (m) of the sensor was estimated by the injection of 10%, 20%, 30%, 40%, 50% (w/v) glucose solutions with varying refractive indexes (RI), which has been a common method to estimate sensor sensitivity in many previous studies [273, 274, 275, 276]. The RI of glucose solutions, as well as the RI of working solutions, was measured by a digital refractometer (Cole-Parmer, Canada). The working background for the sensitivity estimation test was DI water. Glucose solutions were injected into the LPSR system by ascending concentrations, and the LSPR peak (λ) corresponding to each glucose solution was recorded. According to (λ_i) and RI (n_i) of glucose solutions, the local sensitivity (m)

could be obtained by Eq. (7.2),

$$m = \frac{\Delta\lambda}{\Delta n}. \tag{7.2}$$

Estimation of Decay Length by POPC Bilayers

Well-studied POPC bilayers were used to estimate the decay length of LSPR sensors, using a method developed by Nugroho *et al.* [277]. 0.5 mg/mL and 1 mg/mL POPC vesicles were injected into the system perfused with working buffer 1, producing the wavelength shift ($\Delta\lambda_p$) due to the adsorption of POPC membrane on the sensor surface. The RI (n_m) of POPC bilayer is 1.48 and thickness (d_m) is 5 nm [277]; the RI of NaCl buffer is 1.333, measured by the refractometer. Based on these, the RI difference Δn between POPC and NaCl buffer and therefore the decay length (δ) can be calculated according to Eq. (7.1).

7.2.5 AFM Imaging

AFM (JPK NanoWizard II, Bruker) was used to image the surface topography of the gold sensor surface and lipid membranes in hydrated and dehydrated states. The membranes were desposited on LPSR sensors following protocols for LSPR membrane. The hydrated membranes were imaged in liquid by qp-BioAC AFM probes (NanoSensors) in tapping mode at 25 - 35 kHz resonance frequency. The nominal spring constant of the probes was 0.3 N/m. The membrane-covered sensor was kept hydrated in deionized water during imaging. The LSPR gold sensor and dehydrated membranes on the sensor surface were imaged in tapping mode in air by silicon PPP-NCH probes (NanoSensors), with nominal spring constant 42 N/m, and resonance frequency 298 kHz. The dehydrated membranes on the LSPR sensors were imaged as soon as the liquid was observed to evaporate. Depending on the humidity in the experimental environment, wait times varied, but usually lasted 5 - 10 minutes. Surface roughness was calculated by Gwyddion software.

7.3 Results and Discussion

Determination of Decay Length of EM Intensity

According to Eq. (7.1), the decay length can be given by

$$\delta = \frac{-d_m}{\ln\left(1 - \frac{\Delta\lambda_1}{m(n_m - n_s)}\right)}, \tag{7.3}$$

where n_m is the RI of lipid membrane and n_s is the RI of the working solution, and m is the bulk sensitivity of the LSPR sensor, of which the value is 162.44 nm/RIU, measured by the injection of glucose solutions (more details can be found Fig. A.2 in Appendix A). The decay length of electromagnetic field (EM) intensity δ, also known as the probe length of LSPR sensor, was evaluated by well-studied POPC bilayers, with a thickness of 5 nm and refractive index (n_P) of 1.48 [277]. 0.5 mg/mL and 1 mg/mL of POPC vesicles were injected into the LSPR system, forming supported lipid bilayers on the sensor surface. The LSPR wavelength shift ($\Delta\lambda$) in response to the application of 0.5 mg/mL and 1 mg/mL POPC vesicles was 2.28 ± 0.16 nm and 2.41 ± 0.29 nm, respectively. The calculated δ was 50.16 ± 1.77 nm (mean ± SE, $n = 5$) at 0.5 mg/mL POPC and 47.70 ± 2.35 nm ($n = 7$) at 1 mg/mL POPC. The modest difference in binding signals at the two concentrations of vesicles indicates that the binding response by bilayer formation was dose-independent. Although the decay length values varied among individual sensors, the variance is relatively small. The value of δ as 50 nm was used in further calculations.

7.3.1 Determination of Membrane Thickness

Given that RI of cholesterol is 1.47 [278] and RI of DPPC is 1.478 [279, 280], we assumed that the RI of lipid membrane composed of POPC, DPPC and cholesterol was approximately 1.48, within the normal range for biological membranes reported in previous studies [272]. Based on the Eq. (7.1), the thickness of lipid membranes (d_m) can be calculated by

$$d_m = -\delta \ln\left[1 - \frac{\Delta\lambda_1}{m(n_m - n_s)}\right], \tag{7.4}$$

where $\Delta\lambda_1$ is the wavelength shift induced by the binding of lipids.

The estimated membrane thickness in 150 mM NaCl solution (RI = 1.333) is 4.02 ± 0.20 nm ($n = 11$) as shown in Figure 7.2. However, the membrane thickness is significantly decreased to 2.53 ± 0.09 nm in 50 mM Trehalose ($n = 13$) and 2.38 ± 0.13 nm in 100 mM Trehalose solution ($n = 14$) (Turkey's Test, $p < 0.001$).

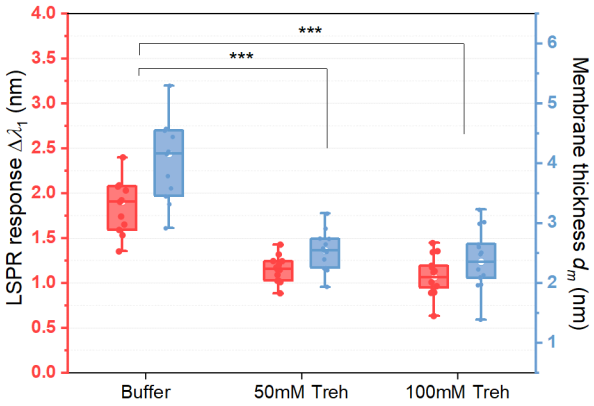


Figure 7.2: LSPR response to membrane formation ($\Delta\lambda_1$) and corresponding membrane thickness in 150 mM NaCl buffer, 50mM trehalose-NaCl buffer and 100 mM trehalose-NaCl buffer. Red: $\Delta\lambda_1$. Blue: membrane thickness. Treh: trehalose. The corresponding values were shown in Table 7.1

.

	NaCl Buffer	50 mM Treh-NaCl	100 mM Treh-NaCl
$\Delta\lambda_1$ (nm)	1.84 ± 0.09	1.15 ± 0.04	1.07 ± 0.06
d_m (nm)	4.02 ± 0.20	2.53 ± 0.09	2.38 ± 0.13

Table 7.1: Lipids-induced LSPR response and membrane thickness

These results indicate that the trehalose accumulation at the water/membrane interface decreases membrane thickness. Previous simulation studies have also noted a reduction in membrane thickness induced by trehalose [139, 270, 184]. It was found that concentrated

trehalose, such as 1 M [139], was necessary in simulations to observe significant changes in lipid membranes [139, 184], as the effect of 100 mM trehalose on membranes was subtle in earlier simulation studies. Whereas simulation results showed that the thickness reduction in the membrane is less than 0.5 nm despite higher concentrations of trehalose [139, 184], it reaches and even exceeds 1.5 nm in 50 mM and 100 mM trehalose in our experimental studies. The dramatic decrease in membrane thickness in our measurement could be attributed to the improved membrane fluidity due to trehalose's membrane modulation, which has also been reported in previous studies [200]. This highlights the significant impact of trehalose on the mechanical properties of lipid membranes experimentally, even at millimolar levels in a fully hydrated environment. Additionally, it is worth noting that while 100 mM trehalose is twice the concentration of 50 mM trehalose, both concentrations have similar effects on the membrane. This observation suggests that the thinning of the lipid membrane may reach saturation at a critical concentration of trehalose in hydration conditions.

7.3.2 Visualization of Membranes on LSPR Sensors

Hydrated Membrane

The gold sensor and membrane-covered sensor surface were imaged by AFM, as shown in Fig. 7.3. The LSPR sensors are mainly composed of spheroid gold nanoparticles with diameters ranging between 80 nm and 100 nm (Fig. 7.3(a)), with a surface roughness of 22.14 nm. The rupture of lipid vesicles at the sensor surface produced lipid bilayers. As shown in Fig. 7.3(b), the membrane successfully covered gold nanoparticles on the sensor in 150 mM NaCl, leading to a decreased surface roughness of 697.67 pm. In 100 mM Trehalose-NaCl solution, the lipid bilayer also formed, and the surface roughness is 1.26 nm (Fig. 7.3(c)). However, despite that the sensor surfaces were almost fully covered by lipid membrane with very few vesicle residues left, they still remained uneven due to the presence of grooves, as shown in Fig. 7.3(b) and Fig. 7.3(c). These grooves appeared due to the exceptional roughness on the original sensor surface and contributed to the increase in

surface roughness. Overall, the AFM images confirmed that the vesicles reached the gold surface and successfully formed lipid bilayers by rupturing in NaCl and Trehalose-NaCl solutions without the assistance of other agents.

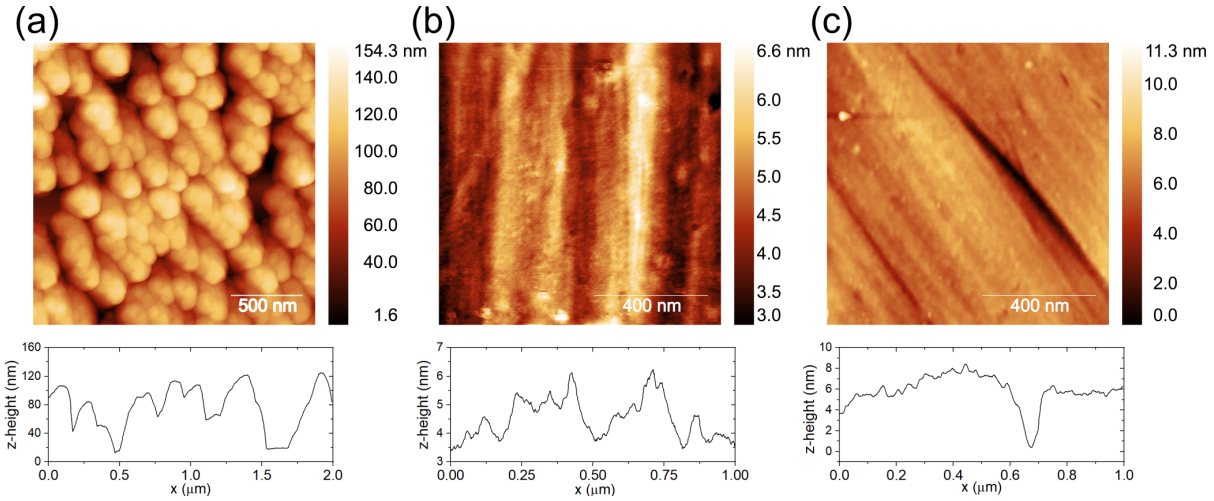


Figure 7.3: AFM images of the LPSR sensor and membranes on the sensors. (a)Bare gold sensor. (b)Lipid membrane formed on the sensor in 150 mM NaCl. (c)Lipid membrane formed in 100 mM Trehalose-NaCl solution.

Membranes Under Dehydration

To investigate the effect of trehalose on lipid membranes, other than reducing the thickness, the dehydrated membranes were imaged by AFM (Fig. 7.4). Figure 7.4(a) shows the self-assembly and crystallization of NaCl-lipid molecules during dehydration. The degradation of the lipid membrane led to the exposure of the gold nanoparticles of the sensor. However, the lipids maintained their bilayer structure during dehydration in a 100 mM trehalose solution, forming membrane plateau islands shown in Fig. 7.4(b). This suggests that trehalose helps maintain the membrane morphology during dehydration, as reported in previous studies [139]. Moreover, the cross-section in Fig. 7.4(b) indicates a membrane height of approximately 1.5 nm. This is lower than the height in the hydrated membrane (2.38 nm) in 100 mM trehalose, as estimated by the LSPR response. It implies that

trehalose decreased the membrane thickness, which was further decreased by dehydration. Recent simulations showed that the interaction between trehalose and lipid head groups depends on the water content level [139]. The water loss enhanced the trehalose-lipid interaction, increasing the distance between lipid molecules and attenuating the fluid-to-gel phase transition induced by dehydration [139].

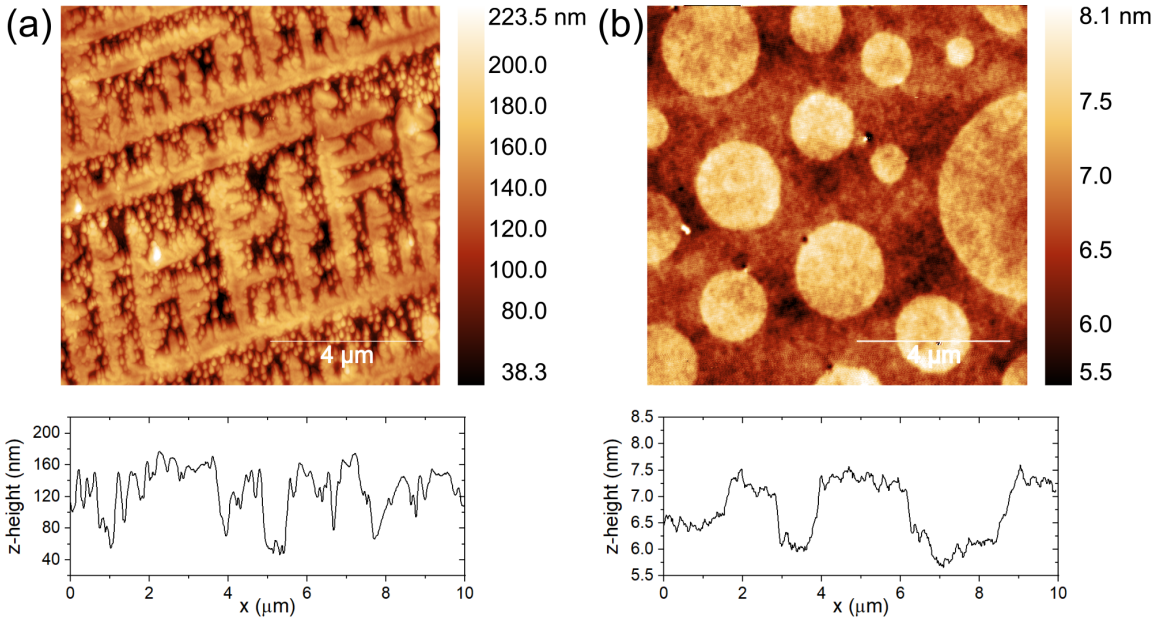


Figure 7.4: AFM images of dehydrated membranes and crossections on gold sensors. (a) Dehydrated membrane in 150mM NaCl. (b) Dehydrated membrane in 100 mM Trehalose-NaCl solution.

7.3.3 Quantitive Estimation on Aβ Adsorbate Layer

After lipid membrane formation on the LSPR sensors, generating the first LSPR signal ($\Delta\lambda_1$), the binding of Aβ1-42 peptides induces the second LSPR signal ($\Delta\lambda_2$), as indicated in Fig. 7.1. Determining the number of proteins that bind to the membrane from the LSPR response is challenging due to the complex density, geometry and dimensions of Aβ binding on membranes [281]. However, as shown in Fig. 7.5, the Aβ protein binding to the

membrane can be simplified as a condensed layer. This is the second adsorbate layer, with the thickness d_a on the surface of the LSPR sensor, quantifying bonded proteins [101, 281].

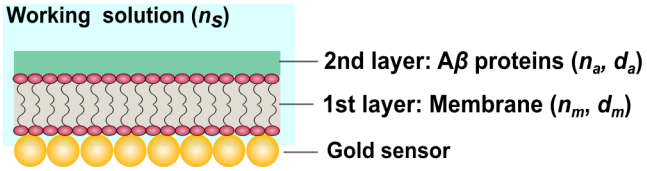


Figure 7.5: Model for LSPR binding layers

The LSPR signal ($\Delta\lambda_2$) generated by the binding of the Aβ1-42 protein to the membrane layer of thickness d_m is determined by Eq. (7.5) [101],

$$\Delta\lambda_2 = m(n_a - n_s)\left[1 - \exp(-\frac{d_a}{\delta})\right]\exp(-\frac{d_m}{\delta}), \tag{7.5}$$

where n_a is the RI of Aβ, which is 1.53 [281]. Based on Eq. (7.5), the thickness of Aβ1-42 layer (d_a) can be derived as

$$d_a = -\delta \ln\left[1 - \frac{\Delta\lambda_2 \exp\left(\frac{d_m}{\delta}\right)}{m(n_a - n_s)}\right]. \tag{7.6}$$

It can be rewritten into Eq. (7.7) according to Eq. (7.1) and Eq. (7.4),

$$d_a = -\delta \ln\left[1 - \frac{\Delta\lambda_2\left(1 - \frac{\Delta\lambda_1}{m(n_m - n_s)}\right)^{-1}}{m(n_a - n_s)}\right]. \tag{7.7}$$

Either Eq. (7.6) or Eq. (7.7) can be used to calculate the thickness of the second layer of Aβ1-42. The thickness parameter d_a is used to estimate the quantity of proteins bound to the lipid membrane.

As shown in Fig. 7.6, the Aβ-induced LSPR response $\Delta\lambda_2$ decreased in the trehalose solutions. It decreased from 0.39 $\pm$ 0.03 nm (Mean $\pm$ SEM) in the NaCl control buffer to 0.33 $\pm$ 0.03 nm in 50 mM and 0.29 $\pm$ 0.02 nm in 100 mM trehalose-NaCl solutions (Tukey test, $p < 0.05$); this dose-dependent behavior is shown in Table 7.2.

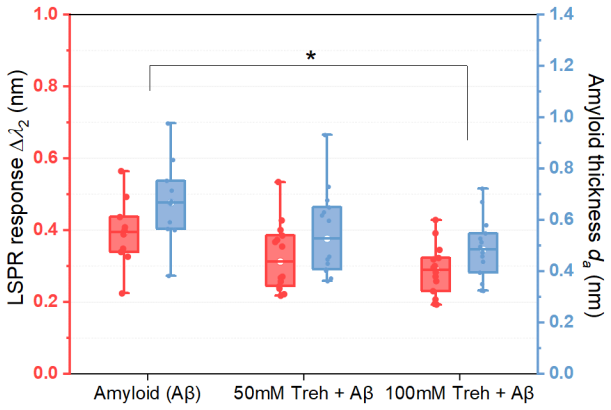


Figure 7.6: LSPR response to Aβ binding to lipid membranes $\Delta\lambda_2$ and corresponding thickness in working buffer 1, 2, 3. Red: $\Delta\lambda_2$. Blue: Aβ layer thickness d_a. The corresponding values are in Table 7.2.

Table 7.2: Aβ-induced LSPR response and 2nd layer thickness

	Aβ	50 mM Treh + Aβ	100 mM Treh + Aβ
$\Delta\lambda_2$ (nm)	0.39 ± 0.03	0.33 ± 0.03	0.29 ± 0.02
d_a (nm)	0.67 ± 0.05	0.55 ± 0.04	0.49 ± 0.03

Equation (7.7) was used to compute d_a according to the LSPR signals collected in the solution with and without trehalose and found the decline of Aβ thickness (d_a) in trehalose solutions, aligned with the trend of $\Delta\lambda_2$. Remarkably, d_a (0.67 ± 0.05 nm, $n = 10$) in NaCl was significantly decreased to 0.49 ± 0.03 nm ($n = 14$) in 100 mM Trehalose (Turkey's test, $p < 0.05$), suggesting less Aβ1-42 peptides bound to lipid membranes in 100 mM trehalose. This implies that 100 mM trehalose effectively reduced the binding of Aβ to the lipid membrane. Our result is consistent with a study by Izmitli *et al.* in 2011, of which simulation studies reported that fewer Aβ1-40 peptides inserted anionic DPPG monolayers in a trehalose solution than in water; this was attributed to the energy profile at the subphase-lipid interface [246]. The smaller difference in free energy at the water-lipid interface compared to the trehalose-lipid interface makes the peptide insertion more

energetically favourable, leading to more insertions in water over trehalose. In addition, the accumulation and interaction of trehalose with lipid headgroups may increase the viscosity near lipid membranes. This is driven by the trehalose concentration and increases the resistance for peptides to access the membrane, thereby inhibiting the adsorption of Aβ to lipid membranes.

Previous studies found that Aβ peptides penetrated deeper into lipids in water than in trehalose, leading to severe membrane expansion [246]. Another membrane study by Xu *et al.* demonstrated that the Aβ-induced membrane damage level was alleviated by trehalose, which can enhance membrane stability as Aβ insertion occurs [156]. These results and our findings suggest that the protective role of trehalose is not only attributed to its interference with peptides but also to its modulation of membrane properties, protecting the biomembranes from Aβ neurotoxicity.

7.4 Conclusion

The influence of trehalose on model lipid membranes (DPPC-POPC-Chol) and its effect on the binding of Aβ1-42 to a lipid membrane was studied by LSPR and AFM. We observed by AFM that trehalose delayed the membrane degradation during dehydration. The LSPR results showed that trehalose can decrease the lipid membrane thickness in a fully hydrated environment. Moreover, trehalose can effectively reduce the binding of Aβ1-42 to membranes in a concentration-dependent manner. This effect could potentially attenuate Aβ-related membrane destruction and cytotoxicity, beneficial to the membrane-targeted drug development for AD. This work significantly fills the void of experimental studies in trehalose-related Aβ-membrane studies and explores the quantitative analysis for the non-specific binding of biomolecules in LSPR-dominated biosensing.

Chapter 8

Trehalose, but not Other Sugars, Protects HT22 Cells against Amyloid-β Toxicity

Aim of the Work Summary. Since trehalose can protect lipid membranes from Aβ's attack by enhancing its stability (Chapter 6) and reducing Aβ's binding (Chapter 7), it is worth exploring whether the membrane-targeted protection from trehalose can protect neuronal cells from Aβ's damage. In this chapter, we estimated the cell viability of hippocampal-derived HT22 cells exposure to Aβ1-42 oligomers, trehalose and other common sugars (fructose, lactulose, sucrose). Our results revealed the unique neuronal protection of trehalose rescued the survival rate of HT22 cells from Aβ-induced cell death.

This chapter is drafted into a manuscript and prepared for submission to a peer-reviewed journal.

8.1 Introduction

Misfolded proteins play a vital role in the pathogenesis of several neurodegenerative diseases like Parkinson's disease (PD), amyotrophic lateral sclerosis (ALS), Huntington's Disease (HD), and Alzheimer's Disease (AD) [172]. Although the associated protein species differ between diseases, they commonly exhibit neurotoxicity and can aggregate and form deposits in patients' brains. Hence, a major pharmaceutical strategy is to develop drugs that can inhibit the genesis and aggregation of these pathologic proteins. Trehalose, a disaccharide, is one of the promising candidates being studied for preventing protein-associated neurodegenerative diseases.

Like other common sugars such as sucrose and fructose, trehalose is found in nature, abundant in plants and fungi, non-toxic, and regularly ingested in the diet [242]. Interestingly, trehalose exhibits neuroprotection that can rescue neurons from pathogenic protein disorders by stimulating autophagy, modulating misfolded proteins as a chemical chaperone, and promoting anti-inflammatory and anti-oxidant effects [282].

Trehalose also exhibits its therapeutic potential in AD, of which the hallmark is the amyloid protein. Amyloid-beta (Aβ) proteins are believed to be one of the main pathogenic factors leading to cognitive deficit [2, 283]. The Aβ deposition is caused by the self-aggregation and accumulation of Aβ peptides originating from transmembrane Aβ precursor protein (APP). The intermediate products of Aβ aggregation, like Aβ monomers and oligomers, display neurotoxicity by disrupting neuronal membranes and inducing neuronal cell death and neurodegeneration [284, 28, 144]. An animal study conducted by Portbury *et al.* discovered that Aβ-induced cognition decline in transgenic mice can be improved by dietary trehalose, where the mouse model overexpressing APP was fed with 2 % trehalose for one month [285]. However, the principal therapeutic mechanism of trehalose in AD may not be attributed to its enhancement to autophagy. A recent study by Benito-Cuesta *et al.* found that trehalose-induced autophagy only lasted several hours and disappeared in long-term (24 h) treatment in primary neuron cells, implying that enhanced autophagic flux is not the main mechanism for lowering the Aβ level in AD [286]. Instead, trehalose reduced

the production and level of Aβ proteins secreted by cells by regulating APP [286, 129] and beta-secretase [286], which are two essential proteins that contribute to producing Aβ peptides. In addition, trehalose can inhibit the aggregation of Aβ peptides [133], thereby reducing fibrils and plaque formation [248]. Liu *et al.* found that trehalose (50 mM) inhibits the oligomerization of Aβ1-40 before applying them to cells, thus effectively lowering their neurotoxicity to cells by incubating Aβ1-40 peptides [133]. Whereas trehalose failed to inhibit the formation of Aβ1-42 oligomers, a more toxic species in the Aβ family, and thus, the cell viability was not improved [133]. Hence, the therapeutic mechanism of trehalose in AD is still under debate. Other protection mechanisms may exist independent of Aβ aggregation and production. For instance, the membrane study by Xu *et al.* showed that trehalose-treated lipid membranes are more resistant to membrane disruption caused by the binding of Aβ1-42 oligomers, emphasizing trehalose's non-specific positive effects on lipid membranes [156]. Since Aβ oligomers were found to predominantly lead to cell death compared to other Aβ aggregates like fibrils [287], we wonder whether trehalose can rescue neuronal-derived cells from the mortality caused by direct exposure to toxic Aβ1-42 oligomers.

In order to solve the problem, we incubated HT22 hippocampal-derived cells with trehalose at different concentrations and Aβ1-42 oligomers for 24 hours and compared the cell survival rate by MTT assay. In addition, we compared the efficacy of various sugars (trehalose, sucrose, fructose, glucose) against Aβ1-42 oligomer's neurotoxicity and revealed the ubiquitous neuroprotection of trehalose.

8.2 Materials and Methods

Cell Culture. HT22 cells were cultured in DMEM/F12 (Gibco, USA) supplemented with 10 % fetal bovine serum (Gibco, USA) and 1% penicillin/streptomycin (Gibco, USA). Cells were plated into 96-well TC treated plates at a cell density of 10,000 cells per well. 24 h after plating, the media was exchanged with Neurobasal media (Gibco, USA), with N2 (Gibco, USA), and GlutaMax (Gibco, USA). Cells were then left to differentiate for 20-24

h or until a confluency of 75% was reached. Cells were then treated with 5 μM Aβ1-42 oligomers along with the respective sugars and returned to the incubator for 24 h.

Sugar Preparation. Trehalose, sucrose, fructose, lactulose were purchased from Sigma-Aldrich (Oakville, CA). They were dissolved in deionized water and sterile-filtered prior to treatment.

MTT Assay. The 3-(4,5-dimethylthiazol-2-yl)-2,5-diphenyltetrazolium bromide (MTT) assay, obtained from Sigma-Aldrich (USA), was used to evaluate cell viability. After treatment, cell culture medium was replaced with phenol red-free DMEM containing 0.5 mg/mL MTT. Cells were then incubated for a further 3.5 h at 37 °C in a 5% CO_2. The formazan crystals were then solubilized in 100 μL of MTT solubilization buffer (90% isopropanol, 10% Triton X-100, and 0.1% hydrochloric acid). Absorbance measurements were obtained using a spectrophotometric plate reader at wavelengths of 570 nm and 690 nm. The background signal at 690 nm was subtracted from the absorbance values at 570 nm for data analysis.

Amyloid-β Oligomers Preparation. The preparation of Aβ1-42 oligomers followed the protocol by Stine *et al.* [157]. Aβ1-42 (rPeptide, USA) was dissolved in HFIP (hexafluoroisopropanol) to a concentration of 1 mg/mL, then aliquoted into microcentrifuge tubes and allowed to evaporate under desiccant for 24 h. These tubes were then stored at -20 °C under desiccant. Immediately prior to use, the Aβ1-42 film was resuspended in DMSO (dimethyl sulfoxide) at a concentration of 5 mM, vortexed for 30 s, and then sonicated for 10 min at room temperature. The Aβ1-42 solution was then diluted to 100 μM in cold neurobasal media and incubated for 24 h at 4 °C to obtain Aβ1-42 oligomers for the MTT study.

Data Analysis and Statistics. At least four repeats were performed for each treatment. Data visualization and statistical analysis (One-way ANOVA, Tukey's test) were

conducted in OriginPro 2020. The MTT results were indicated as mean ± SE. The statistical significance was 5% ($p < 0.05$).

8.3 Results

HT22 cells were incubated with trehalose solutions from 25 mM to 125 mM to explore the potential neurotoxicity of trehalose by MTT viability assay. As shown in Fig. 8.1(a), the cell viability appeared to increase when incubated with trehalose in the range of 25 mM to 100 mM in a dose-dependent manner. Incubating with 100 mM trehalose (population size $N = 4$) for 24 hrs significantly improved cell viability, showing a maximum increase in cell number compared to other concentrations (ANOVA, $p < 0.01$; Tukey's test, $p < 0.05$).

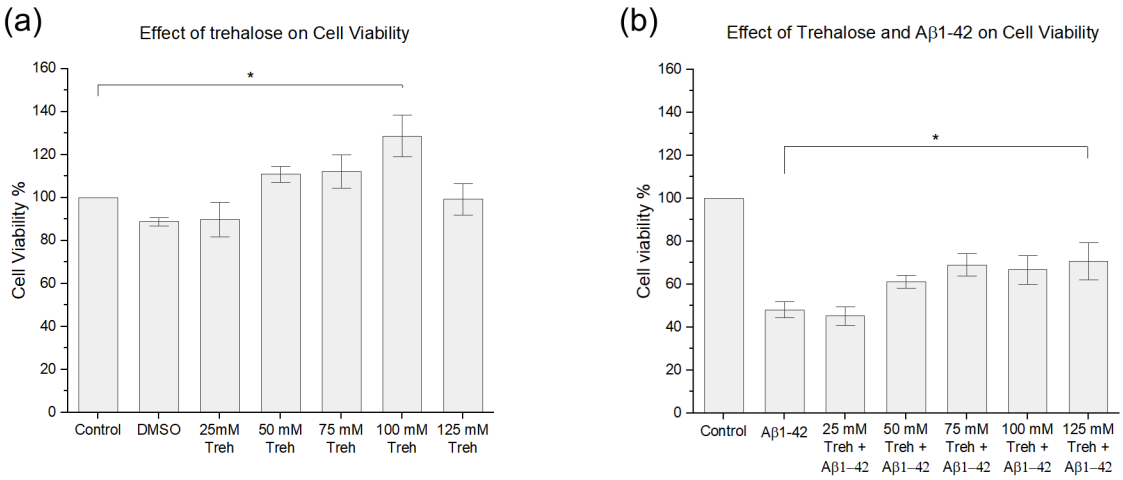


Figure 8.1: Viability of HT22 cells incubated with trehalose and Aβ1-42 oligomers. (a) Cell viability after incubation in trehalose (Treh) solutions (25 mM, 50 mM, 75 mM, 100 mM, 125 mM). (b) Cell viability after incubation with 5 μM Aβ1-42 oligomers for 24 h. The results showed the cell viability (mean ± SE.). normalized to control. $^*p < 0.05$.

Additionally, to investigate whether trehalose can directly protect cells from neurotoxicity of Aβ1-42 oligomers, the HT22 cells were treated with 5 μM Aβ1-42 oligomers and

trehalose solutions simultaneously and were incubated for 24 hrs. MTT results showed Aβ1-42 oligomers killed $\sim$50 % of HT22 cells after 24 hrs (N =10) (Fig. 8.1(b)). The cell viability also decreased significantly in all the treatments due to Aβ1-42 oligomers (ANOVA, Tukey's test, $p < 0.05$) compared to the control without any treatment. However, the Aβ1-42-induced cell death was potentially alleviated in trehalose solutions from 50 mM and significantly reduced at 125 mM ($N = 10$, Tukey's test, $p < 0.05$).

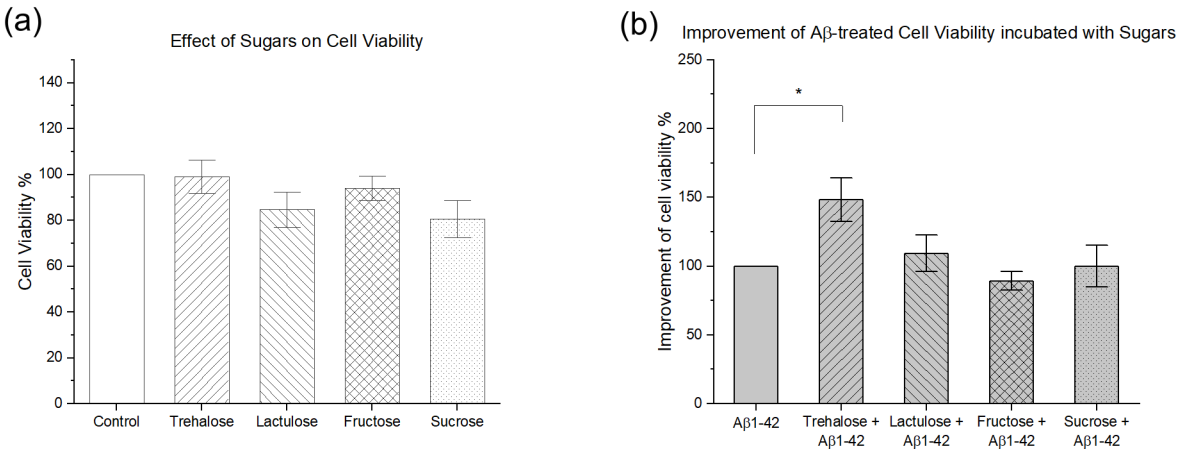


Figure 8.2: Viability of HT22 cells incubated with sugars and Aβ1-42 oligomers. (a) Cell viability after incubation in 125 mM sugars (trehalose, lactulose, fructose, and sucrose) for 24 hrs, normalized to control. (b) Improvement of Aβ1-42 oligomers-treated cell viability (%) incubated with 125 mM sugars for 24 hrs, normalized to Aβ1-42. It was calculated by the cell viability incubated with 5 μM oligomers and 125 mM sugars divided by the cell viability treated with 5 μM Aβ1-42 oligomers only in the absence of sugars. Results represent mean $\pm$ SE. *$p < 0.05$.

In addition to trehalose, the HT22 cells were incubated with lactulose, fructose, and sucrose at 125 mM to explore whether other sugars show similar improvement in cell survival rate against the neurotoxicity of Aβ1-42 oligomers. MTT results in Fig. 8.2 (a) indicated that all four sugars at 125 mM had minimal effect on cell viability compared to the control without any sugar applied. Figure 8.2 (b) showed cell viability after 24 h incubation with 125 mM sugars and 5 μM Aβ1-42 oligomers. the viability involving

sugars was normalized to Aβ1-42 treatment without sugar to observe the effectiveness of sugars against cell death caused by Aβ1-42 oligomers. The cell viability when treated with Aβ1-42 oligomers in 125 mM trehalose (N =10) was significantly higher compared to the viability exposure to Aβ1-42 without sugar treatment (N = 10) (ANOVA, $p < 0.01$; Tukey's test, $p < 0.05$). Lactulose, fructose, and sucrose (N = 6) failed to rescue HT22 cells from Aβ1-42 oligomers.

8.4 Discussion

Our study compared the cell viability of HT22 cells incubated with different doses of trehalose in response to Aβ1-42 oligomers' cytotoxicity and found a protective effect by trehalose at high concentrations on cell survival from Aβ1-42 oligomers, which is unique for trehalose and is not observed for other sugars (lactulose, fructose, and sucrose). The unique neuroprotection of trehalose was also reported in another vitro study by Sarkar *et al.* in 2007, which found that 100 mM trehalose reduced the cell death caused by mutant Huntingtin (mutHTT) aggregates relating to HD, of which effect was absent with other sugars and sugar alcohol (sucrose, raffinose, sorbitol) [288]. The distinction of trehalose from other sugars excludes the possibility that trehalose's neuroprotection is due to the osmotic effect [288]. It also excludes the potential of trehalose elevating cell survival as an energy source to supply nutrients for cells by metabolism, which should be common for other sugars.

Several possible mechanisms have been suggested to explain trehalose's neuroprotective effect on cells against the cytotoxicity of extrinsic Aβ1-42 oligomers. Many studies attributed the trehalose's protective role to its enhancement of autophagy, which prompts the clearance of misfolded proteins and aggregates, including mutHTT in HD and α-synuclein in PD [288, 173]. However, Benito-Cuesta *et al.* reported the short-term effect of trehalose-stimulated autophagy, which only lasted several hours and disappeared after 24 h [286], implying stimulating autophagy may not be sufficient to explain trehalose's neuroprotection mechanisms. Therefore, other mechanisms should be considered. For example, the

membrane protection mechanism proposed by Xu *et al.* suggested trehalose's protection on lipid membranes from the damage caused by Aβ1-42 oligomers, which can contribute to attenuating the cytotoxicity of Aβ1-42 oligomers [156].

Another noticeable result is that, at the control treatment with trehalose alone in the absence of Aβ1-42 oligomers, the cell viability was improved by trehalose with a dose-dependent effect and significantly increased at 100 mM. Similarly, Redmann *et al.* also observed trehalose-induced improvement in neuronal survival where both 10 and 25 mM trehalose elevated the viability of mouse neurons after exposure to trehalose for 15 days, while 25 mM sucrose failed to change it [289], suggesting that the trehalose's neuroprotection is unique from other sugars regardless the concentration. Moreover, both Redmann's and our results suggest that trehalose may benefit cell growth, thus maintaining or even increasing cell viability.

8.5 Conclusion

Based on our cell viability study, we found that trehalose can protect HT22 cells from Aβ1-42 oligomers. This protection may be due to trehalose's positive impact on cells. Further studies are needed to understand the influences of trehalose on neuronal activities.

Part II Lithium

Chapter 9

Introduction of Part II

Lithium (Fig. 9.1) is a chemical element, a member of the alkali metals, and exists in natural aqueous systems as a monovalent cation (Li^+) at micromolar concentrations [290]. Even though physiological Li^+ concentrations are much lower than other cations like Na^+ and Mg^{2+}, similarities in physical properties result in competition between ions for protein binding sites and transport via ion channels [290]. Therefore, the ability of Li^+ to influence biological processes requires tight regulation of its administration as a drug or treatment.

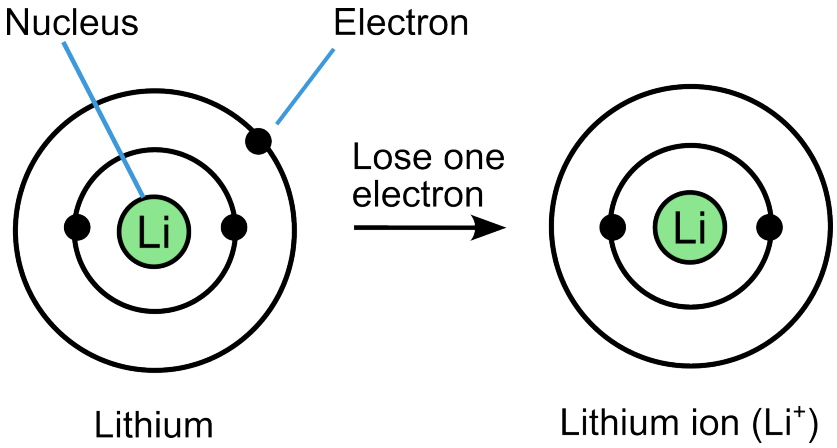


Figure 9.1: Lithium and lithium ion. A lithium atom loses one electron and becomes a lithium ion (Li^+).

9.1 Lithium as a Medical Treatment in Bipolar Disorder

Lithium has been used as a medication for the treatment of bipolar disorder (BD) for several decades [291]. It is regarded as an effective mood stabilizer and the first choice for adult BD patients experiencing acute episodes [292]. Although the underlying mechanisms of lithium's therapeutic effect on mood disorders have not been fully understood, evidence shows that lithium modulates various metabolic cascades in brains, including enzyme activities, brain neurotrophic factors, protein receptors, etc. [292].

One of the most significant effects of Li^+'s ability to influence biological systems is its ability to compete for transport through ion channels[290]. Previous studies confirmed that Li^+ can be transported through various ion channels, such as voltage-gated sodium channels, sodium proton pumps, Na^+-Ca^{2+} antiporters, pentameric ligand-gated ion channels etc. [290]. The passage of Li^+ may suppress the flux of competitive ions (Na^+, Ca^{2+}, etc.), thereby modulating the homeostasis in living cells. Apart from ion channels, Li^+ may also interfere with the coupling of metal ions and biomacromolecules. For example, adenosine triphosphate (ATP), a direct energy source in biological systems, is usually stabilized by Mg^{2+} binding to all three phosphate groups [293, 294], forming ATP-Mg^{2+} complex. The presence of Li^+ encourages the formation of ATP-Mg^{2+}-Li^+ complex, influencing multiple ATP-dependent enzymatic reactions and cell signaling in brains [294].

The competition between Li^+ and Mg^{2+} may also directly affect the bioactivity of specific enzymes. Particularly, lithium can suppress the activity of inositol monophosphatase (IMPase), Protein kinase C (PKC) and glycogen-synthase-kinase (GSK)-3 [295, 296]. The Li^+-associated inhibition on these key enzymes modulates many important cellular activities like apoptosis, inflammation, oxidative stress, autophagy, etc., thus contributing to the neuroprotective effect of Li^+ against BD.

9.2 Impact of Li^+ on Lipid Membranes

In addition to competing with other cations for transmembrane ion channels, lithium ions can bind to the surface of membrane and alter membrane properties [297]. Among all alkali metal ions, Li^+ exhibits the strongest binding affinity to phospholipid membranes [297, 298, 299]. An NMR study revealed that lithium has a deeper penetration into the membrane compared to K^+ and Na^+, but not as deep as Ca^{2+} and Mg^{2+} [300]. The penetration of Li^+ to the lipid head group induces noticeable membrane structural changes. A molecular simulation study showed that Li^+-penetrated POPC bilayers form a cage-like tetrahedral structure enclosing the Li^+, which resembles the water cage surrounding Li^+ in an aqueous solution [299]. This unique tetrahedral structure in Li^+-lipid interaction increases the molecular area per lipid molecule while Na^+ and K^+ have opposite effect [299]. In 1988, Lopez-Corcuera *et al.* found that chronic administration of Li^+ changed membrane composition and fluidity in rat brains [301]. While this effect can be attributed in part to Li^+-induced metabolic lipid alteration, it does not exclude the possibility of direct Li^+-membrane interaction. A recent study using cryo-electron microscopy and X-ray diffraction showed the remarkable structural and morphological change of pig brain lipid extracts treated with low concentrations of Li^+, implying the direct modulation of lipid membranes by Li^+ [302]. This direct effect on lipid membranes cannot be ignored in the study of the pharmacodynamic mechanism of Li^+ in BD.

9.3 Connection between BD and AD

While bipolar disorder is classified as a mood disorder, it is strongly associated with neurodegenerative diseases. BD leads to cognitive impairment among patients and increases the risk of AD, especially in the elderly [303]. In addition, a recent longitudinal study elucidated that the fluctuation of biomarkers levels (Aβ and tau proteins in cerebrospinal fluid and plasma) characteristically present in AD progression also appear in acute BD episodes with the same pattern, implying a strong correlation between BD and AD-associated amy-

logenesis [304].

9.4 Lithium as a Potential Neuroprotective Agent for AD

Nunes *et al.* in 2007 demonstrated that Li^+-treated BD patients had significantly lower incidence of AD compared to untreated BD patients, suggesting Li^+ as a potential neuroprotective agent for AD [303]. Li^+ can mitigate cognitive decline in dementia cases [305, 306], which may be linked to lithium's ability to modulate GSK-3 [296]. GSK-3 is the core enzyme involved in the metabolism of the amyloid precursor protein and phosphorylation of tau protein; by inhibiting this enzyme Li^+ can reduce both Aβ production and tau phosphorylation [307, 308]. However, inhibiting GSK-3 can also reduce autophagy, attenuating the clearance of aberrant proteins [306], therefore more investigation is needed to unravel the mechanism of Li^+ protection in AD.

9.5 Conclusion

Lithium, an effective agent for bipolar disorder, also exhibits potential neuroprotective effects against neurodegenerative diseases, such as AD. However, investigations into the molecular mechanisms of Li^+ in human brains still focus on metabolic changes alone and ignore the alteration of biophysical properties associated with this drug. The unique behaviors of Li^+ on the lipid membrane are worth more investigation, despite low physiological concentrations.

Chapter 10

Influence of Lithium and Potassium on the Electrostatic Properties of Lipid Membranes

Aim of the Work and Summary. Given that Li ions have deeper penetration to lipid hydrophilic regions due to their tiny size as opposed to other monovalent ions, we aimed to investigate how this penetration influences the biophysical properties of the lipid membranes. The monolayer fluidity was compared in KCl and LiCl solutions by Langmuir-Blodgett Trough and surface topological structure and electric potential distribution of monolayers were measured by AFM and KPFM. It was found that LiCl can increase the fluidity of lipid monolayers, competing with the KCl interacting with lipid headgroups. In addition, the electric potential differences between liquid-ordered and disorder domains within lipid monolayers were increased in LiCl (20 mM) while decreased accordingly in LiCl and KCl solutions at 150 mM, implying the screening effect of ions at physiological concentration on lipid headgroups.

This chapter is drafted into a manuscript and prepared for submission to a peer-reviewed journal.

10.1 Introduction

Cellular membranes, composed of phospholipids, cholesterol, glycoprotein, etc., play a vital role in various cell functions and activities, such as maintaining the morphology and structure of cells, mediating cell signal and trafficking, molecule and ion transportation and so on. As an essential part of cells, Lipid membrane in physiological environment is surrounded by ions and water. These ions not only travel across cell membranes via ion channels embedded in the membranes but also influence their electrostatic properties. In particular, these ions affect the local surface electric potential, contributing to membrane potential, which is vital for various biological functions, such as the opening and closing of voltage-gated protein ion channels, depolarization and polarization of neuronal membranes, and regulation of the local pH, among others [188]. Other than the common electrostatic interactions between charged lipids and counterions, ions like sodium and potassium can also adsorb to zwitterionic lipids and change lipid packing and ordering [197], as well as physical properties [309]. A recent breakthrough by Scott *et al.* in 2022 revealed that the structural and dielectric changes in the zwitterionic phospholipid membranes due to ion accumulation considerably contributed to long-term potentiation (LTP), associated with learning and memory [310].

The adsorption affinity and preference of ions for biomembranes can be described by the Hofmeister effect, which was used to describe the adsorption preference of ions to proteins and influence strength on protein solubility and structures [311]. According to the Hofmeister series, lithium ions (Li^+) have the strongest binding affinity for lipid headgroup regions among the monovalent cations studied [312].

Lithium ion (Li^+), present in the human body at the millimolar level, is of benefit to mental health and physiological well-being, even though it is not as abundant as Na^+ and K^+. Daily intake of lithium element from food and water potentially contributes to lowering the suicide rate in society [313, 314]. Moreover, lithium compound has been used as an effective clinical medication for depression and bipolar disorder, even though the underlying molecular mechanisms have not been fully understood. One of the known

mechanisms is attributed to the competition of Li^+ with magnesium (Mg^{2+}) due to their similarity in size [290]. Li^+ can competitively bind to the Mg^{2+}-regulated enzymes such as Inositol Monophosphatase (IMPase) [315] and glycogen synthase kinase 3-beta (GSK-3β) and inhibit enzyme activities, thereby regulating the metabolic and signalling pathways and stabilizing patients' mood [290]. However, thousands of proteins with Mg^{2+} binding sites exist in the human body [316], and it is very challenging to figure out the specific Mg^{2+}-related pathways that can be interfered with by Li^+. Besides Mg^{2+}, Li^+ can compete with Na^+, K^+ and Ca^{2+} to enter ion channels on the lipid membranes, altering the ion flux through the channels [290]. The competition of Li^+ with other ions also exists in ion-membrane interactions, changing the physical properties of lipid membranes [312]. Therefore, Li^+ influences the biological systems not only biochemically but also biophysically.

The most recent studies by Scott *et al.* in 2023 revealed that LTP was suppressed by Li^+ but elevated by K^+; this is due to their different effects on membrane capacitance and dissipation energy in membrane capacitors. These effects are attributed to their distinct interactions with the headgroups of zwitterionic phosphatidylcholine (PC) lipids and their influence on dipole potential at the lipid/water interface [317]. Many experimental and theoretical studies have demonstrated the unique binding and influence of Li^+ on lipid membranes compared to other monovalent ions due to its small size and strong charge density [318, 317]. In a simulation study, Kruczek *et al.* found that 200 mM Li^+ has little effect on the area per lipid molecule compared to water, but it increases the dipole potential of POPC (1-palmitoyl-2-oleoyl-sn-glycero-3-phosphocholine) [299]. In contrast, another simulation study by Cordomi *et al.* showed that the area per lipid molecule is dramatically reduced in 200 mM Li^+ [319]. Klasczyk *et al.* measured the zeta potential of POPC vesicles in different salt solutions by dynamic light scattering and discovered that Li^+ in a low concentration regime ($\sim$ 150 mM) increases the zeta potential of POPC to a positive value and saturates above 150 mM, which means more Li^+ accumulates in the vicinity of membranes [312]. Distinctly, the zeta potential of the membrane remains negative or neutral in the presence of other ions. Their isothermal titration calorimetry results showed that Li^+ has a larger binding constant than K^+, implying a stronger binding

affinity to zwitterionic lipid membranes [312], leading to more Li^+ accumulating at the lipid headgroup than K^+ [319]. Additionally, the binding of K^+ is very unstable and has little effect on the stiffness and structure of PC membranes [320]. These findings confirmed that Li^+ and K^+ interact with lipid membranes very differently, resulting in distinguishable effects on membrane properties. Nevertheless, the physiological environment is full of ions, and K^+ abundantly exists inside the cells. Since Li^+ ions can enter the cells easily, it would be interesting to see how they interfere with the lipid membranes in the presence of other ions.

PC lipids, particularly POPC, are the most frequently used zwitterionic phospholipids in ion-lipid interaction studies [299]. Most studies utilize single-component lipid models, which deviate from real membranes. Moreover, cholesterol accounts for 30% of cell membranes [321], but is rarely considered despite its effects on the structure, fluidity, and dipole potential of the lipid membrane, among other factors [322]. Cholesterol has a dipole moment of 1.9 D and it can increase the dipole potential of the lipid membranes [322]. Therefore, it is worth taking cholesterol into account for ion-membrane studies.

In this work, we explored the influence of Li^+ on ternary-component lipid model composed of DPPC, POPC and cholesterol, using K^+ as a comparison. A Langmuir-Blodgett trough (LB) was employed to obtain pressure-area isotherms, which is used to measure the area per lipid molecule and the compressibility modulus of the lipid monolayers in aqueous solutions of Li^+ and K^+. It was also utilized to deposit lipid monolayers on mica substrates. Atomic force microscopy (AFM) and Kelvin probe force microscopy (KPFM) were employed to study the changes in topography and electrostatic properties of the lipid monolayers.

10.2 Materials and Methods

10.2.1 Materials

Lipids, including DPPC (1,2-dipalmitoyl-sn-glycero-3-phosphocholine), POPC, cholesterol, and LiCl salts were purchased from Sigma Aldrich (ON, Canada). KCl was purchased from VWR (ON, Canada). The lipid mixture of DPPC, POPC and cholesterol in 4:4:2 mass ratio was suspended in chloroform at 1 mg/mL for compression isotherms and monolayer deposition. LiCl and KCl were dissolved in Milli-Q ultrapure water to produce 20 mM LiCl, 150 mM LiCl, 150 mM KCl, and 130 mM KCl 20 mM LiCl solutions, which were used as the aqueous subphases for pressure-area isotherms and monolayer deposition.

10.2.2 Pressure-Area Isotherm

Pressure-area isotherms that monitor monolayer properties as function of surface pressure were obtained by compression experiments. The monolayer compression was performed in the LB trough at a temperature of $22 \pm 1°$C. The lipid mixture of 10 μL 1mg/mL in chloroform was spread onto the subphase between two symmetric barriers in the trough and kept for 15 - 20 min to evaporate choloroform. The lipid molecules were dispersed loosely at the water/air interface, oriented with the hydrophilic headgroups interacting with the water, and hydrophobic tails flexibly staying in the air. Then, lipid monolayers were compressed by the barriers at a speed of 5 mm/min. The isotherm curve obtained can be converted to the change of surface pressure with respect to the molecular area per lipid A_m by estimating the total amount of lipid molecules via the following formula [323]:

$$A_m = \frac{A \cdot M_W}{c \cdot N_\mathrm{A} \cdot V}. \tag{10.1}$$

Here, A is the measured area between the two barriers, M_W is the average molecular weight of the lipids, c is the concentration of the lipid solution (1 mg/mL), N_A is Avogadro's constant, and V is the volume of lipids added on the subphase surface. At least five

isotherms were collected for each subphase condition to guarantee the reproducibility of the curves.

10.2.3 Monolayer Deposition

The lipid monolayer was deposited on mica using LB trough to produce a lipid monolayer supported on the mica substrate. Prior to spreading lipids, the cleaved mica was immersed in the subphase. The lipid mixture in chloroform was spread on the surface of the aqueous subphase, and left to wait for chloroform evaporation. Then, the monolayer was compressed to the target pressure of 25 mN/m and left to stabilize for 12 - 14 min. Lastly, the mica slide was lifted out of the subphase at a speed of 2 mm/min, resulting in the deposition of a lipid monolayer on the mica surface. The prepared monolayer samples were dried and stored in the desiccator perfused with N_2 for at least 24 h before imaging by AFM and KPFM. At least three samples were produced for each condition.

10.2.4 AFM, KPFM Imaging and Image analysis

JPK Nanowizard II was used for AFM imaging, to obtain the topography images (z-height) of the monolayers. PPP-NCH probes (NanoSensors) with a nominal spring constant of 42 N/m and resonance frequency of 300 kHz were used for imaging in AFM tapping mode. Aist-NT SmartSPM was used for KPFM imaging to collect the surface electrical potential distribution. The contact potential difference (CPD) was mapped in Amplitude Modulated KPFM (AM-KPFM) mode by the scanning of an HQ:NSC14/Cr-Au conductive probe (MikroMasch) over the monolayer sample surface with a nominal probe resonance frequency of 160 kHz and spring constant of 5.0 N/m. The image processing and cross-section measurements were implemented using Gwyddion software and JPK image processing software.

10.3 Results and Discussion

10.3.1 Compression Isotherms

Pressure-area isotherms were collected using an LB trough in different subphases: water, 20 mM LiCl, 150 mM LiCl, 20 mM LiCl + 130 mM KCl and 150 mM KCl. The surface pressure was calculated as a function of the molecular area and the resulting curves are shown in Fig. 10.1.

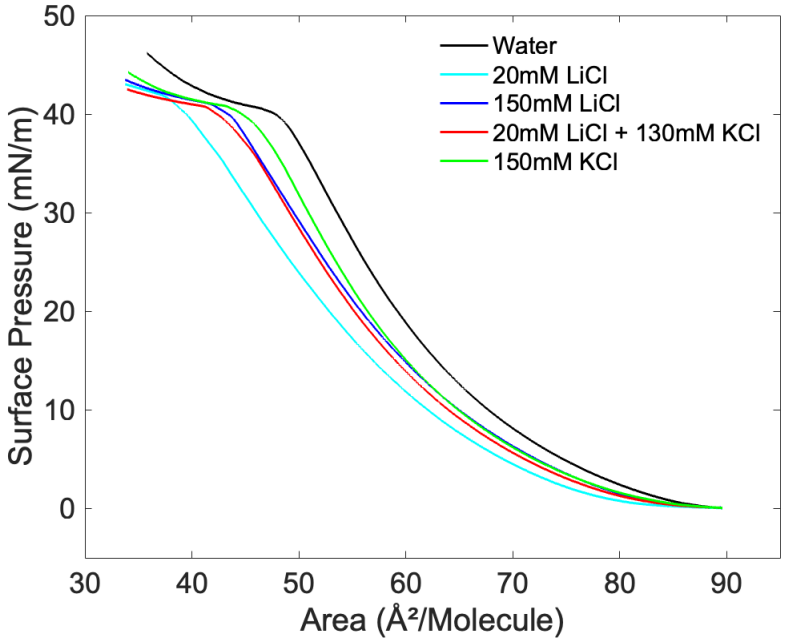


Figure 10.1: Pressure-area isotherms of the DPPC-POPC-Chol lipid mixture measured in the subphases of water (black), 20 mM LiCl (light blue), 150 mM LiCl (dark blue), 20 mM LiCl + 130 mM KCl (red), and 150 mM KCl (green).

As shown in Fig. 10.1, the pressure-area isotherm depicts the surface pressure change resulting from the reduction of the molecular area per lipid during compression. The isotherm of the DPPC-POPC-Chol lipid mixture in water featured a smooth curve; this

aligns with a previous study with a similar ratio of the same lipid components [263]. The smoothing of the isotherm can be attributed to the addition of abundant cholesterol to the lipids, which modulates the phase and fluidity of lipid membranes. The isotherm curves shift to the left in the salt solutions, according to the order: 20 mM LiCl > 20 mM LiCl + 130 mM KCl ≈ 150 mM LiCl > 150 mM KCl. The left shift of the isotherm curve at a particular pressure represents the shrinkage of molecular area induced by the adsorption of substances from the subphase [191]. The binding of KCl and LiCl salts with the lipid headgroup squeezed the space of the lipid molecules, thus reducing their molecular area and inducing condensation at different extents.

Using Eq. (10.1), the molecular area was calculated and averaged for measured surface pressures of 20, 25, 30 and 35 mN/m. The results are shown in Fig. 10.2.

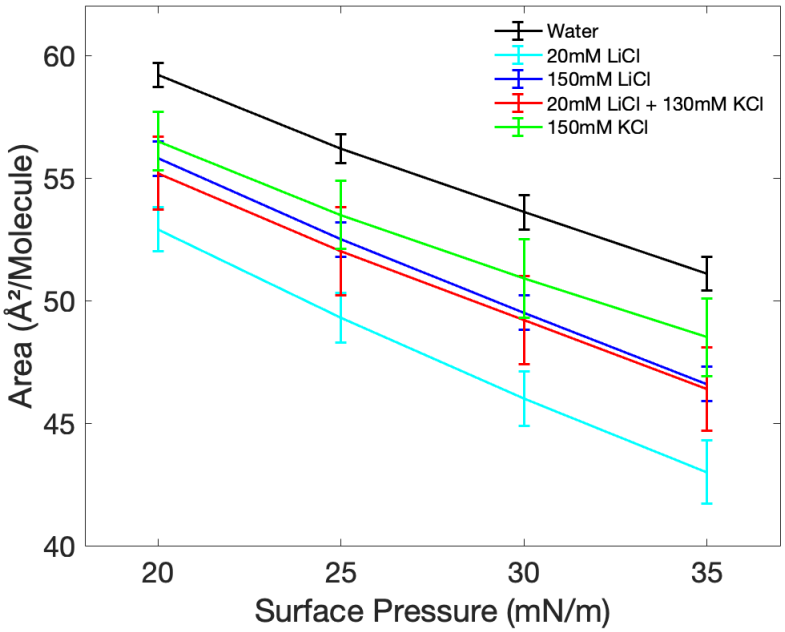


Figure 10.2: The average change in molecular area with respect to the increase of surface pressure in the subphases of water (black), 20 mM LiCl (light blue), 150 mM LiCl (dark blue), 20 mM LiCl + 130 mM KCl (red), 150 mM KCl (green). Error bar: mean ± SE.

Subphase	**Deposition pressure**			
	20 mN/m	**25 mN/m**	**30 mN/m**	**35 mN/m**
Water	59.2 ± 0.5	56.2 ± 0.6	53.6 ± 0.7	51.1 ± 0.7
20 mM LiCl	52.9 ± 0.9	49.3 ± 1.0	46.0 ± 1.1	43.0 ± 1.3
150 mM LiCl	55.8 ± 0.7	52.5 ± 0.7	49.5 ± 0.7	46.6 ± 0.7
20 mM LiCl + 130 mM KCl	55.2 ± 1.5	52.0 ± 1.8	49.2 ± 1.8	46.4 ± 1.7
150 mM KCl	56.5 ± 1.2	53.5 ± 1.4	50.9 ± 1.6	48.5 ± 1.6

Table 10.1: Average molecular area of lipid molecules (A_m) in $\mathring{A}^2$ as a function of subphase and surface pressure. Results represent mean ± SE.

The average molecular area per lipid (A_m) is reduced linearly as the surface pressure increases (Fig. 10.2 & Table 10.1). In the water subphase, A_m is 56.2 ± 0.6 $\mathring{A}^2$ at 25 mN/m and decreased to 53.6 ± 0.7 $\mathring{A}^2$ at 30 mN/m. The lipid condensation due to KCl and LiCl shrunk the molecular area at the pressure of 20 to 35 mN/m. Compared to salt subphases at high concentrations (150 mM KCl, 150 mM LiCl, and 130 mM KCl-20 mM LiCl), the condensation effect on the lipid monolayer is most profound in 20 mM LiCl, reducing A_m to 49.3 ± 1.0 $\mathring{A}^2$. This effect is weaker in 150 mM LiCl, with an area of 52.5 ± 0.7 $\mathring{A}^2$ at 25 mN/m. KCl showed the least reduction A_m, compared to the other subphases containing Li^+, and decreased A_m to 53.5 ± 1.4 $\mathring{A}^2$, implying weak binding of K^+ with the lipid headgroup. Interestingly, the minor amount of Li^+ within the K^+-dominated subphase shifts the trend toward LiCl, making the lipid area 52.0 ± 1.8 $\mathring{A}^2$. The strong reduction in A_m due to Li^+ and the weak effect of K^+ are consistent with observations in previous studies [319]. The larger contribution of Li^+ over K^+ to lipid packing aligns with the prediction of the Hofmeister series, which demonstrates the binding preference and strength of ions to biomolecules [324]. Li^+ has a stronger binding affinity than K^+ because of its smallest radii compared to other ions (Na^+, K^+, etc.) [324]. Compared to 20 mM LiCl, the increased A_m in the 150 mM salt solutions (150 mM LiCl, 150 mM KCl, and 20 mM LiCl + 130 mM KCl) implies that the lipid monolayers are more expanded.

This is caused by the swelling of neutral lipid membranes due to electrostatic repulsion in salt solutions at physiological concentrations [209].

10.3.2 Elastic Compressibility Modulus

The elastic compressibility modulus C_s^{-1} defines the ability of the lipid monolayer to be compressed. The higher the compressibility modulus value is, the harder it is to compress the monolayer. The compressibility modulus value also reflects the phase of the phospholipids. In a single-component phospholipid monolayer, a C_s^{-1} value between 50 and 100 mN/m implies a liquid (L) phase, while 100 - 250 mN/m denotes a liquid-condensed (LC) phase [325]. For our ternary lipid model, the C_s^{-1} reached 105.5 $\pm$ 2.0 mN/m at 30 mN/m on the water subphase, implying our monolayer is between L and LC phases. Figure 10.3 shows that C_s^{-1} decreased to under 100 mN/m in all salt buffers and reached its lowest value (75.0 $\pm$ 4.8 mN/m) in 20 mM LiCl at 30 mN/m, which suggests the monolayers became more liquid-like in salt buffers.

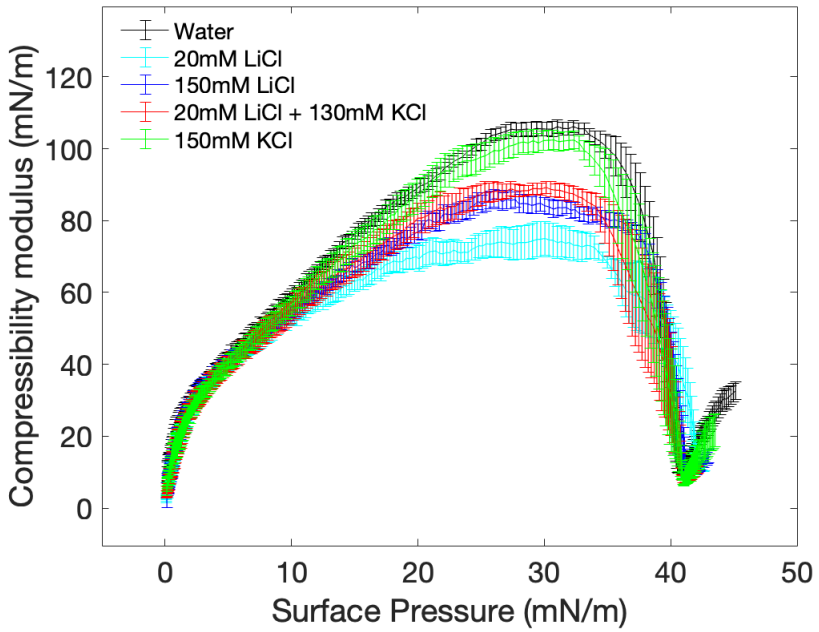


Figure 10.3: The elastic compressibility modulus of lipid monolayers in the subphases of water (black), 20 mM LiCl (light blue), 150 mM LiCl (dark blue), 20 mM LiCl -130 mM KCl (red), 150 mM KCl (green). Error bar: mean ± SE.

Subphase	**Surface Pressure**			
	20 mN/m	**25 mN/m**	**30 mN/m**	**35 mN/m**
Water	89.7 ± 2.0	101.2 ± 1.7	105.5 ± 2.0	100.7 ± 3.4
20 mM LiCl	69.4 ± 3.6	72.9 ± 3.4	75.0 ± 4.8	68.3 ± 1.7
150 mM LiCl	76.9 ± 2.1	84.6 ± 2.5	84.1 ± 2.3	80.6 ± 2.2
20 mM LiCl + 130 mM KCl	80.7 ± 4.2	87.3 ± 3.0	89.3 ± 1.6	77.7 ± 7.5
150 mM KCl	87.1 ± 4.4	97.6 ± 3.8	102.2 ± 2.7	90.4 ± 8.0

Table 10.2: Elastic compressibility modulus values (mN/m) of monolayers on different subphases in response to pressure increase.

Figure 10.3 and Table 10.2 show the change in compressibility modulus of the monolayers in response to the increase in surface pressure, indicating the mechanical properties of the lipid monolayers at different pressures and on different subphases. The elastic compressibility modulus is defined by [200]:

$$C_s{}^{-1} = -A\frac{\mathrm{d}\pi}{\mathrm{d}A}, \tag{10.2}$$

where π is surface pressure, and A is the area per lipid. In addition to phases, the $C_s{}^{-1}$ value correlates to the fluidity of lipid monolayers; the decreased $C_s{}^{-1}$ represents increased fluidity [191]. Therefore, according to the corresponding $C_s{}^{-1}$ of the monolayer compressed on each subphase, the fluidity of lipid monolayers was significantly enhanced in 20 mM LiCl, descending in the sequence of 150 mM LiCl, 20 mM LiCl + 130 mM KCl, and 150 mM KCl. In combining the results shown in Fig. 10.3 and Fig. 10.2, the salts that cause the greatest decrease in compressibility modulus are also those that decrease the lipid area in response to an increase in pressure. The 20 mM LiCl has the lowest compressibility modulus, indicating reduced lipid area and increased space between lipid molecules, thereby making the lipid more flexible, lowering the compressibility modulus, and improving fluidity.

At 30 mN/m, the 150 mM KCl subphase had the least influence on membrane compressibility modulus (102.2 ± 2.7 mN/m), while both 150 mM LiCl and 20mM LiCl + 130 mM KCl decreased the compressibility modulus to 84.1 ± 2.3 mN/m and 89.3 ± 1.6 mN/m, respectively. The pronounced performance of Li^+ in changing the lipid area and compressibility modulus is attributed to its size and extraordinary interaction with lipid headgroups. The smaller radius of Li^+ compared to other monovalent ions provides Li^+ with a profound ability to interact with the phosphate and carbonyl groups at the lipid head [299]. A study by Kruczek *et al.* simulated the interaction of 200 mM LiCl and 200 mM KCl with POPC and found a greater number of Li^+ ions bound to POPC compared to K^+ [299]. Moreover, as shown in Fig. 10.4, due to the small radius of Li^+, a large portion of Li^+ predominantly prefers to bind the phosphate group (PO_4^-) and carbonyl group on the unsaturated chain simultaneously (the inset and the column of 'PO_4 and CO-Sn2' in Fig. 10.4); this phenomenon is absent with other monovalent ions of larger size, including Na^+, K^+ and Rb^+ [299]. Therefore, the deep penetration of Li into lipid headgroups ro-

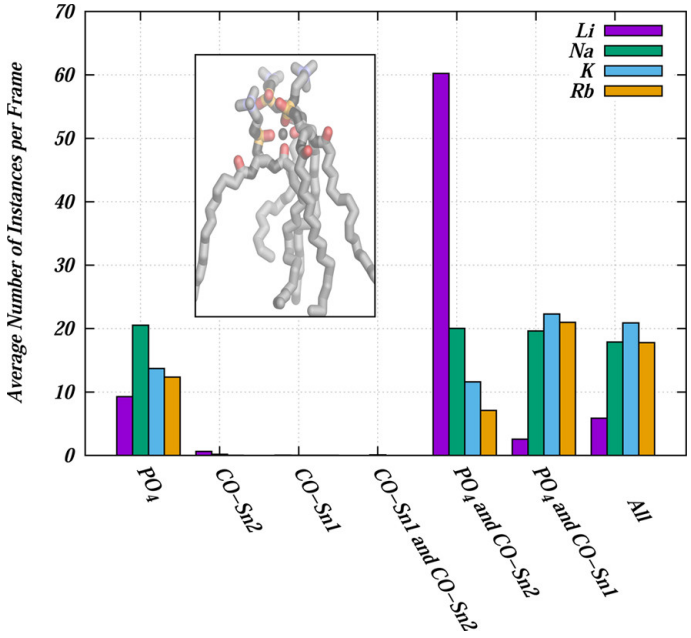


Figure 10.4: Molecular simulation results of the average number of monovalent cations bound to the sites on POPC lipid molecules with possible combinations. PO_4: phosphate group at POPC head group. CO-Sn1: carbonyl group (C=O) on POPC saturated chain. CO-Sn2: carbonyl group on POPC unsaturated chain. Inset: one Li^+ (black sphere) coordinates with four oxygen (red) of phosphate groups and carbonyl groups from three POPC lipid molecules. Reprinted with permission from *Langmuir*, Effects of lithium and other monovalent ions on palmitoyl oleoyl phosphatidylcholine bilayer. J. Kruczek, S-W. Chiu, E. Jakobsson, and S. A. Pandit. 33(4):1105–1115, 2017. Copyright 2017 American Chemical Society.

bustly altered the packing of lipid molecules, thereby contributing to the reduced molecular area and improved fluidity. Furthermore, the binding energy of Li^+ with the PO_4^- is larger than that of K^+ [326], making it favourable when binding to PO_4^- in the lipid headgroup. Despite 20 mM Li^+ being less than 130 mM K^+ in quantity, the advantages of Li^+ in size, charge density and binding energy with PO_4^- allow it to interact with lipid headgroups more competitively. This allows it to make more contributions in regulating lipid packing and properties, shifting the isotherm and compressibility modulus in 20 mM LiCl 130mM KCl solution towards Li-dominated changes.

In addition, although some studies suggested that the chloride-lipid interaction is subtle compared to the binding and penetration of cations with lipid headgroups [299, 210], recent evidence has shown that the adsorption of cations to lipid membranes could promote the binding of Cl^- [324, 327]. The abundant accumulation of Li^+ could attract more Cl^- to interact with lipid headgroups, increasing the spacing between lipid molecules and improving fluidity.

Another notable phenomenon is that the influence of LiCl on lipid membranes is determined by its concentration. Compared to 150 mM LiCl, 20 mM LiCl has a greater effect on the structural and mechanical properties of lipid monolayers. At a dilute concentration, the interaction between ions and polar subunits in PC headgroups is dominated by electrostatic forces. However, as the ions at higher concentrations accumulate in the vicinity of headgroups, they may attract more water molecules and rearrange the alignment of water molecules at headgroups due to the osmotic effect, thereby changing the lipid packing [299].

10.3.3 AFM and KPFM Images

Images of lipid monolayers obtained from AFM and KPFM were used to investigate the topographic and electrostatic differences in nanodomains as a result of the inclusion of cations, as shown in Fig. 10.5.

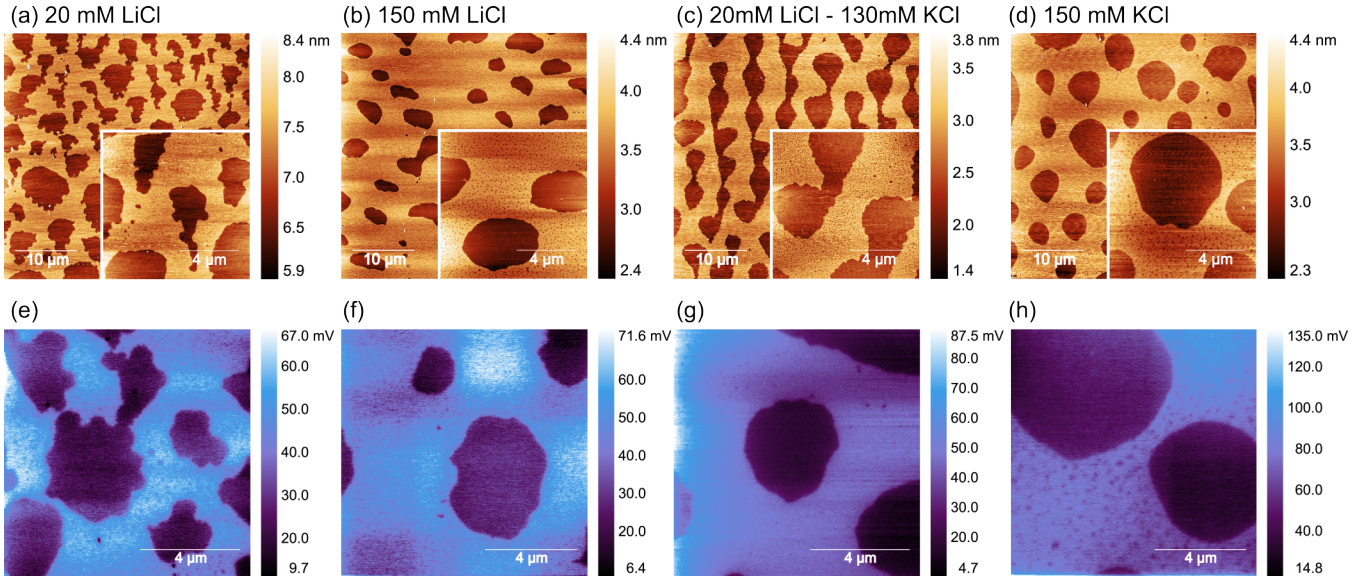


Figure 10.5: Topographical images (a-d) obtained by AFM and CPD images (e-h) obtained by KPFM of lipid monolayers deposited in 20 mM LiCl (a&e), 150 mM LiCl (b&f), 20 mM LiCl 130 mM KCl (c&g), and 150 mM KCl (d&f) subphases at 25 mN/m. The size of AFM image is 40 × 40 μm and 10 × 10 μm (inset). The size of CPD image is 10 × 10 μm.

	20mM LiCl	**150mM LiCl**	**20mM LiCl-130mM KCl**	**150mM KCl**
Δh **(nm)**	0.62 ± 0.02	0.66 ± 0.05	0.65 ± 0.02	0.58 ± 0.03
ΔESP (mV)	35.05 ± 2.72	25.15 ± 0.71	24.88 ± 1.07	24.21 ± 1.62

Table 10.3: Height (Δh) and potential difference (ΔESP) between L_o and L_d domains of monolayers deposited in different subphases. Results represent mean ± SE.

AFM images in Fig. 10.5(a-d) show that the lipid monolayers deposited in all salt solutions share the features of explicit phase separation between the liquid-ordered phase (L_o) and liquid-disordered phase (L_d), with abundant discrete L_d nanodomains spread within an interconnected L_o phase. The L_o phase is enriched with DPPC and cholesterol.

Cholesterol with a portion larger than 25 mol% in lipid model can greatly increase the fluidity of the DPPC [328]. The L_d phase is enriched with fluid-like POPC, with less cholesterol incorporated. As discussed in Chapter 5, the L_d nanodomains are absent within the lipid monolayers deposited on water, while they exist universally in salt solutions (NaCl, LiCl, and KCl), implying that the binding of ions to the lipid headgroups influences the lipid distributions.

KPFM measures the contact potential difference (CPD) between the scanning probe and monolayer samples and produces CPD images that show the electrostatic distribution on the sample surface (Fig. 10.5(e-h)). Due to the distinct dipole potentials of different lipid species, their contributions to electric surface potential (ESP) are also different. The bright region in the KPFM image in Fig. 10.5(e-h) represents higher ESP, while the dark region represents lower ESP. According to AFM and CPD images (Fig. 10.5), the potential distribution in CPD images is associated with the L_d - L_o phase separation in AFM images; the L_o region has higher ESP while the L_d region has lower ESP. The relative electric surface potential difference between L_o and L_d domains ΔESP was measured from CPD images, as shown in Table 10.3. The height difference Δh between L_o and L_d domains within monolayer samples, measured from AFM images, were also indicated in Table 10.3.

The height difference Δh between L_o and L_d domains has subtle changes in the salt solutions. Compared to the monolayers deposited in water with a potential difference ΔESP of 31.38 $\pm$ 0.79 mV (Table 5.3 in Chapter 5) between ordered and disordered domains, ΔESP is increased to 35.05 $\pm$ 2.72 mV in 20 mM LiCl. Conversely, the potential difference drops to $\sim$ 25 mV in the remaining three solutions that have a total salt concentration of 150 mM (Table 10.3). The increased ΔESP in 20 mM LiCl could be attributed to the deep penetration and strong electrostatic interaction of Li^+ with the lipid headgroups in a low concentration regime, which could become saturated above 150 mM [312].

The decrease of ΔESP in 150 mM salt solutions (LiCl, KCl, LiCl + KCl) could be caused by the screening effect of salt at higher concentrations. Gaddam and Ducker experimentally confirmed that the Debye length of concentrated monovalent cationic solutions (LiCl, NaCl, CsCl) monotonically increases as the concentration increases, indicating that

the electrostatic screening is enhanced by elevated salt concentration [329]. This could occur in a low-concentration regime [209]. The electrostatic screening at 150 mM changes the charge and dipole of lipid molecules completely, thereby reducing the ΔESP. Bohinc *et al.* established a rigid-rod model for zwitterionic PC lipids to describe the structure of the headgroups and to investigate their changes due to their interactions with cations [330]. They found that the tilting angle of rod-like PC headgroups is influenced by ion concentration: the tilting angle is more perpendicular at low concentrations but tends to be parallel to the interface as the ion concentration increases, as a consequence of electrostatic screening enhanced by the high ionic concentration [330]. Hence, the presence of a substantial number of ions can alter the structure of lipid headgroups, charge distribution, and lipid packing, resulting in the reduction of potential differences between domains and influencing membrane fluidity.

Besides ionic species, the lipid composition is another factor worth consideration. A small-angle X-ray scattering (SAXS) study by Hishida *et al.* reported that the adsorption affinity of ions for lipid molecules varies between POPC and POPE (1-palmitoyl-2-oleoyl-sn-glycero-3-phosphoethanolamine), suggesting that the Hofmeister series varies with the composition of the adsorbed lipid molecules. The influence of ion identity and binding preference can differ between POPC-enriched and DPPC-enriched regions. The situation is further complicated by the inclusion of cholesterol, which enhances the electric surface potential of lipid membranes [331]. Thus, the ion-membrane interactions and their effects on complex membrane systems are worth more investigation, as the ubiquitous existence and dynamics of ions regulate various properties and activities in the physiological environment.

10.4 Conclusion

This work studied the effect of Li^+ and K^+ on the mechanical and electrostatic properties of cholesterol-enriched lipid monolayers. Our results demonstrated the distinct influence of Li^+ and K^+ on the molecular area of lipid molecules, membrane fluidity and the electric

surface potential difference between lipid domains in the DPPC-POPC-Chol lipid model. Li^+ has a pronounced effect on reducing the lipid molecular area, increasing monolayer fluidity, and strongly competing with K^+ in interacting with lipid monolayers. The efficacy of Li^+ in altering membrane properties relies on its concentration, as robust effects are observed at low concentrations (20 mM), but weaker effects are observed at high concentrations (150 mM). The electric potential difference between liquid-ordered and disordered domains within the lipid monolayers is enhanced at 20 mM Li^+, while it decreased in all 150 mM salt solutions (LiCl, KCl, LiCl + KCl). This suggests that there is a screening effect on lipid dipole potentials by salts at physiological concentrations. This study emphasizes the contributions of ions in biological systems and displays the unique influence of Li^+ on membranes, which can help understand the regulation mechanism of Li^+ for neuronal systems.

Chapter 11

Lithium Reduces Amyloid-β induced Damage in DPPC-POPC-Cholesterol Membranes

Aim of the Work and Summary. This chapter investigates the protective effect of LiCl on lipid membranes against Aβ's attack, considering that LiCl can increase the fluidity of lipid membranes, as demonstrated in Chapter 10. The transmembrane ion currents were measured by BLM electrophysiology to evaluate the permeability of suspended model lipid membranes exposed to Aβ1-42 oligomers and LiCl at therapeutic level (0.8 mM) and toxic level (4 mM). The BLM results found that LiCl has little effect on Aβ1-42 ion channels embedded in the membranes, but 0.8 mM LiCl can significantly reduce membrane permeability caused by Aβ-induced transient pores. Our findings suggested LiCl at the therapeutic level can enhance the membrane durability and stability when Aβ-induced disruption occurs, which may be attributed to its adequate influence on membrane fluidity.

This chapter is drafted into a manuscript and prepared for submission to a peer-reviewed journal.

11.1 Introduction

Lithium has been confirmed to be an effective drug for the clinical treatment of mood disorders that include bipolar disorder (BD), mania and depression. Given the excellent clinical performance of lithium in BD and its potential neuroprotection effect, scientists are exploring its role in treating Alzheimer's disease (AD), the major neurodegenerative disease that leads to dementia and cognitive decline among the elderly. A meta-analysis by Velosa *et al.* showed that lithium treatment for BD patients could lower the risk of dementia, which is increased in BD [332], implying the strong correlation between BD and dementia and the therapeutic potential of lithium for dementia-associated AD.

The abnormal production and deposition of amyloid-beta (Aβ) plaques have been correlated to neuron mortality and degeneration in AD, known as the "Amyloid-cascade hypothesis". The Aβ peptide is a protein fragment generated from membrane-spanning amyloid precursor protein (APP). It can refold, aggregate, and eventually form amyloid plagues, universally found in AD patients' brains. The aggregation process produces toxic Aβ1-42 oligomers, which have a profound membrane affinity and lead to membrane destabilization through multiple mechanisms, including inducing penetrating lipid membranes [145], dissociating lipid molecules from membranes [21], embedding the membrane to form ion channels [20, 145]and so on. This eventually dysregulates neuronal homeostasis and increases neuron vulnerability [19], accelerating neurodegeneration in AD. While the prevailing therapeutic strategy is to develop anti-Aβ drugs aimed at lowering and removing Aβ aggregates, there is a lot of controversy that exists given their efficacy and side effects in clinical trials. A meta-analysis study conducted by Terao *et al.* in 2022 suggested that Li^+ may have better efficacy in treating cognition decline than Aducanumab, which is an FDA-approved anti-Aβ drug for AD treatment; additionally, the annual cost of lithium is much lower than Aducanumab for patients, allowing it to be a promising candidate for AD treatment [333].

Recent clinical studies find that low-dose lithium improved clinical global impression in AD [334], which is an overall evaluation of disease severity and drug efficacy [335]. Cell

studies by Alvarez *et al.* revealed that incubation with 10 mM lithium rescued neurons and lowered the mortality rate caused by fibrillar Aβ1-40 [336]. Abundant evidence supports that lithium exhibits neuroprotection and enhances the cognition of AD patients through multiple pathways [305, 306], some of which overlap with its regulation in BD [306]. Lithium can suppress glycogen synthase kinase-3β (GSK-3β) activity [337] and inositol monophosphatase (IMP), increase the level of brain-derived neurotrophic factor (BDNF) and promote autophagy in BD [306]. These metabolic changes caused by lithium also regulate the pathological pathways in AD, thereby showing the potential of lithium as a therapeutic drug for AD. GSK-3β associates with amylogenesis [308]. Transgenic cell and animal studies found that lithium suppressing GSK-3β activity regulates APP phosphorylation, thereby reducing Aβ production [338, 339]. The release of BDNF enhanced by lithium can protect neurons from neurotoxicity, stimulate neuron growth, and eventually contribute to cognitive improvement [306]. Autophagy is a metabolic process that degrades and cleans reductant substances, including misfolded proteins. Li^+-stimulated autophagy can counteract the autophagy decline occurring in AD and promote the clearance of Aβ aggregates [340]. However, the regulation pathways cannot be clearly determined given that lithium's inhibition on GSK-3β and IMPase have opposite effects on autophagy [306].

Many in-vivo studies utilizing transgenic cell or animal models involving Aβ overexpression evidenced that lithium reduced the production of Aβ proteins and implicated the regulation of lithium on metabolic pathways [338, 339, 341, 342, 343]. Nonetheless, lithium influences the neuronal system not only metabolically but also biophysically.

Lithium is present in the aqueous biological environment as free ions. Lithium ions actively interact with diverse components in the plasma membranes. It competitively enters sodium, potassium and calcium ion channels and alters the ionic flux [290]. It also can bind to enzymes competing with Mg^{2+} and cause changes in their conformation and activity [290, 344]. Other than proteins, lithium has a stronger binding affinity to the lipid hydrophilic region and a deeper penetration at the lipid headgroup than other monovalent ions [290]. The preferred binding and accumulation of lithium ions at the membrane surface can change the membrane's biophysical properties. As evidenced in Chapter 10, the membrane fluidity was found to be greatly improved due to the presence of Li^+.

As mentioned earlier, Aβ oligomers exhibit a strong binding affinity and can cause damage to membranes, producing various defects, including pores and ion channels [145, 28]. The interaction of lithium with lipid membranes may influence the membranes' response to Aβ oligomers-induced damage, potentially serving as a mechanism for lithium to mitigate Aβ neurotoxicity. To verify this hypothesis, we used black lipid membrane electrophysiology to evaluate the quality of lipid membranes incubated with Aβ1-42 oligomers and lithium at the therapeutic level (0.8 mM) [345] and toxic level (4 mM) [346, 347]. The measured ion currents across the membrane were used to evaluate the Aβ's damage level to the membranes quantitatively. In addition, the conductance of ion channels formed by Aβ1-42 oligomers was evaluated by stepwise voltages. Our results demonstrated that lithium at 0.8 mM can alleviate Aβ-induced membrane damage. This study suggests that lithium's modulation of lipid membranes could be one of the underlying molecular mechanisms for understanding lithium's functional role in AD-associated lipid studies.

11.2 Materials and Methods

11.2.1 Materials

Lipid components (DPPC, POPC, and cholesterol), lithium chloride (LiCl), potassium chloride (KCl), and HEPES were purchased from Sigma-Aldrich (Canada). Aβ1-42 (NaOH) was available from rPeptide (USA). Salt solutions (150 mM KCl - 20 mM HEPES, 0.8 mM LiCl + 150 mM KCl - 20 mM HEPES, 4 mM LiCl + 150 mM KCl - 20 mM HEPES) were prepared by dissolving corresponding chemicals in Milli-Q ultra-pure water and pH was adjusted to 7.4 by a pH meter.

11.2.2 Lipid Preparation and Lipid Membrane Formation

DPPC, POPC and cholesterol in the mass ratio of 4:4:2 was pre-dissolved in chloroform/methanol (9:1 v/v) and reached a final concentration of 10 mg/mL. After evaporating

chloroform by nitrogen gas, the dried lipid mixture was resuspended in decane/butanol (50:1 v/v) at 10 mg/mL. The lipid decane solution was painted by a shaved pipette tip over the 150 μL aperture on the BLM cuvette, and an artificial membrane could form.

11.2.3 Aβ Preparation

Aβ1-42 powder was dissolved at 0.5mg/mL by 150 mM KCl and 20 mM HEPES buffer (adjusted to pH 7.4) and subdivided into aliquots. Aβ1-42 salt solution was stored at -20 °C. The Aβ1-42 was naturally warmed to room temperature before being applied for BLM tests.

11.2.4 Black Lipid Membrane Electrophysiology

Electrophysiological measurement was performed by an Elements eOne amplifier (USA) connecting two Ag/AgCl electrodes, which were placed in two separate chambers filled with electrolyte solutions. The lipid mixture dissolved in the organic solvent was painted over a 150 μm cavity on the wall separating two chambers using a shaved pipette tip. The suspended lipid bilayers formed at the cavity due to lipids' self-assembly. The amplifier applied voltages and recorded ion currents across the lipid membrane via electrodes.

Single-event Recording

A single event represents the transient current increase induced by the temporary pore formation due to Aβ interacting lipid membranes recorded at consistent voltages from 60 mV to 135 mV. The current would return to 0 pA in a short duration when the membrane integrity recovered. The maximum current and mean current amplitude within a single event were measured to evaluate the pore size caused by Aβ in the membrane, reflecting the destruction level of Aβ in the lipid membranes.

Voltage-dependence Test

The voltage-dependence measurement evaluates the stability of lipid membranes without Aβ incorporation, as well as Aβ1-42 ion channel conductance [20], by measuring transmembrane currents with step-wise voltages [94]. Voltage-dependent ion current amplitude (I) was measured by applying voltage gradients (V) from -120 mV to 120 mV, increased by 10 mV as a step voltage, to produce an I-V profile that indicates the dependency of ion currents on voltage changes. The conductance obtained by the linear-fitted slope of the I-V curve represents the intrinsic permeability of lipid membranes to ions and membrane permeability at the incorporation of Aβ1-42 ion channels.

11.3 Results and Discussion

11.3.1 Membrane Suspended in KCl and LiCl solutions

The membrane quality in KCl and LiCl solutions was assessed by voltage-dependence measurements, which provide the current-voltage (I-V) profiles of lipid membranes in different solutions. The I-V profiles of lipid membranes display the transmembrane ion current changes in response to step-wise voltages to evaluate the permeability and quality of pure lipid membranes composed of DPPC, POPC and cholesterol without Aβ1-42 proteins (Fig. 11.1 & Fig. 11.2).

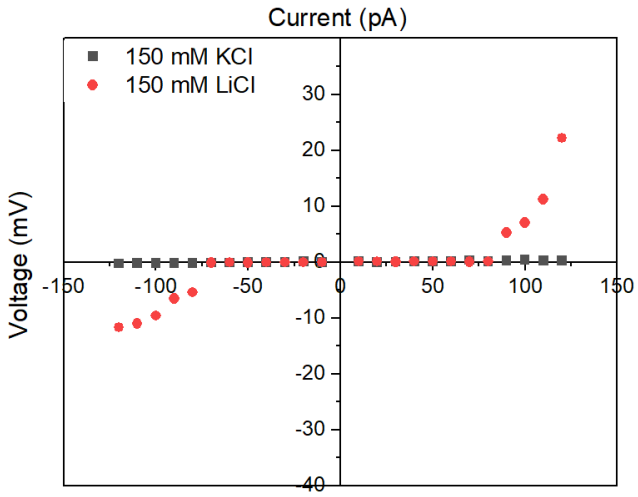


Figure 11.1: Single I-V profile of DPPC-POPC-Chol lipid bilayers suspended in 150 mM KCl (black square) versus 150 mM LiCl (red dot).

Figure 11.1 shows single representative I-V profiles of model lipid bilayers in 150 mM LiCl and 150 mM KCl. Unlike membranes in 150 mM KCl solution, which keep stable with low ionic permeability during the voltage alteration from -120 mV to 120 mV, the membranes produced in 150 mM LiCl became more sensitive to the voltage increase accompanied by robust ion current increase, which suggested that they became unstable as absolute voltage amplitude was larger than 80 mV ($|V| > 80$ mV). This means the membrane became fragile and leaked at larger voltages in the 150 mM LiCl solution. This is caused by lithium ions (Li^+) can enhance the membrane fluidity significantly compared to the K^+, according to our previous studies in Chapter 10, thereby leading to the instability of suspended lipid membranes. Hence, the unstable membranes suspended in 150 mM LiCl are not ideal for introducing the Aβ1-42 oligomers to the membrane systems and evaluating Aβ-induced damage to membranes.

Figure 11.2 displays the averaged I-V profiles of membranes suspended in 150 mM KCl

solutions with and without 0.8 mM and 4 mM LiCl. The symmetry of the I-V profiles in all three solutions indicates the symmetry of lipid bilayers where lipid molecules were evenly distributed in membranes. The linear I-V profile (Fig. 11.2, black square) represents the intrinsic leakage conductance (g_L) of pure lipid membranes due to the ion current leakage across the membranes without ion channels or pores [94].

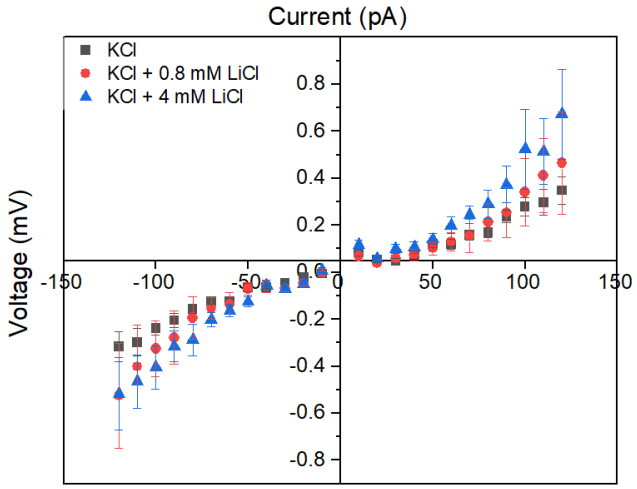


Figure 11.2: I-V profiles of DPPC-POPC-Chol lipid bilayers suspended in 150 mM KCl (black square), 150 mM KCl + 0.8 mM LiCl (red dot) and 150 mM KCl + 4 mM LiCl (blue triangle) solutions. The results represent mean ± SE. Sample size: $n \geq 8$.

Lipid bilayers suspended in 150 mM KCl electrolyte solution (Fig. 11.2, black square) are featured with a linear I-V relationship, showing the voltage-independency of g_L (2.44 ± 0.32 pS, $n = 10$). The I-V profile tends to be exponential as the voltage increases in the 150 mM KCl solution with 0.8 mM LiCl (Fig. 11.2, red dot) and 4 mM LiCl (blue triangle), respectively. g_L became 3.17 ± 1.27 pS ($n = 8$) in 0.8 mM LiCl and to 4.11 ± 0.95 pS ($n = 10$) in 4 mM LiCl. The modest change in I-V profiles and g_L can be attributed to the increased number of ions in the solutions with LiCl in a concentration-dependent manner.

4 mM of LiCl resulted in more ions in the KCl electrolyte solution compared to 0.8 mM of LiCl, which created a more ionic and conductive aqueous environment, contributing to a slightly higher membrane leakage conductance due to more ion accumulation at the lipid/solution interface. However, the increase of g_L due to the addition of ions is subtle (ANOVA, $p > 0.05$); membranes remain stable with extremely small leakage conductance, implying a minimal permeability to ions in 150 mM KCl electrolytes with minor addition of LiCl at 0.8 mM and 4 mM.

11.3.2 Influence of LiCl on Aβ Ion Channels

After the stability of membranes was confirmed in solutions, Aβ1-42 oligomers were introduced to the suspended membrane systems. Aβ1-42 oligomers assembling in the lipid membranes can form non-selective ion channels in the membrane, featured with permeant ion current increase in electrophysiological studies [20]. The voltage-dependence test measures the ion currents through the protein ion channel in response to voltage change, as shown in Fig. 11.3. The I-V profiles obtained from voltage-dependence measurements evaluated Aβ1-42 ion channel conductance by calculating the slope via linear fitting.

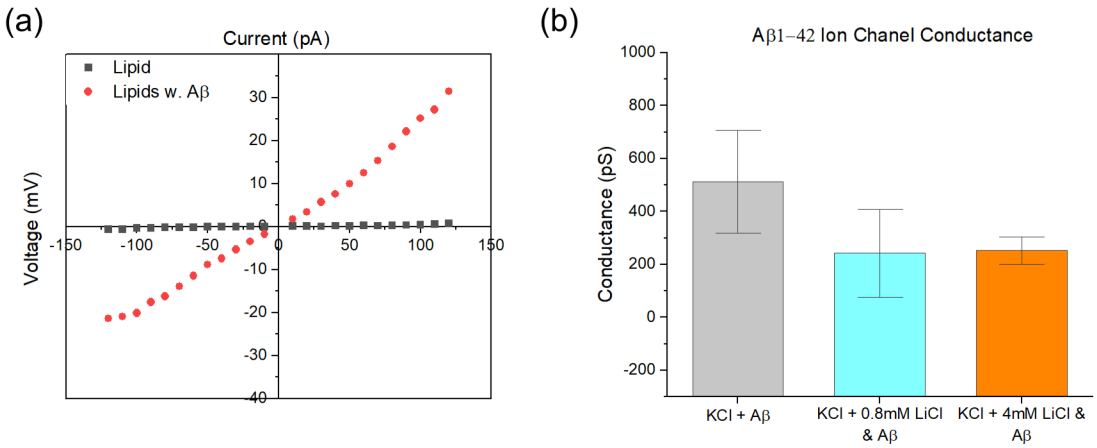


Figure 11.3: Results of voltage-dependence tests of lipid membrane with and without Aβ1-42. (a) Representative single I-V profiles of lipid bilayers without Aβ1-42 and with Aβ1-42 added. The slope of the linear-fitted I-V profile of a pure membrane (black square) is 4.16 pS. The slope of the I-V profile of an Aβ-incorporated membrane (red dot) is 215.75 pS. (b) Ion channel conductance in 150 mM KCl solutions with and without LiCl. Aβ1-42 ion channel conductance in (1) 150 mM KCl (grey): 512.80 $\pm$ 193.79 pS, $n = 8$, in (2) 150 mM KCl + 0.8 mM (blue): 242.20 $\pm$ 165.39 pS, $n = 6$, in (3) 150 mM KCl + 4 mM LiCl (orange): 251.79 $\pm$ 51.93 pS, $n = 6$.

Figure 11.3(a) displayed the representative I-V profile of the single Aβ1-42 ion channel (red dot) formed on the lipid membrane. the Aβ-embedded membrane is more permeable to ion transport with stronger ion current flow across the membrane, compared to the Aβ-free lipid membrane (black square). The I-V profile of the Aβ1-42 ion channel (Fig. 11.3, red dot) is linear, and the average ion-channel conductance is 512.80 $\pm$ 193.79 pS ($n = 8$), independent from voltage changes, implying the Aβ1-42 forms non-gated passive ion channels on the membrane. The linear I-V relationship for Aβ1-42 ion channels is consistent with the electrophysiological study by Bode *et al.* in 2017, where the Aβ1-42 oligomers formed ion channels on the cellular membrane and were measured by voltage clamp [20]. The ion channel conductance was 242.20 $\pm$ 165.39 pS ($n = 6$) in 150 mM KCl with 0.8 mM LiCl and 251.79 $\pm$ 51.93 pS ($n = 6$) in 150 mM KCl with 4 mM LiCl, respectively.

Despite the decreasing tendency in LiCl solutions, no statistically significant difference was observed in ion channel conductance (ANOVA, $p > 0.05$), suggesting the minimal influence of LiCl on Aβ1-42 ion channels. The results can be supported by a recent experimental study in vitro by Berntsson *et al.*, which demonstrated the weak binding of lithium to Aβ peptides and its minor effect on Aβ aggregation [348].

11.3.3 Influence of LiCl on Aβ-induced Transient Pores

In addition to ion channels, the Aβ1-42 oligomers can also disrupt the membrane by forming transient pores, shown as acute current increase with short duration in the BLM electrophysiology output [156]. The amplitude of ion current caused by the binding of Aβ1-42 oligomers shows the Aβ-induced damage level to the lipid membrane, as indicated in Fig. 11.4.

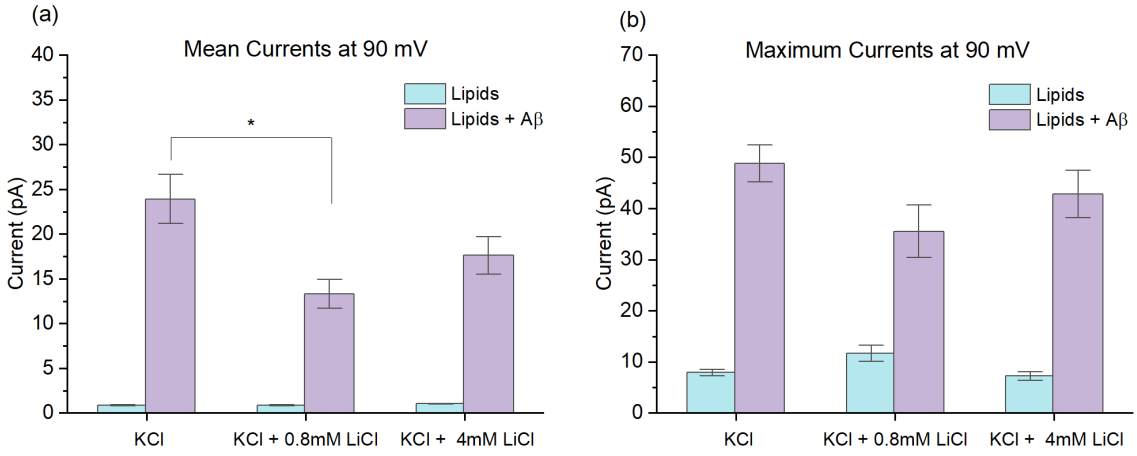


Figure 11.4: Ion currents caused by Aβ1-42 oligomers measured at 90 mV (a) mean and (b) maximum ion currents across lipid bilayers incubated with Aβ1-42 oligomers, which were measured at 90 mV in 150 mM KCl, 150 mM KCl + 0.8 mM LiCl (KCl + 0.8 mM LiCl) and 150 mM KCl + 4 mM LiCl (KCl + 4 mM LiCl) solutions. Error bar: mean ± SE.

The mean and maximum ion current value measured at 90 mV was compared across the conditions in Fig. 11.4. The mean amplitude of current flow at 90 mV across the

membranes in 150 mM KCl solutions was 23.9 ± 2.71 pA ($n = 115$). It was significantly reduced to 13.34 ± 1.60 pA ($n = 41$) in KCl solution with 0.8 mM LiCl (Tukey's test, $p < 0.05$), suggesting the size of transient pores caused by Aβ1-42 in the lipid membranes was reduced in 0.8 mM LiCl. The maximum current flow at 90 mV caused by Aβ1-42 in 150 mM KCl was 48.77 ± 3.61 pA and decreased to 35.52 ± 5.11 pA in 0.8 mM LiCl and 42.84 ± 4.61 pA in 4 mM LiCl. Although the statistically significant difference was absent among maximum current comparisons, the change of maximum current flow in solutions with LiCl aligned with the declining trend in the mean currents.

The membrane conductance was calculated by $g = \frac{I}{V}$ to evaluate the membrane permeability caused by Aβ-induced transient pore (Fig. 11.5).

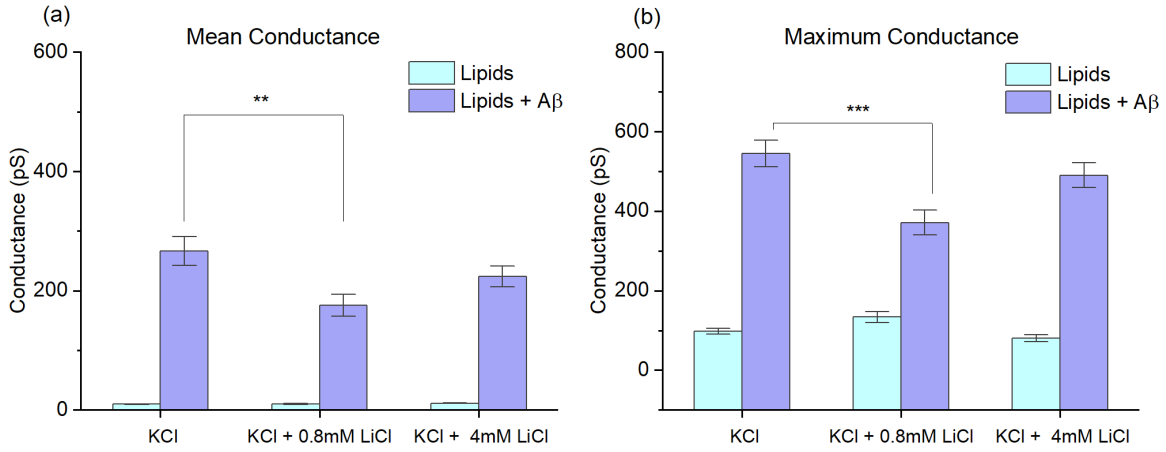


Figure 11.5: Membrane conductance due to Aβ-induced transient pore. (a) mean and (b) maximum instantaneous membrane conductance across lipid bilayers incubated with Aβ1-42 oligomers in 150 mM KCl, 150 mM KCl + 0.8 mM LiCl (KCl + 0.8 mM LiCl) and 150 mM KCl + 4 mM LiCl (KCl + 4 mM LiCl) solutions. They were calculated from the mean/maximum value of the ion current of a single event divided by the corresponding voltage.

Figure 11.5 shows the mean and maximum instantaneous membrane conductance, which was used to evaluate the membrane permeability due to transient pore formation. The transient pore created by Aβ1-42 to the lipid membrane increases the permeation

of the membrane to ions, thereby enhancing the membrane permeability, indicated as the increase of membrane conductance. The mean and maximum membrane conductance caused by Aβ1-42's damage was 266.41 $\pm$ 23.95 pS and 545.54 $\pm$ 33.45 pS (n = 138) respectively. As shown in Fig. 11.5, the mean and maximum values of Aβ-induced membrane conductance were significantly reduced to 175.76 $\pm$ 18.51 pS and 371.44 $\pm$ 31.30 pS (n = 113) in the presence of 0.8 mM LiCl (Tukey's test, $p < 0.01$). This demonstrated that Aβ-damaged membranes became less permeable to ions, suggesting that Aβ-induced membrane disruption was inhibited by the presence of 0.8 mM LiCl. This result aligns with the findings presented in Fig. 11.4, where the ion current flow was reduced in 0.8 mM LiCl. The reduction in both ion current (Fig. 11.4) and in membrane conductance in 0.8 mM LiCl (Fig. 11.5) indicates smaller sizes of transient pores caused by Aβ1-42 oligomers on the membrane. The regulation of LiCl 0.8 mM enables lipid membranes to be more durable against Aβ-induced damage, even though it cannot screen the Aβ's binding and destruction.

Compared to 0.8 mM LiCl, 4 mM LiCl also showed the potential to reduce Aβ-induced ion current (Fig. 11.4) and membrane conductance (Fig. 11.5) despite not being as effective as 0.8 mM. Recalled that 4 mM LiCl increases the intrinsic membrane conductance in the absence of Aβ1-42 oligomers in Fig. 11.2, it can contribute to the overall membrane conductance with the transient pores created by Aβ1-42 [94]. Clinical studies indicated that LiCl with serum concentration higher than 1.5 mM shows toxicity with different severity among patients in a dose-dependent manner [347, 346]. The overmodulation effect of LiCl at higher concentrations on lipid membranes could be one of the reasons leading to its severe toxicity in vivo.

Lithium has minimal effect on permanent membrane damage (Fig. 11.3), which was associated with creating ion channels, while transient pores (Fig. 11.5) are affected by LiCl at 0.8 mM. Considering that Li^+ has little effect on Aβ aggregation [348], we suggest that the protection role of Li^+ is mainly driven by its regulation of lipid membrane. Li^+ at 0.8 mM can adequately improve membrane fluidity, which enhances the membrane stability as the Aβ-induced damage occurs.

11.4 Conclusion

In this study, we explored the potential of lithium's protection effect on lipid membranes against Aβ-induced membrane damage by BLM electrophysiology. The ion current and conductance measured by BLM suggest the quality and permeability of artificial lipid membranes exposure to Aβ1-42 oligomers and lithium at a therapeutic level (0.8 mM) and toxic level (4 mM). Our results show that LiCl at 0.8 mM reduced the membrane permeability caused by Aβ1-42 oligomers-induced transient defects, implying the modulation of 0.8 mM LiCl to lipid membrane makes them more durable when exposed to oligomers. This suggests the membrane-targeted protection of lithium as a potential molecular mechanism for understanding the therapeutic function of lithium in AD.

Chapter 12

Conclusion and Future Work

12.0.1 Conclusion

Oligomeric amyloid-β (Aβ) proteins sourced from neuronal membranes pathogenically contribute to AD progression. Their disruption of membrane integrity is one of the prevalent mechanisms of their neurotoxicity, which can lead to cell apoptosis and neurodegeneration. The current therapeutic orientation focuses on developing anti-Aβ drug that aims to inhibit Aβ aggregation, remove Aβ aggregates and lower Aβ levels in brains. Even though some drugs exhibit successful effectiveness in alleviating cognition decline in patients, their severe and fatal side effects are still a concerning problem. On the other hand, low-level Aβ proteins benefit brain functions and activities, including synaptic plasticity and memory. This brings out the question of whether targeting Aβ is an optimal strategy for AD treatment, given that Aβ proteins can be harmful and beneficial to brains simultaneously. For this reason, I am exploring an alternative strategy with a less aggressive purpose. Instead of concentrating on Aβ itself, I investigate potential agents that may protect the lipid membrane, one of the main targets of toxic Aβ oligomers. The overall objective of this work is to study the impact of two membrane-active substances, trehalose and lithium, on lipid membranes and their potential for defending against Aβ toxicity on lipid membranes.

Before investigating trehalose and lithium, I studied the Aβ-membrane interactions

using membrane electrophysiology techniques. Previous studies reported various routes of Aβ oligomers damaging the membranes; however, it is unclear how these routes contribute to the final destruction extent of the lipid membrane. Hence, different Aβ-membrane interactions were classified and compared in Chapter 1. It was found that small Aβ1-42 oligomers prefer to form ion channels with a size similar to gramicidin channels, as opposed to other interacting routes.

Then, the influence of trehalose on lipids was studied on DPPC-POPC-cholesterol model lipid systems with Langmuir film and scanning probe microscopy techniques. It is found that trehalose can increase the fluidity of lipid monolayers and reduce the electric potential difference within lipid nanodomains, while these effects can be changed by the presence of NaCl. The coexistence of NaCl and trehalose changes the lipid distribution, further enhances the lipid fluidity and has an opposite effect on interdomain potential difference. This study revealed the regulation of trehalose on lipid properties and emphasized the modulating role of NaCl in a physiological environment.

Lateral studies investigated the role of trehalose in Aβ-membrane interactions. AFM images showed that Aβ insertion and induced pore formation appear on supported membranes with and without trehalose. Although membrane impairment caused by Aβ cannot be avoided, trehalose can reduce Aβ-induced membrane permeability by enhancing membrane stability, according to the results of BLM experiments. Additionally, LSPR results showed that 1) Membrane thickness is reduced by trehalose, implying trehalose's fluidization effect on lipid membranes. 2) trehalose at high concentrations can reduce the number of Aβ binding to lipid membranes. These findings suggest trehalose's regulation of membrane properties can protect membranes from Aβ destruction. Lastly, MTT cell studies indicated that the cell mortality rate caused by Aβ cytotoxicity is alleviated by trehalose, which is unique from other several sugars. These results supported the neuroprotection role of trehalose in AD.

Similarly, lithium's contribution to membrane properties were studied by scanning probe microscopy and Langmuir film techniques. Lithium at a low concentration (20 mM) can increase the interdomain electric potential difference, which can be attributed to the

electrostatic interaction between lithium ions and lipid headgroups. Whereas the potential difference was decreased in 150 mM KCl, 150 mM LiCl, and 20 mM LiCl + 130 mM LiCl, implying the screening effect of salts at high concentrations on lipid dipole potentials. Hence, the contribution of Li^+ to altering electrostatic properties in the physiological environment could be limited. However, Li^+ shows a pronounced effect on increasing membrane fluidity even in the presence of abundant K^+. This is attributed to their smaller size and stronger binding affinity than K^+, enabling deeper penetration into lipid hydrophilic regions. Finally, the BLM electrophysiology explores the effect of LiCl on Aβ-membrane interactions. The BLM results demonstrated that LiCl reduces ion current flow and membrane conductance due to Aβ-induced transient pore formation while it has little effect on Aβ ion channels.

In summary, all the results together exhibit the modulation of trehalose and lithium on membrane properties and confirm their membrane-targeted protection in AD. In addition, it emphasizes the crucial role of ions in the physiological environment. They influence the properties of biomolecules and the contribution of agents in biological systems but can be overlooked in research activities.

12.0.2 Future Work

This work in the thesis explores two membrane-active agents with model membranes via biophysical techniques. These agents showed potential protection in AD from a membrane perspective, but there is still a long way to go to verify the efficacy of candidates for developing drugs for clinical use and medication. In addition, more realistic aspects are worth considering in further studies as follows:

- More complex membrane systems that mimic realistic cellular membranes, or real membranes extracted from cells.
- The metabolism of trehalose in the neuronal system. It is still unclear whether trehalose can be hydrolyzed by neurons.

- Cell and animal studies for drug development.
- Drug delivery. It is unknown whether trehalose can be transported through the blood-brain barrier.
- The roles of ions and water in scientific research. They could be one of the reasons explaining the discrepancy in results between studies (such as experiments vs simulation, vitro vs vivo).

References

[1] Z. Breijyeh and R. Karaman. Comprehensive review on Alzheimer's disease: Causes and treatment. *Molecules*, 25(24):5789, 2020.

[2] J. A. Hardy and G. A. Higgins. Alzheimer's disease: The amyloid cascade hypothesis. *Science*, 256(5054):184–185, 1992.

[3] G. Thinakaran and E. H. Koo. Amyloid precursor protein trafficking, processing, and function. *Journal of Biological Chemistry*, 283(44):29615–9, 2008.

[4] M. Citron, T. S. Diehl, G. Gordon, A. L. Biere, P. Seubert, and D. J. Selkoe. Evidence that the 42- and 40-amino acid forms of amyloid beta protein are generated from the beta-amyloid precursor protein by different protease activities. *Proceedings of the National Academy of Sciences*, 93(23):13170–5, 1996.

[5] K. N. Dahlgren, A. M. Manelli, W. B. Stine, L. K. Baker, G. A. Krafft, and M. J. LaDu. Oligomeric and fibrillar species of amyloid-β peptides differentially affect neuronal viability. *Journal of Biological Chemistry*, 277(35):32046–32053, 2002.

[6] A. M. Klein, N. W. Kowall, and R. J. Ferrante. Neurotoxicity and oxidative damage of beta amyloid 1-42 versus beta amyloid 1-40 in the mouse cerebral cortex. *Annals of the New York Academy of Sciences*, 893:314–20, 1999.

[7] I. Benilova, E. Karran, and B. De Strooper. The toxic Aβ oligomer and Alzheimer's disease: an emperor in need of clothes. *Nature Neuroscience*, 15(3):349–57, 2012.

[8] F. Bao, L. Wicklund, P. N. Lacor, W. L. Klein, A. Nordberg, and A. Marutle. Different β-amyloid oligomer assemblies in Alzheimer brains correlate with age of disease onset and impaired cholinergic activity. *Neurobiology of Aging*, 33(4):825.e1–13, 2012.

[9] T. J. Esparza, H. Zhao, J. R. Cirrito, N. J. Cairns, R. J. Bateman, D. M. Holtzman, and D. L. Brody. Amyloid-beta oligomerization in Alzheimer dementia versus high-pathology controls. *Annals of Neurology*, 73(1):104–119, 2013.

[10] H. Zhang, X. Jiang, L. Ma, W. Wei, Z. Li, S. Chang, J. Wen, J. Sun, and H. Li. Role of Aβ in Alzheimer's-related synaptic dysfunction. *Frontiers in Cell and Developmental Biology*, 10:964075, 2022.

[11] C. Cheignon, M. Tomas, D. Bonnefont-Rousselot, P. Faller, C. Hureau, and F. Collin. Oxidative stress and the amyloid beta peptide in Alzheimer's disease. *Redox Biology*, 14:450–464, 2018.

[12] R. Kayed and C. A. Lasagna-Reeves. Molecular mechanisms of amyloid oligomers toxicity. *Journal of Alzheimer's Disease*, 33 Suppl 1:S67–78, 2013.

[13] E. M. Snyder, Y. Nong, C. G. Almeida, S. Paul, T. Moran, E. Y. Choi, A. C. Nairn, M. W. Salter, P. J. Lombroso, G. K. Gouras, and P. Greengard. Regulation of NMDA receptor trafficking by amyloid-beta. *Nature Neuroscience*, 8(8):1051–8, 2005.

[14] G. M. Shankar, B. L. Bloodgood, M. Townsend, D. M. Walsh, D. J. Selkoe, and B. L. Sabatini. Natural oligomers of the Alzheimer amyloid-beta protein induce reversible synapse loss by modulating an NMDA-type glutamate receptor-dependent signaling pathway. *Journal of Neuroscience*, 27(11):2866–75, 2007.

[15] W. Q. Zhao, F. G. De Felice, S. Fernandez, H. Chen, M. P. Lambert, M. J. Quon, G. A. Krafft, and W. L. Klein. Amyloid beta oligomers induce impairment of neuronal insulin receptors. *The FASEB Journal*, 22(1):246–60, 2008.

[16] J. Laurén, D. A. Gimbel, H. B. Nygaard, J. W. Gilbert, and S. M. Strittmatter. Cellular prion protein mediates impairment of synaptic plasticity by amyloid-beta oligomers. *Nature*, 457(7233):1128–32, 2009.

[17] E. Alberdi, M. V. Sánchez-Gómez, F. Cavaliere, A. Pérez-Samartín, J. L. Zugaza, R. Trullas, M. Domercq, and C. Matute. Amyloid beta oligomers induce Ca^{2+} dysregulation and neuronal death through activation of ionotropic glutamate receptors. *Cell Calcium*, 47(3):264–72, 2010.

[18] M. H. Magdesian, M. M. V. F. Carvalho, F. A. Mendes, L. M. Saraiva, M. A. Juliano, L. Juliano, J. Garcia-Abreu, and S. T. Ferreira. Amyloid-β binds to the extracellular cysteine-rich domain of frizzled and inhibits wnt/β-catenin signaling. *Journal of Biological Chemistry*, 283(14):9359–9368, 2008.

[19] M. P. Mattson, B. Cheng, D. Davis, K. Bryant, I. Lieberburg, and R. E. Rydel. beta-amyloid peptides destabilize calcium homeostasis and render human cortical neurons vulnerable to excitotoxicity. *Journal of Neuroscience*, 12(2):376–89, 1992.

[20] David C. Bode, Mark D. Baker, and John H. Viles. Ion channel formation by amyloid-β42 oligomers but not amyloid-β40 in cellular membranes. *Journal of Biological Chemistry*, 292(4):1404–1413, 2017.

[21] D. C. Bode, M. Freeley, J. Nield, M. Palma, and J. H. Viles. Amyloid-β oligomers have a profound detergent-like effect on lipid membrane bilayers, imaged by atomic force and electron microscopy. *Journal of Biological Chemistry*, 294(19):7566–7572, 2019.

[22] Z. Niu, Z. Zhang, W. Zhao, and J. Yang. Interactions between amyloid β peptide and lipid membranes. *Biochimica et Biophysica Acta (BBA) - Biomembranes*, 1860(9):1663–1669, 2018.

[23] N. Arispe, E. Rojas, and H. B. Pollard. Alzheimer disease amyloid beta protein forms calcium channels in bilayer membranes: blockade by tromethamine and aluminum. *Proceedings of the National Academy of Sciences*, 90(2):567–571, 1993.

[24] R. Lal, H. Lin, and A. P. Quist. Amyloid beta ion channel: 3D structure and relevance to amyloid channel paradigm. *Biochimica et Biophysica Acta (BBA) - Biomembranes*, 1768(8):1966–1975, 2007.

[25] S. K. Rhee, A. P. Quist, and R. Lal. Amyloid beta protein-(1-42) forms calcium-permeable, Zn^{2+}-sensitive channel. *Journal of Biological Chemistry*, 273(22):13379–82, 1998.

[26] C. M. Vander Zanden, L. Wampler, I. Bowers, E. B. Watkins, J. Majewski, and E. Y. Chi. Fibrillar and nonfibrillar amyloid beta structures drive two modes of membrane-mediated toxicity. *Langmuir*, 35(48):16024–16036, 2019.

[27] J. Lee, Y. H. Kim, F. T. Arce, A. L. Gillman, H. Jang, B. L. Kagan, R. Nussinov, J. Yang, and R. Lal. Amyloid β ion channels in a membrane comprising brain total lipid extracts. *ACS Chemical Neuroscience*, 8(6):1348–1357, 2017.

[28] E. Drolle, A. Negoda, K. Hammond, E. Pavlov, and Z. Leonenko. Changes in lipid membranes may trigger amyloid toxicity in Alzheimer's disease. *PLOS One*, 12(8):e0182194, 2017.

[29] R. Capone, F. G. Quiroz, P. Prangkio, I. Saluja, A. M. Sauer, M. R. Bautista, R. S. Turner, J. Yang, and M. Mayer. Amyloid-beta-induced ion flux in artificial lipid bilayers and neuronal cells: resolving a controversy. *Neurotoxicity Research*, 16(1):1–13, 2009.

[30] C. M. Rodrigues, S. Solá, M. A. Brito, C. D. Brondino, D. Brites, and J. J. Moura. Amyloid beta-peptide disrupts mitochondrial membrane lipid and protein structure: protective role of tauroursodeoxycholate. *Biochemical and Biophysical Research Communications*, 281(2):468–74, 2001.

[31] P. T. Wong, J. A. Schauerte, K. C. Wisser, H. Ding, E. L. Lee, D. G. Steel, and A. Gafni. Amyloid-β membrane binding and permeabilization are distinct processes influenced separately by membrane charge and fluidity. *Journal of Molecular Biology*, 386(1):81–96, 2009.

[32] E. Y. Chi, C. Ege, A. Winans, J. Majewski, G. Wu, K. Kjaer, and K. Y. Lee. Lipid membrane templates the ordering and induces the fibrillogenesis of Alzheimer's disease amyloid-beta peptide. *Proteins*, 72(1):1–24, 2008.

[33] Y. Hirakura, M-C. Lin, and B. L. Kagan. Alzheimer amyloid aβ1–42 channels: Effects of solvent, pH, and congo red. *Journal of Neuroscience Research*, 57(4):458–466, 1999.

[34] O. Ivankov, D. R. Badreeva, E. V. Ermakova, T. Kondela, T. N. Murugova, and N. Kučerka. Anionic lipids modulate little the reorganization effect of amyloid-beta peptides on membranes. *General Physiology and Biophysics*, 42(1):59–66, 2023.

[35] N. A. Avdulov, S. V. Chochina, U. Igbavboa, C. S. Warden, A. V. Vassiliev, and W. G. Wood. Lipid binding to amyloid β-peptide aggregates: Preferential binding of cholesterol as compared with phosphatidylcholine and fatty acids. *Journal of Neurochemistry*, 69(4):1746–1752, 1997.

[36] S. Banerjee, M. Hashemi, K. Zagorski, and Y. L. Lyubchenko. Cholesterol in membranes facilitates aggregation of amyloid β protein at physiologically relevant concentrations. *ACS Chemical Neuroscience*, 12(3):506–516, 2021.

[37] G. Hussain, J. Wang, A. Rasul, H. Anwar, A. Imran, M. Qasim, S. Zafar, S. K. S. Kamran, A. Razzaq, N. Aziz, W. Ahmad, A. Shabbir, J. Iqbal, S. M. Baig, and T. Sun. Role of cholesterol and sphingolipids in brain development and neurological diseases. *Lipids in Health and Disease*, 18(1):26, 2019.

[38] J. W. Pettegrew, K. Panchalingam, R. L. Hamilton, and R. J. McClure. Brain membrane phospholipid alterations in Alzheimer's disease. *Neurochemical Research*, 26(7):771–782, 2001.

[39] W. Lukiw. Alzheimer's disease (AD) as a disorder of the plasma membrane. *Frontiers in Physiology*, 4, 2013.

[40] H. Chew, V. A. Solomon, and A. N. Fonteh. Involvement of lipids in Alzheimer's disease pathology and potential therapies. *Frontiers in Physiology*, 11:598, 2020.

[41] V. Rudajev and J. Novotny. The role of lipid environment in ganglioside GM1-induced amyloid β aggregation. *Membranes*, 10(9):226, 2020.

[42] S. C. Cunnane, J. A. Schneider, C. Tangney, J. Tremblay-Mercier, M. Fortier, D. A. Bennett, and M. C. Morris. Plasma and brain fatty acid profiles in mild cognitive impairment and Alzheimer's disease. *Journal of Alzheimer's Disease*, 29(3):691–7, 2012.

[43] S. G. Snowden, A. A. Ebshiana, A. Hye, Y. An, O. Pletnikova, R. O'Brien, J. Troncoso, C. Legido-Quigley, and M. Thambisetty. Association between fatty acid metabolism in the brain and Alzheimer disease neuropathology and cognitive performance: A nontargeted metabolomic study. *PLOS Medicine*, 14(3):e1002266, 2017.

[44] M. Belkouch, M. Hachem, A. Elgot, A. Lo Van, M. Picq, M. Guichardant, M. Lagarde, and N. Bernoud-Hubac. The pleiotropic effects of omega-3 docosahexaenoic acid on the hallmarks of Alzheimer's disease. *The Journal of Nutritional Biochemistry*, 38:1–11, 2016.

[45] X. He, Y. Huang, B. Li, C. X. Gong, and E. H. Schuchman. Deregulation of sphingolipid metabolism in Alzheimer's disease. *Neurobiology of Aging*, 31(3):398–408, 2010.

[46] M. Kosicek, H. Zetterberg, N. Andreasen, J. Peter-Katalinic, and S. Hecimovic. Elevated cerebrospinal fluid sphingomyelin levels in prodromal Alzheimer's disease. *Neuroscience Letters*, 516(2):302–5, 2012.

[47] R. G. Cutler, J. Kelly, K. Storie, W. A. Pedersen, A. Tammara, K. Hatanpaa, J. C. Troncoso, and M. P. Mattson. Involvement of oxidative stress-induced abnormalities in ceramide and cholesterol metabolism in brain aging and Alzheimer's disease. *Proceedings of the National Academy of Sciences*, 101(7):2070–2075, 2004.

[48] D. Otzen and R. Riek. Functional amyloids. *Cold Spring Harbor Perspectives in Biology*, 11(12), 2019.

[49] U. C. Müller, T. Deller, and M. Korte. Not just amyloid: physiological functions of the amyloid precursor protein family. *Nature Reviews Neuroscience*, 18(5):281–298, 2017.

[50] M. L. Gosztyla, H. M. Brothers, and S. R. Robinson. Alzheimer's amyloid-β is an antimicrobial peptide: A review of the evidence. *Journal of Alzheimer's Disease*, 62:1495–1506, 2018.

[51] D. M. Fowler, A. V. Koulov, C. Alory-Jost, M. S. Marks, W. E. Balch, and J. W. Kelly. Functional amyloid formation wicitron mammalian tissue. *PLOS Biology*, 4(1):e6, 2006.

[52] S. K. Maji, M. H. Perrin, M. R. Sawaya, S. Jessberger, K. Vadodaria, R. A. Rissman, P. S. Singru, K. P. Nilsson, R. Simon, D. Schubert, D. Eisenberg, J. Rivier, P. Sawchenko, W. Vale, and R. Riek. Functional amyloids as natural storage of peptide hormones in pituitary secretory granules. *Science*, 325(5938):328–32, 2009.

[53] G. R. Dawson, G. R. Seabrook, H. Zheng, D. W. Smith, S. Graham, G. O'Dowd, B. J. Bowery, S. Boyce, M. E. Trumbauer, H. Y. Chen, L. H. Van der Ploeg, and D. J. Sirinathsinghji. Age-related cognitive deficits, impaired long-term potentiation and reduction in synaptic marker density in mice lacking the beta-amyloid precursor protein. *Neuroscience*, 90(1):1–13, 1999.

[54] M. S. Parihar and G. J. Brewer. Amyloid-β as a modulator of synaptic plasticity. *Journal of Alzheimer's Disease*, 22(3):741–63, 2010.

[55] S. J. Soscia, J. E. Kirby, K. J. Washicosky, S. M. Tucker, M. Ingelsson, B. Hyman, M. A. Burton, L. E. Goldstein, S. Duong, R. E. Tanzi, and R. D. Moir. The Alzheimer's disease-associated amyloid beta-protein is an antimicrobial peptide. *PLOS One*, 5(3):e9505, 2010.

[56] B. L. Kagan, H. Jang, R. Capone, F. Teran Arce, S. Ramachandran, R. Lal, and R. Nussinov. Antimicrobial properties of amyloid peptides. *Molecular Pharmaceutics*, 9(4):708–717, 2012.

[57] L. Steinstraesser, R. D. Klein, A. Aminlari, M-H. Fan, V. Khilanani, D. G. Remick, G. L. Su, and S. C. Wang. Protegrin-1 enhances bacterial killing in thermally injured skin. *Critical Care Medicine*, 29(7), 2001.

[58] B. Bechinger and K. Lohner. Detergent-like actions of linear amphipathic cationic antimicrobial peptides. *Biochimica et Biophysica Acta (BBA) - Biomembranes*, 1758(9):1529–1539, 2006.

[59] L-K. Huang, S-P. Chao, and C-J. Hu. Clinical trials of new drugs for Alzheimer disease. *Journal of Biomedical Science*, 27(1):18, 2020.

[60] S. Salomone, F. Caraci, G. M. Leggio, J. Fedotova, and F. Drago. New pharmacological strategies for treatment of Alzheimer's disease: focus on disease modifying drugs. *British Journal of Clinical Pharmacology*, 73(4):504–517, 2012.

[61] W. P. Chang, X. Huang, D. Downs, J. R. Cirrito, G. Koelsch, D. M. Holtzman, A. K. Ghosh, and J. Tang. Beta-secretase inhibitor GRL-8234 rescues age-related cognitive decline in APP transgenic mice. *The FASEB Journal*, 25(2):775–84, 2011.

[62] J. Shen and 3rd Kelleher, R. J. The presenilin hypothesis of Alzheimer's disease: evidence for a loss-of-function pathogenic mechanism. *Proceedings of the National Academy of Sciences*, 104(2):403–9, 2007.

[63] R. C. Green, L. S. Schneider, D. A. Amato, A. P. Beelen, G. Wilcock, E. A. Swabb, and K. H. Zavitz. Effect of tarenflurbil on cognitive decline and activities of daily living in patients with mild Alzheimer disease: a randomized controlled trial. *JAMA*, 302(23):2557–64, 2009.

[64] F. Gervais, J. Paquette, C. Morissette, P. Krzywkowski, M. Yu, M. Azzi, D. Lacombe, X. Kong, A. Aman, J. Laurin, W. A. Szarek, and P. Tremblay. Targeting soluble Aβ

peptide with tramiprosate for the treatment of brain amyloidosis. *Neurobiology of Aging*, 28(4):537–547, 2007.

[65] S. Gauthier, P. S. Aisen, S. H. Ferris, D. Saumier, A. Duong, D. Haine, D. Garceau, J. Suhy, J. Oh, W. Lau, and J. Sampalis. Effect of tramiprosate in patients with mild-to-moderate Alzheimer's disease: exploratory analyses of the MRI sub-group of the Alphase study. *The Journal of Nutrition, Health and Aging*, 13(6):550–7, 2009.

[66] N. G. Faux, C. W. Ritchie, A. Gunn, A. Rembach, A. Tsatsanis, J. Bedo, J. Harrison, L. Lannfelt, K. Blennow, H. Zetterberg, M. Ingelsson, C. L. Masters, R. E. Tanzi, J. L. Cummings, C. M. Herd, and A. I. Bush. PBT2 rapidly improves cognition in Alzheimer's disease: additional phase ii analyses. *Journal of Alzheimer's Disease*, 20(2):509–16, 2010.

[67] J. Cummings, G. Lee, P. Nahed, M. E. Z. N. Kambar, K. Zhong, J. Fonseca, and K. Taghva. Alzheimer's disease drug development pipeline: 2022. *Alzheimer's & Dementia: Translational Research & Clinical Interventions*, 8(1):e12295, 2022.

[68] J. Hey, S. Abushakra, K. Blennow, P. Scheltens, J. Hort, K. Sheardova, N. Prins, S. Rutgers, P. Dautzenberg, L. Pazdera, P. Kesslak, R. Mandelbaum, A. Power, and M. Tolar. Effects of ALZ-801, an oral amyloid oligomer inhibitor, on biomarkers of Alzheimer's disease (AD): 12-month results of phase 2 biomarker study in early AD (s26.007). *Neurology*, 100(17 Supplement 2):3243, 2023.

[69] F. Mantile and A. Prisco. Vaccination against β-amyloid as a strategy for the prevention of Alzheimer's disease. *Biology (Basel)*, 9(12), 2020.

[70] R. Perneczky, F. Jessen, T. Grimmer, J. Levin, A. Flöel, O. Peters, and L. Froelich. Anti-amyloid antibody therapies in Alzheimer's disease. *Brain*, 146(3):842–849, 2023.

[71] A. Rahman, M. A. Hossen, M. F. I. Chowdhury, S. Bari, N. Tamanna, S. S. Sultana, S. N. Haque, A. Al Masud, and K. M. Saif-Ur-Rahman. Aducanumab for the treatment of Alzheimer's disease: a systematic review. *Psychogeriatrics*, 23(3):512–522, 2023.

[72] S. Salloway, S. Chalkias, F. Barkhof, P. Burkett, J. Barakos, D. Purcell, J. Suhy, F. Forrestal, Y. Tian, K. Umans, G. Wang, P. Singhal, S. Budd Haeberlein, and K. Smirnakis. Amyloid-related imaging abnormalities in 2 phase 3 studies evaluating aducanumab in patients with early Alzheimer disease. *JAMA Neurology*, 79(1):13–21, 2022.

[73] J. Cummings. Anti-amyloid monoclonal antibodies are transformative treatments that redefine Alzheimer's disease therapeutics. *Drugs*, 83(7):569–576, 2023.

[74] C. H. van Dyck, C. J. Swanson, P. Aisen, R. J. Bateman, C. Chen, M. Gee, M. Kanekiyo, D. Li, L. Reyderman, S. Cohen, L. Froelich, S. Katayama, M. Sabbagh, B. Vellas, D. Watson, S. Dhadda, M. Irizarry, L. D. Kramer, and T. Iwatsubo. Lecanemab in early Alzheimer's disease. *New England Journal of Medicine*, 388(1):9–21, 2022.

[75] M. Pappolla, P. Bozner, C. Soto, H. Shao, N. K. Robakis, M. Zagorski, B. Frangione, and J. Ghiso. Inhibition of Alzheimer beta-fibrillogenesis by melatonin. *Journal of Biological Chemistry*, 273(13):7185–8, 1998.

[76] T. Murugova, O. Ivankov, E. Ermakova, T. Kondela, P. Hrubovčák, V. Skoi, A. Kuklin, and N. Kučerka. Structural changes introduced by cholesterol and melatonin to the model membranes mimicking preclinical conformational diseases. *General Physiology and Biophysics*, 39(2):135–144, 2020.

[77] E. Drolle, N. Kučerka, M. I. Hoopes, Y. Choi, J. Katsaras, M. Karttunen, and Z. Leonenko. Effect of melatonin and cholesterol on the structure of DOPC and DPPC membranes. *Biochimica et Biophysica Acta (BBA) - Biomembranes*, 1828(9):2247–2254, 2013.

[78] N. Mei, M. Robinson, J. H. Davis, and Z. Leonenko. Melatonin alters fluid phase coexistence in POPC/DPPC/cholesterol membranes. *Biophysical Journal*, 119(12):2391–2402, 2020.

[79] H. Dies, L. Toppozini, and M. C. Rheinstädter. The interaction between amyloid-β peptides and anionic lipid membranes containing cholesterol and melatonin. *PLOS One*, 9(6):e99124, 2014.

[80] J. J. García, R. J. Reiter, J. M. Guerrero, G. Escames, B. P. Yu, C. S. Oh, and A. Muñoz-Hoyos. Melatonin prevents changes in microsomal membrane fluidity during induced lipid peroxidation. *FEBS Letters*, 408(3):297–300, 1997.

[81] A. Thapa, B. C. Vernon, K. De la Peña, G. Soliz, H. A. Moreno, G. P. López, and E. Y. Chi. Membrane-mediated neuroprotection by curcumin from amyloid-β-peptide-induced toxicity. *Langmuir*, 29(37):11713–11723, 2013.

[82] A. Khondker, R. J. Alsop, S. Himbert, J. Tang, A-C. Shi, A. P. Hitchcock, and M. C. Rheinstädter. Membrane-modulating drugs can affect the size of amyloid-β25–35 aggregates in anionic membranes. *Scientific Reports*, 8(1):12367, 2018.

[83] K. S. Moore, S. Wehrli, H. Roder, M. Rogers, J. N. Forrest, D. McCrimmon, and M Zasloff. Squalamine: an aminosterol antibiotic from the shark. *Proceedings of the National Academy of Sciences*, 90(4):1354–1358, 1993.

[84] S. Errico, G. Lucchesi, D. Odino, S. Muscat, C. Capitini, C. Bugelli, C. Canale, R. Ferrando, G. Grasso, D. Barbut, M. Calamai, A. Danani, M. Zasloff, A. Relini, G. Caminati, M. Vendruscolo, and F. Chiti. Making biological membrane resistant to the toxicity of misfolded protein oligomers: a lesson from trodusquemine. *Nanoscale*, 12(44):22596–22614, 2020.

[85] R. Limbocker, B. Mannini, F. S. Ruggeri, R. Cascella, C. K. Xu, M. Perni, S. Chia, S. W. Chen, J. Habchi, A. Bigi, R. P. Kreiser, A. K. Wright, J. A. Albright, T. Kartanas, J. R. Kumita, N. Cremades, M. Zasloff, C. Cecchi, T. P. J. Knowles, F. Chiti, M. Vendruscolo, and C. M. Dobson. Trodusquemine displaces protein misfolded oligomers from cell membranes and abrogates their cytotoxicity through a generic mechanism. *Communications Biology*, 3(1):435, 2020.

[86] R. Limbocker, S. Chia, F. S. Ruggeri, M. Perni, R. Cascella, G. T. Heller, G. Meisl, B. Mannini, J. Habchi, T. C. T. Michaels, P. K. Challa, M. Ahn, S. T. Casford, N. Fernando, C. K. Xu, N. D. Kloss, S. I. A. Cohen, J. R. Kumita, C. Cecchi, M. Zasloff, S. Linse, T. P. J. Knowles, F. Chiti, M. Vendruscolo, and C. M. Dobson. Trodusquemine enhances Aβ42 aggregation but suppresses its toxicity by displacing oligomers from cell membranes. *Nature Communications*, 10(1):225, 2019.

[87] R. Limbocker, R. Staats, S. Chia, F. S. Ruggeri, B. Mannini, C. K. Xu, M. Perni, R. Cascella, A. Bigi, L. R. Sasser, N. R. Block, A. K. Wright, R. P. Kreiser, E. T. Custy, G. Meisl, S. Errico, J. Habchi, P. Flagmeier, T. Kartanas, J. E. Hollows, L. T. Nguyen, K. LeForte, D. Barbut, J. R. Kumita, C. Cecchi, M. Zasloff, T. P. J. Knowles, C. M. Dobson, F. Chiti, and M. Vendruscolo. Squalamine and its derivatives modulate the aggregation of amyloid-β and α-synuclein and suppress the toxicity of their oligomers. *Frontiers in Neuroscience*, 15:680026, 2021.

[88] S. Errico, G. Lucchesi, D. Odino, R. Osman, Enass Y.and Cascella, L. Neri, C. Capitini, M. Calamai, F. Bemporad, C. Cecchi, W. A. Kinney, D. Barbut, A. Relini, C. Canale, G. Caminati, R. Limbocker, M. Vendruscolo, M. Zasloff, and F. Chiti. Quantitative attribution of the protective effects of aminosterols against protein aggregates to their chemical structures and ability to modulate biological membranes. *Journal of Medicinal Chemistry*, 66(14):9519–9536, 2023.

[89] M. Torres, S. L. Price, M. A. Fiol-deRoque, A. Marcilla-Etxenike, H. Ahyayauch, G. Barceló-Coblijn, S. Terés, L. Katsouri, M. Ordinas, D. J. López, M. Ibarguren, F. M. Goñi, X. Busquets, J. Vitorica, M. Sastre, and P. V. Escribá. Membrane lipid modifications and therapeutic effects mediated by hydroxydocosahexaenoic acid on Alzheimer's disease. *Biochimica et Biophysica Acta (BBA) - Biomembranes*, 1838(6):1680–1692, 2014.

[90] D. Mrdenovic, P. Zarzycki, M. Majewska, I. S. Pieta, R. Nowakowski, W. Kutner, J. Lipkowski, and P. Pieta. Inhibition of amyloid β-induced lipid membrane perme-

ation and amyloid β aggregation by K162. *ACS Chemical Neuroscience*, 12(3):531–541, 2021.

[91] A. Camilleri, C. Zarb, M. Caruana, U. Ostermeier, S. Ghio, T. Högen, F. Schmidt, A. Giese, and N. Vassallo. Mitochondrial membrane permeabilisation by amyloid aggregates and protection by polyphenols. *Biochimica et Biophysica Acta (BBA) - Biomembranes*, 1828(11):2532–2543, 2013.

[92] M. Winterhalter. Black lipid membranes. *Current Opinion in Colloid & Interface Science*, 5(3):250–255, 2000.

[93] N. Saigo, K. Izumi, and R. Kawano. Electrophysiological analysis of antimicrobial peptides in diverse species. *ACS Omega*, 4(8):13124–13130, 2019.

[94] K. A. Zecchi and T. Heimburg. Non-linear conductance, rectification, and mechanosensitive channel formation of lipid membranes. *Frontiers in Cell and Developmental Biology*, 8:592520, 2020.

[95] J. L. Hammond, N. Bhalla, S. D. Rafiee, and P. Estrela. Localized surface plasmon resonance as a biosensing platform for developing countries. *Biosensors (Basel)*, 4(2):172–88, 2014.

[96] K. A. Willets and R. P. Van Duyne. Localized surface plasmon resonance spectroscopy and sensing. *Annual Review of Physical Chemistry*, 58:267–97, 2007.

[97] D. A. Stuart, A. J. Haes, C. R. Yonzon, E. M. Hicks, and R. P. Van Duyne. Biological applications of localised surface plasmonic phenomenae. *IEE Proceedings - Nanobiotechnology*, 152(1):13–32, 2005.

[98] J. Svirelis, J. Andersson, A. Stradner, and A. Dahlin. Accurate correction of the "bulk response" in surface plasmon resonance sensing provides new insights on interactions involving lysozyme and poly(ethylene glycol). *ACS Sensors*, 7(4):1175–1182, 2022.

[99] K. M. Mayer and J. H. Hafner. Localized surface plasmon resonance sensors. *Chemical Reviews*, 111(6):3828–3857, 2011.

[100] V. P. Zhdanov. Basics of the LSPR sensors for soft matter at interfaces. *Plasmonics*, 18(3):971–982, 2023.

[101] L. S. Jung, C. T. Campbell, T. M. Chinowsky, M. N. Mar, and S. S. Yee. Quantitative interpretation of the response of surface plasmon resonance sensors to adsorbed films. *Langmuir*, 14(19):5636–5648, 1998.

[102] B. E. Rapp. Chapter 22 - measuring surface tension and free surface energy. In *Microfluidics: Modelling, Mechanics and Mathematics*, pages 453–465. Elsevier, Oxford, 2017.

[103] G. Ma and H. C. Allen. DPPC Langmuir monolayer at the air-water interface: Probing the tail and head groups by vibrational sum frequency generation spectroscopy. *Langmuir*, 22(12):5341–5349, 2006.

[104] S. Akamatsu and F. Rondelez. Fluorescence microscopy evidence for two different LE-LC phase transitions in Langmuir monolayers of fatty acids. *Journal de Physique II*, 1(10):1309–1322, 1991.

[105] B. Krajewska, P. Wydro, and A. Jańczyk. Probing the modes of antibacterial activity of chitosan. effects of pH and molecular weight on chitosan interactions with membrane lipids in Langmuir films. *Biomacromolecules*, 12(11):4144–4152, 2011.

[106] J. T. Davies. *Interfacial Phenomena*. Elsevier, 2012.

[107] D. Correa, E. Medeiros, J. Oliveira, L. Paterno, and L. Mattoso. Nanostructured conjugated polymers in chemical sensors: Synthesis, properties and applications. *Journal of Nanoscience and Nanotechnology*, 14, 2014.

[108] K. Kjaer, J. Als-Nielsen, C. A. Helm, L. A. Laxhuber, and H. Möhwald. Ordering in lipid monolayers studied by synchrotron X-ray diffraction and fluorescence microscopy. *Physical Review Letters*, 58(21):2224–2227, 1987.

[109] P. Dutta, J. B. Peng, B. Lin, J. B. Ketterson, M. Prakash, P. Georgopoulos, and S. Ehrlich. X-ray diffraction studies of organic monolayers on the surface of water. *Physical Review Letters*, 58(21):2228–2231, 1987.

[110] L. F. Chi, M. Anders, H. Fuchs, R. R. Johnston, and H. Ringsdorf. Domain structures in Langmuir-Blodgett films investigated by atomic force microscopy. *Science*, 259(5092):213–216, 1993.

[111] R. K. Gupta and K. A. Suresh. AFM studies on Langmuir-Blodgett films of cholesterol. *The European Physical Journal E*, 14(1):35–42, 2004.

[112] S. Hénon and J. Meunier. Microscope at the brewster angle: Direct observation of first-order phase transitions in monolayers. *Review of Scientific Instruments*, 62(4):936–939, 1991.

[113] JPK. NanoWizard ® AFM Handbook 6.0. 2017.

[114] P. J. de Pablo. Introduction to atomic force microscopy. In *Single Molecule Analysis: Methods and Protocols*, pages 197–212. Humana Press, Totowa, NJ, 2011.

[115] H. Hölscher, W. Allers, U. D. Schwarz, A. Schwarz, and R. Wiesendanger. Interpretation of "true atomic resolution" images of graphite (0001) in noncontact atomic force microscopy. *Physical Review B*, 62(11):6967–6970, 2000.

[116] S Maghsoudy-Louyeh, M Kropf, and BR Tittmann. Review of progress in atomic force microscopy. *The Open Neuroimaging Journal*, 12(1), 2018.

[117] W. Melitz, J. Shen, A.C. Kummel, and S. Lee. Kelvin probe force microscopy and its application. *Surface Science Reports*, 66(1):1–27, 2011.

[118] J. Hölzl and F. K. Schulte. Work function of metals. In *Solid Surface Physics*, pages 1–150. Springer Berlin Heidelberg, 1979.

[119] V. Vogel and D. Möbius. Local surface potentials and electric dipole moments of lipid monolayers: Contributions of the water/lipid and the lipid/air interfaces. *Journal of Colloid and Interface Science*, 126(2):408–420, 1988.

[120] M. Ghasemi, T. Turnbull, S. Sebastian, and I. Kempson. The MTT assay: Utility, limitations, pitfalls, and interpretation in bulk and single-cell analysis. *International Journal of Molecular Sciences*, 22(23), 2021.

[121] M. V. Berridge, P. M. Herst, and A. S. Tan. Tetrazolium dyes as tools in cell biology: new insights into their cellular reduction. *Biotechnology Annual Review*, 11:127–52, 2005.

[122] J. C. Stockert, R. W. Horobin, L. L. Colombo, and A. Blázquez-Castro. Tetrazolium salts and formazan products in cell biology: Viability assessment, fluorescence imaging, and labeling perspectives. *Acta Histochemica*, 120(3):159–167, 2018.

[123] V. Kuete, O. Karaosmanoğlu, and H. Sivas. Chapter 10 - anticancer activities of african medicinal spices and vegetables. In *Medicinal Spices and Vegetables from Africa*, pages 271–297. Academic Press, 2017.

[124] A. B. Richards, S. Krakowka, L. B. Dexter, H. Schmid, A. P. M. Wolterbeek, D. H. Waalkens-Berendsen, A. Shigoyuki, and M. Kurimoto. Trehalose: a review of properties, history of use and human tolerance, and results of multiple safety studies. *Food and Chemical Toxicology*, 40(7):871–898, 2002.

[125] A. B. Pupyshev, T. P. Klyushnik, A. A. Akopyan, S. K. Singh, and M. A. Tikhonova. Disaccharide trehalose in experimental therapies for neurodegenerative disorders: Molecular targets and translational potential. *Pharmacological Research*, 183:106373, 2022.

[126] M. Khalifeh, G. E. Barreto, and A. Sahebkar. Trehalose as a promising therapeutic candidate for the treatment of Parkinson's disease. *British Journal of Pharmacology*, 176(9):1173–1189, 2019.

[127] S. H. Khan and R. Kumar. Trehalose induced conformational changes in the amyloid-β peptide. *Pathology - Research and Practice*, 213(6):643–648, 2017.

[128] Y-S. Yoon, E-D. Cho, W. Jung Ahn, K. Won Lee, S-J. Lee, and H-J. Lee. Is trehalose an autophagic inducer? Unraveling the roles of non-reducing disaccharides on autophagic flux and alpha-synuclein aggregation. *Cell Death & Disease*, 8(10):e3091–e3091, 2017.

[129] N. T. Tien, I. Karaca, I. Y. Tamboli, and J. Walter. Trehalose alters subcellular trafficking and the metabolism of the Alzheimer-associated amyloid precursor protein. *Journal of Biological Chemistry*, 291(20):10528–10540, 2016.

[130] C. S. Pereira, R. D. Lins, I. Chandrasekhar, L. C. G. Freitas, and P. H. Hünenberger. Interaction of the disaccharide trehalose with a phospholipid bilayer: A molecular dynamics study. *Biophysical Journal*, 86(4):2273–2285, 2004.

[131] M. A. Villarreal, S. B. Díaz, E. A. Disalvo, and G. G. Montich. Molecular dynamics simulation study of the interaction of trehalose with lipid membranes. *Langmuir*, 20(18):7844–7851, 2004.

[132] A. Skibinsky, R. M. Venable, and R. W. Pastor. A molecular dynamics study of the response of lipid bilayers and monolayers to trehalose. *Biophysical Journal*, 89(6):4111–21, 2005.

[133] R. Liu, H. Barkhordarian, S. Emadi, C. B. Park, and M. R. Sierks. Trehalose differentially inhibits aggregation and neurotoxicity of beta-amyloid 40 and 42. *Neurobiology of Disease*, 20(1):74–81, 2005.

[134] E. Mari, C. Ricci, S. Pieraccini, F. Spinozzi, P. Mariani, and M. G. Ortore. Trehalose effect on the aggregation of model proteins into amyloid fibrils. *Life (Basel)*, 10(5), 2020.

[135] E. A. Golovina, A. V. Golovin, F. A. Hoekstra, and R. Faller. Water replacement hypothesis in atomic detail—factors determining the structure of dehydrated bilayer stacks. *Biophysical Journal*, 97(2):490–499, 2009.

[136] J. S. Clegg, P. Seitz, W. Seitz, and C. F. Hazlewood. Cellular responses to extreme water loss: The water-replacement hypothesis. *Cryobiology*, 19(3):306–316, 1982.

[137] J. L. Green and C A. Angell. Phase relations and vitrification in saccharide-water solutions and the trehalose anomaly. *The Journal of Physical Chemistry*, 93(8):2880–2882, 1989.

[138] K. L. Koster, M. S. Webb, G. Bryant, and D. V. Lynch. Interactions between soluble sugars and POPC (1-palmitoyl-2-oleoylphosphatidylcholine) during dehydration: vitrification of sugars alters the phase behavior of the phospholipid. *Biochimica et Biophysica Acta*, 1193(1):143–50, 1994.

[139] A. Maiti and S. Daschakraborty. Unraveling the molecular mechanisms of trehalose-mediated protection and stabilization of escherichia coli lipid membrane during desiccation. *The Journal of Physical Chemistry B*, 127(20):4496–4507, 2023.

[140] A. D. Elbein. The metabolism of α,α-trehalose. volume 30 of *Advances in Carbohydrate Chemistry and Biochemistry*, pages 227–256. Academic Press, 1974.

[141] H-J. Lee, Y-S. Yoon, and S-J. Lee. Mechanism of neuroprotection by trehalose: controversy surrounding autophagy induction. *Cell Death & Disease*, 9(7):712, 2018.

[142] G. Martano, L. Gerosa, I. Prada, G. Garrone, V. Krogh, C. Verderio, and M. Passafaro. Biosynthesis of astrocytic trehalose regulates neuronal arborization in hippocampal neurons. *ACS Chemical Neuroscience*, 8(9):1865–1872, 2017.

[143] R. Bhatia, H. Lin, and R. Lal. Fresh and globular amyloid beta protein (1-42) induces rapid cellular degeneration: evidence for abetap channel-mediated cellular toxicity. *The FASEB Journal*, 14(9):1233–43, 2000.

[144] D. Siniscalco, G. Francius, M. Tarek, S. K. Bali, O. Laprévote, C. Malaplate, T. Oster, L. Pauron, and F. Quilès. Molecular insights for Alzheimer's disease: An unexplored storyline on the nanoscale impact of nascent Aβ1–42 toward the lipid membrane. *ACS Applied Materials & Interfaces*, 15(14):17507–17517, 2023.

[145] E. Drolle, F. Hane, B. Lee, and Z. Leonenko. Atomic force microscopy to study molecular mechanisms of amyloid fibril formation and toxicity in Alzheimer's disease. *Drug Metabolism Reviews*, 46(2):207–23, 2014.

[146] J. H. Viles. Imaging amyloid-β membrane interactions: Ion-channel pores and lipid-bilayer permeability in Alzheimer's disease. *Angewandte Chemie International Edition*, 62(25):e202215785, 2023.

[147] E. K. Esbjörner, F. Chan, E. Rees, M. Erdelyi, L. M. Luheshi, C. W. Bertoncini, C. F. Kaminski, C. M. Dobson, and G. S. Kaminski Schierle. Direct observations of amyloid β self-assembly in live cells provide insights into differences in the kinetics of Aβ(1–40) and Aβ(1–42) aggregation. *Chemistry & Biology*, 21(6):732–742, 2014.

[148] Y. Shafrir, S. R. Durell, A. Anishkin, and H. R. Guy. Beta-barrel models of soluble amyloid beta oligomers and annular protofibrils. *Proteins*, 78(16):3458–72, 2010.

[149] H. Jang, J. Zheng, and R. Nussinov. Models of β-amyloid ion channels in the membrane suggest that channel formation in the bilayer is a dynamic process. *Biophysical Journal*, 93(6):1938–1949, 2007.

[150] P. Cizas, R. Budvytyte, R. Morkuniene, R. Moldovan, M. Broccio, M. Lösche, G. Niaura, G. Valincius, and V. Borutaite. Size-dependent neurotoxicity of beta-amyloid oligomers. *Archives of Biochemistry and Biophysics*, 496(2):84–92, 2010.

[151] R. D. Hotchkiss and R. J. Dubos. Fractionation of the bactericidal agent from cultures of a soil bacillus. *Journal of Biological Chemistry*, 132(2):791–792, 1940.

[152] G. Pavithrra and R. Rajasekaran. Gramicidin peptide to combat antibiotic resistance: A review. *International Journal of Peptide Research and Therapeutics*, 26(1):191–199, 2020.

[153] A. M. O'Connell, R. E. Koeppe, and O. S. Andersen. Kinetics of gramicidin channel formation in lipid bilayers: Transmembrane monomer association. *Science*, 250(4985):1256–1259, 1990.

[154] K. Lum, H. I. Ingólfsson, R. E. Koeppe, and O. S. Andersen. Exchange of gramicidin between lipid bilayers: Implications for the mechanism of channel formation. *Biophysical Journal*, 113(8):1757–1767, 2017.

[155] D. A. Kelkar and A. Chattopadhyay. The gramicidin ion channel: A model membrane protein. *Biochimica et Biophysica Acta (BBA) - Biomembranes*, 1768(9):2011–2025, 2007.

[156] Y. Xu, C. T. Filice, and Z. Leonenko. Protective effect of trehalose sugar on amyloid-membrane interactions using BLM electrophysiology. *Biophysical Journal*, 123(12):1690–1704, 2024.

[157] Jr. Stine, W. B., K. N. Dahlgren, G. A. Krafft, and M. J. LaDu. In vitro characterization of conditions for amyloid-beta peptide oligomerization and fibrillogenesis. *Journal of Biological Chemistry*, 278(13):11612–22, 2003.

[158] R. Kayed, Y. Sokolov, B. Edmonds, T. M. McIntire, S. C. Milton, J. E. Hall, and C. G. Glabe. Permeabilization of lipid bilayers is a common conformation-dependent activity of soluble amyloid oligomers in protein misfolding diseases. *Journal of Biological Chemistry*, 279(45):46363–6, 2004.

[159] A. J. Heron, J. R. Thompson, B. Cronin, H. Bayley, and M. I. Wallace. Simultaneous measurement of ionic current and fluorescence from single protein pores. *Journal of the American Chemical Society*, 131(5):1652–1653, 2009.

[160] G. Baaken, M. Sondermann, C. Schlemmer, J. Rühe, and J. C. Behrends. Planar microelectrode-cavity array for high-resolution and parallel electrical recording of membrane ionic currents. *Lab on a Chip*, 8(6):938–944, 2008.

[161] M. Nishio, A. Shoji, and M. Sugawara. Planar lipid bilayers containing gramicidin a as a molecular sensing system based on an integrated current. *Analytical Sciences*, 28(7):661–667, 2012.

[162] S. W. Kowalczyk, A. Y. Grosberg, and C. Rabin, Y.and Dekker. Modeling the conductance and dna blockade of solid-state nanopores. *Nanotechnology*, 22(31):315101, 2011.

[163] M. Serra-Batiste, M. Ninot-Pedrosa, M. Bayoumi, M. Gairí, G. Maglia, and N. Carulla. Aβ42 assembles into specific β-barrel pore-forming oligomers in membrane-mimicking environments. *Proceedings of the National Academy of Sciences*, 113(39):10866–10871, 2016.

[164] A. Finkelstein and O. S. Andersen. The gramicidin a channel: A review of its permeability characteristics with special reference to the single-file aspect of transport. *The Journal of Membrane Biology*, 59(3):155–171, 1981.

[165] A. Quist, I. Doudevski, H. Lin, R. Azimova, D. Ng, B. Frangione, B. Kagan, J. Ghiso, and R. Lal. Amyloid ion channels: a common structural link for protein-misfolding disease. *Proceedings of the National Academy of Sciences*, 102(30):10427–32, 2005.

[166] H. Lin, R. Bhatia, and R. Lal. Amyloid beta protein forms ion channels: implications for Alzheimer's disease pathophysiology. *The FASEB Journal*, 15(13):2433–44, 2001.

[167] H. A. Lashuel, D. Hartley, B. M. Petre, T. Walz, and P. T. Lansbury. Amyloid pores from pathogenic mutations. *Nature*, 418(6895):291–291, 2002.

[168] H. A. Lashuel, D. M. Hartley, B. M. Petre, J. S. Wall, M. N. Simon, T. Walz, and Jr. Lansbury, P. T. Mixtures of wild-type and a pathogenic (E22G) form of Abeta40 in vitro accumulate protofibrils, including amyloid pores. *Journal of Molecular Biology*, 332(4):795–808, 2003.

[169] J. I. Kourie, C. L. Henry, and P. Farrelly. Diversity of amyloid beta protein fragment [1-40]-formed channels. *Cellular and Molecular Neurobiology*, 21(3):255–84, 2001.

[170] R. Capone, H. Jang, S. A. Kotler, B. L. Kagan, R. Nussinov, and R. Lal. Probing structural features of Alzheimer's amyloid-β pores in bilayers using site-specific amino acid substitutions. *Biochemistry*, 51(3):776–785, 2012.

[171] Y. Hu, X. Liu, F. Liu, J. Xie, Q. Zhu, and S. Tan. Trehalose in biomedical cryopreservation–properties, mechanisms, delivery methods, applications, benefits, and problems. *ACS Biomaterials Science & Engineering*, 9(3):1190–1204, 2023.

[172] M. Khalifeh, G. E. Barreto, and A. Sahebkar. Therapeutic potential of trehalose in neurodegenerative diseases: the knowns and unknowns. *Neural Regeneration Research*, 16(10):2026–2027, 2021.

[173] K. Hosseinpour-Moghaddam, M. Caraglia, and A. Sahebkar. Autophagy induction by trehalose: Molecular mechanisms and therapeutic impacts. *Journal of Cellular Physiology*, 233(9):6524–6543, 2018.

[174] A. B. Pupyshev, V. M. Belichenko, M. V. Tenditnik, A. A. Bashirzade, N. I. Dubrovina, M. V. Ovsyukova, A. A. Akopyan, L. A. Fedoseeva, T. A. Korolenko, T. G. Amstislavskaya, and M. A. Tikhonova. Combined induction of mtor-dependent and mtor-independent pathways of autophagy activation as an experimental therapy for Alzheimer's disease-like pathology in a mouse model. *Pharmacology Biochemistry and Behavior*, 217:173406, 2022.

[175] C. S. Pereira and P. H. Hünenberger. Effect of trehalose on a phospholipid membrane under mechanical stress. *Biophysical Journal*, 95(8):3525–3534, 2008.

[176] E. A. Golovina, A. Golovin, F. A. Hoekstra, and R. Faller. Water replacement hypothesis in atomic details: effect of trehalose on the structure of single dehydrated POPC bilayers. *Langmuir*, 26(13):11118–26, 2010.

[177] B. Kent, T. Hunt, T. A. Darwish, T. Hauß, C. J. Garvey, and G. Bryant. Localization of trehalose in partially hydrated DOPC bilayers: insights into cryoprotective mechanisms. *Journal of The Royal Society Interface*, 11(95):20140069, 2014.

[178] O. I. Stanishevskaya, Y. Silyukova, E. Fedorova, N. Pleshanov, A. Kurochkin, V. M. Tereshina, and E. Ianutsevich. Effects of trehalose supplementation on lipid composition of rooster spermatozoa membranes in a freeze/thaw protocol. *Animals*, 13(6):1023, 2023.

[179] J. Wolfe and G. Bryant. Freezing, drying, and/or vitrification of membrane- solute-water systems. *Cryobiology*, 39(2):103–29, 1999.

[180] D. V. Leonov, S. A. Dzuba, and N. V. Surovtsev. Membrane–sugar interactions probed by low-frequency raman spectroscopy: The monolayer adsorption model. *Langmuir*, 36(39):11655–11660, 2020.

[181] K. Søreng, T. P. Neufeld, and A. Simonsen. Chapter one - membrane trafficking in autophagy. volume 336 of *International Review of Cell and Molecular Biology*, pages 1–92. Academic Press, 2018.

[182] J. H. Crowe, L. M. Crowe, and D. Chapman. Preservation of membranes in anhydrobiotic organisms: The role of trehalose. *Science*, 223(4637):701–703, 1984.

[183] C. W. B. Lee, J. S. Waugh, and R. G. Griffin. Solid-state NMR study of trehalose/1,2-dipalmitoyl-sn-phosphatidylcholine interactions. *Biochemistry*, 25(13):3737–3742, 1986.

[184] A. Kumar, A. Cincotti, and S. Aparicio. Insights into the interaction between lipid bilayers and trehalose aqueous solutions. *Journal of Molecular Liquids*, 314:113639, 2020.

[185] M. del C. Luzardo, F. Amalfa, A. M. Nuñez, S. Díaz, A. C. Biondi de Lopez, and E. A. Disalvo. Effect of trehalose and sucrose on the hydration and dipole potential of lipid bilayers. *Biophysical Journal*, 78(5):2452–2458, 2000.

[186] D. Murray, A. Arbuzova, G. Hangyas-Mihalyne, A. Gambhir, N. Ben-Tal, B. Honig, and S. McLaughlin. Electrostatic properties of membranes containing acidic lipids and adsorbed basic peptides: theory and experiment. *Biophysical Journal*, 77(6):3176–88, 1999.

[187] S. McLaughlin. The electrostatic properties of membranes. *Annual Review of Biophysics and Biophysical Chemistry*, 18:113–36, 1989.

[188] S. Eisenberg, E. Haimov, G. F. W. Walpole, J. Plumb, M. M. Kozlov, and S. Grinstein. Mapping the electrostatic profiles of cellular membranes. *Molecular Biology of the Cell*, 32(3):301–310, 2021.

[189] M. Westra, Y. Gutierrez, and H. D. MacGillavry. Contribution of membrane lipids to postsynaptic protein organization. *Frontiers in Synaptic Neuroscience*, 13, 2021.

[190] R. O. Calderon, B. Attema, and G. H. DeVries. Lipid composition of neuronal cell bodies and neurites from cultured dorsal root ganglia. *Journal of Neurochemistry*, 64(1):424–429, 1995.

[191] Jr. Oliveira, O. N., L. Caseli, and K. Ariga. The past and the future of Langmuir and Langmuir–Blodgett films. *Chemical Reviews*, 122(6):6459–6513, 2022.

[192] C. Ybert, W. Lu, G. Möller, and C. M. Knobler. Kinetics of phase transitions in monolayers: collapse. *Journal of Physics: Condensed Matter*, 14(19):4753, 2002.

[193] M. Lundquist. Molecular arrangement in condensed monolayer phases. *Progress in the Chemistry of Fats and other Lipids*, 16:101–124, 1978.

[194] J. Yang, J. Martí, and C. Calero. Pair interactions among ternary DPPC/POPC/cholesterol mixtures in liquid-ordered and liquid-disordered phases. *Soft Matter*, 12(20):4557–4561, 2016.

[195] S. Leekumjorn and A. K. Sum. Molecular investigation of the interactions of trehalose with lipid bilayers of DPPC, DPPE and their mixture. *Molecular Simulation*, 32(3-4):219–230, 2006.

[196] G. A. Clark, J. M. Henderson, C. Heffern, B. Akgün, J. Majewski, and K. Y. C. Lee. Synergistic interactions of sugars/polyols and monovalent salts with phospholipids depend upon sugar/polyol complexity and anion identity. *Langmuir*, 31(46):12688–12698, 2015.

[197] U. M. Ferber, G. Kaggwa, and S. P. Jarvis. Direct imaging of salt effects on lipid bilayer ordering at sub-molecular resolution. *European Biophysics Journal*, 40(3):329–338, 2011.

[198] S. Pöyry, T. Róg, M. Karttunen, and I. Vattulainen. Mitochondrial membranes with mono- and divalent salt: Changes induced by salt ions on structure and dynamics. *The Journal of Physical Chemistry B*, 113(47):15513–15521, 2009.

[199] D. Vollhardt and V. B. Fainerman. Progress in characterization of Langmuir monolayers by consideration of compressibility. *Advances in Colloid and Interface Science*, 127(2):83–97, 2006.

[200] E. M.-E. Aboagla and T. Terada. Trehalose-enhanced fluidity of the goat sperm membrane and its protection during freezing. *Biology of Reproduction*, 69(4):1245–1250, 2003.

[201] G. Pabst, A. Hodzic, J. Štrancar, S. Danner, M. Rappolt, and P. Laggner. Rigidification of neutral lipid bilayers in the presence of salts. *Biophysical Journal*, 93(8):2688–2696, 2007.

[202] R. A. Böckmann, A. Hac, T. Heimburg, and H. Grubmüller. Effect of sodium chloride on a lipid bilayer. *Biophysical Journal*, 85(3):1647–1655, 2003.

[203] R. A. Böckmann and H. Grubmüller. Multistep binding of divalent cations to phospholipid bilayers: A molecular dynamics study. *Angewandte Chemie International Edition*, 43(8):1021–1024, 2004.

[204] J. U. De Mel, S. Gupta, R. M. Perera, L. Ngo, P. Zolnierczuk, M. Bleuel, S. V. Pingali, and G. J. Schneider. Influence of external NaCl salt on membrane rigidity of neutral DOPC vesicles. *Langmuir*, 36(32):9356–9367, 2020.

[205] J. V. Ricker, N. M. Tsvetkova, W. F. Wolkers, C. Leidy, F. Tablin, M. Longo, and J. H. Crowe. Trehalose maintains phase separation in an air-dried binary lipid mixture. *Biophysical Journal*, 84(5):3045–3051, 2003.

[206] R. M. S. Cardoso, P. A. T. Martins, C. V. Ramos, M. M. Cordeiro, R. J. B. Leote, K. Razi Naqvi, W. L. C. Vaz, and M. J. Moreno. Effect of dipole moment on amphiphile solubility and partition into liquid ordered and liquid disordered phases in lipid bilayers. *Biochimica et Biophysica Acta (BBA) - Biomembranes*, 1862(3):183157, 2020.

[207] H. Brockman. Dipole potential of lipid membranes. *Chemistry and Physics of Lipids*, 73(1):57–79, 1994.

[208] H. D. Andersen, C. Wang, L. Arleth, G. H. Peters, and P. Westh. Reconciliation of opposing views on membrane-sugar interactions. *Proceedings of the National Academy of Sciences*, 108(5):1874–8, 2011.

[209] H. I. Petrache, T. Zemb, L. Belloni, and V. A. Parsegian. Salt screening and specific ion adsorption determine neutral-lipid membrane interactions. *Proceedings of the National Academy of Sciences*, 103(21):7982–7987, 2006.

[210] R. Vácha, S. W. I. Siu, M. Petrov, R. A. Böckmann, J. Barucha-Kraszewska, P. Jurkiewicz, M. Hof, M. L. Berkowitz, and P. Jungwirth. Effects of alkali cations and halide anions on the DOPC lipid membrane. *The Journal of Physical Chemistry A*, 113(26):7235–7243, 2009.

[211] I. V. Khavrutskii, A. A. Gorfe, B. Lu, and J. A. McCammon. Free energy for the permeation of Na+ and Cl- ions and their ion-pair through a zwitterionic dimyristoyl phosphatidylcholine lipid bilayer by umbrella integration with harmonic fourier beads. *Journal of the American Chemical Society*, 131(5):1706–1716, 2009.

[212] J. Yang, C. Calero, M. Bonomi, and J. Martí. Specific ion binding at phospholipid membrane surfaces. *Journal of Chemical Theory and Computation*, 11(9):4495–4499, 2015.

[213] C. Lambruschini, A. Relini, A. Ridi, L. Cordone, and A. Gliozzi. Trehalose interacts with phospholipid polar heads in Langmuir monolayers. *Langmuir*, 16(12):5467–5470, 2000.

[214] 2017 Alzheimer's disease facts and figures. *Alzheimer's & Dementia*, 13(4):325–373, 2017.

[215] J. Hardy and D. J. Selkoe. The amyloid hypothesis of Alzheimer's disease: Progress and problems on the road to therapeutics. *Science*, 297(5580):353–356, 2002.

[216] S. Srivastava, R. Ahmad, and S. K. Khare. Alzheimer's disease and its treatment by different approaches: A review. *European Journal of Medicinal Chemistry*, 216:113320, 2021.

[217] V. W. Chow, M. P. Mattson, P. C. Wong, and M. Gleichmann. An overview of APP processing enzymes and products. *Neuromolecular Medicine*, 12(1):1–12, 2010.

[218] C. Cecchi and M. Stefani. The amyloid-cell membrane system. The interplay between the biophysical features of oligomers/fibrils and cell membrane defines amyloid toxicity. *Biophysical Chemistry*, 182:30–43, 2013.

[219] J. V. Rushworth and N. M. Hooper. Lipid rafts: Linking Alzheimer's amyloid-β production, aggregation, and toxicity at neuronal membranes. *International Journal of Alzheimer's Disease*, 2011:603052, 2010.

[220] G. P. Eckert, W. G. Wood, and W. E. Muller. Lipid membranes and beta-amyloid: A harmful connection. *Current Protein and Peptide Science*, 11(5):319–325, 2010.

[221] C. Hertel, E. Terzi, N. Hauser, R. Jakob-Røtne, J. Seelig, and J. A. Kemp. Inhibition of the electrostatic interaction between β-amyloid peptide and membranes prevents β-amyloid-induced toxicity. *Proceedings of the National Academy of Sciences*, 94(17):9412–9416, 1997.

[222] S.-I. Kim, J.-S. Yi, and Y.-G. Ko. Amyloid β oligomerization is induced by brain lipid rafts. *Journal of Cellular Biochemistry*, 99(3):878–889, 2006.

[223] K. M. Grochowska, P. Yuanxiang, J. Bär, R. Raman, G. Brugal, G. Sahu, M. Schweizer, A. Bikbaev, S. Schilling, H-U. Demuth, and M. R. Kreutz. Post-

translational modification impact on the mechanism by which amyloid-β induces synaptic dysfunction. *EMBO Reports*, 18(6):962–981, 2017.

[224] R. Morkuniene, P. Cizas, S. Jankeviciute, R. Petrolis, O. Arandarcikaite, A. Krisciukaitis, and V. Borutaite. Small Aβ1–42 oligomer-induced membrane depolarization of neuronal and microglial cells: Role of N-methyl-D-aspartate receptors. *Journal of Neuroscience Research*, 93(3):475–486, 2015.

[225] R. Mayeux, M-X. Tang, D. M. Jacobs, J. Manly, K. Bell, C. Merchant, S. A. Small, Y. Stern, H. M. Wisniewski, and P. D. Mehta. Plasma amyloid β-peptide 1–42 and incipient Alzheimer's disease. *Annals of Neurology*, 46(3):412–416, 1999.

[226] C. Song, M. S. Manku, and D. F. Horrobin. Long-chain polyunsaturated fatty acids modulate interleukin-1beta-induced changes in behavior, monoaminergic neurotransmitters, and brain inflammation in rats. *The Journal of Nutrition*, 138(5):954–63, 2008.

[227] L. M. Willis, B. Shukitt-Hale, and J. A. Joseph. Dietary polyunsaturated fatty acids improve cholinergic transmission in the aged brain. *Genes & Nutrition*, 4(4):309–314, 2009.

[228] S. Yehuda, S. Rabinovitz, R. L. Carasso, and D. I. Mostofsky. The role of polyunsaturated fatty acids in restoring the aging neuronal membrane. *Neurobiology of Aging*, 23(5):843–53, 2002.

[229] C. I. Janssen and A. J. Kiliaan. Long-chain polyunsaturated fatty acids (lcpufa) from genesis to senescence: the influence of lcpufa on neural development, aging, and neurodegeneration. *Progress in Lipid Research*, 53:1–17, 2014.

[230] S. V. Chochina, N. A. Avdulov, U. Igbavboa, J. P. Cleary, E. O. O'Hare, and W. G. Wood. Amyloid beta-peptide1-40 increases neuronal membrane fluidity: role of cholesterol and brain region. *Journal of Lipid Research*, 42(8):1292–7, 2001.

[231] V. Rudajev and J. Novotny. Cholesterol as a key player in amyloid β-mediated toxicity in Alzheimer's disease. *Frontiers in Molecular Neuroscience*, 15, 2022.

[232] W. G. Wood, F. Schroeder, U. Igbavboa, N. A. Avdulov, and S. V. Chochina. Brain membrane cholesterol domains, aging and amyloid beta-peptides. *Neurobiology of Aging*, 23(5):685–694, 2002.

[233] C. C. Curtain, F. E. Ali, D. G. Smith, A. I. Bush, C. L. Masters, and K. J. Barnham. Metal ions, pH, and cholesterol regulate the interactions of Alzheimer's disease amyloid-beta peptide with membrane lipid. *Journal of Biological Chemistry*, 278(5):2977–82, 2003.

[234] R. S. Doody, M. Raman, R.and Farlow, T. Iwatsubo, B. Vellas, S. Joffe, K. Kieburtz, F. He, X. Sun, R. G. Thomas, P. S. Aisen, E. Siemers, G. Sethuraman, and R. Mohs. A phase 3 trial of semagacestat for treatment of Alzheimer's disease. *New England Journal of Medicine*, 369(4):341–350, 2013.

[235] L. D. Plant, J. P. Boyle, I. F. Smith, C. Peers, and H. A. Pearson. The production of amyloid β peptide is a critical requirement for the viability of central neurons. *The Journal of Neuroscience*, 23(13):5531–5535, 2003.

[236] M. Shukla, P. Govitrapong, P. Boontem, R. J. Reiter, and J. Satayavivad. Mechanisms of melatonin in alleviating Alzheimer's disease. *Current Neuropharmacology*, 15(7):1010–1031, 2017.

[237] Nanqin Mei, Jingwen Liang, Danielle M. McRae, and Zoya Leonenko. Localized surface plasmon resonance and atomic force microscopy study of model lipid membranes and their interactions with amyloid and melatonin. *Nanotechnology*, 35(30):305101, 2024.

[238] S. Errico, H. Ramshini, C. Capitini, C. Canale, M. Spaziano, D. Barbut, M. Calamai, M. Zasloff, R. Oropesa-Nuñez, M. Vendruscolo, and F. Chiti. Quantitative measurement of the affinity of toxic and nontoxic misfolded protein oligomers for

lipid bilayers and of its modulation by lipid composition and trodusquemine. *ACS Chemical Neuroscience*, 12(17):3189–3202, 2021.

[239] M. Milewska, S. Kukowka, I. Wandzik, and K. Kamińska. Trehalose - properties, biosynthesis and applications. *Chemik*, 69:469–476, 2015.

[240] K. Yoshida, F. Ono, T. Chouno, B. R. Perocho, Y. Ikegami, N. Shirakigawa, and H. Ijima. Cryoprotective enhancing effect of very low concentration of trehalose on the functions of primary rat hepatocytes. *Regenerative Therapy*, 15:173–179, 2020.

[241] M. Sola-Penna and J. R. M-Fernandes. Stabilization against thermal inactivation promoted by sugars on enzyme structure and function: Why is trehalose more effective than other sugars? *Archives of Biochemistry and Biophysics*, 360(1):10–14, 1998.

[242] A. Chen and P. A. Gibney. Dietary trehalose as a bioactive nutrient. *Nutrients*, 15(6), 2023.

[243] C. Cejka, S. Kubinova, and J. Cejkova. Trehalose in ophthalmology. *Histol Histopathol*, 34(6):611–618, 2019.

[244] J. Luyckx and C. Baudouin. Trehalose: an intriguing disaccharide with potential for medical application in ophthalmology. *Clinical Ophthalmology*, 5:577–81, 2011.

[245] J. Laihia and K. Kaarniranta. Trehalose for ocular surface health. *Biomolecules*, 10(5):809, 2020.

[246] A. Izmitli, C. Schebor, M. P. McGovern, A. S. Reddy, N. L. Abbott, and J. J. de Pablo. Effect of trehalose on the interaction of Alzheimer's abeta-peptide and anionic lipid monolayers. *Biochimica et Biophysica Acta*, 1808(1):26–33, 2011.

[247] M. Khalifeh, M. I. Read, G. E. Barreto, and A. Sahebkar. Trehalose against Alzheimer's disease: Insights into a potential therapy. *BioEssays*, 42(8):1900195, 2020.

[248] Y. Liu, J. Wang, G-Y. Robin Hsiung, and W. Song. Trehalose inhibits Aβ generation and plaque formation in Alzheimer's disease. *Molecular Neurobiology*, 57(7):3150–3157, 2020.

[249] Y. Luo, F. Li, G. P. Wang, X. H. Yang, and W. Wang. Exogenously-supplied trehalose protects thylakoid membranes of winter wheat from heat-induced damage. *Biologia Plantarum*, 54(3):495–501, 2010.

[250] W. Qi, A. Zhang, T. A. Good, and E. J. Fernandez. Two disaccharides and trimethylamine N-oxide affect abeta aggregation differently, but all attenuate oligomer-induced membrane permeability. *Biochemistry*, 48(37):8908–8919, 2009.

[251] J. M. Alarcón, J. A. Brito, T. Hermosilla, I. Atwater, D. Mears, and E. Rojas. Ion channel formation by Alzheimer's disease amyloid β-peptide (Aβ40) in unilamellar liposomes is determined by anionic phospholipids. *Peptides*, 27(1):95–104, 2006.

[252] M. Eisenberg, J. E. Hall, and C. A. Mead. The nature of the voltage-dependent conductance induced by alamethicin in black lipid membranes. *The Journal of Membrane Biology*, 14(1):143–176, 1973.

[253] G. Boheim. Statistical analysis of alamethicin channels in black lipid membranes. *The Journal of Membrane Biology*, 19(1):277–303, 1974.

[254] E. Pavlov, E. Zakharian, C. Bladen, C. T. M. Diao, C. Grimbly, R. N. Reusch, and R. J. French. A large, voltage-dependent channel, isolated from mitochondria by water-free chloroform extraction. *Biophysical Journal*, 88(4):2614–2625, 2005.

[255] Y. F. Dufrêne, T. Ando, R. Garcia, D. Alsteens, D. Martinez-Martin, A. Engel, C. Gerber, and D. J. Müller. Imaging modes of atomic force microscopy for application in molecular and cell biology. *Nature Nanotechnology*, 12(4):295–307, 2017.

[256] P. K. Hansma, J. P. Cleveland, M. Radmacher, D. A. Walters, P. E. Hillner, M. Bezanilla, M. Fritz, D. Vie, H. G. Hansma, C. B. Prater, J. Massie, L. Fukunaga, J. Gurley, and V. Elings. Tapping mode atomic force microscopy in liquids. *Applied Physics Letters*, 64(13):1738–1740, 1994.

[257] A. L. Hodgkin and A. F. Huxley. The components of membrane conductance in the giant axon of loligo. *The Journal of Physiology*, 116(4):473–96, 1952.

[258] Y. Kim, J-H. Park, H. Lee, and J-M. Nam. How do the size, charge and shape of nanoparticles affect amyloid β aggregation on brain lipid bilayer? *Scientific Reports*, 6(1):19548, 2016.

[259] Y. Sokolov, J. A. Kozak, R. Kayed, A. Chanturiya, C. Glabe, and J. E. Hall. Soluble amyloid oligomers increase bilayer conductance by altering dielectric structure. *Journal of General Physiology*, 128(6):637–47, 2006.

[260] A. S. Reddy, A. Izmitli, and J. J. de Pablo. Effect of trehalose on amyloid β (29–40)-membrane interaction. *The Journal of Chemical Physics*, 131(8):085101, 2009.

[261] D. M. Vadukul, M. Maina, H. Franklin, A. Nardecchia, L. C. Serpell, and K. E. Marshall. Internalisation and toxicity of amyloid-β 1-42 are influenced by its conformation and assembly state rather than size. *FEBS Letters*, 594(21):3490–3503, 2020.

[262] Z. Al-Rekabi and S. Contera. Multifrequency AFM reveals lipid membrane mechanical properties and the effect of cholesterol in modulating viscoelasticity. *Proceedings of the National Academy of Sciences*, 115(11):2658–2663, 2018.

[263] J. Kurniawan, N-N. Yin, G-Y. Liu, and T. L. Kuhl. Interaction forces between ternary lipid bilayers containing cholesterol. *Langmuir*, 30(17):4997–5004, 2014.

[264] S. L. Regen. Cholesterol's condensing effect: Unpacking a century-old mystery. *JACS Au*, 2(1):84–91, 2022.

[265] D. Mrdenovic, M. Majewska, I. S. Pieta, P. Bernatowicz, R. Nowakowski, W. Kutner, J. Lipkowski, and P. Pieta. Size-dependent interaction of amyloid β oligomers with brain total lipid extract bilayer—fibrillation versus membrane destruction. *Langmuir*, 35(36):11940–11949, 2019.

[266] Y-S. Lee, D-M. Lai, H-J. Huang, G-J. Lee-Chen, C-H. Chang, H. M. Hsieh-Li, and G-C. Lee. Prebiotic lactulose ameliorates the cognitive deficit in Alzheimer's disease mouse model through macroautophagy and chaperone-mediated autophagy pathways. *Journal of Agricultural and Food Chemistry*, 69(8):2422–2437, 2021.

[267] J. Perucho, M. J. Casarejos, A. Gomez, R. M. Solano, J. Garcia de Yebenes, and M. A. Mena. Trehalose protects from aggravation of amyloid pathology induced by isoflurane anesthesia in APPswe mutant mice. *Current Alzheimer Research*, 9(3):334–343, 2012.

[268] S. Stewart and X. He. Intracellular delivery of trehalose for cell banking. *Langmuir*, 35(23):7414–7422, 2019.

[269] B. A. C. Horta, L. Perić-Hassler, and P. H. Hünenberger. Interaction of the disaccharides trehalose and gentiobiose with lipid bilayers: A comparative molecular dynamics study. *Journal of Molecular Graphics and Modelling*, 29(3):331–346, 2010.

[270] J. Liu, C. Chen, C. Lu, and W. Li. Different mechanisms on the stabilization of POPC membrane by trehalose upon varied mechanical stress. *Journal of Molecular Liquids*, 275:839–848, 2019.

[271] D. L. M. Rupert, G. V. Shelke, G. Emilsson, V. Claudio, S. Block, C. Lässer, A. Dahlin, J. O. Lötvall, M. Bally, V. P. Zhdanov, and F. Höök. Dual-wavelength surface plasmon resonance for determining the size and concentration of sub-populations of extracellular vesicles. *Analytical Chemistry*, 88(20):9980–9988, 2016.

[272] P. Parkkila, M. Elderdfi, A. Bunker, and T. Viitala. Biophysical characterization of supported lipid bilayers using parallel dual-wavelength surface plasmon resonance and quartz crystal microbalance measurements. *Langmuir*, 34(27):8081–8091, 2018.

[273] A. H. M. Almawgani, S. A. Taya, M. G. Daher, I. Colak, F. Wu, and S. K. Patel. Detection of glucose concentration using a surface plasmon resonance biosensor based on barium titanate layers and molybdenum disulphide sheets. *Physica Scripta*, 97(6):065501, 2022.

[274] H. V. Hsieh, Z. A. Pfeiffer, T. J. Amiss, D. B. Sherman, and J. B. Pitner. Direct detection of glucose by surface plasmon resonance with bacterial glucose/galactose-binding protein. *Biosensors and Bioelectronics*, 19(7):653–660, 2004.

[275] Q. Yang, X. Zhang, S. Kumar, R. Singh, B. Zhang, C. Bai, and X. Pu. Development of glucose sensor using gold nanoparticles and glucose-oxidase functionalized tapered fiber structure. *Plasmonics*, 15(3):841–848, 2020.

[276] N. Mudgal, A. Saharia, A. Agarwal, J. Ali, P. Yupapin, and G. Singh. Modeling of highly sensitive surface plasmon resonance (SPR) sensor for urine glucose detection. *Optical and Quantum Electronics*, 52(6):307, 2020.

[277] F. A. A. Nugroho, D. Świtlik, A. Armanious, P. O'Reilly, I. Darmadi, S. Nilsson, V. P. Zhdanov, F. Höök, T. J. Antosiewicz, and C. Langhammer. Time-resolved thickness and shape-change quantification using a dual-band nanoplasmonic ruler with sub-nanometer resolution. *ACS Nano*, 16(10):15814–15826, 2022.

[278] S. Lafont, H. Rapaport, G. J. Somjen, A. Renault, P. B. Howes, K. Kjaer, J. Als-Nielsen, L. Leiserowitz, and M. Lahav. Monitoring the nucleation of crystalline films of cholesterol on water and in the presence of phospholipid. *Journal of Physical Chemistry B*, 102(5):761–765, 1998.

[279] D. F. Kienle, J. V. de Souza, E. B. Watkins, and T. L. Kuhl. Thickness and refractive index of DPPC and DPPE monolayers by multiple-beam interferometry. *Analytical and Bioanalytical Chemistry*, 406(19):4725–33, 2014.

[280] J. M. Pusterla, A. A. Malfatti-Gasperini, X. E. Puentes-Martinez, L. P. Cavalcanti, and R. G. Oliveira. Refractive index and thickness determination in Langmuir monolayers of myelin lipids. *Biochimica et Biophysica Acta (BBA) - Biomembranes*, 1859(5):924–930, 2017.

[281] J. Vörös. The density and refractive index of adsorbing protein layers. *Biophysical Journal*, 87(1):553–61, 2004.

[282] A. B. Pupyshev, T. A. Korolenko, and M. A. Tikhonova. Multiple mechanisms of the therapeutic effect of trehalose in inhibition of experimental neurodegeneration. *Neurochemical Journal*, 17(4):516–527, 2023.

[283] Dennis J. J. Mucke, L.and Selkoe. Neurotoxicity of amyloid β-protein: synaptic and network dysfunction. *Cold Spring Harbor Perspectives in Medicine*, page a006338, 2012.

[284] E. J. Fernandez-Perez, C. Peters, and L. G. Aguayo. Membrane damage induced by amyloid beta and a potential link with neuroinflammation. *Current Pharmaceutical Design*, 22(10):1295–304, 2016.

[285] S. D. Portbury, D. J. Hare, C. Sgambelloni, K. Perronnes, A. J. Portbury, D. I. Finkelstein, and P. A. Adlard. Trehalose improves cognition in the transgenic Tg2576 mouse model of Alzheimer's disease. *Journal of Alzheimer's Disease*, 60(2):549–560, 2017.

[286] I. Benito-Cuesta, L. Ordoñez-Gutierrez, and F. Wandosell. Trehalose reduces the secreted beta-amyloid levels in primary neurons independently of autophagy induction. *Metabolites*, 11(7):421, 2021.

[287] R. Parodi-Rullán, J. Ghiso, E. Cabrera, A. Rostagno, and S. Fossati. Alzheimer's amyloid β heterogeneous species differentially affect brain endothelial cell viability, blood-brain barrier integrity, and angiogenesis. *Aging Cell*, 19(11):e13258, 2020.

[288] S. Sarkar, J. E. Davies, Z. Huang, A. Tunnacliffe, and D. C. Rubinsztein. Trehalose, a novel mtor-independent autophagy enhancer, accelerates the clearance of mutant huntingtin and alpha-synuclein. *Journal of Biological Chemistry*, 282(8):5641–52, 2007.

[289] M. Redmann, W. Y. Wani, L. Volpicelli-Daley, V. Darley-Usmar, and J. Zhang. Trehalose does not improve neuronal survival on exposure to alpha-synuclein preformed fibrils. *Redox Biology*, 11:429–437, 2017.

[290] E. Jakobsson, O. Argüello-Miranda, S. W. Chiu, Z. Fazal, J. Kruczek, S. Nunez-Corrales, S. Pandit, and L. Pritchet. Towards a unified understanding of lithium action in basic biology and its significance for applied biology. *Journal of Membrane Biology*, 250(6):587–604, 2017.

[291] E. Shorter. The history of lithium therapy. *Bipolar Disorders*, 11(s2):4–9, 2009.

[292] E. L. M. Ochoa. Lithium as a neuroprotective agent for bipolar disorder: An overview. *Cellular and Molecular Neurobiology*, 42(1):85–97, 2022.

[293] N. G. Holm. The significance of Mg in prebiotic geochemistry. *Geobiology*, 10(4):269–79, 2012.

[294] T. Dudev, C. Grauffel, and C. Lim. How native and alien metal cations bind atp: Implications for lithium as a therapeutic agent. *Scientific Reports*, 7(1):42377, 2017.

[295] O. Damri, N. Shemesh, and G. Agam. Is there justification to treat neurodegenerative disorders by repurposing drugs? The case of Alzheimer's disease, lithium, and autophagy. *International Journal of Molecular Sciences*, 22(1), 2020.

[296] P. S. Klein and D. A. Melton. A molecular mechanism for the effect of lithium on development. *Proceedings of the National Academy of Sciences*, 93(16):8455–9, 1996.

[297] J. Kotyńska, I. Dobrzyńska, and Z. A. Figaszewski. Association of alkali metal cations with phosphatidylcholine liposomal membrane surface. *European Biophysics Journal*, 46(2):149–155, 2017.

[298] P. Maity, B. Saha, G. S. Kumar, and S. Karmakar. Binding of monovalent alkali metal ions with negatively charged phospholipid membranes. *Biochimica et Biophysica Acta (BBA) - Biomembranes*, 1858(4):706–714, 2016.

[299] J. Kruczek, S-W. Chiu, E. Jakobsson, and S. A. Pandit. Effects of lithium and other monovalent ions on palmitoyl oleoyl phosphatidylcholine bilayer. *Langmuir*, 33(4):1105–1115, 2017.

[300] M. Roux and M. Bloom. Calcium, magnesium, lithium, sodium, and potassium distributions in the headgroup region of binary membranes of phosphatidylcholine and phosphatidylserine as seen by deuterium NMR. *Biochemistry*, 29(30):7077–7089, 1990.

[301] B. López-Corcuera, C. Giménez, and C. Aragón. Change of synaptic membrane lipid composition and fluidity by chronic administration of lithium. *Biochimica et Biophysica Acta (BBA) - Biomembranes*, 939(3):467–475, 1988.

[302] V. Alfredsson, P. Lo Nostro, B. Ninham, and T. Nylander. Morphologies and structure of brain lipid membrane dispersions. *Frontiers in Cell and Developmental Biology*, 9, 2021.

[303] P. V. Nunes, O. V. Forlenza, and W. F. Gattaz. Lithium and risk for Alzheimer's disease in elderly patients with bipolar disorder. *The British Journal of Psychiatry*, 190:359–60, 2007.

[304] U. Knorr, A. H. Simonsen, C. S. Jensen, H. Zetterberg, K. Blennow, M. Akhøj, J. Forman, S. G. Hasselbalch, and L. V. Kessing. Alzheimer's disease related biomarkers in bipolar disorder – a longitudinal one-year case-control study. *Journal of Affective Disorders*, 297:623–633, 2022.

[305] S. Matsunaga, T. Kishi, P. Annas, H. Basun, H. Hampel, and N. Iwata. Lithium as a treatment for Alzheimer's disease: a systematic review and meta-analysis. *Journal of Alzheimer's Disease*, 48(2):403–410, 2015.

[306] O. V. Forlenza, V. J. R. de Paula, and B. S. O. Diniz. Neuroprotective effects of lithium: Implications for the treatment of Alzheimer's disease and related neurodegenerative disorders. *ACS Chemical Neuroscience*, 5(6):443–450, 2014.

[307] S. Lovestone, D. R. Davis, M. T. Webster, S. Kaech, J. P. Brion, A. Matus, and B. H. Anderton. Lithium reduces tau phosphorylation: effects in living cells and in neurons at therapeutic concentrations. *Biological Psychiatry*, 45(8):995–1003, 1999.

[308] C. J. Phiel, C. A. Wilson, V. M. Lee, and P. S. Klein. GSK-3alpha regulates production of Alzheimer's disease amyloid-beta peptides. *Nature*, 423(6938):435–9, 2003.

[309] E. Deplazes, B. D. Tafalla, C. G. Cranfield, and A. Garcia. Role of ion–phospholipid interactions in zwitterionic phospholipid bilayer ion permeation. *The Journal of Physical Chemistry Letters*, 11(15):6353–6358, 2020.

[310] H. L. Scott, D. Bolmatov, P. T. Podar, Z. Liu, J. J. Kinnun, B. Doughty, R. Lydic, R. L. Sacci, C. P. Collier, and J. Katsaras. Evidence for long-term potentiation in phospholipid membranes. *Proceedings of the National Academy of Sciences*, 119(50):e2212195119, 2022.

[311] B. Kang, H. Tang, Z. Zhao, and S. Song. Hofmeister series: Insights of ion specificity from amphiphilic assembly and interface property. *ACS Omega*, 5(12):6229–6239, 2020.

[312] B. Klasczyk, V. Knecht, R. Lipowsky, and R. Dimova. Interactions of alkali metal chlorides with phosphatidylcholine vesicles. *Langmuir*, 26(24):18951–18958, 2010.

[313] G. N. Schrauzer and K. P. Shrestha. Lithium in drinking water and the incidences of crimes, suicides, and arrests related to drug addictions. *Biological Trace Element Research*, 25(2):105–113, 1990.

[314] H. Ohgami, T. Terao, I. Shiotsuki, N. Ishii, and N. Iwata. Lithium levels in drinking water and risk of suicide. *British Journal of Psychiatry*, 194(5):464–465, 2009.

[315] L. Nemanov, R. P. Ebstein, R. H. Belmaker, Y. Osher, and G. Agam. Effect of bipolar disorder on lymphocyte inositol monophosphatase mRNA levels. *International Journal of Neuropsychopharmacology*, 2(1):25–29, 1999.

[316] D. Piovesan, G. Profiti, P. L. Martelli, and R. Casadio. The human "magnesome": detecting magnesium binding sites on human proteins. *BMC Bioinformatics*, 13(14):S10, 2012.

[317] H. L. Scott, D. Bolmatov, U. I. Premadasa, B. Doughty, J.-M. Y. Carrillo, R. L. Sacci, M. Lavrentovich, J. Katsaras, and C. P. Collier. Cations control lipid bilayer memcapacitance associated with long-term potentiation. *ACS Applied Materials & Interfaces*, 15(37):44533–44540, 2023.

[318] J. J. López Cascales and J. Garcia de la Torre. Effect of lithium and sodium ions on a charged membrane of dipalmitoylphosphatidylserine: A study by molecular dynamics simulation. *Biochimica et Biophysica Acta (BBA) - Biomembranes*, 1330(2):145–156, 1997.

[319] A. Cordomí, O. Edholm, and J. J. Perez. Effect of ions on a dipalmitoyl phosphatidylcholine bilayer. A molecular dynamics simulation study. *The Journal of Physical Chemistry B*, 112(5):1397–1408, 2008.

[320] H. I. Petrache, S. Tristram-Nagle, D. Harries, N. Kučerka, J. F. Nagle, and V. A. Parsegian. Swelling of phospholipids by monovalent salt. *Journal of Lipid Research*, 47(2):302–309, 2006.

[321] J. Zhang, Q. Li, Y. Wu, D. Wang, L. Xu, Y. Zhang, S. Wang, T. Wang, F. Liu, M. Y. Zaky, S. Hou, S. Liu, K. Zou, H. Lei, L. Zou, Y. Zhang, and H. Liu. Cholesterol content in cell membrane maintains surface levels of ErbB2 and confers a therapeutic vulnerability in ErbB2-positive breast cancer. *Cell Communication and Signaling*, 17(1):15, 2019.

[322] T. Starke-Peterkovic, N. Turner, M. F. Vitha, M. P. Waller, D. E. Hibbs, and R. J. Clarke. Cholesterol effect on the dipole potential of lipid membranes. *Biophysical Journal*, 90(11):4060–70, 2006.

[323] R. Çapan, T. H. Richardson, and D. Lacey. The Langmuir properties of a mixed copolysiloxane monolayer. *Turkish Journal of Physics*, 25:445–449, 2001.

[324] R. Friedman. Membrane–ion interactions. *The Journal of Membrane Biology*, 251(3):453–460, 2018.

[325] V. Knecht, M. Müller, M. Bonn, S. Marrink, and A. Mark. Simulation studies of pore and domain formation in a phospholipid monolayer. *The Journal of Chemical Physics*, 122:024704, 2005.

[326] D. S. Marynick and H. F. Schaefer. Theoretical studies of metal-phosphate interactions: interaction of Li+, Na+, K+, Be++, Mg++, and Ca++ with H2PO4- and (CH3O)2PO2-: implications for nucleic acid solvation. *Proceedings of the National Academy of Sciences*, 72(10):3794–3798, 1975.

[327] M. Hishida, Y. Yamamura, and K. Saito. Salt effects on lamellar repeat distance depending on head groups of neutrally charged lipids. *Langmuir*, 30(35):10583–10589, 2014.

[328] M. R. Vist and J. H. Davis. Phase equilibria of cholesterol/dipalmitoylphosphatidylcholine mixtures: deuterium nuclear magnetic resonance and differential scanning calorimetry. *Biochemistry*, 29(2):451–464, 1990.

[329] P. Gaddam and W. Ducker. Electrostatic screening length in concentrated salt solutions. *Langmuir*, 35(17):5719–5727, 2019.

[330] K. Bohinc, M. Špadina, J. Reščič, N. Shimokawa, and S. Spada. Influence of charge lipid head group structures on electric double layer properties. *Journal of Chemical Theory and Computation*, 18(1):448–460, 2022.

[331] S. Haldar, R. K. Kanaparthi, A. Samanta, and A. Chattopadhyay. Differential effect of cholesterol and its biosynthetic precursors on membrane dipole potential. *Biophysical Journal*, 102(7):1561–9, 2012.

[332] J. Velosa, A. Delgado, E. Finger, M. Berk, F. Kapczinski, and T. de Azevedo Cardoso. Risk of dementia in bipolar disorder and the interplay of lithium: a systematic review and meta-analyses. *Acta Psychiatrica Scandinavica*, 141(6):510–521, 2020.

[333] I. Terao, M. Honyashiki, and T. Inoue. Comparative efficacy of lithium and aducanumab for cognitive decline in patients with mild cognitive impairment or

Alzheimer's disease: A systematic review and network meta-analysis. *Ageing Research Reviews*, 81:101709, 2022.

[334] D. P. Devanand, Elizabeth Crocco, Brent P. Forester, Mustafa M. Husain, Seonjoo Lee, Ipsit V. Vahia, Howard Andrews, Laura Simon-Pearson, Nadia Imran, Luminita Luca, Edward D. Huey, Deborah A. Deliyannides, and Gregory H. Pelton. Low dose lithium treatment of behavioral complications in Alzheimer's disease: Lit-AD randomized clinical trial. *The American Journal of Geriatric Psychiatry*, 30(1):32–42, 2022.

[335] J. Busner and S. D. Targum. The clinical global impressions scale: applying a research tool in clinical practice. *Psychiatry (Edgmont)*, 4(7):28–37, 2007.

[336] G. Alvarez, J. R. Muñoz-Montaño, J. Satrústegui, J. Avila, E. Bogónez, and J. Díaz-Nido. Lithium protects cultured neurons against β-amyloid-induced neurodegeneration. *FEBS Letters*, 453(3):260–264, 1999.

[337] J. D. Livingstone, M. J. P. Gingras, Z. Leonenko, and M. A. Beazely. Search for lithium isotope effects in neuronal HT22 cells. *Biochemistry and Biophysics Reports*, 34:101461, 2023.

[338] Y. Su, J. Ryder, B. Li, X. Wu, N. Fox, P. Solenberg, K. Brune, S. Paul, Y. Zhou, F. Liu, and B. Ni. Lithium, a common drug for bipolar disorder treatment, regulates amyloid-beta precursor protein processing. *Biochemistry*, 43(22):6899–908, 2004.

[339] E. Rockenstein, M. Torrance, A. Adame, M. Mante, P. Bar-on, J. B. Rose, L. Crews, and E. Masliah. Neuroprotective effects of regulators of the glycogen synthase kinase-3beta signaling pathway in a transgenic model of Alzheimer's disease are associated with reduced amyloid precursor protein phosphorylation. *Journal of Neuroscience*, 27(8):1981–91, 2007.

[340] S. Puglisi-Allegra, G. Lazzeri, C. L. Busceti, F. S. Giorgi, F. Biagioni, and F. Fornai. Lithium engages autophagy for neuroprotection and neuroplasticity: Translational evidence for therapy. *Neuroscience & Biobehavioral Reviews*, 148:105148, 2023.

[341] Y. Pan, J. L. Short, S. A. Newman, K. H. C. Choy, D. Tiwari, C. Yap, D. Senyschyn, W. A. Banks, and J. A. Nicolazzo. Cognitive benefits of lithium chloride in APP/PS1 mice are associated with enhanced brain clearance of β-amyloid. *Brain, Behavior, and Immunity*, 70:36–47, 2018.

[342] X. Zhang, X. Heng, T. Li, L. Li, D. Yang, X. Zhang, Y. Du, R. S. Doody, and W. Le. Long-term treatment with lithium alleviates memory deficits and reduces amyloid-β production in an aged Alzheimer's disease transgenic mouse model. *Journal of Alzheimer's Disease*, 24:739–749, 2011.

[343] M. Liu, T. Qian, W. Zhou, X. Tao, S. Sang, and L. Zhao. Beneficial effects of low-dose lithium on cognitive ability and pathological alteration of Alzheimer's disease transgenic mice model. *NeuroReport*, 31(13), 2020.

[344] A. Haimovich and A. Goldbourt. How does the mood stabilizer lithium bind atp, the energy currency of the cell: Insights from solid-state NMR. *Biochimica et Biophysica Acta (BBA) - General Subjects*, 1864(1):129456, 2020.

[345] W. A. Nolen, R. W. Licht, A. H. Young, G. S. Malhi, M. Tohen, E. Vieta, R. W. Kupka, C. Zarate, R. E. Nielsen, R. J. Baldessarini, and E. Severus. What is the optimal serum level for lithium in the maintenance treatment of bipolar disorder? A systematic review and recommendations from the ISBD/IGSLI task force on treatment with lithium. *Bipolar Disord*, 21(5):394–409, 2019.

[346] F. J. Dunne. Lithium toxicity: the importance of clinical signs. *British Journal of Hospital Medicine*, 71(4):206–210, 2010.

[347] D. D. Boltan and A. Z. Fenves. Effectiveness of normal saline diuresis in treating lithium overdose. *Proceedings (Baylor University. Medical Center)*, 21(3):261–3, 2008.

[348] E. Berntsson, S. Paul, F. Vosough, S. B. Sholts, J. Jarvet, P. M. Roos, A. Barth, A. Gräslund, and S. Wärmländer. Lithium ions display weak interaction with

amyloid-beta (Aβ) peptides and have minor effects on their aggregation. *Acta Biochimica Polonica*, 68(2):169–179, 2021.

[349] M. Komiya, M. Kato, D. Tadaki, T. Ma, H. Yamamoto, R. Tero, Y. Tozawa, M. Niwano, and A. Hirano-Iwata. Advances in artificial cell membrane systems as a platform for reconstituting ion channels. *The Chemical Record*, 20(7):730–742, 2020.

APPENDICES

Appendix A

Supplementary Materials

A.1 Membranes Embedded with Amyloid-β

Figure A.1 shows SLB embedding with Aβ oligomers. The retention of Aβ peptides in lipid membrane was also observed in the study by Siniscalco *et al.* [144]. The variety in membrane interaction could be due to the diverse sizes of Aβ1-42 oligomers as well as the retention time of Aβ within the membrane. Mrdenovic *et al.* perceived the process of pore expansion and enclosure as Aβ oligomers penetrated and fused membranes from 0 min to 91 min by time-lapse AFM [265]. These AFM images (Fig. A.1, Fig. 6.8 (b) and (d) in the main text) confirm the Aβ-membrane interaction and explain the variety of Aβ-induced current flow observed in our BLM recordings.

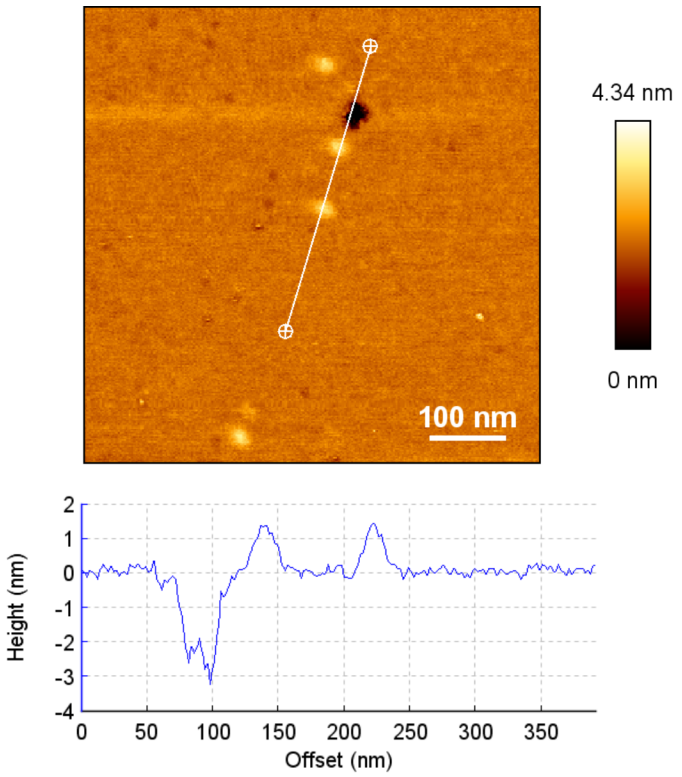


Figure A.1: Supported lipid bilayer (SLB) embedding with Aβ oligomers

A.2 Determination of Sensor Sensitivity m

The calculated bulk sensitivity m is 162.44 nm/RIU (refractive index unit), indicated as the slope in Fig. A.2, evaluated using bulk glucose solutions with a concentration gradient and measured refractive index.

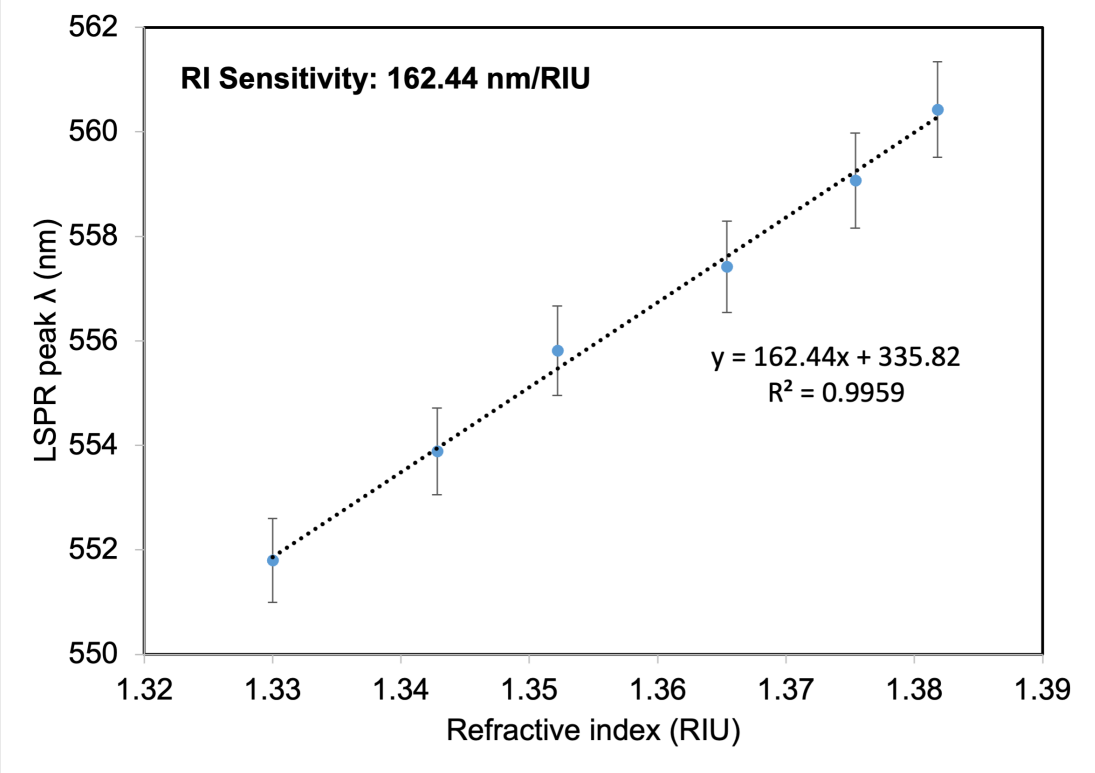


Figure A.2: LSPR peaks corresponding to glucose solutions with different RI. The sensor sensitivity m is determined as the slope of the linear-fit curve.

A.3 Comparison between Vertical BLM and Horizontal BLM

Vertical black lipid membranes (vBLM) were suspended over a 150 μm aperture in a cuvette (Warner Instruments, USA) and transmembrane currents were recorded with an eONE amplifier (Elements, Italy).

The signal-to-noise ratio (SNR) was calculated using the definition SNR $= \mu/\sigma$, where μ is the mean of the current signal and σ is the standard deviation of the baseline in the electrophysiological recordings.

A.3.1 Amyloid-beta Behaviours in Horizontally-suspended Membranes vs Vertically-suspended Membrane

In the electrophysiological recording across vertically suspended planar lipid bilayers, Aβ1-42 oligomers also induced current increase, and the three current features (step, spike and bump) were also observed (Fig. A.3), which was consistent with the observation in horizontal membranes (Fig. 4.4).

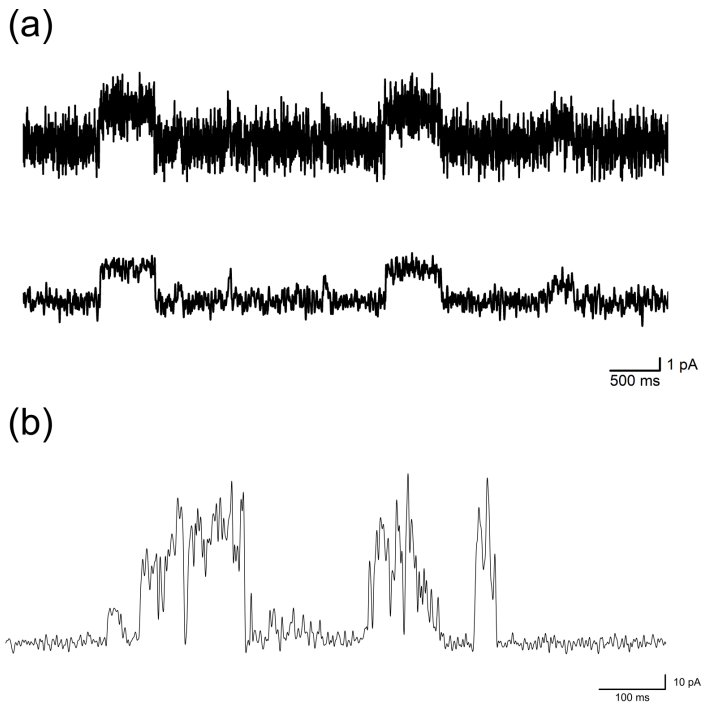


Figure A.3: Characteristic current signals due to Aβ-membrane interaction at 100 mV in vBLM. A) Step, spike and bump signals before (upper) and after (lower) filtered by 50 Hz Bessel filter. B) Irregular current signals by Aβ1-42 oligomers.

To compare the data from the two instruments, the ion-channel conductance with step-like current feature was compared after baseline subtraction. As shown in Fig. A.4, the current at which the plateau occurs at 100 mV in hBLM was 1.22 $\pm$ 0.03 pA (n = 134),

which was significantly smaller than the value (1.91 ± 0.08 pA, $n = 48$) in vBLM ($p < 0.05$). Correspondingly, the conductance of Aβ1-42 ion channels in hBLM was 12.16 ± 0.34 pS while in vBLM it was 19.12 ± 0.82 pS (Table A.1). The discrepancy could be the consequence of systematic differences between instruments. Compared to the built-in electrodes in hBLM, the Ag/AgCl electrodes in vBLM are exposed to the air, introducing more noise to recording, leading to larger baseline conductance before the occurrence of Aβ-membrane interactions and a smaller signal-to-noise ratio (SNR) at the occurrence of Aβ insertion. Consequently, it became difficult to distinguish the signals with small amplitude from the background. Another possible factor contributing to the poor SNR and baseline conductance of pure lipid membranes is the stability of the bilayers, which was higher in hBLM instead of vBLM. However, high membrane stability lowers the probability of protein incorporating lipid membranes [349]. Despite the aperture diameters in both devices being the same, the effective bilayer areas for protein-membrane interaction were different, based on the estimation of membrane capacitance. The membrane capacitance in hBLM was 4 - 6 pF while it lay in the 14 - 20 pF range in vBLM. This suggests that the bilayers in vBLM were less stable but had larger effective areas than those in hBLM — increasing the probability for protein incorporation, especially beneficial for the access of large protein aggregates to membranes. Hence, larger Aβ1-42 oligomers had more opportunity to approach lipid membranes and induce pore formation in membranes. Although these ion channels still have conductance values (19.12 ± 0.82 pS) smaller than previous reports (> 200 pS), the channel open time (598.11 ± 56.37 ms) fits the description of typical Aβ ion channels that opens longer than 500 ms in previous studies [146].

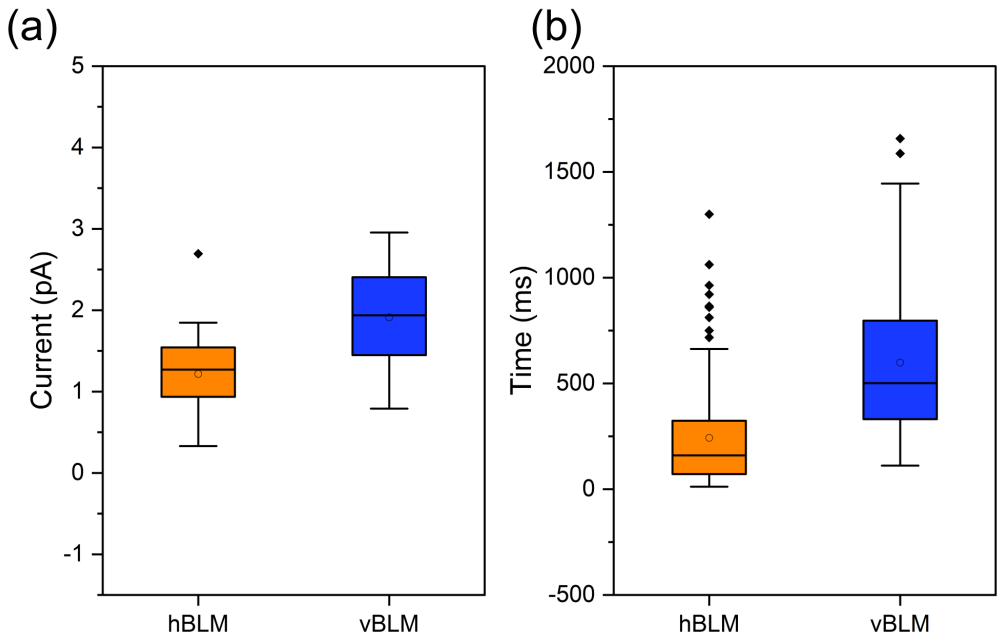


Figure A.4: Comparison of Aβ-induced signals between hBLM and vBLM. A) Step-like currents regarding to the conductance of Aβ ion channels B) Lifetime of Aβ ion channels.

Instruments	**Baseline conductance (pS)**	**Signal to Noise Ratio**	**Amyloid step mean current (pA) after baseline subtraction**	**Conductance after baseline subtraction (pS)**	**Lifetime of ion channels (ms)**
vBLM	1.75 ± 0.19	9.81	1.22 ± 0.03	12.16 $\pm$ 0.34	598.11 $\pm$ 56.37
hBLM	12.05 $\pm$ 0.27	4.29	1.91 ± 0.08	19.12 $\pm$ 0.82	242.65 $\pm$ 20.97

Table A.1: Result comparison between hBLM and vBLM